Autotrophic denitrification coupled to Fe(II)-oxidation driven by aquifer-originating bacteria

Dissertation

der Mathematisch-Naturwissenschaftlichen Fakultät

der Eberhard Karls Universität Tübingen

zur Erlangung des Grades eines

Doktors der Naturwissenschaften

(Dr. rer. nat.)

vorgelegt von

Natalia Jakus

aus Jaworzno, Polen

Tübingen

2021

Gedruckt mit Genehmigung der Mathematisch-Naturwissenschaftlichen Fakultät der Eberhard Karls Universität Tübingen.

Tag der mündlichen Qualifikation:	27.09.2021
Dekan:	Prof. Dr. Thilo Stehle
1. Berichterstatter:	Prof. Dr. Andreas Kappler
2. Berichterstatter:	Prof. Dr. Christian Griebler

Acknowledgements

First, I would like to thank Prof. Dr. Andreas Kappler, for his support, enormous enthusiasm, and guidance during my Ph.D. study. Andreas found my passion and determination in encountering new tasks and... challenged me even more. He gave me countless opportunities to develop new skills, learn new methods and work with incredibly talented people. Without his trust and encouragement, I would not have had so much confidence and experience today.

Second, I would like to thank Jun-Prof. Dr. Sara Kleindienst, who supported me, a *geo-*(logist) in my journey to become a *-microbiologist*. I especially appreciate the freedom that she offered me in exploring the fascinating world of microbial ecology, having full access to molecular biology labs. I am also thankful to Prof. Dr. Peter Grathwohl for all the inspiring meetings and for asking many thought provoking questions. Peter constantly motivated me to think broader and see the bigger picture behind my study. I was fortunate to have such a great team of supervisors!

My biggest thanks go to Dr. Nia Blackwell, who helped me tremendously through my entire Ph.D. by teaching, advising, and supporting me. Her knowledge, organization skills, kindness, and empathy were always inspirational and made me a better student (scientist?) and surely, a better person.

Thanks to all other CAMPOS members, who were very welcoming and heartwarming right from the beginning and quickly made me feel that I am a part of the big CAMPOS family. Special thanks to Dr. Karsten Osenbrück. Without him, fieldwork would not be possible. I also acknowledge CAMPOS Ph.D. students, especially my friends, Stefan and Johanna, who were always there when I needed to vent.

I thank the entire Geomicrobiology group for giving me the tools and strength to complete my studies. It is impossible to list here everything that I learned from each of you. I am grateful for being surrounded by so many excellent scientists and lovely people. Ellen, Lars, Beth, Ulf, Martyna, Verena, Christopher, Lea, Markus, Yuge, Manuel, Casey, James, special thanks to you!

Here I also need to mention my exceptional officemates: Anh, Steffi, and Timm, with whom I have never had the chance to share the office. You are the most extraordinary, chaotic, and crazy group of people I have ever met, yet extremely important in my life.

Thank you for all serious and non-serious, scientific and non-scientific discussions. Thank you for listening and making me laugh, no matter what. Also, thanks to my real ZAG- and GUZ- officemates (Hanna, Kartin, Eric, Diego, Zhe, Zhen, Yuge, Markus), who have seen me staring in bewilderment at my computer screen for most of the time, nevertheless were very sympathetic.

Further, I would like to acknowledge my colleagues from the Microbial Ecology group, in particular: Franzi, Kate, Constantin, Saskia, Yu-Ming, Adrian, Sergey, Daniel, Anjela, and Julia, who were happy to answer any of my questions and helped me to grow as microbial ecologist. Monday seminars were always my absolute favorite!

This work would not be possible without many students who hugely helped me in the lab: Alessandra, Caro, Jonah, Lydia, Jimena, Imke, and others. Thank you!

I would also like to thank my family for accepting my choice and being supportive when I decided to move abroad. Furthermore, I thank my colleagues and friends from Poland, Paweł O., Ewa, Maciek K., Paweł K., Kacha, Aga, and Nikola, for their hospitability and heartwarming enthusiasm whenever I was back in the country. Finally, thanks go to my friends from far away, Karol and Mariola, for believing in me like anyone else.

Last but not least, I thank Michał for his trust in the path I have chosen and for following me all the way to Germany. Your support, patience, and company always empowered me and helped me go through difficult times. I am proud of how well you adapted to live in this peculiar environment/bubble of *wanna-be-scientists* and how enthusiastic you became. By far, you are the most knowledgeable microbe-, mineral- and Mössbauer spectroscopy-amateur among all software engineers! Dziękuję że jesteś, nie mogłabym wymarzyć sobie lepszego wsparcia.

Table of contents

Summary

Autotrophic denitrification coupled to pyrite oxidation is considered a natural nitrate attenuation process in aquifers limited in organic carbon. However, autotrophic nitrate-reducing Fe(II)-oxidizing (NRFeOx) bacteria have neither been isolated nor enriched from this type of habitat and, as such, there are no model cultures to study this environmentally relevant process. As a consequence, identity, physiology, and the genetic repertoire of the microbial key players coupling nitrate reduction to Fe(II) oxidation, which live among groundwater denitrifying communities, is unknown. Moreover, the lack of evidence for direct enzymatic pyrite oxidation by autotrophic NRFeOx bacteria and the poor solubility of this mineral at circumneutral pH, raises a critical question about the underlying oxidation mechanism.

To study autotrophic nitrate-dependent Fe(II) oxidation in aquifers, a pyrite-rich fractured aquifer depleted in organic carbon was selected as a sampling site. The aquifer is located in southwest Germany (Baden-Württemberg), in the catchment of the Ammer River, where most of the landscape is dominated by agriculture. Intensive farming activity in this area has led to elevated nitrate concentrations in groundwater, which locally exceed the maximum limits of nitrate in drinking water defined by European quality standards (50 mg/L). Some of the anoxic parts of this aquifer, however, are characterized by nitrate concentrations approximating 1.5 mg/L (1.5±0.6 mg/L). It was therefore hypothesized that the observed low nitrate values are most likely a result of nitrate reduction driven by autotrophic bacteria, which can oxidize inorganic electron donors such as pyrite that is present within the rock matrix.

To evaluate the hypothesis, and address the knowledge gaps listed above, the goals of this Ph.D. thesis were to: (1) obtain a model culture of autotrophic NRFeOx bacteria to study the physiology of microbial key players involved in nitrate reduction coupled to Fe(II) oxidation in nitrate polluted aquifers limited in organic carbon, (2) characterize the microbial community structure and identity of the enriched NRFeOx culture and (3) determine rates, ratios and solid, liquid and gaseous products of nitrate dependent Fe(II) oxidation in laboratory experiments. Further goals were to: (4) test in culture-based experiments whether the NRFeOx bacteria originating from the aquifer can mediate pyrite oxidation and (5) identify the mechanism, differentiating between indirect (induced) or direct (enzymatic) microbial oxidation of pyrite. Lastly, this work intended to: (6) identify the key genomic features that allow these bacteria to perform autotrophic nitrate reduction coupled to Fe(II) oxidation and (7) evaluate how changing supply of substrates that may occur in the aquifer, influences the structure of denitrifying communities inhabiting the aquifer.

An autotrophic NRFeOx enrichment culture was obtained from the aquifer by incubating crushed pyrite-rich limestone particles in a low-nitrate groundwater monitoring well. The exposure resulted in an enrichment of NRFeOx cells that were then transferred to nitrate- and Fe(II)-containing microbial medium

without the addition of organic carbon. The culture was maintained under these conditions for over 21 transfers, until it was evident that the enriched microbial community could continuously perform nitrate reduction coupled to Fe(II) oxidation and sustain cell growth. Within 7-11 days, the autotrophic NRFeOx enrichment culture reduced 0.3-0.5 mM of nitrate and oxidized 1.3-2 mM of Fe(II), leading to a stoichiometric $NO_3^-{}_{reduced}/Fe(II)_{oxidized}$ ratio of 0.2, suggesting that complete denitrification occurred. However, both N_2 and N_2O were identified as nitrate reduction products. Microorganisms were observed to be closely associated with formed minerals, identified as short-range ordered Fe(III) (oxyhydr)oxides, but only a few cells were encrusted, indicating that most of the bacteria were able to avoid mineral precipitation at their surface. Long-read 16S rRNA gene sequencing of the community revealed that the culture was dominated by bacteria related to the *Gallionellaceae* family. Members of this family, are known as autotrophic, neutrophilic, microaerophilic iron(II)-oxidizers but were also found in NRFeOx communities, suggesting that they may be potential key players in autotrophic nitrate reduction coupled to Fe(II) oxidation.

Next, to identify the mechanism of pyrite oxidation by NRFeOx bacteria and to evaluate whether the oxidation of the more soluble Fe(II)-carbonate ($FeCO_3$) can indirectly drive abiotic pyrite oxidation, the autotrophic culture was incubated together with nitrate, pyrite with natural abundance (^{NA}) of Fe isotopes (^{NA}Fe-pyrite), and ^{57}Fe-labelled siderite. The results showed that in setups where pyrite and nitrate were incubated with bacteria, direct microbial pyrite oxidation contributed ca. 26% to overall nitrate reduction. The rest was attributed to the oxidation of elemental sulfur (S^0) that was present as a residue from pyrite synthesis. Pyrite oxidation was evidenced in setups containing both ^{NA}Fe-pyrite and ^{57}Fe-siderite by maps of ^{56}FeO and ^{32}S obtained using a combination of SEM with NanoSIMS. The maps clearly demonstrated the presence of ^{56}Fe(III) (oxyhydr)oxides that could solely originate from the oxidation of ^{56}FeS2. Based on the fit of a reaction model to the geochemical data and the Fe-isotope distributions from NanoSIMS, it was concluded that the contribution of abiotic pyrite oxidation by Fe^{3+} appeared to be negligible in the experimental setups and anaerobic oxidation of pyrite was mainly driven by the direct enzymatic activity of the NRFeOx bacteria.

Finally, the key microbial players in nitrate removal and the genomic features that allow NRFeOx bacteria to perform continuous autotrophic nitrate reduction coupled to Fe(II) oxidation were identified by a combination of culture-dependent studies, and 16S rRNA gene and metagenome sequencing. Additionally, the impact of O_2, Fe(II), and organic carbon availability on the structure of denitrifying communities originating from the organic-poor, pyrite-rich aquifer was investigated by comparison of three metabolically distinct microbial assemblages, supplemented with acetate, acetate/Fe(II), or Fe(II). The presence of Fe(II) promoted the growth of denitrifying *Burkholderiaceae* spp. and an unclassified *Gallionellaceae* sp. Interestingly, even though *Gallionellaceae* spp. are typically known as microaerophilic Fe(II) oxidizers, *Gallionellaceae* sp. dominating the autotrophic NRFeOx culture, was not able to survive under microoxic conditions, suggesting its adaptation to respire in strictly anoxic environments. The adaptation was confirmed by analysis of the metagenome-assembled genome (MAG) of this microbe, which revealed that the *Gallionellaceae* sp. can perform near-complete denitrification leading to N_2O production (*narGHJI, nirK/S,* and *norBC* genes). Besides the *Gallionellaceae* sp. MAG,

four other MAGs, belonging to a *Curvibacter* spp., *Methyloversatilis* sp., and *Thermomonas* sp. were found to have genes related to both nitrate reduction and Fe(II) oxidation (e.g., *cyc2*), and therefore were classified as putative NRFeOx taxa.

The findings presented in this thesis, provide first insights into physiology, identity, and the genetic traits of the so far only known autotrophic NRFeOx culture originating from an aquifer, giving geochemical and genomic basis to study the mechanisms of nitrate removal in organic-poor subsurface ecosystems. Additionally, the results support that at circumneutral pH, pyrite oxidation coupled to nitrate reduction is an enzymatically driven microbial process, which may explain the decrease in nitrate concentrations at the study field site. Although the pyrite oxidation coupled to nitrate reduction is metabolically feasible, the exact mechanism is still unclear on a molecular level, and as such, future research should focus on the reconstruction of the electron transfer pathway between pyrite, bacterial cells and nitrate. More work also needs to be done on disentangling the potential interspecies interdependencies existing within the aquifer-originating autotrophic NRFeOx culture and identification and quantification of all biotic, and abiotic processes that contribute to overall nitrate removal. This knowledge is necessary to both understand the complexity of nitrate removal in the environment but also to ultimately isolate the most wanted, truly autotrophic NRFeOx bacteria.

Zusammenfassung

Die an Pyrit-Oxidation gekoppelte autotrophe Denitrifikation wird als natürlicher Prozess zur Reduktion von Nitrat in Grundwasserleitern mit wenig organischem Kohlenstoff betrachtet. Jedoch gibt es keine Modellkulturen zur Untersuchung dieses umweltrelevanten Prozesses, da autotrophe nitrat-reduzierende Fe(II)-oxidierende (NRFeOx) Bakterien aus einem solchem Habitat weder isoliert, noch angereichert wurden. Folglich sind Identität, Physiologie und das genetische Repertoire der Mikroorganismen, die in einer, im Grundwasser vorkommenden, denitrifizierenden mikrobiellen Gemeinschaft leben und eine Schlüsselrolle für die Fe(II)-oxidations-gekoppelte Nitrat-Reduktion spielen unbekannt. Des Weiteren lässt dieser Oxidationsmechanismus aufgrund der fehlenden Nachweise für eine direkte enzymatische Pyrit-Oxidation durch autotrophe NRFeOx-Bakterien und der schlechten Löslichkeit dieses Minerals bei zirkumneutralem pH-Wert viele Fragen offen.

Um die autotrophe nitrat-abhängige Fe(II)-Oxidation in Grundwasserleitern zu untersuchen, wurde ein pyrit-haltiger, geklüfteter Grundwasserleiter, welcher arm an organischem Kohlenstoff ist, für die Probenahme ausgewählt. Der Grundwasserleiter befindet sich im Südwesten Deutschlands (Baden-Württemberg), im Einzugsgebiet der Ammer, wo das Land größtenteils landwirtschaftlich genutzt wird. Durch die landwirtschaftliche Belastung ist die Nitratkonzentrationen im Grundwasser in diesem Gebiet erhöht. Teilweise überschreitet sie die durch europäische Qualitätsnormen definierten Höchstwerte für Nitrat im Trinkwasser (50 mg/L). Jedoch weisen einige der anoxischen Teile dieses Grundwasserleiters nur Nitratkonzentrationen von ~ 1.5 mg/L (1.5±0.6 mg/L) auf. Daher wurde die Hypothese aufgestellt, dass die niedrigen Nitratwerte auf die Nitrat-Reduktion zurückzuführen sind, die durch autotrophe Bakterien, die anorganische Elektronendonatoren wie Pyrit, welches im Gestein vorhanden ist, oxidieren können.

Um diese Hypothese zu überprüfen und die oben aufgeführten Wissenslücken zu schließen, waren die Ziele dieser Doktorarbeit: (1) eine Modellkultur aus autotrophen NRFeOx-Bakterien zu erhalten, um die Physiologie der Mikroorganismen zu untersuchen, die hauptsächlich an der Fe(II)-oxidations-gekoppelten Nitrat-Reduktion in Nitrat belasteten und organischem Kohlenstoff armen Grundwasserleitern, beteiligt sind, (2) die Zusammensetzung dieser mikrobiellen Gemeinschaft und die Identität der angereicherten NRFeOx-Kultur zu charakterisieren und (3) die Raten, Verhältnisse und festen, flüssigen und gasförmigen Produkte der nitrat-abhängigen Fe(II)-Oxidation in Laborexperimenten zu bestimmen. Weitere Ziele waren: (4) in Kultivierungs-Experimenten zu testen, ob die aus dem Grundwasserleiter stammenden NRFeOx-Bakterien die Oxidation von Pyrit verursachen können und (5) den Mechanismus zu identifizieren, wobei zwischen indirekter (induzierter) oder direkter (enzymatischer) mikrobieller Oxidation von Pyrit unterschieden wurde. Schließlich beabsichtigte diese Arbeit: (6) die wichtigsten genomischen Merkmale zu identifizieren, die es diesen Bakterien ermöglichen, eine autotrophe Fe(II)-

oxidations-gekoppelte Nitrat-Reduktion durchzuführen und (7) die Beurteilung, wie eine sich verändernde Versorgung vom Grundwasserleiter auftretenden Substraten, die Zusammensetzung der denitrifizierenden mikrobiellen Gemeinschaften, welche den Grundwasserleiter bewohnen, beeinflusst.

Eine autotrophe NRFeOx-Anreicherungskultur wurde aus dem Grundwasserleiter durch Inkubation von zerkleinerten pyrit-haltigen Kalksteinpartikeln in einem nitrat-armen Grundwassermessbrunnen gewonnen. Diese Exposition führte zu einer Anreicherung von NRFeOx-Bakterien, die dann in ein nitrat- und Fe(II)-haltiges Medium ohne Zugabe von organischem Kohlenstoff überführt wurden. Die Kultur wurde über 21 mal überführt und unter diesen Bedingungen gehalten, bis sich zeigte, dass die angereicherte mikrobielle Gemeinschaft kontinuierlich Fe(II)-oxidations-gekoppelte Nitrat-Reduktion durchführt und sein Zellwachstum aufrecht erhält. Innerhalb von 7-11 Tagen reduzierte die autotrophe NRFeOx-Anreicherungskultur 0.3-0.5 mM Nitrat und oxidierte 1.3-2 mM Fe(II). Dies entspricht einem stöchiometrischen $NO_3^-{}_{reduzierten}/Fe(II)_{oxidierten}$ Verhältnis von 0.2. Obwohl das darauf hin deutet, dass eine vollständige Denitrifikation stattfand, konnten sowohl N_2 als auch N_2O als Produkte der Nitrat-Reduktion identifiziert werden. Außerdem, wurde beobachtet, dass die Mikroorganismen eng mit den gebildeten Mineralien assoziiert waren, welche als kurz geordnete Fe(III)-(Oxyhydr)oxide identifiziert wurden. Nur wenige Zellen waren verkrustet, was darauf hindeutet, dass die meisten Bakterien in der Lage waren, die Ausfällung von Mineralien an ihrer Oberfläche zu vermeiden. Die Long-Read 16S rRNS-Gen-Sequenzierung der mikrobiellen Gemeinschaft ergab, dass die Kultur von Bakterien dominiert wurde, die zur Familie der *Gallionellaceae* gehören. Mitglieder dieser Familie, die als autotrophe, neutrophile, mikroaerophile Eisen(II)-Oxidierer bekannt sind, wurden auch in der NRFeOx-Gemeinschaften gefunden, was darauf hindeutet, dass sie potenziell an der autotrophen, Fe(II)-oxidations-gekoppelten Nitrat-Reduktion hauptsächlich beteiligt sind.

Um den Mechanismus der Pyrit-Oxidation durch NRFeOx-Bakterien zu identifizieren und zur Evaluierung ob die Oxidation des löslicheren Fe(II)-carbonats ($FeCO_3$) indirekt die abiotische Pyrit-Oxidation ermöglicht, wurde die autotrophe Kultur mit Nitrat, Pyrit und Siderit inkubiert. Der Pyrit bestand aus Fe-Isotopen natürlicher Häufigkeit (^{NA}Fe-Pyrit) und das Siderit war ^{57}Fe-markiert. Die Ergebnisse aus den Versuchsansätzen, in denen Pyrit und Nitrat mit Bakterien inkubiert wurden zeigten, dass die direkte mikrobielle Pyrit-Oxidation zu ~ 26% zur gesamten Nitrat-Reduktion beitrug. Der verbleibende Anteil wurde der Oxidation von elementarem Schwefel (S^0), ein Nebenproduckt der Pyrit-Synthese, zugeordnet. Die Pyrit-Oxidation wurde in Versuchsansätzen, die sowohl ^{NA}Fe-Pyrit als auch ^{57}Fe-Siderit enthielten, mithilfe von Karten welche das Vorkommen von ^{56}FeO und ^{32}S abbildeten, nachgewiesen. Diese konnten durch die Kombination zweier Methoden, SEM und NanoSIMS erstellt werden. Diese Karten zeigten deutlich das Vorhandensein von ^{56}Fe(III)-(Oxyhydr)oxiden, die ausschließlich aus der Oxidation von $^{56}FeS_2$ stammen konnten. Basierend auf der Ausgleichungsrechnung eines Reaktionsmodells an die geochemischen Daten und die Fe-Isotopenverteilungen aus der NanoSIMS Messung, wurde gefolgert, dass der Anteil der abiotischen Pyrit-Oxidation durch Fe^{3+} in den Versuchsansätzen vernachlässigbar zu sein schien und die anaerobe Oxidation von Pyrit hauptsächlich durch die direkte enzymatische Aktivität der NRFeOx-Bakterien katalysiert wurde.

Schließlich wurden die wichtigsten Mikroorganismen für die Nitratumwandlung identifiziert und die genomischen Merkmale, welche es diesen NRFeOx-Bakterien ermöglichen eine kontinuierliche autotrophe Fe(II)-oxidations-gekopplete Nitratreduktion durchzuführen bestimmt. Diese Ergebnisse konnten aus einer Kombination von Kultivierungs-Experimenten und 16S rRNS-Gen- und Metagenom-Sequenzierungen gewonnen werden. Zusätzlich wurde der Einfluss von O_2, Fe(II) und der Verfügbarkeit von organischem Kohlenstoff auf die Zusammensetzung von der denitrifizierenden mikrobiellen Gemeinschaft aus dem organisch armen, pyrit-reichen Grundwasserleiter untersucht. Hierzu diente der Vergleich von drei metabolisch unterschiedlichen mikrobiellen Kulturen, die jeweils mit Acetat, Acetat/Fe(II) oder Fe(II) supplementiert wurden. Die Präsenz von Fe(II) förderte das Wachstum von denitrifizierenden *Burkholderiaceae* spp. und einer nicht klassifizierten *Gallionellaceae* sp. Die *Gallionellaceae* sp. dominierte die autotrophe NRFeOx-Kultur, konnte jedoch, interessanterweise, nicht unter mikrooxischen Bedingungen überleben, obwohl *Gallionellaceae* spp. typischerweise als mikroaerophile Fe(II)-Oxidierer bekannt sind. Dies deutet darauf hin, dass die hier beschriebene *Gallionellaceae* sp. an eine Atmung in streng anoxischen Umgebungen angepasst ist. Diese Anpassung wurde durch die Analyse des Metagenome Assembled Genomes (MAG) dieser Spezies bestätigt. Sie ergab, dass die *Gallionellaceae* sp. eine nahezu vollständige Denitrifikation durchführen kann, die zur N_2O-Produktion führt (*narGHJI*, *nirK/S* und *norBC* Gene). Neben der *Gallionellaceae* sp. MAG wurden bei vier weiteren MAGs, die zu *Curvibacter* spp., *Methyloversatilis* sp. und *Thermomonas* sp. gehören, Gene gefunden, die sowohl mit der Nitrat-Reduktion als auch mit der Fe(II)-Oxidation zusammenhängen (z. B. *cyc2*). Diese Spezies wurden daher als vermeintliche NRFeOx-Taxa klassifiziert.

Die in dieser Arbeit vorgestellten Ergebnisse geben erste Einblicke in die Physiologie, Identität und die genetischen Eigenschaften der bisher einzigen bekannten autotrophen NRFeOx-Kultur aus einem Grundwasserleiter. Dies bietet eine geochemische und genomische Grundlage für die Untersuchung der Mechanismen des Nitratabbaus in organisch armen unterirdischen Ökosystemen. Zusätzlich unterstützen die Ergebnisse, dass bei zirkumneutralem pH-Wert die Pyrit-Oxidation an Nitrat-Reduktion gekoppelt und ein enzymatisch katalysierter mikrobieller Prozess ist. Dieser Befund, könnte die verringerten Nitrat-Konzentrationen am Untersuchungsstandort erklären. Es konnte zwar gezeigt werden, dass es einen biochemischen Stoffwechselweg für eine Pyrit-oxidations-gekoppelte Nitrat-Reduktion gibt, jedoch ist der genaue Mechanismus auf molekularer Ebene noch unklar. Daher sollte sich zukünftige Forschung auf die Entschlüsselung des Elektronentransferweges zwischen Pyrit, Bakterienzellen und Nitrat konzentrieren. Des Weiteren muss mehr Forschungsarbeit erbracht werden, um die potenziellen Inter-Spezies-Abhängigkeiten der aus dem Grundwasserleiter stammenden autotrophen NRFeOx-Kultur zu verstehen und um alle biotischen und abiotischen Prozesse die zum gesamten Nitratumsatz beitragen, zu identifizieren und zu quantifizieren. Dieses Wissen ist notwendig, um sowohl die Komplexität des Nitratabbaus in der Umwelt zu verstehen, als auch um die wissenschaftlich wertvollen, tatsächlich autotrophen NRFeOx-Bakterien schlussendlich zu isolieren.

Abbreviations

AAI	Average amino acid identity
ANI	Average nucleotide identity
ASV	Amplicon sequence variant
AVS	Acid volatile sulfides
CLSM	Confocal laser scanning microscopy
CRS	Chromium reducible sulfides
DNA	Deoxyribonucleic acid
DNRA	Dissimilatory nitrate reduction to ammonium
EDTA	Ethylenediaminetetraacetic acid
EET	Extracellular electron transfer
FeOB	Fe(II)-oxidizing bacteria
FISH	Fluorescence *in-situ* hybridization
FT-ICR-MS	Fourier transform ion cyclotron resonance mass spectrometry
LPM	Low phosphate medium
MAG	Metagenome-assembled genome
MLSA	Multilocus sequence analysis
MTD	Microbial trapping devices
NRFeOx	Nitrate-reducing Fe(II)-oxidizing
NA	Natural abundance
NanoSIMS	Nanoscale secondary ion mass spectrometry
NDAMO	Nitrite dependent anaerobic methane oxidation
NMR	Nuclear magnetic resonance
PCR	Polymerase chain reaction
RNA	Ribonucleic acid
RuBisCO	Ribulose bisphosphate carboxylase-oxygenase
SEM	Scanning electron microscope
VBF	Voigt Based Fitting
XRD	X-ray diffraction

1. Introduction

1.1. Nitrate pollution in aquifers

Nitrate (NO_3^-) is one of the critical groundwater pollutants, posing a serious threat to drinking water quality and, as a consequence, to human health (World Health Organization 2011). Nitrate is introduced into aquifers through a variety of agricultural activities such as the widespread application of N-containing fertilizers (Kim *et al.* 2015). In 2020, more than half of all monitored European countries (16 out of 28), were reported to have groundwater bodies with an average nitrate concentration above the EU Groundwater Quality Standard of 50 mg/L NO_3^- (European Union 2006), indicating that nitrate pollution is still one of the most important European environmental issues. Only efficient identification of all nitrate removal-controlling elements will allow developing effective strategies for nitrate pollution management in affected regions.

1.2. Nitrate removal pathways

The fate of nitrate in anoxic groundwater depends on the activity of microorganisms that can remove it either by denitrification or dissimilatory nitrate reduction to ammonium (DNRA) (Henson *et al.* 2017). Denitrification is an anaerobic respiratory process in which dissolved nitrate is reduced to nitrite (NO_2^-) and further to nitric oxide (NO), nitrous oxide (N_2O) and dinitrogen (N_2) via a series of enzymatic steps mediated by a wide range of bacterial and archaeal taxa (Kuypers, Marchant and Kartal 2018). Not all microorganisms, however, are capable of complete denitrification and other intermediates (e.g. N_2O) can be formed as a product of nitrate reduction. Similar to denitrification, DNRA is a stepwise reduction of NO_3^- via NO_2^- that is further reduced to NH_4^+ (Robertson and Thamdrup 2017). The factors controlling the dominant nitrate removal pathway are, for example, pH, the type and complexity of the electron donors, the bioavailability of electron acceptors, and the resulting ratio of carbon to nitrate (van den Berg *et al.* 2017). In environments with high nitrogen to carbon ratio, like many oligotrophic aquifers, denitrification is favored over DNRA (Tiedje 1988; Burgin and Hamilton 2010).

Bacteria reducing nitrate via denitrification are called denitrifiers and can be divided into three metabolic types: heterotrophic, autotrophic, and mixotrophic, depending on whether they gain energy from the oxidation of organic compounds, inorganic compounds, or both, respectively (Bryce *et al.* 2018). Additionally, some heterotrophic bacteria may indirectly induce abiotic oxidation of reduced inorganic compounds (e.g. Fe(II)) by the formation of reactive N-intermediates (NO_2^-, NO). Such bacteria are called

chemodenitrifiers and since the enzymatic component involved in the oxidation of the inorganic compound is missing, they do not benefit energetically from this process (Klueglein and Kappler 2013; Bryce *et al.* 2018; Onley *et al.* 2018; Kappler *et al.* 2021).

Groundwater ecosystems are typically poor in organic carbon compounds (Griebler and Lueders 2009; Dvorski *et al.* 2016), which restricts the overall contribution of the heterotrophic microorganisms to nitrate reduction. Under such organics-limited conditions, autotrophic denitrifying microbial communities prevail (Herrmann *et al.* 2017; Kumar *et al.* 2018), utilizing inorganic substrates e.g. reduced S-species or Fe(II). Microorganisms that couple denitrification to Fe(II) oxidation according to the following reaction:

$$10Fe^{2+} + 2NO_3^- + 24H_2O \rightarrow 10Fe(OH)_3 + N_2 + 18H^+$$

are called nitrate-reducing Fe(II) oxidizing (NRFeOx) bacteria (Straub *et al.* 1996a; Bryce *et al.* 2018; Kappler *et al.* 2021). By oxidation of Fe(II) and reduction of NO_3^-, NRFeOx bacteria generate energy that is then partially used for CO_2 fixation needed for biomass production. This process requires circumneutral pH and reducing conditions where Fe(II) can be found as dissolved Fe^{2+}, alternatively complexed by organic matter (Fe(II)-OM) (Hopwood *et al.* 2015; Bhattacharyya *et al.* 2018) or as a component of Fe(II)-bearing minerals such as Fe(II)-rich clays, or Fe(II) minerals like siderite ($FeCO_3$) or pyrite (FeS_2) (Weber, Picardal and Roden 2001).

1.3. Pyrite as a potential electron donor for nitrate reduction

Pyrite is the most abundant iron−sulfur mineral on Earth's surface (Rickard and Luther 2007) and, as such, it is often a prevalent accessory constituent of sedimentary aquifers. The best-studied oxidants at circumneutral pH of pyrite are O_2 and Fe(III) (Moses *et al.* 1987; Campos *et al.* 2016). Although both oxidants abiotically oxidize structural sulfur embedded in pyrite (abiotic pyrite-S oxidation), parallel microbially mediated reactions can enhance the kinetics and extent of pyrite weathering (indirect microbial pyrite-S oxidation).

Oxidation of pyrite-S by O_2 consists of two steps and is initiated by attachment of O_2 molecules to the surface of pyrite and followed by breaking the double bond in the O_2 and displacement by H_2O of an S_2OH^- molecule. The S_2OH^- is then abiotically oxidized to sulfate (SO_4^{2-}) via sulfoxy intermediates e.g. thiosulfate (S_2O_3). In this process, only the sulfur part of pyrite is oxidized and leads to the release of Fe(II). Bacteria can change the kinetics of this process by utilization of sulfoxy intermediates which accelerates the conversion of pyrite-S to SO_4^{2-}. For example, an enrichment culture was shown to increase rates of pyrite oxidation under microoxic pH-neutral conditions by an order of magnitude compared to abiotic rates (Percak-Dennett *et al.* 2017). It is not clear, however, whether microbial oxidation proceeded through oxidation of sulfoxy species by sulfur-oxidizers or by bacterially-mediated oxidation of Fe(II) triggering Fe(III)-driven pyrite oxidation mechanism.

The Fe(III)-driven oxidation can occur only in the presence of Fe(II) (derived either from pyrite-S oxidation or from an external source). In this scenario, Fe(II) adsorbs to the surface of pyrite (Fe(II) is a preferred adsorbate over Fe(III)). After that, Fe(II) is oxidized by O_2 and forms reactive Fe(III), which due to electron transfer from pyrite to oxygen, undergoes rapid reduction to form Fe(II) again. The process can be repeated until a stable sulfoxy species (e.g., SO_4^{2-}) dissociates from the surface. Fe(II)-oxidizing bacteria can accelerate pyrite oxidation by oxidizing adsorbed Fe(II) to produce reactive Fe(III). Although Fe(III) is the preferred reactant over O_2, this reaction mechanism involves electron transfer from adsorbed Fe(II) to dissolved O_2, meaning that the reaction can be only sustained in the presence of oxygen. Additionally, in circumneutral environments, the reaction is limited by the immediate precipitation of aqueous Fe^{3+} to Fe(III) (Peiffer and Stubert 1999; Schippers and Jorgensen 2002), however isotopic evidence has provided support for anaerobic FeS_2 oxidation with Fe(III) as the oxidant in marine sediments (Bottrell *et al.* 2000).

Many studies have linked the oxidation of iron sulfides to nitrate reduction (Peiffer and Stubert 1999; Haaijer *et al.* 2007; Torrentó *et al.* 2011, 2012; Bosch *et al.* 2012; Vaclavkova *et al.* 2015) and emphasized the importance of this process in sandy (Postma *et al.* 1991; Jørgensen *et al.* 2009; Zhang *et al.* 2012), schist (Pauwels *et al.* 1998), clay and gravel (Schwientek *et al.* 2008), and limestone (Visser *et al.* 2020) aquifers. The mechanisms of pyrite-mediated denitrification, however, remain unclear, with several studies arriving at contradictory conclusions (Yan *et al.* 2019). The discrepancy between observations has recently been linked to an overestimation of Fe(III) due to possible abiotic reaction of nitrite with pyrite during acidic Fe(II) extraction, a procedure often used to quantify pyrite oxidation (Yan, Kappler and Peiffer 2015), or overestimation of sulfate that can derive not only from pyrite oxidation but also form oxidation of elemental sulfur, a common residue after pyrite synthesis, or internally cell-stored sulfur (Yan *et al.* 2019).

Two recent studies focused on the understanding the mechanisms underlying denitrification coupled to pyrite oxidation, pointed on the key role of electron shuttles or organic ligands in this process. Pang and Wang (2020) proposed that bacteria can facilitate pyrite oxidation via extraction of redox-active molecules, which can transfer the electron from insoluble pyrite to nitrate, releasing S-intermediates such as S^0 that may further be used as an electron donor for autotrophic denitrifying bacteria. Other studies demonstrated that the process of microbial pyrite oxidation coupled to nitrate reduction may be accelerated by addition of ethylenediaminetetraacetic acid (EDTA; Liu *et al.* 2021), an organic ligand, leading to formation of Fe(III)-EDTA complex that was earlier shown to oxidize pyrite abiotically at neutral pH (Peiffer and Stubert 1999). It has been also proposed that microbially mediated oxidation of pyrite coupled to nitrate reduction may occur directly via. extracellular electron transfer (EET) between the pyrite and a dedicated protein at the cell membrane, however this mechanism has been never confirmed for autotrophic NRFeOx bacteria.

Deciphering the mechanisms of autotrophic pyrite oxidation coupled to nitrate reduction is in particularly challenging, since it requires batch incubation experiments and the examples of autotrophic NRFeOx cultures are scarce and to date, there is no model culture originating from a pyrite-rich anoxic environment.

1.4. Nitrate-dependent Fe(II)-oxidizing bacteria

The only NRFeOx culture that was unequivocally demonstrated to be truly autotrophic, is the well-studied enrichment culture KS (named after Kristina Straub) (Straub *et al.* 1996b; Bryce *et al.* 2018). Culture KS, together with recently enriched culture BP (named after the location of isolation, Bremen Pond), originate from organic carbon-rich freshwater sediments collected from a town ditch and a pond in Bremen (Germany) (Huang *et al.* 2021a). Yet, the cultures were shown to continuously grow without the addition of organic carbon over several transfers and generate energy from nitrate reduction coupled to Fe(II) oxidation. Both cultures are mixed bacterial communities dominated (86-98% relative abundance) by *Gallionellaceae* spp. (Huang *et al.* 2021a), which are typically known as autotrophic microaerophilic Fe(II) oxidizers (Emerson *et al.* 2013). Besides autotrophs, the cultures consist of other bacteria, including heterotrophic denitrifiers. Therefore, nitrate reduction coupled to Fe(II) oxidation performed by these cultures was concluded to be a result of metabolic hand-offs occurring within the bacterial assemblage rather than a process mediated by a particular member of the community. For example, the metagenome-assembled genome (MAG) of the *Gallionellaceae* sp. from culture KS, contains genes involved in Fe(II) oxidation (putative Fe(II)-oxidases, e.g. *cyc2, mtoAB*), carbon fixation (e.g. *rbcL*), reduction of NO_3^- (e.g. *narG*) and NO2- (e.g. *nirK/S*) but lacks genes involved in NO (e.g. *norBC*) and N_2O reduction, suggesting that other bacteria, such as denitrifying *Rhodanobacter* sp., are required to remove toxic NO and complete nitrate reduction to N_2 (He *et al.* 2017; Huang *et al.* 2021a). A similar network of microbial interactions between *Gallionellaceae* sp. and several other Fe(II)-oxidizers and denitrifiers was recently reconstructed in culture BP, in a study using a combination of cultivation-based and multiple meta'omic techniques (Huang *et al.* 2021b). Although denitrification is not linked to phylogeny (Jones *et al.* 2008), several other recent culture-independent studies, also pointed to the potential key role of *Gallionellaceae* spp. in nitrate reduction coupled to Fe(II) oxidation in aquifers (Jewell *et al.* 2016; Bethencourt *et al.* 2020), however the extent of nitrate reduction coupled to Fe(II) oxidation by these *Gallionellaceae* spp. dominated groundwater communities remains unknown.

1.5. The study field site

The aquifer elected to study autotrophic nitrate reduction coupled to Fe(II) oxidation, is situated in the "Oberes Gäu", southwest Germany (Baden-Württemberg), approximately 30 km southwest of Stuttgart. Part of this regional aquifer underlies the catchment of the Ammer river and it is the major drinking water supply in the area. The geological setting of the aquifer is dominated by karstified and fractured Triassic carbonates of the Upper Muschelkalk (Figure 1). The bedrock consists of dolomitic, micritic, and bioclastic pyrite-bearing limestones with a pyrite concentration of 4.1±1.4 mg/g of rock. The land use of this catchment at the regional scale is homogeneous with about 67% of the area being used for agriculture. Intensive agriculture activities lead to elevated nitrate concentrations in the groundwater with the median nitrate concentrations between 29.8 and 38.3 mg/L, as measured in the monitoring wells located in uncovered Muschelkalk layers. Similar or slightly higher concentrations of 35 to 54.4 mg/L are observed

at the karstic spring of the Ammer river that integrates over part of the catchment (Figure 1). Low nitrate concentrations observed in this aquifer were, according to hydrochemical and isotopic data, attributed to bacterial activity leading to nitrate reduction. However, there was no clear evidence on which electron donor is involved in this process, since the DOC concentrations were generally low (<0.3 mM), suggesting that other pathways than heterotrophic denitrification may play a role. A low-nitrate (1.5±0.6 mg/L of NO_3^-) and anoxic (dissolved O_2 of 0.1±0.1 mg/L) artesian well (48° 33' 47.52" N, 8° 53' 59.279" E) was therefore selected as a potential hot spot for *in-situ* driven autotrophic microbial nitrate reduction to test the hypothesis of whether pyrite, abundant in the rock matrix, can serve as the electron donor.

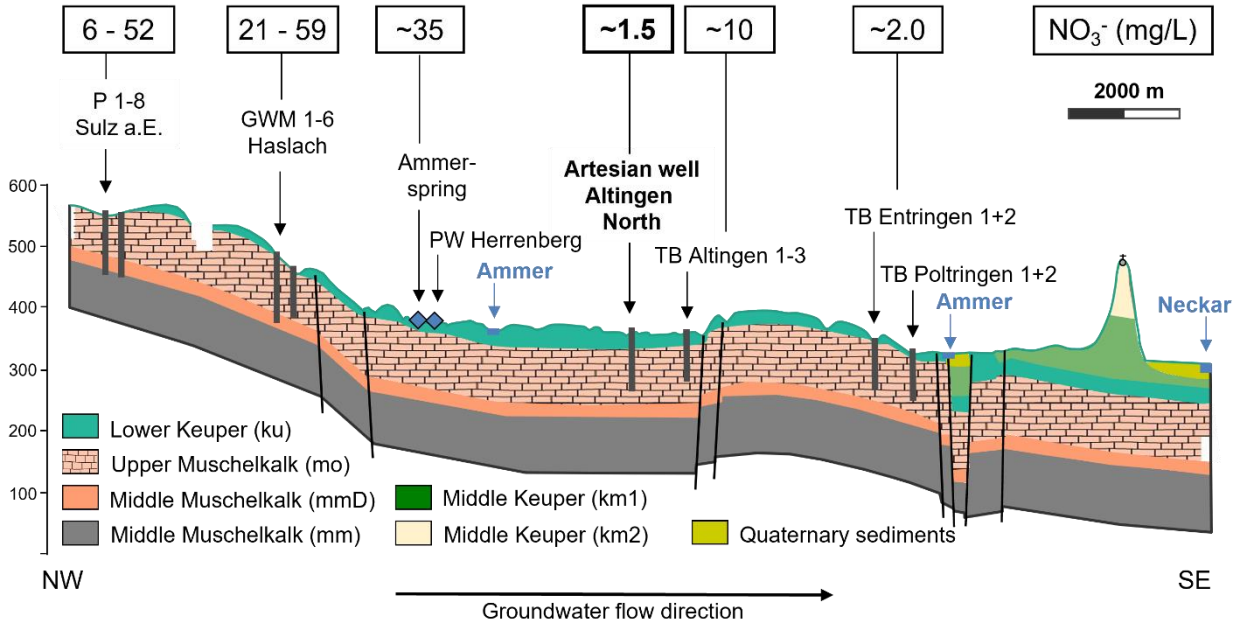

Figure 1. Geological cross section and location of selected wells, including artesian well selected for sampling (**bold font**), following the general groundwater flow direction (horizontal arrow) in the studied fractured aquifer. Values above indicate average nitrate concentrations determined for the wells.

1.6. Open questions and the focus of this thesis

Autotrophic denitrification coupled to pyrite oxidation is considered a natural nitrate attenuation process in organic carbon-limited aquifers and it was hypothesized to be one of the possible nitrate removal mechanisms in the pyrite-rich aquifer underlying the Ammer river catchment in southwestern Germany. Yet, autotrophic nitrate-reducing Fe(II)-oxidizing (NRFeOx) bacteria have not been isolated from any aquifer, and as such, there are no model cultures to study this environmentally important process. Therefore the open questions are: (1) what is the identity of microbial key players driving nitrate reduction coupled to Fe(II) oxidation in aquifers and what are the rates of this reaction?, (2) what is the mechanism of pyrite oxidation mediated by NRFeOx bacteria?, (3) what are the key genetic traits that allow

groundwater-inhabiting NRFeOx bacteria to continuously perform nitrate reduction Fe(II) oxidation under autotrophic conditions and how the community structure changes depending on the supply of substrates?.

To evaluate the hypothesis and answer these open questions, the work featured in this thesis focused on the following objectives:

I. Obtain a model lithoautotrophic NRFeOx culture to study autotrophic denitrification in aquifers.
   a. Isolate/enrich an autotrophic culture from the pyrite-rich aquifer polluted with nitrate.
   b. Determine the rates of nitrate reduction and Fe(II), and characterize products of this reaction.
   c. Evaluate the capacity of the culture to perform continued autotrophic denitrification coupled to Fe(II) oxidation over several growth transfers by monitoring the consumption of substrates and cell growth.
   d. Characterize the community structure and the identity of the bacterial in the culture.

II. Determine the mechanism of pyrite oxidation by autotrophic NRFeOx bacteria.
   a. Perform incubation experiments using the lithoautotrophic enrichment NRFeOx culture, pyrite, and siderite (representing Fe(II)-rich carbonates present in the field site).
   b. Determine the extent of nitrate reduction when coupled to microbially mediated oxidation of Fe(II) minerals.
   c. Identify the mineral products of pyrite and siderite oxidation.
   d. Differentiate between direct and indirect microbial oxidation of pyrite.

III. Identify microbial key players in nitrate removal in the aquifer.
   a. Investigate how the availability of organic carbon, O_2, and Fe(II) shapes the community structure of denitrifiers living in the aquifer.
   b. Investigate the metagenome of the lithoautotrophic enrichment NRFeOx culture to identify genetic traits involved in nitrate reduction coupled to Fe(II) oxidation and predict the metabolism of the most abundant microorganisms growing in the enrichment culture.
   c. Evaluate the potential role of the *Gallionellaceae* sp. growing in the aquifer-originating microbial assemblage in nitrate reduction coupled to Fe(II) oxidation and compared the results to the so-far best-studied autotrophic NRFeOx enrichment cultures KS and BP.

References

van den Berg EM, Rombouts JL, Kuenen JG *et al.* Role of nitrite in the competition between denitrification and DNRA in a chemostat enrichment culture. *AMB Express* 2017;**7:91**:1–7.

Bethencourt L, Bochet O, Farasin J *et al.* Genome reconstruction reveals distinct assemblages of *Gallionellaceae* in surface and subsurface redox transition zones. *FEMS Microbiol Ecol* 2020;**96**:1–13.

Bhattacharyya A, Schmidt MP, Stavitski E *et al.* Iron speciation in peats: Chemical and spectroscopic evidence for the co-occurrence of ferric and ferrous iron in organic complexes and mineral precipitates. *Org Geochem* 2018;**115**:124–37.

Bosch J, Lee KY, Jordan G *et al.* Anaerobic, nitrate-dependent oxidation of pyrite nanoparticles by *Thiobacillus denitrificans*. *Environ Sci Technol* 2012;**46**:2095–101.

Bottrell SH, Parkes RJ, Cragg BA *et al.* Isotopic evidence for anoxic pyrite oxidation and stimulation of bacterial sulphate reduction in marine sediments. *J Geol Soc London* 2000;**157**:711–4.

Bryce C, Blackwell N, Schmidt C *et al.* Microbial anaerobic Fe(II) oxidation - ecology, mechanisms and environmental implications. *Environ Microbiol* 2018;**20**:3462–83.

Burgin AJ, Hamilton SK. Have we overemphasized the role of denitrification in aquatic ecosystems? A review of nitrate removal pathways. *Front Ecol Environ* 2010;**5**:89–96.

Campos E, Santos D, Cec J *et al.* Pyrite oxidation mechanism by oxygen in aqueous medium. 2016;**120**:2760–2768Dvorski SE, Gonsior M, Hertkorn N *et al.* Geochemistry of dissolved organic matter in a spatially highly resolved Groundwater petroleum hydrocarbon plume cross-section. *Environ Sci Technol.* 2016; **50(11)**:5536-46

Emerson D, Field EK, Chertkov O *et al.* Comparative genomics of freshwater Fe-oxidizing bacteria: Implications for physiology, ecology, and systematics. *Front Microbiol* 2013;**4**:1–17.

European Union. Directive 2006/118/EC of the European Parliament and of the council of 12 December 2006 on the protection of groundwater against pollution and deterioration. *Off J Eur Union* 2006;**19**:19–31.

Griebler C, Lueders T. Microbial biodiversity in groundwater ecosystems. *Freshw Biol* 2009;**54**:649–77.

Haaijer SCM, Lamers LPM, Smolders AJP *et al.* Iron sulfide and pyrite as potential electron donors for microbial nitrate reduction in freshwater wetlands. *Geomicrobiol J* 2007;**24**:391–401.

He S, Barco RA, Emerson D *et al.* Comparative genomic analysis of neutrophilic iron(II) oxidizer genomes for candidate genes in extracellular electron transfer. *Front Microbiol* 2017;**8**:1–17.

Henson WR, Huang L, Graham WD *et al.* Nitrate reduction mechanisms and rates in an unconfined eogenetic karst aquifer in two sites with different redox potential. *J Geophys Res Biogeosciences* 2017;**122**:1062–77.

Herrmann M, Opitz S, Harzer R *et al.* Attached and suspended denitrifier communities in pristine limestone aquifers harbor high fractions of potential autotrophs oxidizing reduced iron and sulfur compounds. *Microb Ecol* 2017;**74**:264–77.

Hopwood MJ, Statham PJ, Skrabal SA *et al.* Dissolved iron(II) ligands in river and estuarine water. *Mar Chem* 2015;**173**:173–82.

Huang Y-M, Straub D, Blackwell N *et al.* Meta-omics reveal *Gallionellaceae* and *Rhodanobacter* as interdependent key players for Fe(II) oxidation and nitrate reduction in the autotrophic enrichment culture KS. *Revis* 2021a, DOI: 10.1128/aem.00496-21.

Huang Y-M, Straub D, Kappler A *et al.* A novel enrichment culture highlights core features of microbial networks contributing to autotrophic Fe(II) oxidation coupled to nitrate reduction. *Microb Physiol* 2021b;**In press**.

Jewell TNM, Karaoz U, Brodie EL *et al.* Metatranscriptomic evidence of pervasive and diverse chemolithoautotrophy relevant to C, S, N and Fe cycling in a shallow alluvial aquifer. *ISME J* 2016;**10**:2106–17.

Jones CM, Stres B, Rosenquist M *et al.* Phylogenetic analysis of nitrite, nitric oxide, and nitrous oxide respiratory enzymes reveal a complex evolutionary history for denitrification. *Mol Biol Evol* 2008;**25**:1955–66.

Jørgensen CJ, Jacobsen OS, Elberling B *et al.* Microbial oxidation of pyrite coupled to nitrate reduction in anoxic groundwater sediment. *Environ Sci Technol* 2009;**43**:4851–7.

Kappler A, Bryce C, Mansor M *et al.* An evolving view on biogeochemical cycling of iron. *Nat Rev Microbiol* 2021, DOI: 10.1038/s41579-020-00502-7.

Kim H, Kaown D, Mayer B *et al.* Identifying the sources of nitrate contamination of groundwater in an agricultural area (Haean basin, Korea) using isotope and microbial community analyses. *Sci Total Environ* 2015;**533**:566–75.

Klueglein N, Kappler A. Abiotic oxidation of Fe(II) by reactive nitrogen species in cultures of the nitrate-reducing Fe(II) oxidizer *Acidovorax* sp. BoFeN1 – questioning the existence of enzymatic Fe(II) oxidation. *Geobiology* 2013;**11**:180–90.

Kumar S, Herrmann M, Blohm A *et al.* Thiosulfate- and hydrogen-driven autotrophic denitrification by a microbial consortium enriched from groundwater of an oligotrophic limestone aquifer. *FEMS Microbiol Ecol* 2018;**94**:1–13.
Kuypers MMM, Marchant HK, Kartal B. The microbial nitrogen-cycling network. *Nat Rev Microbiol* 2018;**16**:263–76.
Liu T, Hu Y, Chen N *et al.* High redox potential promotes oxidation of pyrite under neutral conditions: Implications for optimizing pyrite autotrophic denitrification. *J Hazard Mater* 2021;**416**:125844.
Moses CO, Kirk Nordstrom D, Herman JS *et al.* Aqueous pyrite oxidation by dissolved oxygen and by ferric iron. *Geochim Cosmochim Acta* 1987;**51**:1561–71.
Onley JR, Ahsan S, Sanford RA *et al.* Denitrification by *Anaeromyxobacter dehalogenans*, a common soil bacterium lacking the nitrite reductase genes *nirS* and *nirK*. *Appl Environ Microbiol* 2018;**84**:1–14.
Pang Y, Wang J. Insight into the mechanism of chemoautotrophic denitrification using pyrite (FeS_2) as electron donor. *Bioresour Technol* 2020;**318**:124105.
Pauwels H, Kloppmann W, Foucher JC *et al.* Field tracer test for denitrification in a pyrite-bearing schist aquifer. *Appl Geochemistry* 1998;**13**:767–78.
Peiffer S, Stubert I. The oxidation of pyrite at pH 7 in the presence of reducing and nonreducing Fe(III)-chelators. *Geochim Cosmochim Acta* 1999;**63**:3171–82.
Percak-Dennett E, He S, Converse B *et al.* Microbial acceleration of aerobic pyrite oxidation at circumneutral pH. *Geobiology* 2017;**15**:690–703.
Postma D, Boesen C, Kristiansen H *et al.* Nitrate reduction in an unconfined sandy aquifer: water chemistry, reduction processes, and geochemical modeling. *Water Resour Res* 1991;**27**:2027–45.
Robertson EK, Thamdrup B. The fate of nitrogen is linked to iron(II) availability in a freshwater lake sediment. *Geochim Cosmochim Acta* 2017;**205**:84–99.
Schippers A, Jorgensen BB. Biogeochemistry of pyrite and iron sulfide oxidation in marine sediments. *Geochim Cosmochim Acta* 2002;**66**:85–92.
Schwientek M, Einsiedl F, Stichler W *et al.* Evidence for denitrification regulated by pyrite oxidation in a heterogeneous porous groundwater system. *Chem Geol* 2008;**255**:60–7.
Straub KL, Benz M, Schink B *et al.* Anaerobic, nitrate-dependent microbial oxidation of ferrous iron. *Appl Environ Microbiol* 1996a;**62**:1458–60.
Straub KL, Benz M, Schink B *et al.* Anaerobic, nitrate-dependent oxidation of ferrous iron. *Appl Environ Microbiol* 1996b;**62**:1458–60.
Tiedje JM. Ecology of denitrification and dissimilatory nitrate reduction to ammonium. *Environ Microbiol Anaerobes* 1988:179–244.
Torrentó C, Urmeneta J, Edwards KJ *et al.* Characterization of attachment and growth of *Thiobacillus denitrificans* on pyrite surfaces. *Geomicrobiol J* 2012;**29**:379–88.
Torrentó C, Urmeneta J, Otero N *et al.* Enhanced denitrification in groundwater and sediments from a nitrate-contaminated aquifer after addition of pyrite. *Chem Geol* 2011;**287**:90–101.
Vaclavkova S, Schultz-Jensen N, Jacobsen OS *et al.* Nitrate-controlled anaerobic oxidation of pyrite by *Thiobacillus* cultures. *Geomicrobiol J* 2015;**32**:412–9.
Visser AN, Lehmann MF, Rügner H *et al.* Fate of nitrate during groundwater recharge in a fractured karst aquifer in Southwest Germany. *Hydrogeol J* 2020;**29**:1153–71.
Weber KA, Picardal FW, Roden EE. Microbially catalyzed nitrate-dependent oxidation of biogenic solid-phase Fe(II) compounds. *Environ Sci Technol* 2001;**35**:1644–50.
World Health Organization. Guidelines for drinking-water quality, forth ed. 2011.
Yan R, Kappler A, Muehe EM *et al.* Effect of reduced sulfur species on chemolithoautotrophic pyrite oxidation with Nntrate. *Geomicrobiol J* 2019;**36**:19–29.
Yan R, Kappler A, Peiffer S. Interference of nitrite with pyrite under acidic conditions: Implications for studies of chemolithotrophic denitrification. *Environ Sci Technol* 2015;**49**:11403–10.
Zhang Y-C, Slomp CP, Broers HP *et al.* Isotopic and microbiological signatures of pyrite-driven denitrification in a sandy aquifer. *Chem Geol* 2012;**300**–**301**:123–32.

2. Nitrate removal by a novel lithoautotrophic nitrate-reducing iron(II)-oxidizing culture enriched from a pyrite-rich limestone aquifer

Natalia Jakus[a,b], Nia Blackwell[b], Karsten Osenbrück[c], Daniel Straub[b,d], James M. Byrne[a], Zhe Wang[e], David Glöckler[f], Martin Elsner[f], Tillmann Lueders[e], Peter Grathwohl[c], Sara Kleindienst[b], Andreas Kappler[a]

[a]Geomicrobiology, Center for Applied Geoscience, University of Tuebingen, Germany

[b]Microbial Ecology, Center for Applied Geoscience, University of Tuebingen, Germany

[c]Hydrogeochemistry, Center for Applied Geoscience, University of Tuebingen, Germany

[d]Quantitative Biology Center (QBiC), University of Tuebingen, Germany

[e]Chair of Ecological Microbiology, Bayreuth Center of Ecology and Environmental Research (BayCEER), University of Bayreuth, Germany

[f]Analytical Chemistry and Water Chemistry, Technical University of Munich, Munich, Germany

Abstract

Nitrate removal in oligotrophic environments is often limited by the availability of suitable organic electron donors. Chemolithoautotrophic bacteria may play a key role in denitrification in aquifers depleted in organic carbon. Under anoxic and circumneutral pH conditions, iron(II) was hypothesized to serve as an electron donor for microbially mediated nitrate reduction by Fe(II)-oxidizing (NRFeOx) microorganisms. However, lithoautotrophic NRFeOx cultures have never been enriched from any aquifer and as such there are no model cultures available to study the physiology and geochemistry of this potentially environmentally relevant process. Using iron(II) as an electron donor, we enriched a lithoautotrophic NRFeOx culture from nitrate-containing groundwater of a pyrite-rich limestone aquifer. In the enriched NRFeOx culture that does not require additional organic co-substrates for growth, within 7-11 days 0.3-0.5 mM of nitrate was reduced and 1.3-2 mM of iron(II) was oxidized leading to a stoichiometric NO_3^-/Fe(II) ratio of 0.2, with N_2 and N_2O identified as the main nitrate reduction products. Short-range ordered Fe(III) (oxyhydr)oxides were the product of iron(II) oxidation. Microorganisms were observed to be closely associated with formed minerals but only few cells were encrusted, suggesting that most of the bacteria were able to avoid mineral precipitation at their surface. Analysis of the microbial community by

long-read 16S rRNA gene sequencing revealed that the culture is dominated by members of the Gallionellaceae family that are known as autotrophic, neutrophilic, microaerophilic iron(II)-oxidizers. In summary, our study suggests that NRFeOx mediated by lithoautotrophic bacteria can lead to nitrate removal in anthropogenically impacted aquifers.

Importance

Removal of nitrate by microbial denitrification in groundwater is often limited by low concentrations of organic carbon. In these carbon-poor ecosystems, nitrate-reducing bacteria that can use inorganic compounds such as Fe(II) (NRFeOx) as electron donors could play a major role in nitrate removal. However, no lithoautotrophic NRFeOx culture has been successfully isolated or enriched from this type of environment and as such there are no model cultures available to study the rate-limiting factors of this potentially important process. Here we present the physiology and microbial community composition of a novel lithoautotrophic NRFeOx culture enriched from a fractured aquifer in southern Germany. The culture is dominated by a putative Fe(II)-oxidizer affiliated with the *Gallionellaceae* family and performs nitrate reduction coupled to Fe(II) oxidation leading to N_2O and N_2 formation without the addition of organic substrates. Our analyses demonstrate that lithoautotrophic NRFeOx can potentially lead to nitrate removal in nitrate-contaminated aquifers.

2.1. Introduction

High concentrations of nitrate (NO_3^-) in groundwater cause negative effects both on human health and the environment (World Health Organization 2011; Ward *et al.* 2018). In agricultural areas, nitrate is mostly derived from application of nitrogen-based chemicals and organic fertilizers (Kim *et al.* 2015). This nitrate input can lead to excessive nitrate concentrations that are responsible for low groundwater quality and pollution of drinking water supplies (Wick, Heumesser and Schmid 2012; Opazo, Aravena and Parker 2016). The guideline value for nitrate present in freshwaters set by the World Health Organization and the European Union to protect groundwater is 50 mg/L (Drinking Water Directive 98/83/EC, (World Health Organization 2011)). Therefore, water remediation and nitrate removal are necessary to protect public health and the entire ecosystem.

Industrial technologies for nitrate removal from drinking water include approaches divided into separation-based and elimination-based methods. Many of those methods are considered inefficient and expensive or may generate hazardous concentrated waste that requires careful disposal (Jensen *et al.* 2014; Rezvani *et al.* 2019). In natural ecosystems, nitrate removal is usually mediated in the absence of oxygen or at low oxygen concentrations by different microbial processes. In denitrification, nitrate is reduced stepwise to dinitrogen (N_2) gas. Denitrifying bacteria mediate a series of sequential reduction reactions as follows:

$$NO_3^- \rightarrow NO_2^- \rightarrow NO \rightarrow N_2O \rightarrow N_2.$$

Gaseous intermediates and end products are released to the atmosphere. A second process, called dissimilatory nitrate reduction to ammonium (DNRA), results in the production of ammonium and the retention of nitrogen in the ecosystem (Robertson and Thamdrup 2017). The factors that may determine the activity of these different pathways are e.g. pH, sulfide concentrations, the type and complexity of the electron donors, the bioavailability of electron acceptors, and the resulting ratio of carbon to nitrate (van den Berg *et al.* 2017). Under carbon-limited conditions, when the ratio is low, denitrification is favored over DNRA (Tiedje 1988; Burgin and Hamilton 2010). Most of the microbial denitrifiers described so far are heterotrophs and therefore need an organic carbon source to be able to reduce nitrate (Rivett *et al.* 2008). However, in oligotrophic systems such as many aquifers, bacteria are often limited in organic carbon compounds, which influences the potential of microbially mediated nitrate reduction and inhibits the activity of heterotrophs (Herrmann *et al.* 2017; Kumar *et al.* 2018a).

Besides organic matter, denitrifying microorganisms can also utilize various inorganic electron donors, such as iron(II), reduced sulfur compounds, H_2 or even U(IV) (Capua *et al.* 2019). Bacteria that require organic carbon in addition to iron(II) as a co-substrate (e.g. acetate) were called mixotrophic nitrate-reducing iron(II)-oxidizing (NRFeOx) bacteria (Benz, Brune and Schink 1998; Kappler, Schink and Newman 2005; Muehe *et al.* 2009; Liu *et al.* 2019). It seems that none of the well-studied mixotrophic strains are actually able to oxidize Fe(II) enzymatically (Bryce *et al.* 2018). Instead, most of them probably cause Fe(II) oxidation by triggering an abiotic reaction of Fe(II) with reactive nitrogen species

that are by-products of heterotrophic denitrification (Klueglein and Kappler 2013; Nordhoff *et al.* 2017). Therefore, they are not considered true mixotrophs and instead have been called chemodenitrifiers (Bryce *et al.* 2018; Kappler *et al.* 2021). Purely autotrophic NRFeOx bacteria such as the lithoautotrophic NRFeOx culture KS, enriched about two decades ago from a freshwater sediment (Straub *et al.* 1996a; Blöthe and Roden 2009; Tominski *et al.* 2018), were shown to use only inorganic carbon (HCO_3^-) to build biomass and enzymatically mediate the oxidation of iron(II) coupled to the complete reduction of NO_3^- (Beller 2005; Bryce *et al.* 2018; Capua *et al.* 2019) according to the following reaction:

$$10Fe^{2+} + 2NO_3^- + 24H_2O \rightarrow 10Fe(OH)_3 + N_2 + 18H^+ \quad (1)$$

This process requires reducing conditions where iron(II) is present as dissolved Fe^{2+}(aq) or as a component of iron(II)-bearing minerals (Weber, Picardal and Roden 2001), such as iron sulfides, e.g. pyrite (FeS_2) (Jørgensen *et al.* 2009; Herndon *et al.* 2017). Pyrite is often a prevalent accessory constituent of carbonate-rock (limestone, dolomite) aquifers and can serve as a source of reduced sulfur species and iron(II) promoting iron-dependent chemolithoautotrophic denitrification (Rimstidt and Vaughan 2003; Herrmann *et al.* 2015, 2017). A number of studies linked pyrite oxidation to nitrate reduction (Peiffer and Stubert 1999; Haaijer *et al.* 2007; Torrentó *et al.* 2011; Bosch *et al.* 2012; Vaclavkova *et al.* 2015; Percak-Dennett *et al.* 2017) and emphasize the importance of the NRFeOx process in freshwater aquifers (Postma *et al.* 1991; Pauwels 1994; Pauwels *et al.* 1998; Schwientek *et al.* 2008; Torrentó *et al.* 2010; Zhang *et al.* 2012; Jewell *et al.* 2016). Despite the environmental relevance, to date no lithoautotrophic NRFeOx bacteria have been isolated or even enriched from an oligotrophic aquifer and as such there are no model cultures to study the biogeochemistry of this potentially environmentally relevant process.

The objectives of the present work therefore were i) to enrich a lithoautotrophic Fe(II)-oxidizing denitrifying culture from a pyrite-rich and nitrate-contaminated aquifer and ii) to determine the rates of nitrate reduction coupled to iron(II) oxidation. We further intended to iii) evaluate the capacity of the culture to perform continued autotrophic denitrification coupled to iron(II) oxidation over several growth transfers and iv) to characterize the microbial community in the enrichment culture.

2.2. Materials and methods

2.2.1. Field site and sampling

The studied aquifer is located in southwest Germany (Baden-Württemberg) and is the major drinking water supply across the Ammer catchment. The land use of this catchment at the regional scale is homogeneous with about 67% of the area being used for agriculture. The geological setting of the aquifer is dominated by Triassic carbonates of the Upper Muschelkalk. Fractured bedrock consists of dolomitic, micritic and bioclastic pyrite-bearing limestones (Visser *et al.* 2020a) with a pyrite concentration of 4.1±1.4 mg/g of rock (determined by the AVS/CRS method, see SI). Groundwater is accessible for sampling via production wells and monitoring wells, which have a broad range of nitrate concentrations

(Figure S1). The median nitrate concentrations in the monitoring wells located in uncovered Muschelkalk layers are between 29.8 and 38.3 mg/L (0.35 and 0.45 mM). Similar or slightly higher concentrations of 42.5 to 54.4 mg/L (0.5 to 0.64 mM) were observed at the karstic spring of the Ammer river that integrates over part of the catchment. Based on that, we hypothesized that the changes of nitrate concentration were mainly driven by *in-situ* transformations and low nitrate concentrations were indicators of potential hot spots of microbial nitrate turnover. A low-nitrate anoxic artesian well (48° 33' 47.52" N, 8° 53' 59.279" E) was therefore selected for the enrichment of microbial key players involved in nitrate removal. During the observation period (2004-2018) the average nitrate concentration (n = 8) was 1.5±0.6 mg/L (0.02±0.01 mM), with a mean conductivity of 885.1±75.1 µS/cm (n = 9), circumneutral pH (7.1±0.1, n = 9) and an average temperature of 12.5±1.6°C (n = 9) was measured. The groundwater well had anoxic to suboxic conditions (dissolved O_2 of 0.1±0.1 mg/L, n = 4) and a mean dissolved organic carbon (DOC) concentration of 1.2±0.3 mg/L (n = 4).

Microbial communities used for enrichment cultures were sampled using passive samplers called microbial trapping devices (MTDs) (adapted from previous publications; (Griebler *et al.* 2002; Küsel *et al.* 2016; Herrmann *et al.* 2017)) filled with representative *in-situ* rock material (SI Figure S2). Fresh pyrite-bearing limestone was collected from Upper Muschelkalk outcrops, crushed with a hammer and a jaw crusher to 3-mm fragments, sterilized by autoclaving under anoxic conditions to minimize mineral transformations and exposed to UV light (8 W, S/L; Herolab GmbH Laborgeräte, Germany, UVC at 254 nm, exposure time 1 h). Rock particles were then transferred into sterile 10 cm-long Teflon tubing with 2 mm-diameter randomly distributed hole sizes (SI Figure S2). Rock material was fixed with sterile glass wool on both sides of the tubing to prevent loss of the material. MTDs were attached to a stainless-steel wire, deployed into the artesian well to the depth were water-conducting fractures were found (29-35 m below the ground) by deploying a camera into the well, and incubated for 4 months. This approach enabled the enrichment of microorganisms inhabiting pyrite-rich limestone that is building the aquifer. After incubation, the MTDs were collected, transferred to sterile anoxic jars filled with N_2, and stored wet for 4 weeks at 4°C in the dark until enrichment cultures were set up.

2.2.2. Setup of microbial enrichments and incubation conditions

Rock material with attached microbial communities obtained from incubated MTDs was distributed in a glovebox (100% N_2) and approximately 4 g were then transferred into separate sterile serum bottles (58 mL) that were filled with 25 mL of anoxic bicarbonate-buffered (22 mM) low phosphate medium (LPM), adjusted to pH 7.0-7.1 (Hegler *et al.* 2008). The concentration of selenite–tungstate solution (Widdel 1980) was decreased from 1.0 mL/L to a final concentration of 0.1 mL/L to eliminate a potential inhibitory effect of tungsten on the nitrate reductase, as it was reported previously by Burke et al. (Burke, Calder and Lascelles 1980). Bottles were closed with butyl rubber stoppers and crimped, the headspace flushed with N_2/CO_2 (90:10), and amended with 2 mM of $NaNO_3$ and 2 mM of $FeCl_2$. Adding Fe(II) was followed by the precipitation of vivianite and siderite (Kappler *et al.* 2010) that resulted in a final concentration of ca. 1.3 mM of dissolved iron(II), i.e. Fe^{2+}(aq). Enrichments were incubated at room

temperature in the dark and transferred to fresh medium every 2-3 weeks (for about a year in total) after complete oxidation of iron(II).

For quantification of rates and the extent of nitrate-dependent iron(II) oxidation, medium was prepared as described above (2 mM $NaNO_3$, 2 mM $FeCl_2$, pH 7.0-7.1) and inoculated with 10% (vol/vol) of the NRFeOx enrichment culture (that was cultivated over 21 subsequent transfers under lithoautotrophic conditions). Once at least 90% of Fe(II) has been oxidized, the microbial culture was transferred to fresh medium. Three continuous transfers were carried out to follow rates of Fe(II) oxidation and nitrate reduction over these three successive transfers. Sterile setups were used as controls. All cultures and abiotic controls were conducted in triplicates and incubated at room temperature in the dark. Final rates and ratios were calculated as an average of rates and ratios from each individual replicate.

Additionally, to analyze the gaseous products of nitrate reduction coupled to Fe(II) during growth of the autotrophic NRFeOx enrichment culture, a separate experimental setup was run using the same medium, substrates and inoculum volume as described above, except the medium was amended with ^{15}N-labeled $NaNO_3^-$ (for details see SI).

2.2.3. Cell counts, light microscopy and scanning electron microscopy (SEM)

Cell numbers were quantified using an Attune NxT flow cytometer (Thermo Fisher Scientific) equipped with a blue laser beam as an excitation source (488 nm). Prior to flow cytometry, an aliquot of the cells was stained using BacLight green stain (Thermo Fisher Scientific). Cells were distinguished from debris by their properties in the side-scatter and fluorescence parameters. All measurements were conducted in triplicates and the results reported as an average. A two-way ANOVA was used to test the effects of Fe(II) concentration on cell numbers using R (R Core Team 2018).

Transmission light and fluorescence microscopy was performed with a Leica DM5500 B epifluorescence microscope equipped with a 40x air objective (numerical aperture, 0.75). The filter sets applied were L5 (excitation filter, band-pass [BP] 480/40 nm; dichromatic mirror, 505 nm; suppressor filter, BP 527/39) and Y3 (excitation filter, BP 543/30; dichromatic mirror, 565 nm; suppressor filter, BP 610/75). Cells were stained with the LIVE/DEAD BacLight bacterial viability kit (Molecular Probes, Carlsbad, CA, USA). For SEM, samples were fixed with glutaraldehyde (2.5% final concentration) and left at 4°C overnight. A stepwise dehydration was performed by an ethanol dilution series with increasing ethanol concentrations (30%, 75%, 95% and twice 100%). Samples were then treated with hexamethyldisilazane (HMDS; Sigma-Aldrich, St. Louis, MO, USA) (Zeitvogel *et al.* 2016). Micrographs were collected at the Centre for Light-Matter Interaction, Sensors & Analyics ($LISA^+$), University of Tübingen. JEOL JSM-6500F field emission SEM with a Schottky-field-emitter were used. Working distances were approximately 10 mm and the acceleration voltage was 5.0 kV.

2.2.4. Chemical analyses

Samples were taken from the cultures daily in an anoxic glovebox (100% N_2) using a syringe with a needle through the butyl-rubber stopper and centrifuged (14,000 g, 10 min). For quantification of Fe(II) and Fe(III), a revised ferrozine protocol for nitrite-containing samples was used to eliminate the abiotic reaction of nitrite with Fe(II) during acidification (Klueglein and Kappler 2013; Schaedler, Kappler and Schmidt 2018). The purple ferrozine-Fe(II) complex was quantified at 562 nm using a microtiter plate reader; all ferrozine measurements were done in triplicate. Nitrate, nitrite, and ammonium samples were diluted with anoxic Milli-Q H_2O and stored under anoxic conditions at 4°C until analysis using a continuous-flow analyzer (flow injection analysis (FIA) system) was done, following standard protocols provided by the instrument manufacturer. The system is equipped with a dialysis membrane for Fe removal to prevent side reactions during analysis (3-Quattro; Bran & Luebbe, Seal Analytical, Norderstedt, Germany). Rates of microbial Fe^{2+} oxidation and nitrate reduction were calculated from the slope between the first and last data point in each of the three Fe(II) oxidation phases specified in detail later in the manuscript**.**

2.2.5. Mineralogical analysis

X-ray diffraction (XRD) was performed using Bruker's D8 Discover GADDS XRD^2 micro-diffractometer equipped with a standard sealed tube with a Co-anode (Co Kα radiation, $\lambda = 0.17903$ nm) at parameters of 30 kV/30 mA. The total time of measurement was 240 s at two detector positions (15 and 40°). Resulting diffractograms were analyzed using the software Match! (version 3.6.2.121). Phase identification of minerals was performed using Mössbauer spectroscopy. Liquid suspended mineral precipitates were passed through a filter (0.45 µm, Millipore) and then sealed between two layers of oxygen-impermeable adhesive polyimide film (Kapton) and sealed in a Schott bottle. The sample was inserted into a closed-cycle exchange gas cryostat (Janis cryogenics) with spectra measured at 77 K using a constant acceleration drive system (WissEL) in transmission mode with a ^{57}Co/Rh source and calibrated against a 7 µm thick α-^{57}Fe foil measured at room temperature. Spectra were analyzed using Recoil (University of Ottawa) by applying the Voigt Based Fitting (VBF) routine (Rancourt and Ping 1991). The half width at half maximum (HWHM) was fixed to a value of 0.125 mm/s for all samples, which was determined to be the inner line broadening of the calibration foil at room temperature.

2.2.6. Phylogenetic analysis

DNA from the enrichment culture was extracted with the FastDNA™ Spin Kit for Soil (MP Biomedicals) according to the user manual. 16S rRNA gene amplicons were analyzed using PacBio Sequel SMRT long-read amplicon sequencing. Two rounds of PCR were applied for DNA amplification. The first PCR was performed using the KAPA HiFi ReadyMix PCR Kit (KAPA BioSystems, Cape Town, South Africa) and universal 16S primers tailed with PacBio universal sequencing adapters (universal tags) and 5' amino modifiers C6 in a first round of PCR (27F gcagtcgaacatgtagctgactcaggtcacAGRGTTYGATYMTGGCTCAG, 1492R

tggatcacttgtgcaagcatcacatcgtagRGYTACCTTGTTACGACTT) (Eurofins Genomics, Ebersberg, Germany). The following PCR program was used for the first PCR with 26 cycles: initial denaturation for 3 minutes at 95°C, denaturation for 30 seconds at 95°C, annealing for 30 seconds at 57°C and extension for 60 seconds at 72°C. Amplicons were purified with the QIAquick PCR purification kit (QIAGEN, Hilden, Germany) according to the user manual. The second PCR was performed using the KAPA HiFi ReadyMix PCR Kit and PacBio Barcoded Universal F/R Primers Plate – 96 (Pacific Biosciences, California, USA), followed by AMPure PB bead kit (PacBio biosciences, California, USA) purification according to the user manual. The following PCR program was used for the second PCR with 20 cycles: denaturation for 30 seconds at 95°C, annealing for 30 seconds at 57°C and extension for 60 seconds at 72°C. The quality and quantity of PCR products were checked by an Agilent 2100 Bioanalyzer System (Agilent, California, USA) after each PCR. SMRTbell library preparation and further purification were achieved by SMRTbell Template Prep Kit (PacBio biosciences, California, USA) and by following the user instructions.

Circular consensus sequencing reads were analyzed with DADA2 v1.10.0 (Callahan *et al.* 2019) in R v 3.5.1 (R Core Team 2018) by sequentially orienting reads and removing primers, filtering (no ambiguous nucleotides and maximum 2 expected errors) and trimming (1000bp to 1600bp read length), dereplicating sequences, learning error rates, removing bimera de novo and finally assigning taxonomy to the detected sequences based on SILVA v132 (Callahan 2018). Results are discussed in the manuscript as relative bacterial 16S rRNA gene sequence abundance of ASVs as a proportion of the total number of reads per sample.

For constructing a phylogenetic tree, selected full-length 16S rRNA gene sequences (minimum length 1460 bp) from close relatives of dominant bacteria in the culture, as well as more distantly related known potential NRFeOx bacteria were downloaded from the NCBI database. Bacterial 16S rRNA gene sequence from *Mariprofundus ferrooxydans* PV-1, a microaerophilic Fe(II)-oxidizer belonging to the novel *Zetaproteobacteria* class, was chosen as an outgroup. MUSCLE implemented in the MEGA X software (Kumar *et al.* 2018b) was used for alignment of the 16S rRNA gene sequences with default parameters. A consensus Neighbor-Joining tree of the most abundant taxa from the enrichment culture was constructed in MEGA X using the maximum-likelihood method with 1000 bootstrap replicates.

2.3. Results and discussion

2.3.1. Identity of the enriched lithoautotrophic NRFeOx culture

Primary enrichment cultures from MTDs were incubated at room temperature in the dark and transferred to fresh medium every 2nd to 3rd week, when the cultures turned visually orange and dissolved Fe^{2+} was completely oxidized. In 7 out of 10 cultures, we observed Fe(II) oxidation and cell growth; one of these 7 was selected for further transfers and characterization. After 21 continuous transfers under neutrophilic Fe(II)-oxidizing and nitrate-reducing conditions with 2 mM of Fe(II) as the only electron donor, 2 mM

nitrate as the only electron acceptor added and CO_2 as the only carbon source, it was evident that the enriched microbial culture does not require any addition of organic carbon to sustain cell growth and therefore can be considered as a potentially lithoautotrophic culture. To our best knowledge, the enriched culture is only the third known lithoautotrophic NRFeOx culture that was shown to be continuously transferred under lithoautotrophic conditions, besides culture KS (Straub *et al.* 1996b) and the recently described culture BP (Huang *et al.* 2021). In addition, it is the only known lithoautotrophic NRFeOx culture enriched from an oligotrophic aquifer. Long-read 16S rRNA gene amplicon sequencing of the microbial community in the culture showed that it is dominated by *Betaproteobacteria* with the highest relative abundance of bacteria belonging to *Nitrosomonadales* order, related to the *Gallionellaceae* family (49%; Figure 1A.). Members of this family are known as obligate microaerophilic bacteria capable of autotrophic growth with Fe(II) as electron and energy source (Emerson *et al.* 2013).

Analysis of the long-read 16S rRNA gene analysis furthermore revealed that the dominant *Gallionellaceae sp.* in our culture has only 96.24% and 96.17% sequence similarity to the next closely-related, cultured microorganisms, *Ferrigenium kumadai* and *Gallionella capsiferriformans* ES-2, respectively. This suggests that the enriched microorganisms might represent a new species or genus within the *Gallionellaceae* family. Due to the limitation of 16S rRNA in gene comparison for novel taxa, the whole genome needs to be obtained for further phylogenic analysis. Closely related sequences were previously found in *in-situ* communities in aquifers and mineral springs of groundwater (Figure 1B). Additionally, bacteria belonging to the *Gallionellaceae* family were found to dominate the microbial community present in the groundwater monitoring well from which our culture was enriched, with up to 50% relative abundance of the population (Blackwell et al, unpublished data). This implies that *Gallionellaceae* spp. may be important members in freshwater communities and their environmental role should be further investigated using meta'omics studies.

The other culture for which lithoautotrophic Fe(II) oxidation coupled to nitrate reduction has been demonstrated unequivocally is culture KS, enriched from a freshwater ditch in Bremen, Germany (Straub *et al.* 1996a). Similar to our NRFeOx culture, culture KS is dominated by bacteria affiliated to *Gallionellaceae* family (Blöthe and Roden 2009; He *et al.* 2017), however, the most abundant presumed Fe(II)-oxidizer (*Gallionellaceae* sp.) from culture KS is 97.06% similar based on 16S rRNA gene sequence analysis to the *Gallionellaceae* sp. from this study. Recent metagenomic studies of culture KS further revealed that in this culture *Gallionellaceae* sp. is lacking NO and N_2O reductase genes, suggesting that, as complete denitrification is occurring in the culture (based on stoichiometry), toxic NO must be consumed and then converted to N_2 by other flanking community members (potentially heterotrophic NO- and N_2O-reducers). *Gallionellaceae* sp. in the culture KS, probably utilizes cyc2, MtoAB system or OmpB to transfer electrons from Fe(II) to cytochromes present in the inner membrane to reduce the quinone pool. Reduced ubiquinol could then be passed to the nitrate reductase in one direction for energy generation and in the other direction to generate NAD(P)H for carbon fixation. Therefore, as an autotroph, *Gallionellaceae* sp. may later support the community by providing reducing equivalents (potentially as organic carbon) for complete denitrification (He *et al.* 2016). This suggests that an efficient cooperation between *Gallionellaceae* sp. and other strains present in the culture KS guarantees robust and continuous

chemolithoautotrophic NRFeOx. Similar observations were recently made for another autotrophic enrichment NRFeOx culture, also originating from freshwater sediments (culture BP) which like the KS culture and the culture presented here, is also dominated by a member of the *Gallionellaceae* family. The metagenome-assembled genome of *Gallionellaceae* sp. from BP culture lacks NO_3^- and N_2O reductases therefore complete nitrate reduction and Fe(II) oxidation occurring in this culture were suggested to result rather from a complex network of microbial interactions among several Fe(II)-oxidizers and denitrifiers than by the activity of one species (Huang *et al.* 2021). However, it should be noted that since the ASVs of *Gallionellaceae* spp. in cultures KS, BP and the culture presented here, are different, the genomic traits and the role they play in the community may differ.

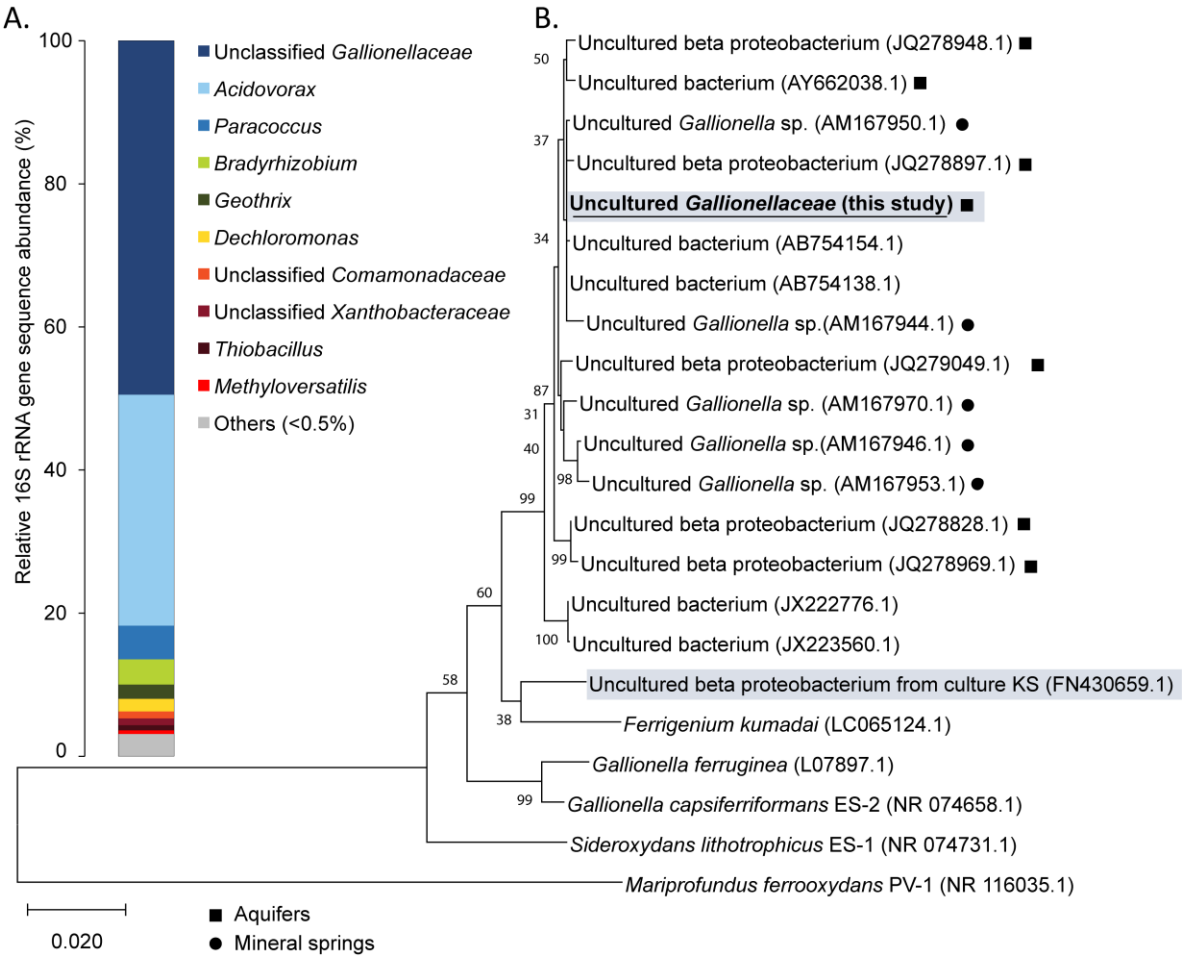

Figure 1. Relative abundance of taxa (A.) found in the autotrophic NRFeOx enrichment culture based on long-read 16S rRNA gene sequences, where sequence similarities to cultured representatives at family and genus level ranged from 96 to 100% (query coverage >99%), based on SINAsearch (Pruesse, Peplies and Glöckner 2012) using the SILVA 132 database. Neighbor-Joining phylogenetic tree (B.) constructed showing the relation of the most dominant bacterium in the enrichment culture (blue background, bold and underlined) and representative microaerophilic Fe(II)-oxidizers related to *Gallionella* spp. and *Sideroxydans* sp. including the most abundant representative of Gallionellaceae family present in culture KS (blue background). *Mariprofundus ferrooxydans* PV-1, a microaerophilic Fe(II)-oxidizer, was included as outgroup. The scale bar corresponds to 0.02 nucleotide substitutions per site. At the branches, high confidence (>50) bootstrap values (from 1000 replications) are shown. GenBank

accession numbers are shown in parentheses next to the organism names. Squares indicate bacteria enriched from aquifers and circles indicate bacteria originating from mineral springs.

The second most abundant bacterium present in our culture also belongs to the *Betaproteobacteria* and was affiliated to *Acidovorax*. Some species of this genus, such as *Acidovorax ebreus, Acidovorax* sp. strain 2AN, or *Acidovorax* sp. strain BoFeN1, were found to be proficient at mediating nitrate-dependent iron(II) oxidation (Kappler, Schink and Newman 2005; Chakraborty *et al.* 2011; Carlson *et al.* 2013). However, at least *Acidovorax* strain BoFeN1 was shown not to be a true mixotrophic nitrate-dependent iron(II)-oxidizer (using both Fe(II) and the organic co-substrate as electron source), but instead, producing nitrite during heterotrophic denitrification causing an abiotic oxidation of the Fe(II) (chemodenitrification) (Kappler, Schink and Newman 2005; Klueglein and Kappler 2013). Nevertheless, the *Acidovorax* sp. in our enrichment might potentially also play an important role in nitrate turnover (and maybe to a small extent in Fe(II) oxidation) by oxidizing organic carbon provided by the autotrophs.

Besides iron(II)-oxidizers, other community members in our enrichment culture have 16S rRNA gene sequences most similar to bacteria known as nitrate-reducers such as *Rhodocyclaceae* (2.75%), closely related to *Dechloromonas* spp. that are often dominant in denitrifying populations in sediments (Zhang, Shao and Ye 2012; Chourey *et al.* 2013; Mcilroy *et al.* 2016), including strain UWNR4 obtained from river sediments that oxidizes Fe(II) in the presence of nitrate and acetate (Chakraborty and Picardal 2013). Some ASVs were assigned to be closely related to other nitrate-reducing taxa such as *Bradyrhizobium* spp. (Polcyn and Luciński 2003; Siqueira, Minamisawa and Sánchez 2017) belonging to *Xanthobacteraceae* (5.8%). Interestingly, *Bradyrhizobium* is also present in culture KS and was found to possess RuBisCO genes that can be used to fix CO_2. If so, *Bradyrhizobium* in culture KS is likely conducting Fe(II) oxidation coupled with denitrification to obtain reducing equivalents and ATP needed for CO_2 fixation (He *et al.* 2017). Our culture comprises microorganisms related to *Geothrix* sp. (2%) (*Holophagaceae*), potential iron(III)-reducers also found previously in aquatic environments such as aquifers (Coates *et al.* 1999). The presence of iron(III)-reducers suggests the possibility for iron cycling in the culture using internally produced organic compounds.

2.3.2. Physiology of the enriched lithoautotrophic NRFeOx culture

To measure rates of denitrification coupled to iron(II) oxidation, the lithoautotrophic NRFeOx enrichment culture was cultivated continuously on fresh medium containing Fe(II) and NO_3^- as the only electron donor and acceptor. The cultivation was repeated over three transfers, i.e. the first transfer (generation of the culture) was used to inoculate the second that was then used to inoculate the third. Since no organic carbon sources were provided externally to the denitrifying culture, and since we observed Fe(II) oxidation, nitrate reduction, and growth of cells over time, the reduction of nitrate must be mediated by microorganisms and is mainly linked to iron(II) oxidation. An addition of 2 mM of $FeCl_2$ and 2 mM of nitrate (molar ratio of 1:1, representing the electron acceptor, i.e. nitrate, in excess) to sodium carbonate buffered low phosphate medium was followed by iron(II) carbonate and iron(II) phosphate precipitation, which resulted in a final concentration of ca. 1.3 mM of Fe^{2+}(aq). Oxidation of total Fe(II) was never complete, but ceased when approximately 90% of the added iron was oxidized (Figure S3, Figure S4). In

contrast, dissolved Fe^{2+}(aq) was always completely removed (i.e. oxidized) after each transfer (Figure 2). The reason for that could be the difference in bioavailability of Fe(II) in aqueous and solid form, i.e. precipitation of siderite and vivianite might lead to formation of Fe(II)-solids which the culture is unable to use as electron donor. Per 1 mM of oxidized Fe(II), the NRFeOx culture formed $6.9x10^5$ cells/mL (Figure S5).

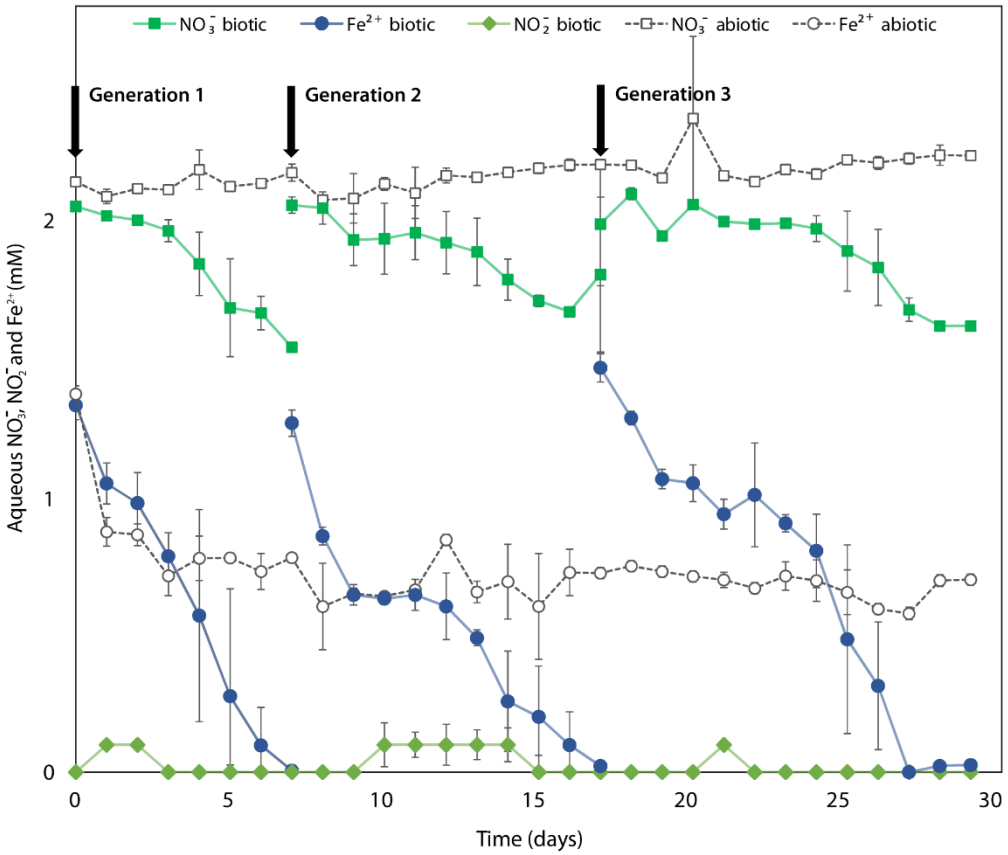

Figure 2. Concentrations of dissolved NO_3^-, NO_2^- and Fe^{2+} in three consecutive transfers of the enriched autotrophic nitrate-reducing Fe(II)-oxidizing culture. All data points are mean values of samples from three replicate bottles, error bars represent standard deviations. The transfers on days 0, 7 and 17 are indicated by arrows.

Because Fe(II) oxidation by truly autotrophic NRFeOx bacteria is enzymatic, mediated by a dedicated Fe(II) oxidase and probably happening in the cell periplasm (Carlson *et al.* 2013; He *et al.* 2017), we specifically only present the removal of Fe^{2+}(aq) here, i.e. the Fe-species that can enter the periplasm. Additional plots showing concentrations of total Fe(II) over time are presented in the supplementary data (Figure S3). The overall rates of NO_3^- reduction and removal of Fe^{2+}(aq) (most probably by oxidation as indicated by the stoichiometric formation of Fe(III), Figure S3) were similar over all three consecutive transfers, showing the reproducibility of the microbially catalyzed process. Complete removal of Fe^{2+}(aq) occurred within 7-11 days at the expense of nitrate, i.e., the culture reduced 0.3-0.5 mM of nitrate and oxidized 1.3-2 mM of Fe^{2+}(aq). Generally, Fe^{2+}(aq) conversion can be divided into three phases (Figure 2). In phase 1 (0 to 2 days after inoculation), the decrease of Fe^{2+}(aq) concentration (0.40 ± 0.08 mM) was always observed immediately after addition of Fe(II) to the medium followed by inoculation, which may

be associated with the precipitation of siderite and vivianite and the sorption of the iron(II) to the glass wall. This might be supported by the fact that the same decrease of iron(II) concentration (ca. 0.5 mM) was also observed in abiotic controls between day 0 and 1 (first transfer) (Figure 2). The same non-inoculated bottles were used as an abiotic control for the two subsequent transfers, therefore, no further fluctuation in substrate concentrations in the abiotic controls was found. After approximately 2 days (2nd phase), Fe^{2+}(aq) oxidation slowed down which may be related to a microbial adaptation phase or potentially also to NO_2^- production and the resulting lowering or even inhibition of the Fe(II) oxidase activity due to nitrite toxicity (Bollag and Henninger 1978; Bosch *et al.* 2012; Guerbois *et al.* 2014). However, although we observed the accumulation of nitrite, it was minor and never exceeded 0.1 mM. In contrast, nitrite accumulation in nitrate-dependent iron(II)-oxidizing cultures at mM concentrations has been described previously by Kappler et al. (2005) for *Acidovorax* strain BoFeN1 and by Weber et al. (2006) for *Pseudogulbenkiania* sp. strain 2002. These two strains cannot grow purely autotrophically with Fe(II) and nitrate but are known to require an additional organic substrate or at least pre-cultivation on organic substrate (Chen *et al.* 2018) that probably leads to internal carbon storage and heterotrophic denitrification, nitrite formation and chemodenitrification. However, nitrite in pure cultures of strain BoFeN1 and strain 2002 remained in solution until the end of incubation whereas in our culture, nitrite was always low and had been completely removed by the end of the incubation. The complete removal of nitrite in our culture may be explained by the presence of denitrifying bacteria potentially equipped with nitrite reductases which might have used internally produced carbon compounds derived by primary biomass producers. However, a part of the nitrite could also have been reduced by an abiotic reaction with iron(II) (Buresh and Moraghan 1976; Van Cleemput and Baert 1983). Additionally, the presence of Fe(II) minerals like siderite (Rakshita, Matocha and Coyne 2008) could have catalyzed the process by providing reactive surfaces (Visser *et al.* 2020b). The 3rd phase of the incubation (last 5 to 6 days) was characterized again by rapid removal, i.e. oxidation, of Fe^{2+}(aq) in the biotic setups with a maximum Fe^{2+} removal rate of 0.5±0.1 mM/day. The multi-stage nature of the process might be related to the accessibility to Fe^{2+}(aq) which is limited by dissolution of solid phases present in the medium (siderite, vivianite) or to inhibitory effects of the accumulated nitrite. In the abiotic controls, no changes in nitrate, nitrite nor Fe(II) concentrations were observed within the time of the experiment.

The average $nitrate_{reduced}$/$total\text{-}Fe(II)_{oxidized}$ ratio over three transfers of 0.28±0.1 (Table 1) is slightly higher but still approximating the theoretical stoichiometry of Equation 1 suggesting almost complete reduction of NO_3^- to N_2. Similar ratios were shown for culture KS growing autotrophically (Tominski *et al.* 2018), yielding ratios of 0.21 to 0.24 and in a marine sediment microcosm study (Laufer, Røy and Jørgensen 2016) in which $nitrate_{reduced}$/$Fe(II)_{oxidized}$ ratio 0.22 to 0.28 was measured. This suggests that less Fe(II) is oxidized or slightly more nitrate is removed than expected from the 1:5 ratio of nitrate (reduced) and Fe(II) oxidized. In fact, the theoretical ratio should be even lower than 0.2 because some of the electrons from Fe(II) oxidation must also be used for the reduction of CO_2 (for biomass production) rather than reduction of nitrate (for energy generation) (Laufer, Røy and Jørgensen 2016).

Table 1. Decreases of NO_3^- and Fe(II) concentrations, rates and stoichiometries of NO_3^- reduction and Fe(II) oxidation in three transfers of the microcosm experiment.

		Rate of NO_3^- reduction [mM/day]	Rate of Fe(II) oxidation [mM/day]	Rate of Fe^{2+}(aq) oxidation [mM/day]	Ratio of $NO_3^-{}_{reduced}$/ $Fe(II)_{oxidized}$	Ratio of $NO_3^-{}_{reduced}$/ $Fe^{2+}(aq)_{oxidized}$
Transfer 1	Culture 1.1	0.12	0.39	0.27	0.31	0.45
	Culture 1.2	0.08	0.30	0.25	0.22	0.30
	Culture 1.3	0.05	0.30	0.18	0.23	0.26
	Average	0.08 ± 0.03	0.33 ± 0.04	0.24 ± 0.04	**0.26 ± 0.04**	**0.33 ± 0.08**
Transfer 2	Culture 2.1	0.04	0.14	0.14	0.32	0.32
	Culture 2.2	0.05	0.18	0.13	0.22	0.34
	Culture 2.3	0.04	0.19	0.19	0.21	0.21
	Average	0.04 ± 0.00	0.30 ± 0.02	0.15 ± 0.03	**0.25 ± 0.05**	**0.29 ± 0.06**
Transfer 3	Culture 3.1	0.05	0.17	0.22	0.28	0.21
	Culture 3.2	0.05	0.18	0.22	0.26	0.22
	Culture 3.3	0.05	0.20	0.23	0.25	0.23
	Average	0.05 ± 0.00	0.25 ± 0.01	0.22 ± 0.00	**0.26 ± 0.01**	**0.22 ± 0.01**

In our setups amended with ^{15}N-$NaNO_3^-$, from the 0.61 mM of ^{15}N-nitrate that was removed, 0.11±0.02 of nitrate was reduced to ^{15}N-N_2, while 0.25±0.01 mM was reduced to ^{15}N-N_2O (Table S1). If directly coupled to autotrophic Fe(II) oxidation, these reactions would lead to oxidation of ca.1.55 mM of Fe(II) of the initial 2.0 mM of Fe(II). This suggests that with the remaining 0.45 mM of Fe(II) (that were also oxidized based on our geochemical analyses), ca. 0.25 mM of nitrate could have been converted to ^{15}N-NO (or maybe also ^{15}N-NH_4^+), which both were not measured in the ^{15}N-isotope analyses. Quantification of dissolved ammonium by FIA showed that its overall concentration decreased over time of incubation from 5.52±0.01 to 5.38±0.06 (Figure S7) meaning that if any ammonium was produced due to nitrate reduction, its concentration was lower than the amount of ammonium that was consumed by the microbes during the incubation.. Overall, this shows that nitrate removal by the studied NRFeOx culture results from multiple metabolic reactions in which both Fe(II) and to small extent, organic carbon compounds are used as electron donors. Potential sources of organic carbon for nitrate reduction by the heterotrophic bacteria are internally produced organic carbon by the autotrophic Fe(II)-oxidizers (leading to cross-feeding), or traces of organic carbon present as a background contaminant in MQ water used for medium preparation (measured to be in the range of 0.3-0.9 mg/L). Additional explanations for the extra nitrate consumption are the storage of nitrate in the cells or maybe also the use of nitrate as N-source for assimilation. In order to verify to which extent the culture can grow solely on nitrate and organic carbon stemming from the background in the water, the culture was inoculated in the same medium with nitrate but without any addition of Fe(II). As controls, separate microcosms with nitrate and 1, 2 and 3 mM of

Fe(II) were used. Bacteria in setups with no Fe(II) reduced 0.24±0.06 mM of nitrate, i.e. less than in incubations with 1 mM of Fe(II) (0.36±0.03 mM) (Table S2, Figure S5 C and D). In setups where 2 mM and 3 mM of Fe(II) was added, the amount of nitrate reduced was higher and reached 0.61±0.04 and 0.76±0.03 mM, respectively. Interestingly, in all microcosms where Fe(II) was present, the ratio of $nitrate_{reduced}/Fe(II)_{oxidized}$ was again between 0.24 and 0.33, independently on Fe(II) concentration (Table S2). In addition, cell numbers were counted at the beginning (day 0) of the experiment and at day 5, respectively, when reduction of nitrate and/or oxidation of Fe(II) has stopped. The results (Table S3) show that the final number of cells growing in the cultures with Fe(II) was higher than in setups with no Fe(II) but there was no statistically significant pair of treatments (p-value = 0.76). These results show that direct coupling of nitrate reduction to Fe(II) oxidation and ultimately results in carbon fixation leading to biomass production is favorable for the community as whole, but is not necessarily mediated by all members of the community. To confirm this result and to clearly demonstrate autotrophic growth, we performed an additional experiment with several sequential spikes of Fe(II) that are expected to lead to additional cell growth after each spike. For this experiment, incubations were prepared using the same medium amended with 2 mM Fe(II), 2 mM NO_3^- and 10% (vol/vol) of inoculum as described above but with a difference that once all Fe(II) has been completely oxidized, the same bottles were spiked with additional 2 mM of Fe(II). Three continuous Fe(II) oxidation phases were carried out to follow cell numbers. Since all trace carbon stemming from the water should be consumed in the initial incubation, all nitrate reduction in the 2nd and 3rd phase (after the 2nd and 3rd spike with Fe(II)) can be attributed to Fe(II) oxidation only. As expected for a culture performing autotrophic Fe(II) oxidation coupled to nitrate reduction, the spiking experiment indeed resulted not only in an enhanced rate of Fe(II) oxidation after the 2nd and 3rd spike of Fe(II), but in particular to an incremental increase in cell numbers after each spike of Fe(II) resulting in $7.73x10^6 \pm 4.37x10^5$ cells/ml at the end of incubation (Figure S6.).

2.3.3. Cell-mineral interactions

As a consequence of Fe(II) oxidation, Fe(III) mineral precipitates were formed. Mössbauer spectroscopy identified the formation of a short range ordered Fe(III) (oxyhydr)oxide mineral phase with hyperfine parameters that were similar to ferrihydrite (Table S4) (Eickhoff *et al.* 2014) (Figure 3B). Mössbauer data also revealed up to 10% Fe(II) remained in the precipitate. X-ray diffraction was unable to resolve any clear reflections corresponding to any Fe mineral (Figure 3A) which combined with the results of the Mössbauer data provides clear evidence that ferrihydrite was the formation product of microbial Fe(II) oxidation.

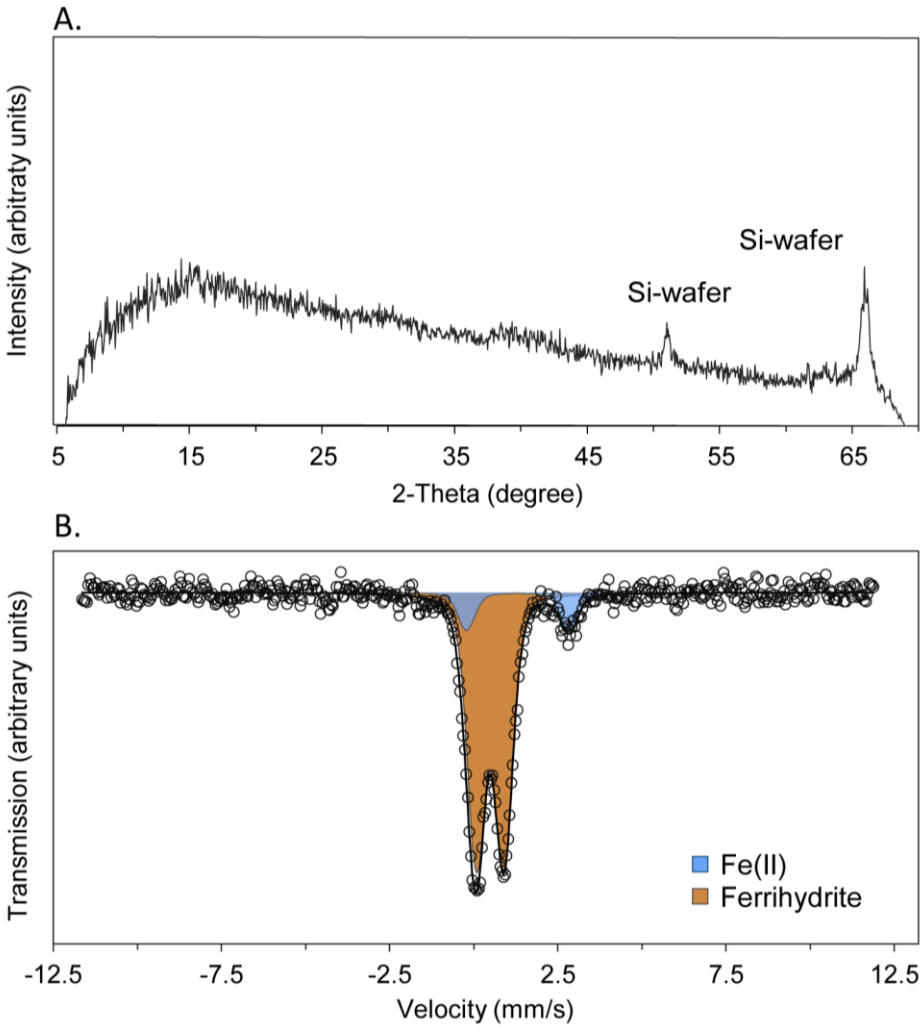

Figure 3. X-ray diffractogram (A) and Mössbauer spectrum (B) of the minerals formed during oxidation of 2 mM of Fe(II) by the Fe(II)-oxidizing nitrate-reducing enrichment culture. Samples were taken after 11 days. The diffraction reflexes at 51.0 °2θ and 65.9 °2θ belong to Si-wafer (sample holder). In the Mössbauer spectrum, the black circles indicate raw data, the brown area represents short range ordered Fe(III) oxyhydroxide, likely ferrihydrite and the blue shading represents Fe(II).

Scanning electron micrographs and light microscopy images of the NRFeOx culture showed that bacteria are closely associated with the Fe(III) precipitates but only a few of the cells were encrusted in minerals at the end of Fe(II) oxidation phase (Figure 4). This suggested that most of the cells are able to avoid mineral precipitation at their cell surface. Several possible mechanisms have been suggested in the literature to explain how cells can avoid encrustation e.g. via excretion of Fe(III)-complexing ligands that can retain Fe(III) in solution or by maintaining a slightly acidic microenvironment around cells (Kappler and Newman 2004; Sobolev and Roden 2004; Hegler *et al.* 2008; Muehe *et al.* 2009). For the cells present in our culture, the change of pH could be local (in the direct cell environment) since the overall pH of medium did change only to a minor extent during the incubation time (decrease from 7.04±0.00 to 6.93±0.03). The culture, however, was observed to perform nitrate reduction coupled to Fe(II) oxidation

also at lower pH values of 6.0 and 6.5 (Figure S5 A and B), showing that the cells were capable of metabolizing under these lower-pH conditions. Additionally, such an acidification of the local environment around cells may also stimulate the dissolution of carbonates such as siderite (Kappler and Newman 2004). This may have important implications for the environments where siderite or iron-bearing carbonates are present (e.g. in carbonate-rich aquifers) and may serve as a Fe(II)-source for chemolithotrophic bacteria.

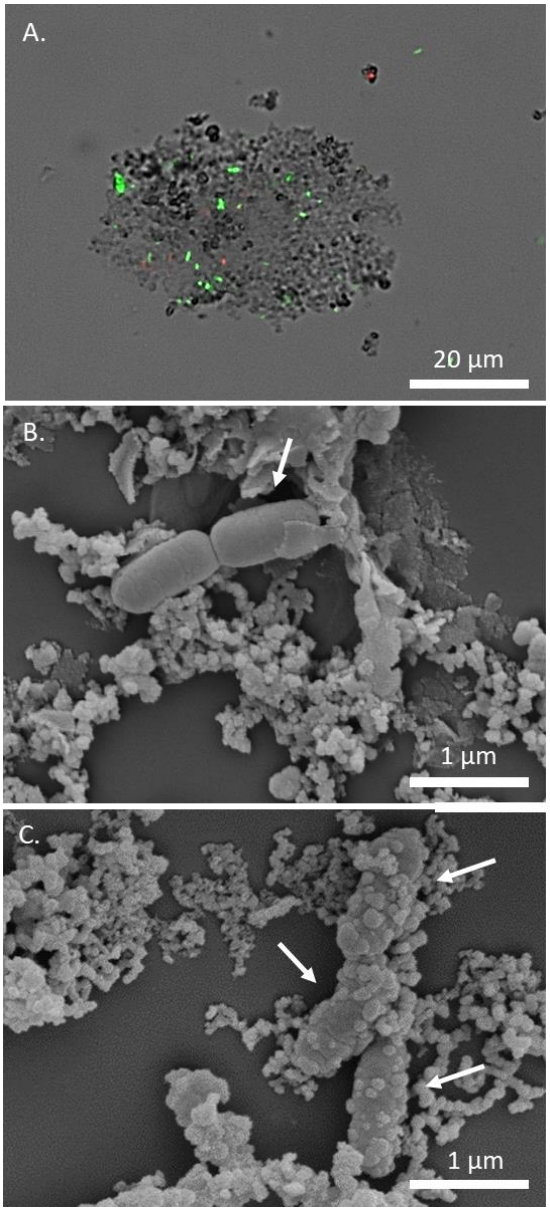

Figure 4. Overlay of fluorescence and transmission light microscopic pictures of the autotrophic NRFeOx culture enriched in this study. Cells were stained with the LIVE/DEAD stain (green-alive, red-dead) (A). Scanning electron micrographs of the culture after 11 days of incubation showing non-encrusted (B) and encrusted (C) cells. Arrows indicate cells

2.3.4. Relevance of Gallionellaceae-related strains for Fe(II) oxidation in anoxic, nitrate-rich environments such as aquifers

Knowledge of the microbial key players, the mechanisms, and the controlling factors of anaerobic nitrate-reducing Fe(II) oxidation is critical for understanding the fate of nitrate, one of the pollutants in groundwater aquifers. Under *in-situ* conditions, rates of NRFeOx can be controlled by various process-limiting factors. Depending on the aquifer either the electron acceptor nitrate (determined by the input from agriculture) or the electron donor (Fe(II), potentially limited by the solubility of the available Fe(II)-containing minerals) can limit the NRFeOx process, while the carbon source, CO_2, is usually not limiting in such systems. This is supported by numerous environmental studies, which provided evidence for the importance of autotrophic processes mediated by microorganisms in the subsurface. As an example, in one previous study where the response of an aquifer microbial community to an increase in the flux of electron acceptor, i.e. nitrate was characterized, metatranscriptomic data showed an unexpected increase of the activity of *Gallionellaceae* spp. (known autotrophic microaerophilic Fe(II)-oxidizers), although the influx of a thermodynamically favorable electron acceptor like nitrate was expected to stimulate microbial oxidation of organic electron donors (Jewell *et al.* 2016). In the studied aquifer, Fe(II) originates mainly from mineral phases such as pyrite, Fe(II)-bearing carbonates and clays. The availability of aqueous Fe^{2+} is therefore determined by the solubility of Fe(II) minerals and activity of sulfide-oxidizing microorganisms, like potentially *Thiobacillus* sp. present in this culture, and the maximum concentration measured in groundwater at our field site was 0.02 mM. However, some microorganisms can directly oxidize Fe(II)-containing minerals. For instance, an *mto* gene cluster that forms a pathway that couples extracellular oxidation of Fe(II) to the reduction of quinone to quinol in the cytoplasmic membrane has been found in *Sideroxydans lithotrophicus* ES-1 (*Gallionellaceae family)* (Shi *et al.* 2016). This indicates that some representatives of this family have the metabolic potential to directly oxidize solid iron(II)-phases. The same bacterial strain, *Sideroxydans lithotrophicus* ES-1, was also observed in high abundance in the rock-attached communities of passive samplers incubated in a pristine limestone aquifer, along with other potential autotrophs related to *Thiobacillus* (Herrmann *et al.* 2017). Taken together with our results, these findings highlight the potential importance of chemolithoautotrophic bacteria in linking biogeochemical cycles of N, C, S and Fe species in aquifers and raises the question about the exact role of typically microaerophilic iron(II)-oxidizing *Gallionellaceae*-related bacteria in mediating denitrification under anoxic conditions. The isolation of an individual strain of the relevant *Gallionellaceae* sp. from the nitrate-dependent iron(II)-oxidizing co-cultures KS and the enrichment culture presented here, together with genome analyses, are the key for future studies to understand the ecological importance of NRFeOx in natural environments, in particular groundwater aquifers.

2.4. Data availability

Raw sequencing data have been deposited at DDBJ/ENA/GenBank under BioProject accession number PRJNA592904 (https://www.ncbi.nlm.nih.gov/bioproject/PRJNA592904).

2.5. Acknowledgements

This work is supported by the Collaborative Research Center 1253 CAMPOS (Project 5: Fractured Aquifer and P2: Sub-Catchments), funded by the German Research Foundation (DFG, Grant Agreement SFB 1253/1). Daniel Straub is funded by the Institutional Strategy of the University of Tübingen (DFG, ZUK63). Sara Kleindienst is funded by an Emmy Noether grant (grant # 326028733) from the DFG. The authors acknowledge support by the state of Baden-Württemberg through bwHPC and the German Research Foundation (DFG) through grant no INST 37/935-1 FUGG (bwForCluster BinAC). We thank Ellen Röhm for nitrate and nitrite analyses, André Pellerin for AVS measurements, Anna-Neva Visser for the development of Microbial Trapping Devices (MTDs) and Franziska Schädler for help with DNA extractions.

References

Beller HR. Anaerobic , Nitrate-dependent oxidation of U(IV) oxide minerals by the chemolithoautotrophic bacterium *Thiobacillus denitrificans*. *Appl Environ Microbiol* 2005;**71**:2170–4.

Benz M, Brune A, Schink B. Anaerobic and aerobic oxidation of ferrous iron at neutral pH by chemoheterotrophic nitrate-reducing bacteria. *Arch Microbiol* 1998;**169**:159–65.

van den Berg EM, Rombouts JL, Kuenen JG *et al.* Role of nitrite in the competition between denitrification and DNRA in a chemostat enrichment culture. *AMB Express* 2017;**7:91**:1–7.

Blöthe M, Roden EE. Composition and activity of an autotrophic Fe(II)-oxidizing, nitrate-reducing enrichment culture. *Appl Environ Microbiol* 2009;**75**:6937–40.

Bollag J-M, Henninger NM. Effects of nitrite toxicity on soil bacteria aerobic and anaerobic. *Soil Biol Biochem* 1978;**10**:377–81.

Bosch J, Lee KY, Jordan G *et al.* Anaerobic, nitrate-dependent oxidation of pyrite nanoparticles by *Thiobacillus denitrificans*. *Environ Sci Technol* 2012;**46**:2095–101.

Bryce C, Blackwell N, Schmidt C *et al.* Microbial anaerobic Fe(II) oxidation - ecology, mechanisms and environmental implications. *Environ Microbiol* 2018;**20**:3462–83.

Buresh RJ, Moraghan JT. Chemical reduction of nitrate by ferrous iron. *J Environ Qual* 1976;**5**:320–5.

Burgin AJ, Hamilton SK. Have we overemphasized the role of denitrification in aquatic ecosystems? A review of nitrate removal pathways. *Front Ecol Environ* 2010;**5**:89–96.

Burke KA, Calder K, Lascelles J. Effects of molybdenum and tungsten on induction of nitrate reductase and formate dehydrogenase in wild type and mutant *Paracoccus denitrificans*. *Arch Microbiol* 1980;**126**:155–9.

Callahan BJ. Silva taxonomic training data formatted for DADA2 (Silva version 132) [Data set]. Zenodo. 2018.

Callahan BJ, Wong J, Heiner C *et al.* High-throughput amplicon sequencing of the full-length 16S rRNA gene with single-nucleotide resolution. *Nucleic Acids Res* 2019;**47**:1–12.

Capua F Di, Pirozzi F, Lens PNL *et al.* Electron donors for autotrophic denitrification. *Chem Eng J* 2019;**362**:922–37.

Carlson HK, Clark IC, Blazewicz SJ *et al.* Fe(II) oxidation is an innate capability of nitrate-reducing bacteria that involves abiotic and biotic reactions. *J Bacteriol* 2013;**195**:3260–8.

Chakraborty A, Picardal F. Neutrophilic, nitrate-dependent, Fe(II) oxidation by a *Dechloromonas* species. *World J Microbiol Biotechnol* 2013;**29**:617–23.

Chakraborty A, Roden EE, Schieber J *et al.* Enhanced growth of *Acidovorax* sp. strain 2AN during nitrate-dependent Fe(II) oxidation in batch and continuous-flow systems. *Appl Environ Microbiol* 2011;**77**:8548–56.

Chen D, Liu T, Li X *et al.* Biological and chemical processes of microbially mediated nitrate-reducing Fe(II) oxidation by *Pseudogulbenkiania* sp. strain 2002. *Chem Geol* 2018;**476**:59–69.

Chourey K, Nissen S, Vishnivetskaya T *et al.* Environmental proteomics reveals early microbial community responses to biostimulation at a uranium- and nitrate-contaminated site. *Proteomics* 2013;**13**:2921–30.

Van Cleemput O, Baert L. Nitrite stability influenced by iron compounds. *Soil Biol Biochem* 1983;**15**:137–40.

Coates JD, Ellis DJ, Gaw C V. *et al. Geothrix fermentans* gen. nov., sp. nov., a novel Fe(III)-reducing bacterium from a hydrocarbon-contaminated aquifer. *Int J Syst Evol Microbiol* 1999;**49**:1614–22.

Eickhoff M, Obst M, Schro C *et al.* Nickel partitioning in biogenic and abiogenic ferrihydrite : The influence of silica and implications for ancient environments. *Geochim Cosmochim Acta* 2014;**140**:65–79.

Emerson D, Field EK, Chertkov O *et al.* Comparative genomics of freshwater Fe-oxidizing bacteria: Implications for physiology, ecology, and systematics. *Front Microbiol* 2013;**4**:1–17.

Griebler C, Mindl B, Slezak D *et al.* Distribution patterns of attached and suspended bacteria in pristine and contaminated shallow aquifers studied with an *in situ* sediment exposure microcosm. *Aquat Microb Ecol* 2002;**28**:117–29.

Guerbois D, Ona-Nguema G, Morin G *et al.* Nitrite reduction by biogenic hydroxycarbonate green rusts: evidence for hydroxy-nitrite green rust formation as an intermediate reaction product. *Environ Sci Technol* 2014;**48**:4505–14.

Haaijer SCM, Lamers LPM, Smolders AJP *et al.* Iron sulfide and pyrite as potential electron donors for microbial nitrate reduction in freshwater wetlands. *Geomicrobiol J* 2007;**24**:391–401.

He S, Barco RA, Emerson D *et al.* Comparative genomic analysis of neutrophilic iron(II) oxidizer genomes for candidate genes in extracellular electron transfer. *Front Microbiol* 2017;**8**:1–17.

He S, Tominski C, Kappler A *et al.* Metagenomic analyses of the autotrophic Fe(II)-oxidizing, nitrate-reducing enrichment culture KS. *Appl Environ Microbiol* 2016;**82**:2656–68.

Hegler F, Posth NR, Jiang J *et al.* Physiology of phototrophic iron(II)-oxidizing bacteria: implications for modern and ancient environments. *FEMS Microbiol Ecol* 2008;**66**:250–60.

Herndon E, Albashaireh A, Singer D *et al.* Influence of iron redox cycling on organo-mineral associations in Arctic tundra soil. *Geochim Cosmochim Acta* 2017;**207**:210–31.
Herrmann M, Opitz S, Harzer R *et al.* Attached and suspended denitrifier communities in pristine limestone aquifers harbor high fractions of potential autotrophs oxidizing reduced iron and sulfur compounds. *Microb Ecol* 2017;**74**:264–77.
Herrmann M, Rusznyák A, Akob DM *et al.* Large fractions of CO_2-fixing microorganisms in pristine limestone aquifers appear to be involved in the oxidation of reduced sulfur and nitrogen compounds. *Appl Environ Microbiol* 2015;**81**:2384–94.
Huang Y-M, Straub D, Kappler A *et al.* A novel enrichment culture highlights core features of microbial networks contributing to autotrophic Fe(II) oxidation coupled to nitrate reduction. *Microb Physiol* 2021;**In press**.
Jensen VB, Darby JL, Seidel C *et al.* Nitrate in potable water supplies: alternative management strategies. *Crit Rev Environ Sci Technol* 2014;**44**:2203–86.
Jewell TNM, Karaoz U, Brodie EL *et al.* Metatranscriptomic evidence of pervasive and diverse chemolithoautotrophy relevant to C, S, N and Fe cycling in a shallow alluvial aquifer. *ISME J* 2016;**10**:2106–17.
Jørgensen CJ, Jacobsen OS, Elberling B *et al.* Microbial oxidation of pyrite coupled to nitrate reduction in anoxic groundwater sediment. *Environ Sci Technol* 2009;**43**:4851–7.
Kappler A, Bryce C, Mansor M *et al.* An evolving view on biogeochemical cycling of iron. *Nat Rev Microbiol* 2021, DOI: 10.1038/s41579-020-00502-7.
Kappler A, Johnson CM, Crosby HA *et al.* Evidence for equilibrium iron isotope fractionation by nitrate-reducing iron(II)-oxidizing bacteria. *Geochim Cosmochim Acta* 2010;**74**:2826–42.
Kappler A, Newman DK. Formation of Fe(III)-minerals by Fe(II)-oxidizing photoautotrophic bacteria. *Geochim Cosmochim Acta* 2004;**68**:1217–26.
Kappler A, Schink B, Newman K. Fe(III) mineral formation and cell encrustation by the nitrate-dependent Fe(II)-oxidizer strain BoFeN1. *Geobiology* 2005;**3**:235–45.
Kim H, Kaown D, Mayer B *et al.* Identifying the sources of nitrate contamination of groundwater in an agricultural area (Haean basin, Korea) using isotope and microbial community analyses. *Sci Total Environ* 2015;**533**:566–75.
Klueglein N, Kappler A. Abiotic oxidation of Fe(II) by reactive nitrogen species in cultures of the nitrate-reducing Fe(II) oxidizer *Acidovorax* sp. BoFeN1 – questioning the existence of enzymatic Fe(II) oxidation. *Geobiology* 2013;**11**:180–90.
Kumar S, Herrmann M, Blohm A *et al.* Thiosulfate- and hydrogen-driven autotrophic denitrification by a microbial consortium enriched from groundwater of an oligotrophic limestone aquifer. *FEMS Microbiol Ecol* 2018a;**94**:1–13.
Kumar S, Stecher G, Li M *et al.* MEGA X: Molecular evolutionary genetics analysis across computing platforms. *Mol Biol Evol* 2018b;**35**:1547–9.
Küsel K, Totsche KU, Trumbore SE *et al.* How deep can surface signals be traced in the critical zone? Merging biodiversity with biogeochemistry research in a central German Muschelkalk landscape. *Front Earth Sci* 2016;**4**:1–18.
Laufer K, Røy H, Jørgensen B. Evidence for the existence of autotrophic nitrate-reducing Fe(II)-oxidizing bacteria in marine coastal sediment. *Appl Environ Microbiol* 2016;**82**:6120–31.
Liu T, Chen D, Li X *et al.* Microbially mediated coupling of nitrate reduction and Fe(II) oxidation under anoxic conditions. *FEMS Microbiol Ecol* 2019;**95**:1–12.
Mcilroy SJ, Starnawska A, Starnawski P *et al.* Identification of active denitrifiers in full-scale nutrient removal wastewater treatment systems. *Environ Microbiol* 2016;**18**:50–64.
Muehe EM, Gerhardt S, Schink B *et al.* Ecophysiology and the energetic benefit of mixotrophic Fe(II) oxidation by various strains of nitrate-reducing bacteria. *FEMS Microbiol Ecol* 2009;**70**:335–43.
Nordhoff M, Tominski C, Halama M *et al.* Insights into nitrate-reducing Fe(II) oxidation mechanisms through analysis of cell-mineral associations, cell encrustation, and mineralogy in the chemolithoautotrophic enrichment culture KS. *Appl Env Microbiol* 2017;**83**:1–19.
Opazo T, Aravena R, Parker B. Nitrate distribution and potential attenuation mechanisms of a municipal water supply bedrock aquifer. *Appl Geochem* 2016;**73**:157–68.
Pauwels H. Natural denitrification in groundwater in the presence of pyrite: preliminary results obtained at Naizin (Brittany, France). *Mineral Mag* 1994;**58A**:696–7.
Pauwels H, Kloppmann W, Foucher JC *et al.* Field tracer test for denitrification in a pyrite-bearing schist aquifer. *Appl Geochemistry* 1998;**13**:767–78.
Peiffer S, Stubert I. The oxidation of pyrite at pH 7 in the presence of reducing and nonreducing Fe(III)-chelators. *Geochim Cosmochim Acta* 1999;**63**:3171–82.

Percak-Dennett E, He S, Converse B *et al.* Microbial acceleration of aerobic pyrite oxidation at circumneutral pH. *Geobiology* 2017;**15**:690–703.
Polcyn W, Luciński R. Aerobic and anaerobic nitrate and nitrite reduction in free-living cells of *Bradyrhizobium* sp. (*Lupinus*). *FEMS Microbiol Lett* 2003;**226**:331–7.
Postma D, Boesen C, Kristiansen H *et al.* Nitrate reduction in an unconfined sandy aquifer: water chemistry, reduction processes, and geochemical modeling. *Water Resour Res* 1991;**27**:2027–45.
Pruesse E, Peplies J, Glöckner FO. SINA: Accurate high-throughput multiple sequence alignment of ribosomal RNA genes. *Bioinformatics* 2012;**28**:1823–9.
R Core Team. R: A language and environment for statistical computing. R Foundation for Statistical Computing, Vienna, Austria. 2018.
Rakshita S, Matocha CJ, Coyne MS. Nitrite reduction by siderite. *Soil Sci Soc Am J* 2008;**72**:1070–7.
Rancourt DG, Ping JY. Voigt-based distributions methods for arbitrary-shape in Mössbauer spectroscopy static hyperfine parameter. *Nucl Instruments Methods Phys Res* 1991;**58**:85–97.
Rezvani F, Sarrafzadeh M-H, Ebrahimi S *et al.* Nitrate removal from drinking water with a focus on biological methods: a review. *Environ Sci Pollut Res* 2019;**26**:1124–41.
Rimstidt DD, Vaughan DJ. Pyrite oxidation: A state-of-the-art assessment of the reaction mechanism. *Geochim Cosmochim Acta* 2003;**67**:873–80.
Rivett MO, Buss SR, Morgan P *et al.* Nitrate attenuation in groundwater: A review of biogeochemical controlling processes. *Water Res* 2008;**42**:4215–32.
Robertson EK, Thamdrup B. The fate of nitrogen is linked to iron(II) availability in a freshwater lake sediment. *Geochim Cosmochim Acta* 2017;**205**:84–99.
Schaedler F, Kappler A, Schmidt C. A revised iron extraction protocol for environmental samples rich in nitrite and carbonate. *Geomicrobiol J* 2018;**35**:23–30.
Schwientek M, Einsiedl F, Stichler W *et al.* Evidence for denitrification regulated by pyrite oxidation in a heterogeneous porous groundwater system. *Chem Geol* 2008;**255**:60–7.
Shi L, Dong H, Reguera G *et al.* Extracellular electron transfer mechanisms between microorganisms and minerals. *Nat Rev Microbiol* 2016;**14**:651–62.
Siqueira AF, Minamisawa K, Sánchez C. Anaerobic reduction of nitrate to nitrous oxide is lower in *Bradyrhizobium japonicum* than in *Bradyrhizobium diazoefficiens*. *Microbes Environ* 2017;**32**:398–401.
Sobolev D, Roden EE. Characterization of a neutrophilic, chemolithoautotrophic Fe(II)-oxidizing *β-proteobacterium* from freshwater wetland sediments. *Geomicrobiol J* 2004;**21**:1–10.
Straub KL, Benz M, Schink B *et al.* Anaerobic, nitrate-dependent microbial oxidation of ferrous iron. *Appl Environ Microbiol* 1996a;**62**:1458–60.
Straub KL, Benz M, Schink B *et al.* Anaerobic, nitrate-dependent oxidation of ferrous iron. *Appl Environ Microbiol* 1996b;**62**:1458–60.
Tiedje JM. Ecology of denitrification and dissimilatory nitrate reduction to ammonium. *Environ Microbiol Anaerobes* 1988:179–244.
Tominski C, Heyer H, Lösekann-Behrens T *et al.* Growth and population dynamics of the anaerobic Fe(II)-oxidizing and nitrate-reducing enrichment culture KS. *Appl Env Microbiol* 2018;**84**:1–15.
Torrentó C, Cama J, Urmeneta J *et al.* Denitrification of groundwater with pyrite and *Thiobacillus denitrificans*. *Chem Geol* 2010;**278**:80–91.
Torrentó C, Urmeneta J, Otero N *et al.* Enhanced denitrification in groundwater and sediments from a nitrate-contaminated aquifer after addition of pyrite. *Chem Geol* 2011;**287**:90–101.
Vaclavkova S, Schultz-Jensen N, Jacobsen OS *et al.* Nitrate-controlled anaerobic oxidation of pyrite by *Thiobacillus* cultures. *Geomicrobiol J* 2015;**32**:412–9.
Visser AN, Lehmann MF, Rügner H *et al.* Fate of nitrate during groundwater recharge in a fractured karst aquifer in Southwest Germany. *Hydrogeol J* 2020a;**29**:1153–71.
Visser AN, Wankel SD, Niklaus PA *et al.* Impact of reactive surfaces on the abiotic reaction between nitrite and ferrous iron and associated nitrogen and oxygen isotope dynamics. *Biogeosciences* 2020b;**17**:4355–74.
Ward MH, Jones RR, Brender JD *et al.* Drinking water nitrate and human health: An updated review. *Int J Environ Res Public Health* 2018;**15**:1–31.
Weber KA, Picardal FW, Roden EE. Microbially catalyzed nitrate-dependent oxidation of biogenic solid-phase Fe(II) compounds. *Environ Sci Technol* 2001;**35**:1644–50.
Weber KA, Pollock J, Cole KA *et al.* Anaerobic nitrate-dependent iron(II) bio-oxidation by a novel lithoautotrophic Betaproteobacterium, strain 2002. *Appl Environ Microbiol* 2006;**72**:686–94.
Wick K, Heumesser C, Schmid E. Groundwater nitrate contamination: Factors and indicators. *J Environ Manage* 2012;**111**:178–86.
Widdel F. Anaerober Abbau von Fettsäuren und Benzoesäure durch neu isolierte Arten. *Diss Thesis, Univ Göttingen* 1980.

World Health Organization. Guidelines for drinking-water quality, forth ed. 2011.
Zeitvogel F, Burkhardt CJ, Schroeppel B *et al.* Comparison of preparation methods of bacterial cell-mineral aggregates for SEM imaging and analysis using the model system of *Acidovorax* sp . *Geomicrobiol J* 2016;**34**:317–27.
Zhang T, Shao MF, Ye L. 454 Pyrosequencing reveals bacterial diversity of activated sludge from 14 sewage treatment plants. *ISME J* 2012;**6**:1137–47.
Zhang Y-C, Slomp CP, Broers HP *et al.* Isotopic and microbiological signatures of pyrite-driven denitrification in a sandy aquifer. *Chem Geol* 2012;**300**–**301**:123–32.

3. **Supplementary information on:** Nitrate removal by a novel lithoautotrophic nitrate-reducing iron(II)-oxidizing culture enriched from a pyrite-rich limestone aquifer

3.1. Supplementary materials and methods

3.1.1. Determination of pyrite concentration in rock samples (AVS/CRS method)

The inorganic sulfur was divided into two fractions, acid volatile sulfides (AVS: H_2S + FeS) and chromium reducible sulfides (CRS: S^o, FeS_2), and their digestions were performed following a two-step procedure. First, acid volatile sulfide was distilled from a weighed amount of homogenized rock powder, second, the chromium-reducible sulfur was determined in the sediment slurry remaining from AVS distillation as described by Fossing and Jorgensen (1989). The total concentration of pyrite was calculated from the total concentration of CRSs assuming that pyrite is the only source of chromium-reducible inorganic sulfur in limestone.

3.1.2. pH dependence of Fe(II) oxidation rates

For quantifying the effect of pH on Fe(II) oxidation and NO_3^- reduction, the NRFeOx enrichment culture was incubated in medium with different pH values, ranging from pH 6.0 to 7.0. The pH of the medium was adjusted using 1 M HCl. The tested pH values were as follows: 6.0, 6.5 and 7.0. Incubations for all pH values were carried out in triplicates. Samples for Fe(II) and NO_3^- quantification and cell counts were taken every 24 h over a period of 7 days. Medium preparation and sampling were done as described in the Materials and Method section for the setup of microbial enrichments and incubation conditions.

3.1.3. Dependence of growth on Fe(II) concentrations

For quantifying the effect of various Fe(II) concentrations on cell growth, the NRFeOx enrichment culture was incubated in medium with the following Fe(II) concentrations: 0 mM (no Fe(II)), 1 mM, 2 mM and 3 mM. For all incubations microbial medium was prepared as described before and amended with 2 mM $NaNO_3$ and inoculated with 10% (vol/vol) of the NRFeOx enrichment culture. Initial pH of the medium used for this experiment was 7.0 and was the same for all setups with various Fe(II) concentrations.

To assess whether the cell growth of the culture solely depends on Fe(II) oxidation and is independent from trace organic carbon present in MQ water used for medium preparation, a spiking experiment was performed. In this experiment, incubations were prepared using low phosphate freshwater microbial medium with 2 mM Fe(II), 2 mM NO_3^-, at pH 7.0 and inoculated with 10% (vol/vol) of the NRFeOx enrichment culture. Fe(II) and NO_3^- concentrations and cell numbers were monitored by sampling every 24 h. Once all Fe(II) has been oxidized, the same bottles were spiked each with 2 mM additional Fe(II). This was repeated for three continuous Fe(II) oxidation phases to follow cell numbers after each spike of Fe(II).

Sampling for quantification of Fe(II), NO_3^- and cell numbers in all incubations described above was done as described in the Materials and Method section for the setup of microbial enrichments and incubation conditions. All incubations were conducted in triplicates and incubated at room temperature in the dark.

3.1.4. Statistics

Significance tests on differences between cell numbers at day 3 in setups with 0 mM (no Fe(II)) and 1 mM, 2 mM or 3 mM of Fe (II) added were performed in R (R Core Team, 2013) using a two-way ANOVA at 95 percent confidence interval.

3.1.5. Gas phase analysis – experiments with ^{15}N-labeled $NaNO_3$

To analyze the gaseous products of nitrate reduction coupled to Fe(II) during the growth of the autotrophic NRFeOx enrichment culture, the culture was incubated in biological triplicates in medium with 2 mM of Fe(II) and 2 mM ^{15}N-labeled $NaNO_3$. For all incubations microbial medium was prepared as described in the manuscript and inoculated with 10% (vol/vol) of the NRFeOx enrichment culture. To analyze the liquid and solid phases, the setups were sampled and analyzed using methods described in the Material and Methods section. Additionally, to analyze the composition of the gaseous phase, a set of 9 cultures was set up in parallel using the same medium, substrates and inoculum volume. At each sampling point (day 0, 2, and 4, when no further reduction of nitrate was observed), three bottles were sacrificed and the entire volume of the headspace (22.5 mL) was withdrawn from each bottle and injected into a crimped serum vial with rubber butyl stopper that had been pre-filled with He. Hence, all N_2O and N_2 in the headspace of these vials stemmed from the experimental bottles, and there was no dilution with N_2 from the atmosphere. The samples were further analyzed using GS-MS.

GC-MS analysis

Quantification of N_2 and N_2O was performed on an Agilent 7890A GC coupled to an Agilent 5975C quadrupole MS in electron impact mode. The inlet was held at 250°C and 10 µL of headspace were manually injected with a 10:1 split ratio. Separation was accomplished at a constant He flow rate of 2.5 mL/min (corresponding to 51.8 cm/s linear flow velocity) at a 35°C isotherm with an Agilent J&W GS-Q column (30 m length x 0.32 mm diameter). Temperatures of the MS transfer line, ion source and quadrupole were set at 250°C, 230°C and 150°C, respectively. Under these conditions, N_2 and N_2O eluted

after 3.29 and 4.83 min, respectively, and signals at m/z 28, 29, 30 (for N_2) and 44, 45, 46 (for N_2O) were acquired in SIM mode with a dwell time of 100 ms for each signal. All MS parameters were obtained by standard autotuning using perfluorotributylamine (PFTBA) at m/z 69, 219 and 502.

Quantification of N_2 from denitrification.

N_2 formed by denitrification was determined according to the isotope dilution approach based on comparison of isotope ratios of ^{15}N -labeled samples with those at natural abundance (NA). The mass m/z 30 was chosen, because the amount of labelled N_2 was so small that it did not lead to significant changes in the mass m/z 29 of the background N_2.

$$\left(\frac{^{30}N_2}{^{28}N_2}\right)_{labeled} = \frac{\left[^{30}N_2\right]_{NA} + \left[^{30}N_2\right]_{denitrification}}{\left[^{28}N_2\right]}$$

$$\left(\frac{^{30}N_2}{^{28}N_2}\right)_{labeled} = \frac{\left(\left(\frac{^{30}N_2}{^{28}N_2}\right)_{NA} \times \left[^{28}N_2\right]\right) + \left[^{30}N_2\right]_{denitrification}}{\left[^{28}N_2\right]}$$

$$\left[^{30}N_2\right]_{denitrification} = \left(\left(\frac{^{30}N_2}{^{28}N_2}\right)_{labeled} - \left(\frac{^{30}N_2}{^{28}N_2}\right)_{NA}\right) \times \left[^{28}N_2\right]$$

Here, measured isotope ratios are given in parenthesis and amount of substance in squared brackets. $[^{28}N_2]$ in the headspace (80 vol% N_2) was calculated according to the natural abundance of ^{15}N and the ideal gas law:

$$\left[^{28}N_2\right] = [N_2] \times (1 - 2 \times 0.00364)$$

with:

$$[N_2] = \frac{pV}{RT} \times 0.8$$

where p, V, R and T are the pressure, headspace volume, ideal gas constant and temperature, respectively.

Quantification of N_2O from denitrification.

Denitrification-derived N_2O of samples at natural abundance and ^{15}N labeled samples was determined by calibration of the quantitative ions 44 ($^{14}N_2O$) and 46 ($^{15}N_2O$), respectively. Since all N_2O and N_2 in the sample vials stemmed from the experimental bottles, the increase of N_2O over time could be quantified relative to the mass m/z 29 of nitrogen (N_2) as an internal standard. Further, since samples were taken only from the headspace, but N_2O was also present in aqueous solution, this additional mass was taken into account by correcting for partitioning between the liquid and gaseous phase according to Henry's law (dimensionless Henry's constant of 1.68

Mass balance of transformation

Finally, the nitrogen transformed from $NaNO_3$ to both N_2 and N_2O was calculated as follows:

$$p(N_{trans.\ to\ N_2}) = \frac{2 \times [^{30}N_2]_{denitrification}}{[NaNO_3]} \times 100$$

$$p(N_{trans.\ to\ N_2O}) = \frac{2 \times [N_2O]}{[NaNO_3]} \times 100$$

where $[^{30}N_2]_{denitrifiaction}$ and $[N_2O]$ refer to the amount of substance formed by denitrification and $[NaNO_3]$ refers to the initial amount of $NaNO_3$ added to the microbial medium.

3.2. Supplementary Figures and Tables

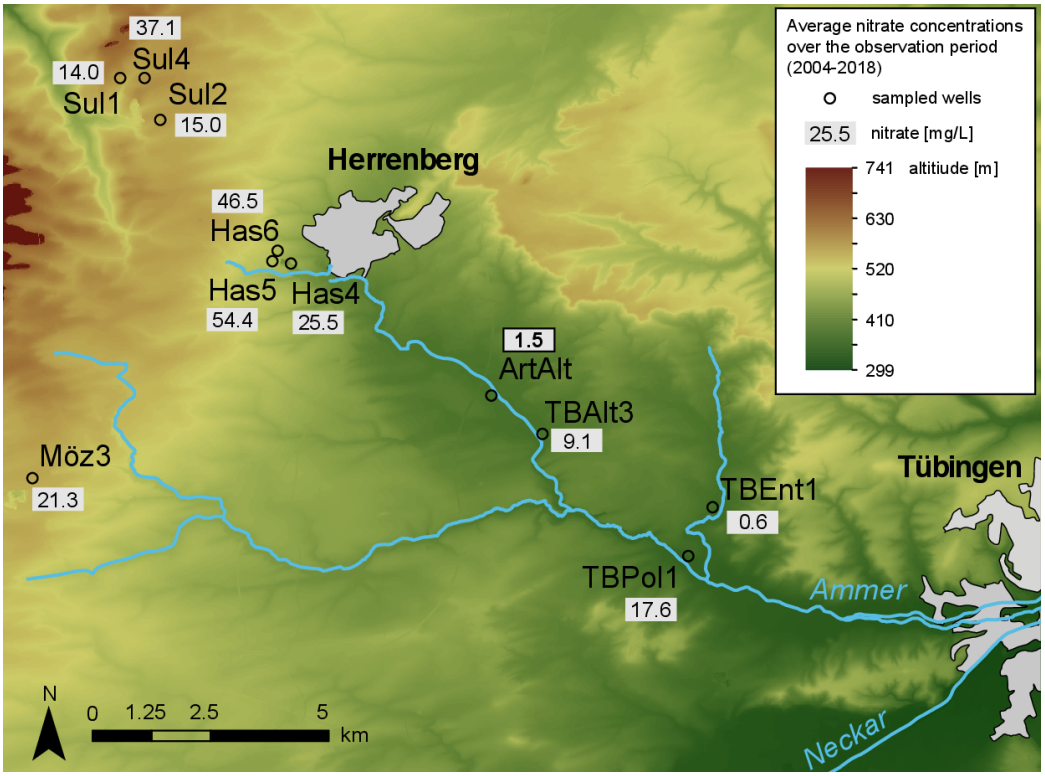

Figure S1. Location of selected groundwater monitoring wells in the Ammer catchment. Average concentrations of nitrate are shown in grey boxes in mg/L. The value in box with a black outline represents the nitrate concentration in a low-nitrate artesian well (ArtAlt) from which the sample for the enrichment of the autotrophic nitrate-reducing Fe(II)-oxidizing culture was collected.

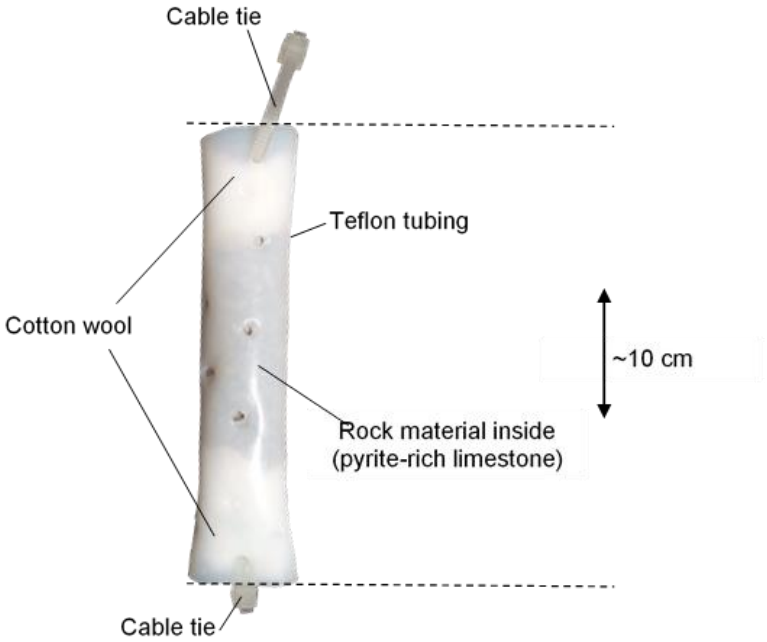

Figure S2. Microbial Trapping Device (MTD) which was filled with pyrite-rich limestone and deployed to the groundwater well in order to isolate autotrophic nitrate-reducing Fe(II)-oxidizing microorganisms.

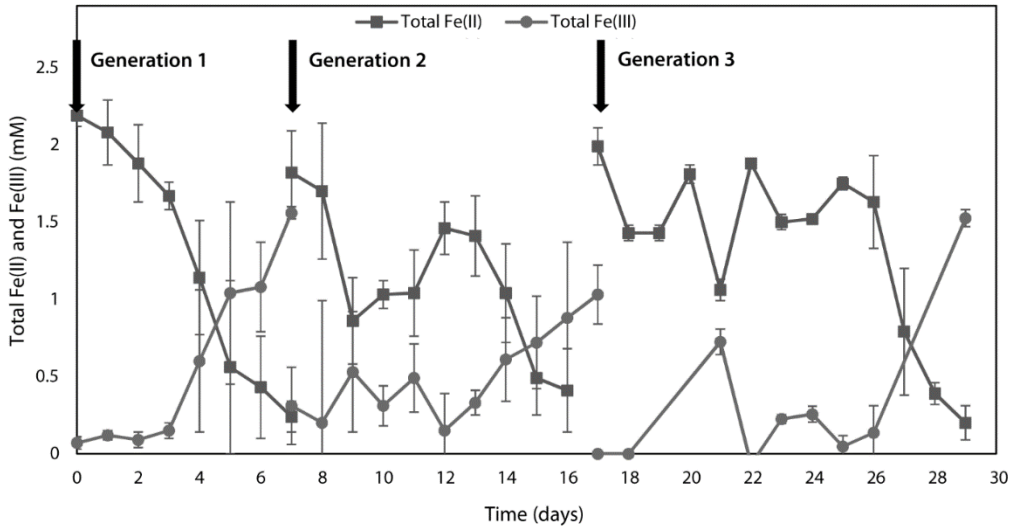

Figure S3. Total Fe(II) and Fe(III) concentration measured in three consecutive transfers (Generation 1, 2 and 3) of the autotrophic nitrate-reducing Fe(II)-oxidizing enrichment culture. All data points are mean values of samples from three replicate bottles, error bars represent standard deviations. The transfers on days 0, 7 and 17 are indicated by arrows.

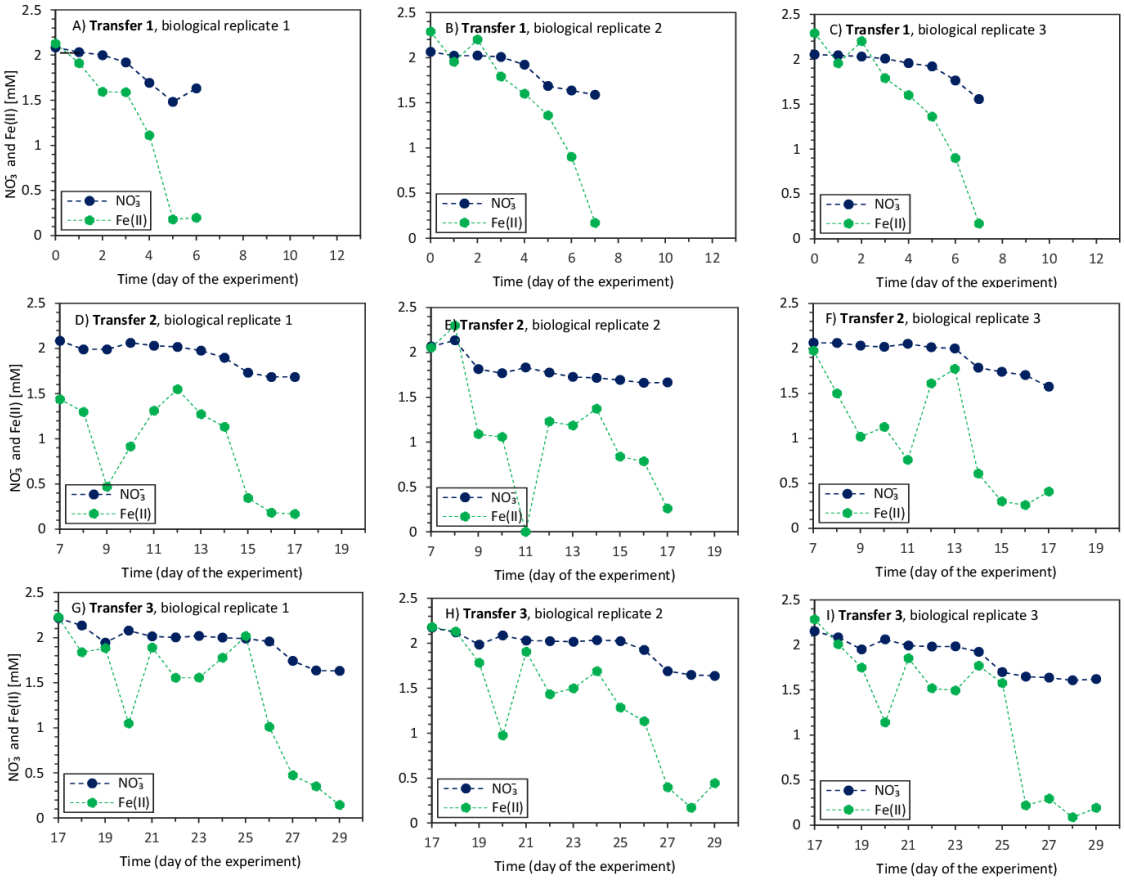

Figure S4. Concentrations of dissolved NO_3^- and Fe^{2+} in three consecutive transfers of the autotrophic nitrate-reducing Fe(II)-oxidizing enrichment culture. Each plot represents a single biological replicate. During the experiment the culture was transferred on day 0, 7 and 17.

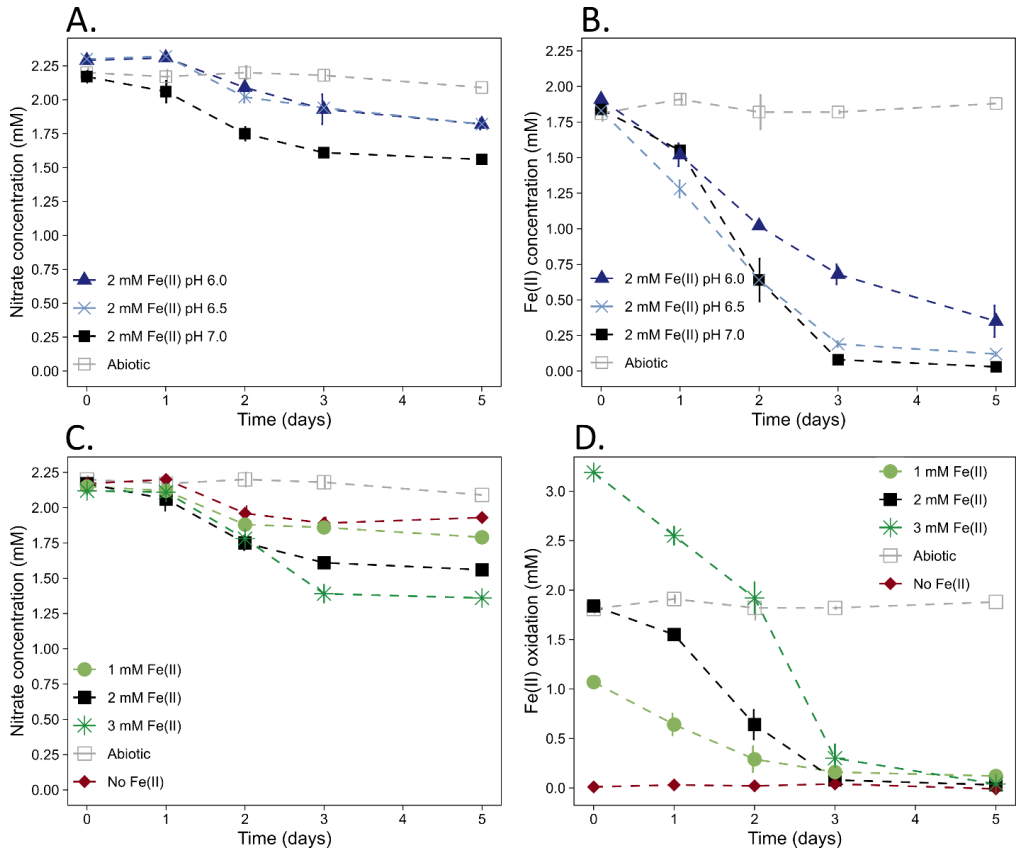

Figure S5. NO_3^- and Fe(II) concentrations over time during cultivation of the NRFeOx enrichment culture in medium with 2 mM of Fe(II) and pH 6.0, 6.5, 7.0 (A and B) and at pH 7.0 with various concentrations of Fe(II): 1 mM, 2 mM and 3 mM (C and D). Data points are shown as averages. Error bars indicate standard deviations calculated from three independent parallel biological replicates.

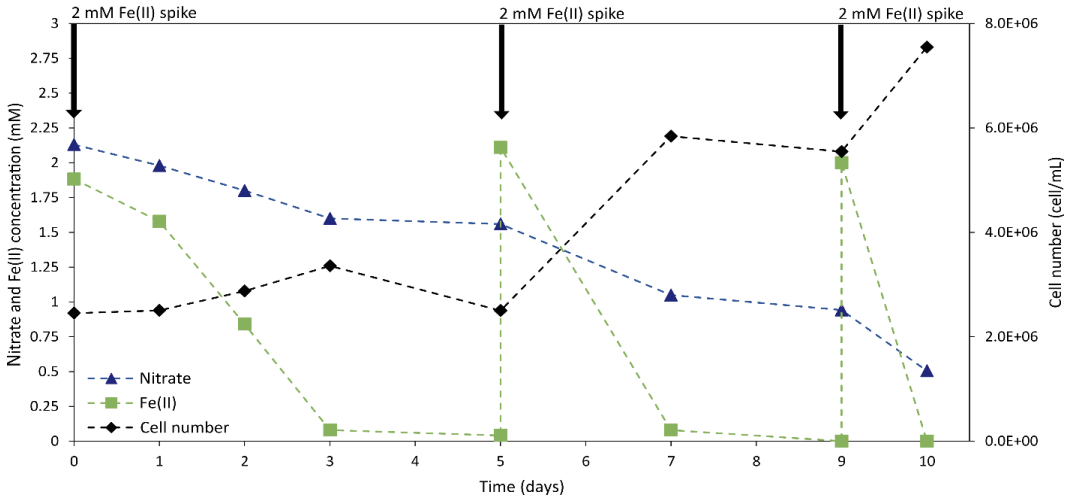

Figure S6. Cell numbers as well as Fe(II) and NO_3^- concentrations over time during cultivation of the NRFeOx enrichment culture in the growth experiment where cultures were spiked with 2 mM Fe(II) once all Fe(II) was consumed. Due to variations in cell numbers and individual lag phases of different cultures, a representative data set is shown. Averages of cell numbers calculated from three independent biological replicates together with standard deviation are presented in Table S1.

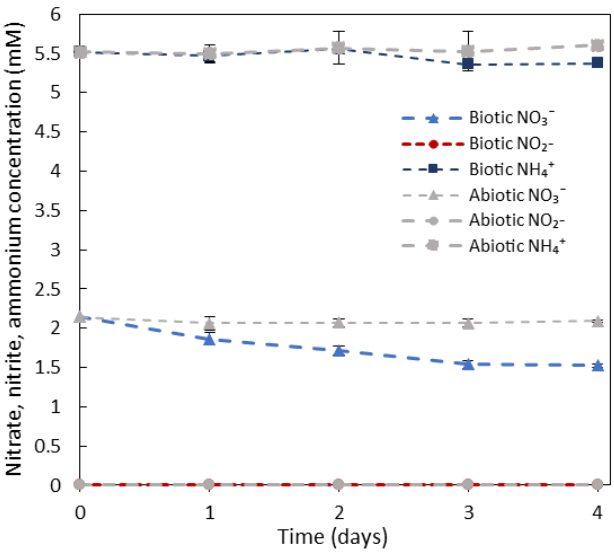

Figure S7. Total NO_3^-, NO_2^-, NH_4^+ concentrations over time during cultivation of the NRFeOx enrichment culture in medium with 2 mM of Fe(II) and pH 7.0. Data points are shown as averages. Error bars indicate standard deviations calculated from three independent parallel biological replicates.

Table S1. Average concentrations of $^{15}N\text{-}NO_3^-$ transformed (0.61±0.02 mM) to $^{15}N\text{-}N_2O$ and $^{15}N\text{-}N_2$ over time of incubation at day 0, 2, and 4. The averages are calculated from three independent biological replicates together with standard deviation (SD).

	Day 0		**Day 2**		**Day 4**	
	Concentration (mM)	SD	Concentration (mM)	SD	Concentration (mM)	SD
$^{15}N\text{-}N_2O$	0.00	0.00	0.10	0.02	0.25	0.01
$^{15}N\text{-}N_2$	0.00	0.00	0.07	0.02	0.11	0.02

Table S2. NO_3^- reduced, Fe(II) oxidized and ratio of $NO_3^-{}_{reduced}/Fe(II)_{oxidized}$ for the NRFeOx enrichment culture measured under 4 different growth conditions (0 mM, 1 mM, 2 mM, 3 mM of Fe(II)) at pH 7.0 at the beginning (day 0) and the end of Fe(II) oxidation/NO_3^- reduction (day 5, Figure S5) shown as averages of three independent parallel biological replicates. Errors represent standard deviation (SD).

Setup	**NO_3^- reduced (mM)**	**Fe(II) oxidized (mM)**	**ratio $NO_3^-{}_{reduced}/Fe(II)_{oxidized}$**
0 mM Fe(II)	0.24±0.06	-	-
1 mM Fe(II)	0.36±0.03	0.96±0.02	0.33
2 mM Fe(II)	0.61±0.04	1.82±0.04	0.31
3 mM Fe(II)	0.76±0.03	3.16±0.00	0.24

Table S3. Cell numbers for the of NRFeOx culture measured under 4 different growth conditions (0 mM, 1 mM, 2 mM, 3 mM of Fe(II)) at pH 7.0 at the beginning (day 0) and the end of Fe(II) oxidation/NO_3^- reduction (day 5, Figure S5) shown as averages of triplicate flow cytometry measurements. Standard deviations (SD) were calculated from three independent parallel biological replicates.

	0 mM Fe(II)		**1 mM Fe(II)**		**2 mM Fe(II)**		**3 mM Fe(II)**	
Day	Cell counts (cells/ml)	SD	Cell counts (cells/ml)	SD	Cell counts (cells/ml)	SD	Cell counts (cells/ml)	SD
0	1.76E+06	1.10E+05	1.88E+06	2.92E+05	2.01E+06	3.67E+05	1.89E+06	3.46E+05
5	3.02E+06	7.68E+05	3.18E+06	1.13E+06	3.34E+06	7.68E+05	4.28E+06	7.28E+05

Table S4. Mössbauer hyperfine parameters for the Fe mineral precipitate formed by microbial Fe(II) oxidation. CS – center shift, Q – quadrupole splitting, R.A. relative abundance, χ^2 – goodness of fit.

	CS (mm/s)	**ΔE_Q (mm/s)**	**R.A. %**	**Error %**	**χ^2**
Fe(III)	0.49	0.83	87.8	1.7	0.548
Fe(II)	1.31	3.05	12.2	1.7	

4. Anaerobic neutrophilic pyrite oxidation by a chemolithoautotrophic nitrate-reducing iron(II)-oxidizing culture enriched from a fractured aquifer

Natalia Jakus[a,b], Adrian Mellage[c], Carmen Hoeschen[d], Markus Maisch[a], James M. Byrne[a,e], Carsten W. Mueller[d,f], Peter Grathwohl[g] and Andreas Kappler[a]

[a]Geomicrobiology, Center for Applied Geoscience, University of Tuebingen, Germany

[b]Microbial Ecology, Center for Applied Geoscience, University of Tuebingen, Germany

[c]Hydrogeology, Center for Applied Geosciences, University of Tuebingen, Germany

[d]Soil Science, TUM School of Life Sciences, Technical University of Munich, Germany

[e]Now: School of Earth Sciences, University of Bristol, UK

[f]Now: Department of Geosciences and Natural Resource Management, University of Copenhagen, Denmark

[g]Hydrogeochemistry, Center for Applied Geoscience, University of Tuebingen, Germany

Abstract

Neutrophilic microbial pyrite (FeS_2) oxidation coupled to denitrification is thought to be to be an important natural nitrate attenuation pathway in nitrate-contaminated aquifers. However, the poor solubility of pyrite raises questions about its bioavailability and the mechanisms underlying its oxidation. Here, we investigated direct microbial pyrite oxidation by a neutrophilic chemolithoautotrophic nitrate-reducing Fe(II)-oxidizing culture enriched from a pyrite-rich aquifer. We used pyrite with natural abundance (NA) of Fe isotopes (^{NA}Fe-pyrite) and ^{57}Fe-labelled siderite to evaluate whether the oxidation of the more soluble Fe(II)-carbonate ($FeCO_3$) can indirectly drive abiotic pyrite oxidation. Our results showed that in setups where only pyrite was incubated with bacteria, direct microbial pyrite oxidation contributed ca. 26% to overall nitrate reduction. The rest was attributed to the oxidation of elemental sulfur (S^0), present as a residue from pyrite synthesis. Pyrite oxidation was evidenced in the ^{NA}Fe-pyrite/^{57}Fe-siderite setups by maps of ^{56}FeO and ^{32}S obtained using a combination of SEM with NanoSIMS which showed the presence of ^{56}Fe(III) (oxyhydr)oxides that could solely originate from $^{56}FeS_2$. Based on the fit of a reaction model to the

geochemical data and the Fe-isotope distributions from NanoSIMS, we conclude that anaerobic oxidation of pyrite by our neutrophilic enrichment culture was mainly driven by direct enzymatic activity of the cells. The contribution of abiotic pyrite oxidation by Fe^{3+} appeared to be negligible in our experimental setup.

4.1. Introduction

In low-oxygen environments, nitrate can be naturally attenuated via denitrification or dissimilatory nitrate reduction to ammonium (DNRA). Among several environmental factors controlling the dominant nitrate removal pathway, carbon limitation in the presence of excess nitrate has been shown to favor denitrification.(Tiedje 1988; Nizzoli *et al.* 2010; Kraft *et al.* 2014) Denitrification is the stepwise reduction of nitrate via nitrite (NO_2^-), nitric oxide (NO), nitrous oxide (N_2O) to dinitrogen gas (N_2), where each step can be catalyzed by microbes equipped with specific reductase enzymes.(Kuypers, Marchant and Kartal 2018) While organic matter oxidation yields the most energy, in many ecosystems the availability of organic carbon is limited and inorganic compounds become alternative electron donors for denitrifiers.(Kumar *et al.* 2018) These chemolithoautotrophic bacteria produce energy for CO_2 fixation from the reduction of nitrate coupled to oxidation of compounds such as reduced sulfur-species or Fe(II).(Rivett *et al.* 2008; Liu *et al.* 2019)

In anoxic, circumneutral-pH environments, Fe(II) can be found as dissolved Fe^{2+}, complexed by organic matter (Fe(II)-OM) (Hopwood *et al.* 2015; Bhattacharyya *et al.* 2018) or adsorbed onto mineral surfaces. However, Fe(II) is predominantly embedded within the structure of Fe(II)-rich clays or minerals like siderite ($FeCO_3$) and pyrite (FeS_2) (Weber, Picardal and Roden 2001). Denitrification at neutral pH coupled to Fe(II) sulfides oxidation has been examined extensively in many environments such as surface sediments(Hayakawa *et al.* 2013), marine sediments (Schippers and Jorgensen 2002), freshwater wetlands and coastal sites (Vaclavkova *et al.* 2014), and in different types of aquifers like: sandy (Postma *et al.* 1991; Jørgensen *et al.* 2009; Zhang *et al.* 2012), schist (Pauwels *et al.* 1998), clay and gravel (Schwientek *et al.* 2008) aquifers. Pyrite oxidation has been also proposed recently to drive denitrification in a fractured carbonate aquifer (Schwientek *et al.* 2008; Visser *et al.* 2020). The mechanisms enabling pyrite-mediated denitrification, however, remain a matter of contention in the literature, with several studies arriving at contradictory conclusions (Yan *et al.* 2019). The ambiguity in the current process understanding hints at a more complex picture than currently thought. For instance nitrate reduction, which was previously attributed to pyrite oxidation, may also occur as a result of oxidation of intracellularly stored sulfur or residual elemental sulfur that typically is associated with synthetized FeS_2.(Yan *et al.* 2019).

In pH-neutral environments, pyrite oxidation can be coupled to the abiotic reduction of two other oxidants: O_2 and Fe(III) (Moses *et al.* 1987). Indeed, isotopic evidence has provided support for anaerobic FeS_2 oxidation with Fe(III) as oxidant in marine sediments (Bottrell *et al.* 2000). Although both reactions occur abiotically, parallel microbially mediated reactions can enhance the kinetics and extent of pyrite weathering. In a study investigating subglacial habitats, chemolithotrophic bacteria were found to oxidize pyrite using oxygen in carbonate-buffered system (Boyd *et al.* 2014). Similarly,

in another study, an enrichment culture was shown to increase rates of pyrite oxidation under oxic pH-neutral conditions by an order of magnitude compared to abiotic rates (Percak-Dennett *et al.* 2017). Microorganisms were also proposed to be indirectly involved in a Fe(III)-driven pyrite oxidation pathway (Sand *et al.* 2001). In this "indirect" mechanism, enzymatic oxidation of aqueous Fe^{2+} resulted in the formation of Fe^{3+} ions that abiotically oxidized pyrite yielding a release of sulfate and regeneration of aqueous Fe^{2+} that can be further oxidized microbially. This mechanism is, however, limited by the immediate precipitation of Fe^{3+} (Peiffer and Stubert 1999; Schippers and Jorgensen 2002). The direct attachment of cells onto the surface of pyrite, however, can lead to the formation of a slightly acidic pH microenvironment at the cell-mineral interface or the release of organic ligands which may increase pyrite dissolution and oxidation rates (Peiffer and Stubert 1999; Sand *et al.* 2001; Percak-Dennett *et al.* 2017). One remaining question is whether in anoxic environments nitrate can substitute O_2 and serve as an electron acceptor for direct or indirect pyrite oxidation.

The primary goal of this study was therefore to determine if, at neutral pH, autotrophic bacteria can mediate pyrite oxidation and couple it to the reduction of nitrate either by direct or indirect pyrite oxidation. We incubated a lithoautotrophic nitrate-reducing Fe(II)-oxidizing (NRFeOx) culture, that was enriched using Fe(II)-rich crushed limestone particles exposed to groundwater, in nitrate-containing medium with siderite and/or pyrite. Combining geochemical monitoring of dissolved species and HCl-extractable iron with a reaction model, we determined the relative contributions of the dominant reaction mechanisms driving denitrification coupled to solid-phase Fe(II) oxidation. We also identified the mineral products and their spatial associations using NanoSIMS in combination with SEM, Mössbauer spectroscopy and ^{57}Fe-labelled (100%) siderite to differentiate it from non-labelled pyrite and pyrite-derived oxidation products with naturally abundant iron isotopes, including ^{56}Fe (2.20%) which was used as a isotopic marker.

4.2. Materials and methods

4.2.1. Preparation and characterization of iron minerals

^{57}Fe-siderite and ^{NA}Fe-siderite (natural abundance of Fe isotopes) were synthetized and characterized as described in the SI. Synthesized pyrite was boiled in 1 M HCl for 1 h and then washed three times with MQ water, three times with acetone and ten times with petroleum ether to remove residual unreacted elemental sulfur following the protocol described by Yan et al., (2018). The final ^{NA}Fe-pyrite contained 3.12 ± 0.1 mass% elemental sulfur (determined using HPLC, see SI) which was slightly lower than the 4.6 mass% elemental sulfur reported by Yan et al., (2018).

4.2.2. Cultivation of microorganisms

A chemolithoautotrophic NRFeOx culture was enriched from an anoxic, pyrite-rich limestone aquifer in southwest Germany (Jakus *et al.* 2021). Before the experiments, the culture was pre-grown in anoxic bicarbonate-buffered (22 mM) freshwater low phosphate medium (LPM) modified

from Ehrenreich & Widdel (1994) containing 0.6 g/L KH_2PO_4, 0.3 g/L NH_4Cl, 0.5 g/L $MgSO_4 \cdot 7H_2O$, and 0.1 g/L $CaCl_2 \cdot 2H_2O$, adjusted to pH 7.0-7.1, and supplemented with 2 mM of $NaNO_3$ and 2 mM of $FeCl_2$ as described in detail in the SI. 16S rRNA gene sequencing revealed that the culture consists of microorganisms which are related to bacteria previously reported in pyrite-oxidizing and nitrate-reducing communities, such as *Gallionellaceae* sp., *Acidovorax* sp., and *Thiobacillus denitrificans* (Jakus *et al.* 2021).

4.2.3. Batch pyrite oxidation experiments

Batch pyrite oxidation experiments were conducted at 25°C in serum glass bottles (58 mL volume, 25 mL medium) sealed with butyl rubber stoppers and flushed with CO_2/N_2 (20/80%) (Figure S2). Bicarbonate-buffered (22 mM, pH 7.0) LMP medium was prepared for precultivation (SI). All experimental setups were amended with 2 mM $NaNO_3$. In three different biotic setups either (1) ^{57}Fe-siderite, (2) ^{NA}Fe-pyrite or (3) ^{NA}Fe-pyrite and ^{57}Fe-siderite were added to reach concentrations of 2, 5, and 7 mM of total Fe(II), respectively. Additionally, another biotic experiment was conducted with (4) both ^{NA}Fe-pyrite and ^{NA}Fe-siderite as a control for isotopic enrichment in siderite. All biotic setups were inoculated with 10% (vol/vol) of the NRFeOx enrichment (ca. 2E+06 cells mL^{-1}). Two abiotic controls containing both ^{NA}Fe-pyrite and ^{57}Fe-siderite were prepared: (5) with 10% autoclaved cells to determine the potential influence of the presence of inactive cells, and (6) without cells to assess a potential isotopic exchange between pyrite and siderite. All experiments were run in triplicate.

4.2.4. Sampling and chemical analysis

Batch incubations were sampled in an anoxic glovebox (100% N_2) by withdrawing 0.4 mL aliquots using sterile syringes. Samples were centrifuged (14,000 g, 10 min) to separate the supernatant from iron minerals and biomass. Samples for nitrate, nitrite and sulfate analysis were diluted in anoxic MQ and stored anoxically until measurements. Nitrate and nitrite were quantified following the DIN 38405/ISO 13395 standard quantification method using AA3 HR AutoAnalyzer System (Seal Analytical, Germany) equipped with a dedicated dialysis membrane delivered by the manufacturer to eliminate potential interference with any solids that could remain in the samples after centrifugation. Sulfate was measured using ion chromatography (Eco IC, Metrohm). Samples containing dissolved Fe^{2+} were diluted with anoxic 1 M HCl to prevent oxidation and analyzed using the ferrozine method (Klueglein and Kappler 2013; Schaedler, Kappler and Schmidt 2018). Treatment and analyses of the solid-phase are describe in the SI.

4.2.5. Conceptual and numerical reaction model

Based on the results from our incubation experiments, we postulated two competing conceptual models to qualitatively and quantitatively describe the measured geochemical data (Figure 1). Scenario 1 (S1) assumes that oxidation of all available solid-phase electron donors (siderite, pyrite and S^0) is independently biologically catalyzed, coupled to the reduction of nitrate, and does not consider additional reversible redox feedback loops (Figure 1A, C, D). Scenario 2 (S2) includes all processes in S1 in addition to the abiotic oxidation of pyrite by Fe^{3+}, produced from siderite oxidation.

The additional abiotic step releases Fe^{2+} (and SO_4^{2-}) into solution adding an additional electron donor that can contribute to sustained nitrate reduction, by closing the Fe-redox cycle (Figure 1E).

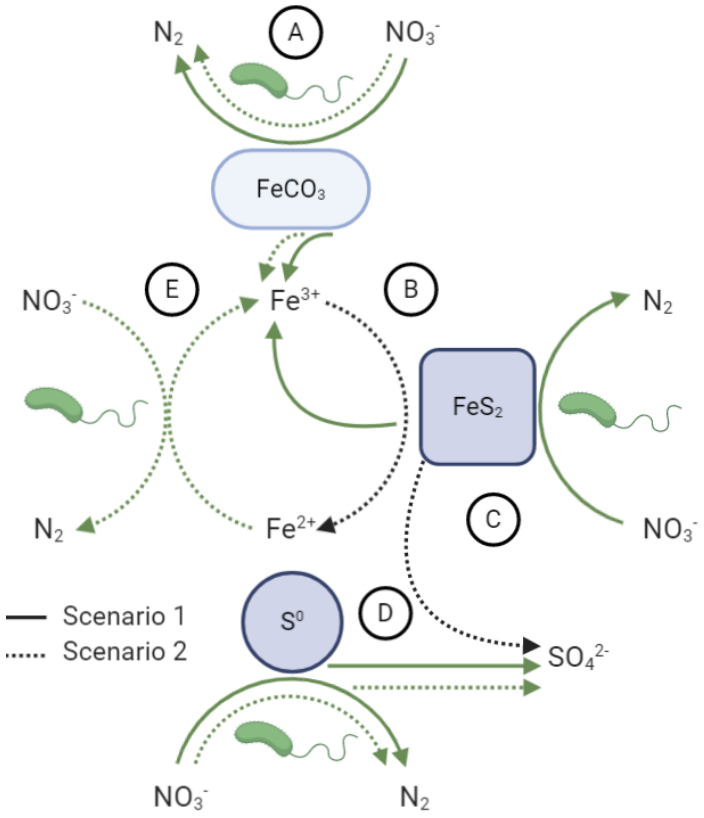

Figure 1. Conceptual figure showing a network of abiotic (black lines) and bacterially mediated reactions (green lines) that might lead to nitrate removal: A) microbial siderite oxidation coupled to nitrate reduction, B) abiotic pyrite oxidation coupled to Fe^{3+}reduction, C) microbial pyrite oxidation coupled to nitrate reduction, D) microbial elemental sulfur oxidation coupled to nitrate reduction, E) microbial Fe^{2+} oxidation coupled to nitrate reduction. The two different line types represent two scenarios modeled in this study. Scenario 1 (S1, solid lines), include reactions A, C and D and represents a model where oxidation of all available electron donors, i.e., siderite, pyrite and elemental sulfur happened independently from each other, with nitrate serving as the electron acceptor (Figure 1A, C, D). Scenario 2 (S2, dashed lines) includes (in addition to the processes in S1) the abiotic oxidation of In turn, pyrite oxidation produces Fe^{2+} which can be microbially oxidized and form Fe^{3+} again closing the feedback loop (E). Models assume that denitrification and sulfur oxidation are complete, leading to formation of N_2 and SO_4^{2-}, respecively. Created with BioRender.com .

We formulated our conceptual model(s) into a reaction model, assuming well-mixed conditions without explicitly considering mineral surface interactions such as the sorption of Fe(III) onto pyrite prior to pyrite oxidation. The model, written in MATLAB and described in detail in the SI, assumes that nitrate is reduced to N_2 and that reduced sulfur species (S_2^{2-} and S^0) are oxidized to SO_4^{2-}. In our model, both oxidation of pyrite and oxidation of S^0 contribute to the total SO_4^{2-} pool. The S1 formulation of our simplified model was calibrated jointly to the experimental data of the siderite- and pyrite-only incubations, as these allowed to separate the reactive contributions of siderite and pyrite from one another, which were then lumped in a validation step of the "mixed" experiment. Thus, allowing us to propose potentially dominant reaction pathways based on quantitative rate-law formulations.

4.2.6. SEM and NanoSIMS imaging

Samples (100 µL) for SEM and NanoSIMS were withdrawn with a syringe in an anoxic glovebox (100% N_2) from the treatments containing 1) ^{NA}Fe-pyrite, ^{57}Fe-siderite and bacterial cells, 2) ^{NA}Fe-pyrite, ^{NA}Fe-siderite and bacterial cells, and 3) ^{NA}Fe-pyrite, ^{57}Fe-siderite and autoclaved bacterial cells. Each sample was mixed with 400 µL of 0.2 µm-filtered anoxic MQ water. Thereafter, an aliquot of 60 µL of was loaded on a silica wafer and left until dry in the glovebox. The wafers were mounted on SEM stubs and stored anoxically until sputter-coated with Pd (~12 nm). To characterize the distribution and spatial relation between pyrite, siderite and Fe(III) (oxyhydr)oxides, SEM (JEOL JSM-6500F field emission SEM with a Schottky field emitter (JEOL Ltd., Japan), equipped with secondary electron detector (acceleration voltage 10 kV; working distance 5.29 mm), was used. NanoSIMS analyses were performed using a Cameca NanoSIMS to map the distribution of siderite and pyrite products revealed by the secondary ions ^{56}Fe, ^{57}Fe (O^- primary beam, RF source) and ^{56}FeO, ^{32}S (Cs^+ primary beam). The measuring procedure and parameters are described in the SI.

4.3. Results and discussion

4.3.1. Nitrate attenuation

To determine the extent of oxidation of Fe(II) minerals coupled to nitrate reduction, we incubated an autotrophic NRFeOx enrichment culture with siderite, pyrite or a mix of both minerals and followed concentrations of NO_3^-, SO_4^{2-} and HCl-extractable Fe(II)/Fe(III) over time (Figure 2). The abiotic treatment exhibited negligible nitrate reduction indicated by NO_3^- concentrations that remained constant throughout the experiment (Figure 2A, Table S2). Conversely, in all biotic treatments, NO_3^- exhibited a significant drop from the starting 2 mM concentrations, indicating that biological activity mediated denitrification either in the presence of only siderite, only pyrite, or a mixture of pyrite and siderite. During 146-day incubation in the presence of ^{57}Fe-siderite (no pyrite), the autotrophic NRFeOx enrichment culture reduced 0.16 ± 0.13 mM of NO_3^- (Figure 2A, Table S2). The reduction started right after inoculation and lasted until day 4 with an average integrated nitrate reduction rate of 0.05 ± 0.01 mM day^{-1}. No further changes in NO_3^- concentrations were measured after day 4. In contrast, in microcosms with only pyrite, the concentration of nitrate decreased steadily from 2 to 1.2 mM, levelling off to a constant value at day 27, yielding an integrated consumption of 0.79 ± 0.19 mM of nitrate over the 146-day incubation. In the presence of both pyrite and ^{57}Fe- or ^{NA}Fe-siderite, the NRFeOx culture reduced 0.84 ± 0.04 mM and 0.90 ± 0.06 mM of nitrate in 146 days, respectively. Nitrate reduction commenced without a detectable lag phase. Analogous to the pyrite-only treatment, NO_3^- concentrations dropped steadily from 2 to 1 mM until day 27. In both setups no further changes in nitrate were observed thereafter. The amount of nitrate reduced in all pyrite-containing microbially active batches was higher than the amount of nitrate that can be reduced by this culture when no electron donors are supplied to the medium (0.24 ± 0.06 mM of nitrate consumption). This background nitrate consumption is probably due to the oxidation of substrates that are carried over from the pre-culture, stored within cells, or organic carbon background present in MQ water used to

prepare microbial medium, as it was previously discussed by Jakus et al., 2021. Therefore the most of nitrate reduction observed in our inoculated experiments can be attributed to microbial oxidation of siderite, pyrite and traces of elemental sulfur.

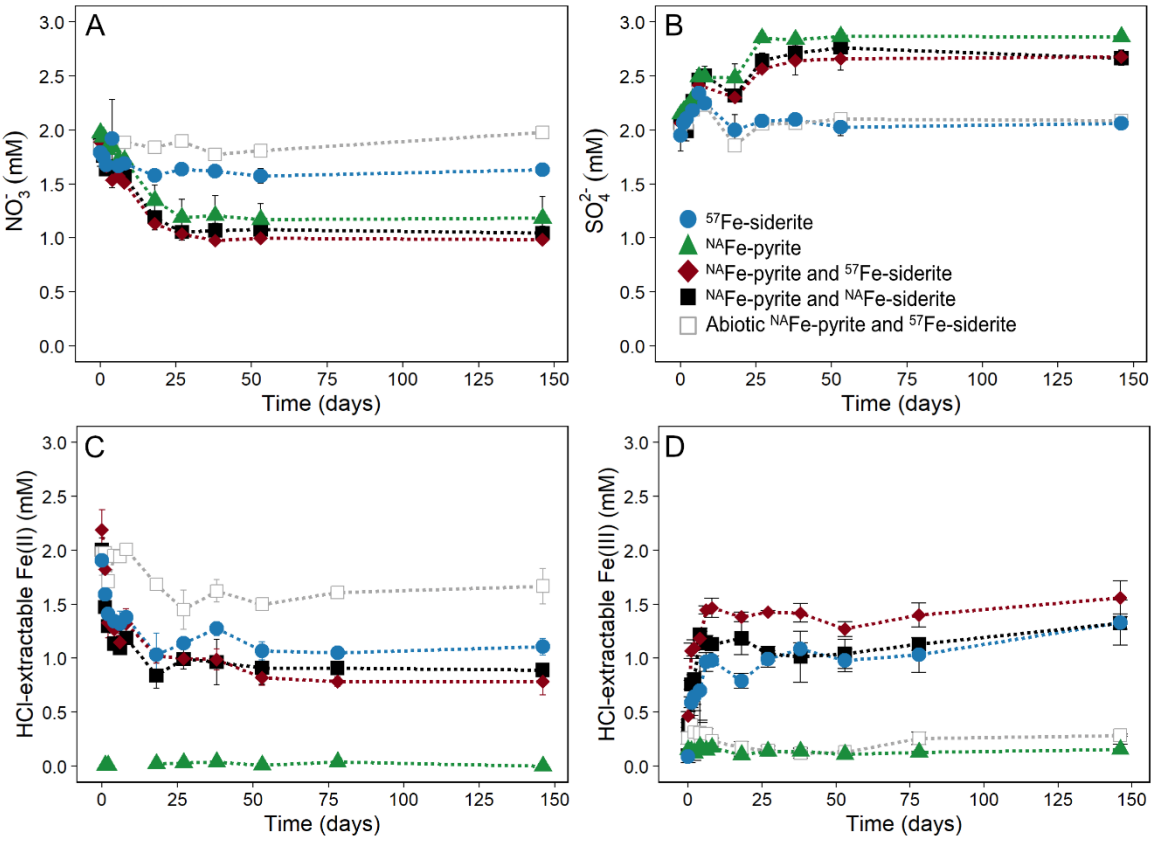

Figure 2. Nitrate (A), sulfate (B), HCl-extractable Fe(II) (C) and Fe(III) concentration (D) in setups where the autotrophic NRFeOx enrichment culture was incubated with nitrate and ^{57}Fe-siderite (blue circles), ^{NA}Fe-pyrite (green triangles), both ^{NA}Fe-pyrite and either or ^{57}Fe-siderite (black squares) or ^{NA}Fe-siderite (red diamonds) under anoxic, pH-neutral conditions. Abiotic controls contained 10% vol. of the same culture that was inactivated by autoclaving. All data points are average values of samples from three independent biological replicates, error bars represent standard deviations. Please note that the higher sulfate concentration measured at day 10 in all samples (B) resulted from an analytical problem at the ion chromatograph. Additional plots of the data for the first 30 days can be found in the SI (Figure S3).

4.3.2. Sulfate formation and $Fe^{2+}_{(aq)}$ release

The abiotic experiments containing siderite and pyrite and the biotic incubations with ^{57}Fe-siderite (no pyrite), exhibited a minor increase in SO_4^{2-} concentrations between day 0 and 10 resulting probably from measurement errors which was followed by a drop to the initial SO_4^{2-} concentration (Figure 1B). Therefore we conclude that in abiotic controls and batches containing ^{57}Fe-siderite (no pyrite), there were no changes in SO_4^{2-} concentrations during the experiment. In experiments where both ^{NA}Fe-pyrite and ^{57}Fe-siderite or ^{NA}Fe-pyrite and ^{NA}Fe-siderite were incubated, 0.61 ± 0.08 and 0.60 ± 0.07 mM of sulfate were produced between day 0 and day 27, respectively. The highest concentration of sulfate appeared in the setups with only pyrite (0.72 ± 0.2 mM; Table S2). In all setups, no accumulation of dissolved Fe^{2+} was observed (Table S2) since all available Fe^{2+} was most probably

immediately consumed by microbes. This can be supported by accumulation of Fe^{2+} in the abiotic control containing pyrite and ^{57}Fe-siderite, where 0.21 ± 0.02 mM of Fe^{2+} originating from dissolution of minerals was measured after 146 days. We speculate that the accumulation was due to the lack of Fe(III) precipitates that would have otherwise sorbed Fe(II). To quantify the concentration of Fe^{2+} that could potentially adsorb to mineral particles and serum bottle glass walls, we further measured HCl-extractable Fe(II) (see next section).

4.3.3. Fe(II) oxidation and formation of Fe(III) (oxyhydr)oxides

Using 1 M HCl, we extracted all HCl-soluble Fe(II), mainly derived from siderite together with Fe(II) potentially sorbed to the surface of Fe(III) (oxyhydr)oxide minerals. The synthetized pyrite was insoluble in 1 M HCl, therefore Fe(II) originating from pyrite was not quantified using this method. We found that in all biotic setups containing siderite, a concentration of total HCl-extractable Fe(II) (2 mM) rapidly decreased by 27.4-48.7% within the first 8 days (Figure 2C). In the setups containing siderite with or without pyrite, a fraction of the HCl-extractable Fe(II) was converted to HCl-extractable Fe(III) (Figure 2D). Specifically, in incubations where only siderite (2 mM) was present, our ferrozine spectrophotometric analyses showed that the concentration of HCl-extractable Fe(II) decreased by 0.78 ± 0.01 mM while 1.28 ± 0.2 mM of HCl-extractable Fe(III) was formed (Table S2). This suggests that some of the "missing" Fe(II) either transformed to more stable Fe(II) phases non-dissolvable in 1 M HCl (after 1 h extraction at room temperature) such as magnetite, or, probably more likely, sorbed to the walls of the glass bottles, since our mineral analyses did not show evidence for magnetite (see below) (Notini *et al.* 2019).

In incubations containing both pyrite and ^{57}Fe-siderite or pyrite and ^{NA}Fe-siderite, slightly more Fe(II) was depleted (removal of 1.11 ± 0.08 mM and 1.40 ± 0.14 mM of Fe(II), respectively) than Fe(III) formed (0.94 ± 0.07 mM and 1.09 ± 0.14 mM of Fe(III) formed, respectively) (Table S2). In the abiotic setups, the concentration of HCl-extractable Fe(II) decreased by 0.31 ± 0.29 over time of the experiment, but no Fe(III) was formed. Hence, supporting our hypothesis of Fe(II) loss via siderite dissolution, as evidenced by the presence of Fe^{2+}(aq), followed by Fe(II) adsorption to the glass walls of the incubation bottles (Table S2). This is further supported by the total HCl-extractable Fe(II)/Fe(tot) ratio (Figure S2), where the abiotic control remained stable over the complete time of incubation.

4.3.4. Reaction model results

Reaction model-simulated concentration time series were compared to experimental data obtained from the siderite-only, pyrite-only and the mixed pyrite/siderite incubations (Figure 3). (Note: The "mixed" model output was compared to the dataset collected using isotopically labeled siderite). For both the siderite- and pyrite-only cases, the simulated concentrations of all species aligned well with measurements (Figure 3). However, the model slightly underestimated the final amount of Fe(III) formed in the siderite incubation, likely related to the issue with Fe quantification discussed in the section above. In addition to the model output accounting for direct biotic pyrite oxidation, we also plotted the output of a version that excluded biotic pyrite oxidation and only accounted for sulfur-

dependent denitrification, to test whether concentration time series could be matched based on the presence of elevated levels of S^0, alone (see dashed lines in Figure 3B and G). Despite the large amount of S^0, the inclusion of microbial pyrite oxidation best fit the results, supporting our conceptual model that direct microbial pyrite oxidation contributed to nitrate reduction (Figure 3B) (and sulfate formation, Figure 3G). Thus, when comparing scenarios S1 and S2 in the mixed case we considered biotic pyrite oxidation in both. The solid lines in Figure 3C, F and G are the model-simulated concentrations for S1, considering mixed biotic siderite and pyrite oxidation and S^0-mediated denitrification. The combined reactions of the siderite oxidation and pyrite oxidation alone (S1) adequately captured the time series behavior of nitrate, Fe(II)/Fe(III), and sulfate. Conversely, the inclusion of an additional feedback loop, S2 (dashed lines Figure 3C, H), led to an over-estimation of nitrate consumption and sulfate production. Meaning that iron(II) released from the abiotic oxidation of pyrite would led to more denitrification and sulfate production than was measured. Instead, the reaction was limited and most of the reduction stopped at around day 30 (Figure 3A). The reaction was most probably constrained by the rapid precipitation of the Fe^{3+} as Fe(III) (oxyhydr)oxides (discussed below), suggesting that siderite-mediated pyrite oxidation played a negligible role in our experiments.

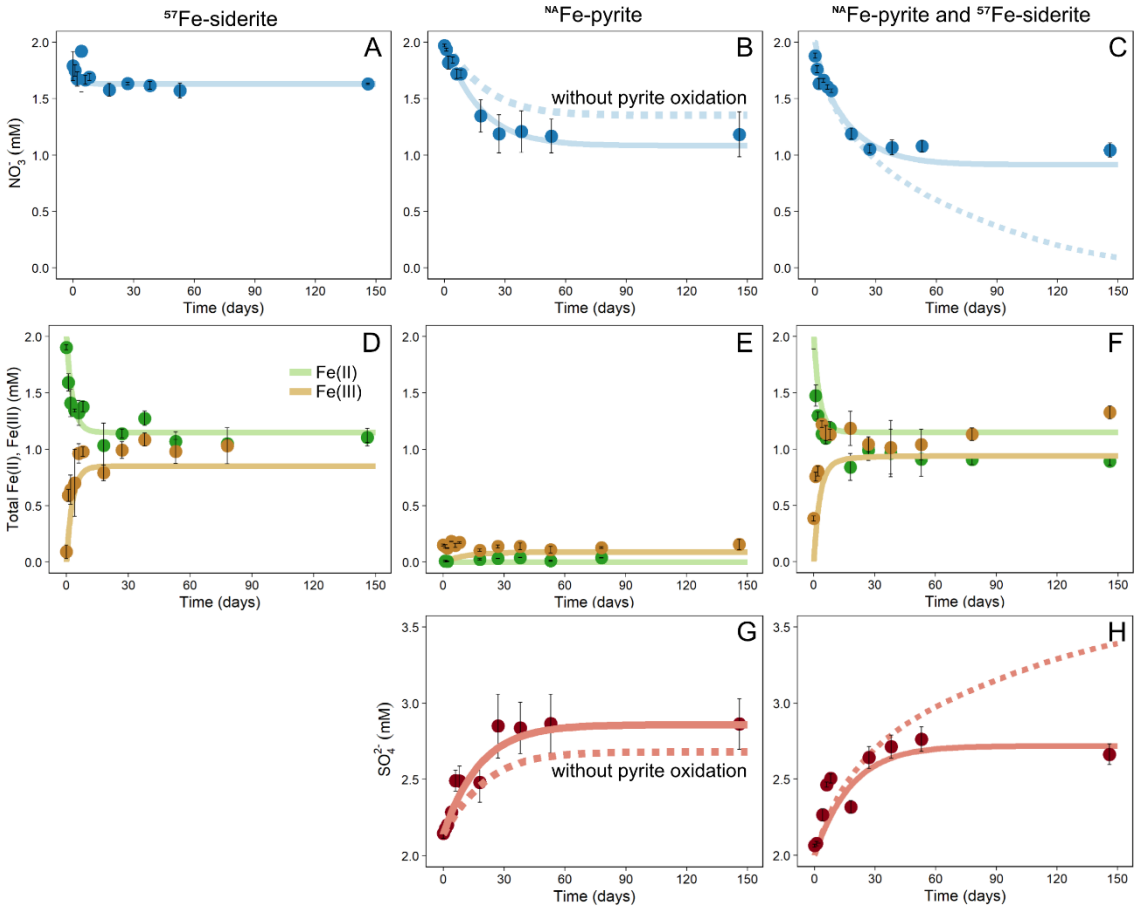

Figure 3. Simulation results (lines) and experimental data (circles) showing nitrate (1st row), iron (2nd row) and sulfate (3rd row) concentrations in three experimental setups where autotrophic NRFeOx culture was incubated with nitrate and ^{57}Fe-siderite (1st column), ^{NA}Fe-pyrite (2nd column) and both ^{NA}Fe-pyrite and ^{57}Fe-siderite (3rd column) under anoxic, pH-neutral conditions. Dashed lines in panels B and G, correspond to the case where no pyrite oxidation takes place but instead, nitrate is reduced by oxidation of elemental sulfur, leading to formation

of sulfate. Dashed lines on panels C, F and H represent scenario 1, which, in addition to reactions simulated in S1, includes the feedback loop of abiotic pyrite oxidation by Fe^{3+}.

4.3.5. Relative abundance and identity of solid phases

Mössbauer spectroscopy was used to follow the fate of pyrite and to identify the products of Fe(II) oxidation formed during the experiment. In the setup where both pyrite and ^{57}Fe-siderite were present, the initial relative abundance of siderite and pyrite was 94.2% and 5.2%, respectively (Figure 4). The sample contained also a small amount of a short-range ordered Fe(III) phase (SRO) (0.6%), likely Fe(III) (oxyhydr)oxides which most probably was transferred together with bacterial cells from the preculture (Figure 4). In samples collected after 8 and 146 days of incubation, we observed an increase in the relative abundance of the SRO Fe(III) phase to up to 33.1 and 43.4%, respectively. Considering a balance of relative phase abundances from day 0 to 146, the Voigt Based Fitting (VBF) models (see SI) suggest a predominant shift in phases from ^{57}Fe-siderite to SRO Fe(III) phases (Figure 4, Table S3), which can be attributed to the formation of e.g. ferrihydrite. Due to the low relative abundance of ^{57}Fe originating from pyrite (natural enrichment, ca. 2.2%) compared to ^{57}Fe originating from siderite (100% enrichment), pyrite oxidation evidenced by our geochemical and modelling data (see above) could be neither confirmed nor denied using the Mössbauer data. Furthermore, other highly crystalline Fe(II)-Fe(III) phases, insoluble in 1 M HCl after 1 h extraction at room temperature, that could potentially form in our setups (e.g. magnetite) were not detected. Finally, since the relative abundances of pyrite and siderite (in the abiotic setup) in the ^{57}Fe-specific Mössbauer spectrum did not change during incubation (Table S3), there was no isotopic exchange between ^{57}Fe-siderite and pyrite. This was a relevant control for the later NanoSIMS investigations, i.e. it allowed us to use ^{57}Fe from siderite to follow the formation of ^{57}Fe(III) as consequence of ^{57}Fe-siderite oxidation.

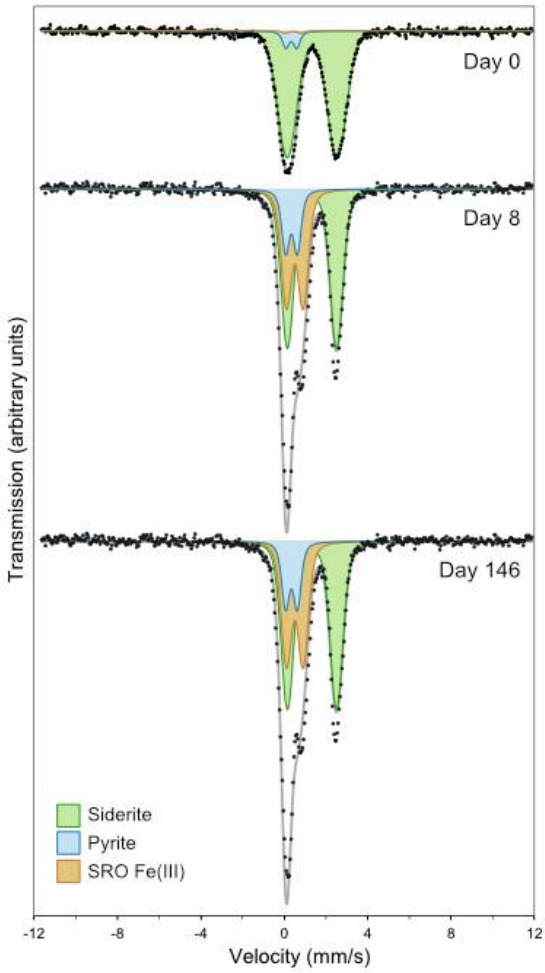

Figure 4. Mössbauer spectra (collected at 77 K) of setups containing both pyrite and siderite at the beginning of experiment (day 0), during incubation (day 8) and at the end of the experiment (day 146) showing the formation of short-range ordered (SRO) Fe(III) phases as a result of oxidation induced by the autotrophic NRFeOX culture. Black dots represent raw data, grey line shows the fitted spectrum, the green shading represents siderite and blue indicates pyrite, while brown area represents SRO Fe(III), likely ferrihydrite.

4.3.6. Spatial distribution of pyrite, siderite and formed Fe(III) (oxyhydr)oxides

SEM images of samples collected on day 8 of the incubation showed that mineral aggregates consisted of phases with various morphologies reflecting the presence of both pyrite and siderite (abiotic controls, Figure S3A) or pyrite, siderite and Fe(III) (oxyhydr)oxides (biotic controls, Figure 5A, Figure S3B). Using NanoSIMS, we obtained the spatial distribution of the two iron isotopes: ^{56}Fe (Figure 5A), predominantly originating from pyrite, and ^{57}Fe (Figure 5B), predominantly originating from siderite (purity 97.83%) and, to a much lower extent, from pyrite (with a natural abundance of ^{57}Fe of 2.12%). We used the $^{56}Fe/^{57}Fe$ isotopic ratio to identify phases relatively enriched in ^{56}Fe. (Note: This was only possible in samples where ^{57}Fe was used since in non-labeled setups the distribution of $^{56}Fe/^{57}Fe$ ratio was homogenous and close to theoretical value of 43.28, as shown in Figure S4). Most areas analyzed in the particle associations displayed a mean $^{56}Fe/^{57}Fe$ ratio of 1.44 ± 0.52 (Fig 5D, yellow numbers), which is close to the theoretical value of 2.18 that is expected

from setups containing a mixture of 5 mM ^{NA}Fe-pyrite and 2 mM ^{57}Fe-siderite (4.59 mM ^{56}Fe and 2.11 mM ^{57}Fe in total), meaning that minerals containing both isotopes were well mixed and homogeneously distributed. Some areas, however, displayed elevated ratios of ^{56}Fe/^{57}Fe (Figure 5D), reflecting local enrichment in ^{56}Fe, which indicated the presence of pyrite itself or of Fe(III) (oxyhydr)oxides stemming from oxidation of pyrite. Please note that all areas with elevated amounts of ^{56}Fe represent a mixture of different phases containing both ^{56}Fe and ^{57}Fe rather than pure ^{56}Fe phases (Figure 5), being a result of precipitation of Fe(III) (oxyhydr)oxides stemming from oxidation of both siderite and pyrite since isotopic exchange between the two minerals did not occur (Table S3). We further investigated the distribution of ^{32}S (Figure 5E) to localize S-containing phases, such as S^0 and pyrite. By comparing the distribution maps of S^0 and ^{56}Fe, we were then able to identify areas where ^{56}Fe was present in the absence of sulfur. This allowed us to localize ^{56}Fe(III) oxyhydroxides (^{56}Fe-enriched spots not containing any sulfur), that could only be the products of pyrite oxidation. By the overlay of ^{56}FeO and ^{32}S maps (Figure 5F) we finally confirmed the presence of Fe(III) (oxyhydr)oxides enriched in ^{56}Fe, demonstrating that pyrite oxidation occurred.

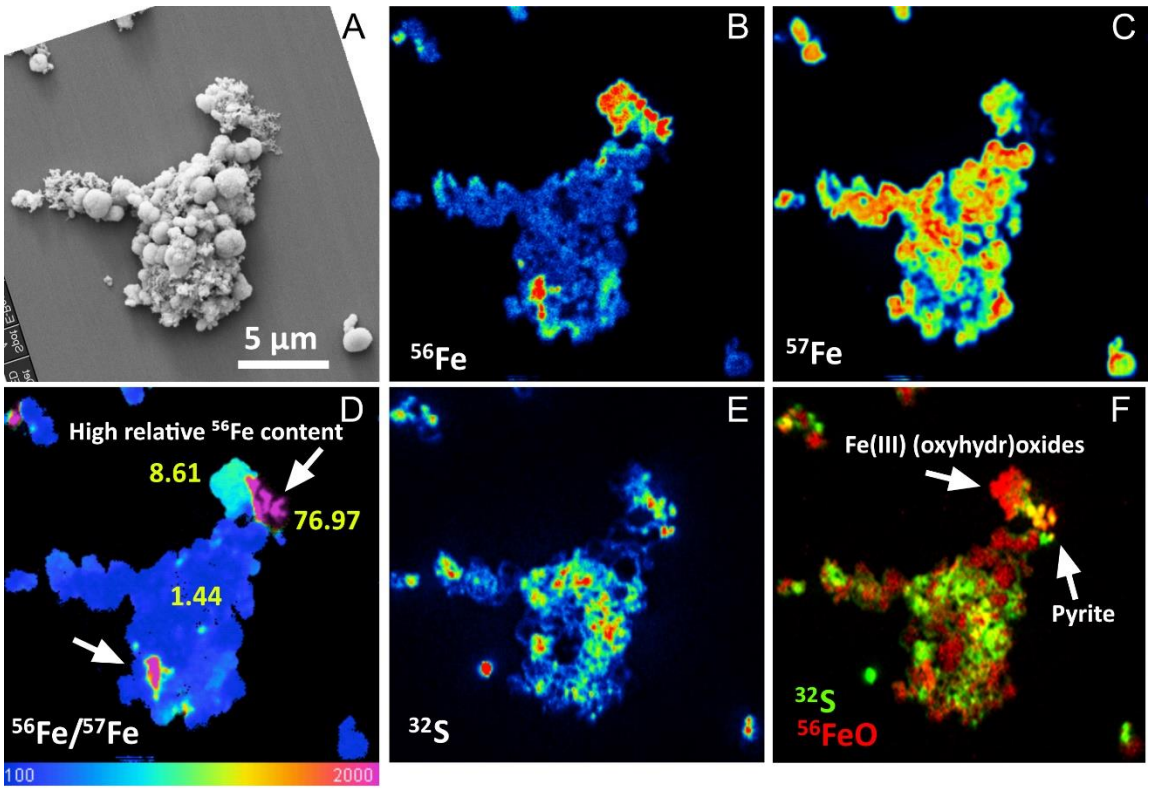

Figure 5. SEM image of a minerals aggregate (A) together with high spatial resolution NanoSIMS analysis of two isotopes of iron: ^{56}Fe (B) and ^{57}Fe (C) along with ratio image ^{56}Fe/^{57}Fe showing areas enriched in ^{56}Fe (D, arrows). Average ^{56}Fe/^{57}Fe ratios are shown next to the investigated areas (D, yellow font). Further, ^{32}S distribution (E) and composite image of ^{32}S and ^{56}FeO (E) are shown. All images were collected at the 8th day of incubation of ^{57}Fe-siderite and ^{NA}Fe-pyrite with NRFeOx culture. ^{57}Fe and ^{56}Fe were used as signatures of siderite and pyrite respectively. Zones with high ^{56}Fe/^{57}Fe ratio correlating with the distribution of ^{32}S indicate pyrite while the absence of sulfur indicates products of pyrite oxidation (Fe(III) (oxyhydr)oxides). ^{56}Fe and ^{57}Fe were measured with O^- source, ^{32}S and ^{56}FeO with Cs^+ source presenting different distortion. The values on scale for HSI images are multiplied by 10000.

4.3.7. Evidence for anaerobic pyrite oxidation by NRFeOx bacteria

For a long time, *Thiobacillus denitrificans* was the only bacterium described to couple pyrite oxidation to nitrate reduction at neutral pH. However, it was recently shown that *T. denitrificans* does not oxidize pyrite, but rather the reduced sulfur that is stored intracellularly or present as a contamination in the pyrite (Yan *et al.* 2019). Here we provide two lines of evidence in support of anaerobic pyrite oxidation mediated by nitrate-dependent Fe(II)-oxidizing bacteria. First, the overall agreement between the reaction model simulation and experimental results obtained from setups containing only ^{NA}Fe-pyrite (and S^0) supports the conceptual assumption that direct microbial oxidation of pyrite coupled to nitrate occurred in our experiments. Second, NanoSIMS composite maps of ^{56}FeO and S obtained from setups containing both ^{NA}Fe-pyrite and ^{57}Fe-labelled siderite revealed the presence of ^{56}Fe-enriched Fe(III) (oxyhydr)oxides that could stem only from oxidation of $^{56}FeS_2$, thus, providing compelling evidence for direct microbial oxidation and implying an enzymatic process. Additionally, based on the modelling results, we demonstrated that in setups where a mix of pyrite and siderite was incubated with the NRFeOx culture, indirect abiotic oxidation of pyrite induced by dissolved Fe^{3+} did not contribute significantly to overall pyrite oxidation. However, our model did highlight that a major process contributing to denitrification in all pyrite-containing treatments was S^0 oxidation (Figure S5E, F). We also observed that, although sufficient electron donor (pyrite and siderite) was available to theoretically reduce all nitrate, the reaction was limited and most of the reduction stopped at around day 30 (Figure 3 A). Below we discuss potential factors limiting this reaction.

4.3.8. Factors limiting siderite and pyrite oxidation

The theoretical maximum concentration of nitrate that the autotrophic NRFeOx culture could reduce to N_2 in our experimental setup with both pyrite and siderite was 1.4 mM, assuming that all 7 mM of Fe(II) present as both siderite and pyrite were bioavailable. Considering oxidation of the S^0 associated with the pyrite that could be potentially mediated by autotrophic sulfur-oxidizing nitrate-reducing bacteria, another 0.65 mM of nitrate could be reduced meaning that there was enough electron donor present for all nitrate (2 mM) to be reduced in our experiments. However, in setups with both pyrite and ^{NA}Fe-siderite we observed a reduction of a maximum of 0.90 mM of nitrate, suggesting a limited bioavailability of the Fe(II) in siderite and/or pyrite. A bioavailability limitation was parameterized into the rates of siderite and pyrite oxidation, r_{sidox} and r_{ndiox}, respectively (described in detail in the SI). Accounting for a non-bioavailable mass fraction allowed the model to capture the measured amount of nitrate remaining. The fitted model parameters suggest that only about 40-50% of the siderite was bioavailable. The limited siderite and pyrite oxidation, and thus limited bioavailability, could result either from limited dissolution of both minerals or from limited access of the cells to the mineral surfaces preventing direct oxidation of the solid Fe(II). In particular, the precipitation of Fe(III) (oxyhydr)oxides on the surface of the mineral particles could potentially limit or even prevent direct cell-mineral contact, and therefore inhibit transfer of electrons from minerals to outer membrane proteins putatively participating in direct oxidation of Fe(II) such as cytochrome Cyc2.(Shi *et al.* 2016; He *et al.* 2017) Other potential factors limiting siderite and pyrite bioavailability could be the absence of defects and imperfections (steps and kinks) as their presence make crystals more prone

to dissolution and oxidation (Chandra and Gerson 2010; Renard *et al.* 2016). The precipitation of Fe(III) minerals close to the cells or at the cell surface can lead to cell encrustation (Kappler, Schink and Newman 2005), which was also observed in our study (Figure S3), and can cause inhibition of the enzymatic cell activity or limits access to proteins or compounds other than enzymes that can mediate oxidation (Miot *et al.* 2011).

4.3.9. Environmental implications

Our study provides evidence for a direct microbial (enzymatic) contribution to oxidation of pyrite by an autotrophic nitrate-reducing enrichment culture, obtained from an organic-poor, pyrite-, Fe(II)-carbonate-, and nitrate-containing aquifer. Furthermore, microbially driven lithoautotrophic oxidation of bioavailable Fe(II) coupled to denitrification leading to Fe(III) formation, does not seem to cause abiotic pyrite oxidation. Our results have important implications for predicting the fate of nitrate in environmental systems such as freshwater water bodies or sediments that are poor in organic carbon but contain other electron donors like Fe(II)- and S-phases. Specifically, it emphasizes the need of implementing direct enzymatic nitrate-dependent pyrite oxidation into reaction simulations when building field scale models. The extent to which biologically catalyzed pyrite oxidation drives denitrification, however, will depend on the availability of other, more preferential electron donors for nitrate reduction and may be greatly limited by the bio-availability of pyrite and/or dictated by the presence of specialized microbial communities that are able to facilitate the direct oxidation of pyrite as solid Fe(II) source. Thus, future studies should aim to identify potential controlling factors determining solid-phase electron donor bio-availability such as crystallinity, the presence of trace metals, the presence of nonreducing ligands, and the role of surface availability for direct cell-minerals interactions to shed light on potential electron transfer pathways between mineral surfaces and microbes.

4.4. Acknowledgements

This work is supported by the Collaborative Research Center 1253 CAMPOS (Project 5: Fractured Aquifer), funded by the German Research Foundation (DFG, Grant Agreement SFB 1253/1). NanoSIMS analysis were done at the Institute of Analytical Sciences and Physico-Chemistry for Environment and Materials (IPREM UMR 5254, CNRS/UPPA, Pau, France) with Cameca courtesy. We thank Celine Defouilloy for collecting NanoSIMS data, Dirk Schaumlöffel and Maria Angels Subirana for an access to faculties at IPREM. We acknowledge Stefan Peiffer, Jutta Eckert and Karel As for sharing protocols and practical advices for elemental sulfur measurements. Zhe Zhou is acknowledged for measurements of Mössbauer samples and help with interpretation. SEM was conducted at the Center for Light-Matter Interaction, Sensors & Analytics (LISA$^+$) with a help of Timm Bayer. We thank Ellen Röhm for help with IC and HPLC measurements and Franziska Schädler for nitrate and nitrite analysis.

References

Bhattacharyya A, Schmidt MP, Stavitski E *et al.* Iron speciation in peats: Chemical and spectroscopic evidence for the co-occurrence of ferric and ferrous iron in organic complexes and mineral precipitates. *Org Geochem* 2018;**115**:124–37.

Bottrell SH, Parkes RJ, Cragg BA *et al.* Isotopic evidence for anoxic pyrite oxidation and stimulation of bacterial sulphate reduction in marine sediments. *J Geol Soc London* 2000;**157**:711–4.

Boyd ES, Hamilton TL, Havig JR *et al.* Chemolithotrophic primary production in a subglacial ecosystem. *Appl Environ Microbiol* 2014;**80**:6146–53.

Chandra AP, Gerson AR. The mechanisms of pyrite oxidation and leaching : A fundamental perspective. *Surf Sci Rep* 2010;**65**:293–315.

Ehrenreich A, Widdel F. Anaerobic oxidation of ferrous iron by purple bacteria, a new type of phototrophic metabolism. *Appl Environ Microbiol* 1994;**60**:4517–26.

Hayakawa A, Hatakeyama M, Asano R *et al.* Nitrate reduction coupled with pyrite oxidation in the surface sediments of a sulfide-rich ecosystem. *J Geophys Res Biogeosciences* 2013;**118**:639–49.

He S, Barco RA, Emerson D *et al.* Comparative genomic analysis of neutrophilic iron(II) oxidizer genomes for candidate genes in extracellular electron transfer. *Front Microbiol* 2017;**8**:1–17.

Hopwood MJ, Statham PJ, Skrabal SA *et al.* Dissolved iron(II) ligands in river and estuarine water. *Mar Chem* 2015;**173**:173–82.

Jakus N, Blackwell N, Osenbrück K *et al.* Nitrate removal by a novel lithoautotrophic nitrate-reducing iron(II)-oxidizing culture enriched from a pyrite-rich limestone aquifer. *Appl Environ Microbiol* 2021, DOI: 10.1128/AEM.00460-21.

Jørgensen CJ, Jacobsen OS, Elberling B *et al.* Microbial oxidation of pyrite coupled to nitrate reduction in anoxic groundwater sediment. *Environ Sci Technol* 2009;**43**:4851–7.

Kappler A, Schink B, Newman DK. Fe(III) mineral formation and cell encrustation by the nitrate-dependent Fe(II)-oxidizer strain BoFeN1. *Geobiology* 2005;**3**:235–45.

Klueglein N, Kappler A. Abiotic oxidation of Fe(II) by reactive nitrogen species in cultures of the nitrate-reducing Fe(II) oxidizer *Acidovorax* sp. BoFeN1 – questioning the existence of enzymatic Fe(II) oxidation. *Geobiology* 2013;**11**:180–90.

Kraft B, Tegetmeyer HE, Sharma R *et al.* The environmental controls that govern the end product of bacterial nitrate respiration. *Science (80-)* 2014;**345**:676–9.

Kumar S, Herrmann M, Blohm A *et al.* Thiosulfate- and hydrogen-driven autotrophic denitrification by a microbial consortium enriched from groundwater of an oligotrophic limestone aquifer. *FEMS Microbiol Ecol* 2018;**94**:1–13.

Kuypers MMM, Marchant HK, Kartal B. The microbial nitrogen-cycling network. *Nat Rev Microbiol* 2018;**16**:263–76.

Liu T, Chen D, Li X *et al.* Microbially mediated coupling of nitrate reduction and Fe(II) oxidation under anoxic conditions. 2019;**95**:1–12.

Miot J, MacLellan K, Benzerara K *et al.* Preservation of protein globules and peptidoglycan in the mineralized cell wall of nitrate-reducing, iron(II)-oxidizing bacteria: A cryo-electron microscopy study. *Geobiology* 2011;**9**:459–70.

Moses CO, Kirk Nordstrom D, Herman JS *et al.* Aqueous pyrite oxidation by dissolved oxygen and by ferric iron. *Geochim Cosmochim Acta* 1987;**51**:1561–71.

Nizzoli D, Carraro E, Nigro V *et al.* Effect of organic enrichment and thermal regime on denitrification and dissimilatory nitrate reduction to ammonium (DNRA) in hypolimnetic sediments of two lowland lakes. *Water Res* 2010;**44**:2715–24.

Notini L, Byrne JM, Tomaszewski EJ *et al.* Mineral defects enhance bioavailability of goethite toward microbial Fe(III) Reduction. *Environ Sci Technol* 2019;**53**:8883–91.

Pauwels H, Kloppmann W, Foucher JC *et al.* Field tracer test for denitrification in a pyrite-bearing schist aquifer. *Appl Geochemistry* 1998;**13**:767–78.

Peiffer S, Stubert I. The oxidation of pyrite at pH 7 in the presence of reducing and nonreducing Fe(III)-chelators. *Geochim Cosmochim Acta* 1999;**63**:3171–82.

Percak-Dennett E, He S, Converse B *et al.* Microbial acceleration of aerobic pyrite oxidation at circumneutral pH. *Geobiology* 2017;**15**:690–703.

Postma D, Boesen C, Kristiansen H *et al.* Nitrate reduction in an unconfined sandy aquifer: water chemistry, reduction processes, and geochemical modeling. *Water Resour Res* 1991;**27**:2027–45.

Renard F, Putnis C V, Montes-Hernandez G *et al.* Siderite dissolution coupled to iron oxyhydroxide precipitation in the presence of arsenic revealed by nanoscale imaging. *Chem Geol* 2016, DOI: 10.1016/j.chemgeo.2016.12.001.

Rivett MO, Buss SR, Morgan P *et al.* Nitrate attenuation in groundwater: A review of biogeochemical controlling processes. *Water Res* 2008;**42**:4215–32.

Sand W, Gehrke T, Jozsa PG *et al.* (Bio)chemistry of bacterial leaching - direct vs. indirect bioleaching. *Hydrometallurgy* 2001;**59**:159–75.
Schaedler F, Kappler A, Schmidt C. A revised iron extraction protocol for environmental samples rich in nitrite and carbonate. *Geomicrobiol J* 2018;**35**:23–30.
Schippers A, Jorgensen BB. Biogeochemistry of pyrite and iron sulfide oxidation in marine sediments. *Geochim Cosmochim Acta* 2002;**66**:85–92.
Schwientek M, Einsiedl F, Stichler W *et al.* Evidence for denitrification regulated by pyrite oxidation in a heterogeneous porous groundwater system. *Chem Geol* 2008;**255**:60–7.
Shi L, Dong H, Reguera G *et al.* Extracellular electron transfer mechanisms between microorganisms and minerals. *Nat Rev Microbiol* 2016;**14**:651–62.
Tiedje JM. Ecology of denitrification and dissimilatory nitrate reduction to ammonium. *Environ Microbiol Anaerobes* 1988:179–244.
Vaclavkova S, Jørgensen CJ, Jacobsen OS *et al.* The Importance of Microbial Iron Sulfide Oxidation for Nitrate Depletion in Anoxic Danish Sediments. *Aquat Geochemistry* 2014;**20**:419–35.
Visser AN, Lehmann MF, Rügner H *et al.* Fate of nitrate during groundwater recharge in a fractured karst aquifer in Southwest Germany. *Hydrogeol J* 2020;**29**:1153–71.
Weber KA, Picardal FW, Roden EE. Microbially catalyzed nitrate-dependent oxidation of biogenic solid-phase Fe(II) compounds. *Environ Sci Technol* 2001;**35**:1644–50.
Yan R, Kappler A, Muehe EM *et al.* Effect of reduced sulfur species on chemolithoautotrophic pyrite oxidation with Nitrate. *Geomicrobiol J* 2019;**36**:19–29.
Zhang Y-C, Slomp CP, Broers HP *et al.* Isotopic and microbiological signatures of pyrite-driven denitrification in a sandy aquifer. *Chem Geol* 2012;**300**–**301**:123–32.

5. **Supplementary information on**: Anaerobic neutrophilic pyrite oxidation by a chemolithoautotrophic nitrate-reducing iron(II)-oxidizing culture enriched from a fractured aquifer

5.1. Supplementary materials and methods

5.1.1. Solid phase treatment and Fe quantification

Batch incubations were sampled in an anoxic glovebox (100% N_2) by withdrawing 0.4 ml aliquots using sterile syringes. Samples were centrifuged (14,000 g, 10 min) to separate the supernatant from iron minerals and biomass. After centrifugation the supernatant was removed and 0.4 ml of 1 M HCl was added to the pellet (iron minerals and biomass) to dissolve all HCl-extractable iron (siderite and Fe(III) (oxyhydr)oxides). The samples were then shaken outside the glovebox at 1400 rpm at 25°C for 1 h (Eppendorf Thermomixer R Mixer). After extraction, the samples were diluted 1:3 with 1 M HCl. All measurements were performed in technical triplicate. Both Fe(II) and total Fe were quantified at 562 nm(Stookey 1970) using a microtiter plate reader (FlashScan 550, Analytic, Jena, Germany).

5.1.2. X-ray diffractometry (XRD) and Mössbauer spectroscopy

Samples for XRD analysis of siderite were collected from a stock mineral suspension and dried in an anoxic glovebox (100 % N_2) and together with a powdered pyrite sample kept in a glovebox until the measurements were done. XRD was performed using Bruker's D8 Discover GADDS XRD2 micro-diffractometer equipped with a standard sealed tube with a Co-anode (Co Kα radiation, $\lambda = 0.17903$ nm) at parameters of 30 kV/30 mA. The total time of measurement was 240 s at two detector positions (15 and 40°). Resulting diffractograms were analyzed using the software Match! (version 3.6.2.121).

Phase identification of iron minerals was performed using Mössbauer spectroscopy. Within an anoxic glovebox (100% N_2), mineral suspension samples taken from the batch incubation experiments were passed through a filter (0.45 µm, Millipore), sealed between two layers of oxygen-impermeable adhesive polyimide film (Kapton), and kept frozen at -20°C in a sealed bottle until measurement. The sample was transferred to the instrument within an airtight bottle that was only removed prior to loading the samples inside the closed-cycle exchange gas cryostat (Janis cryogenics) under a

backflow of helium. Measurements were collected at 77 K and 295 K with a constant acceleration drive system (WissEL) in transmission mode with a ^{57}Co/Rh source and calibrated against a 7 µm thick α-^{57}Fe foil measured at room temperature. All spectra were analyzed using Recoil (University of Ottawa) by applying a Voigt Based Fitting (VBF) site analysis. The half width at half maximum (HWHM) was fixed to a value of 0.12 mm/s for all samples. Absorbance spectra collected from biotic incubations (day 0, 8 and 146) were fitted with a 3- component model with fixed hyperfine parameters for pyrite (CS and QS of Db1, table S2) obtained from the reference pyrite material, but floating relative area to account for changes in the relative phase abundances in the analyzed samples.

XRD patterns and Mössbauer spectroscopy confirmed the synthesized minerals to consist of siderite (Figure S1) and a mixture of pyrite and marcasite as previously described by (Peiffer and Stubert 1999; Yan *et al.* 2019). Mössbauer parameters (Table S2) were more similar to values characteristic for marcasite instead of pyrite. However, both parameters are very close (Evans *et al.* 1982), and it is almost impossible to differentiate and quantify the abundance of both phases using Mössbauer spectroscopy. In the following we will therefore use pyrite as a general term for both minerals.

5.1.3. Quantification of elemental sulfur content

To quantify elemental sulfur in the solid phase, 0.1 g of synthesized FeS_2 was added to 50-mL glass serum bottles in triplicates, each containing 5 mL of cyclohexane. The suspensions were shaken for 3 h to extract elemental sulfur. Thereafter, an aliquot of 500 µL of each sample was collected and diluted further in 50 mL methanol, followed by dilution of the cyclohexane-methanol solution with a 1:9 mixture of methanol and MQ water to reach a final dilution of 1000x. The concentration of the elemental sulfur in the methanol filtrate was analyzed by HPLC (class VP with RID 10 A and DAD 457 SPD M 10A VP detectors (Shimadzu, Japan)) equipped with ReproSil-Pur 200 ODS-3 column (250 x 4 mm, 5 µm, Dr. Maisch GmbH, Germany), using 80% methanol in MQ as eluent. The sulfur concentration was determined using a calibration with Fluka™ Sulfur, purum p.a., ≥99.5%. The calibration standards were dissolved following the same procedure as was used to prepare samples. Despite extensive washing, some residual elemental sulfur was still present and was quantified after incubation of the synthetic pyrite in cyclohexane. The elemental sulfur content was 3.12±0.1 mass%.

5.1.4. Reaction model

Based on the conceptual model presented in the main manuscript and outlined in Figure 1, we formulated a reaction model to fit the results from all experimental variants (without distinguishing between isotopically labeled vs. non-labeled siderite), thereby quantitatively testing our conceptual reaction network. The “batch reactor model” assumed well-mixed conditions in the incubations and neglected transport limitations.

Kinetic reaction rates for chemical equations 1, 2 and 3 were formulated assuming dual-Monod kinetics for biotic reactions and second-order kinetics for the abiotic Fe(III)-driven oxidation of pyrite. The dual-Monod rate formulations were biomass implicit, that is, without explicitly accounting for abundance of the NRFeOx culture because cell density was not monitored during the incubations. The rate of nitrate dependent siderite oxidation, r_{sidox} [mM d^{-1}], is given by:

$$r_{sidox} = r_{sidox}^{max}\left(\frac{C_{Sid}^{bio}}{K_{Fe(II)} + C_{Sid}^{bio}}\right)\left(\frac{C_{NO_3}}{K_{NO_3} + C_{NO_3}}\right)$$

where, r_{sidox}^{max} [mM d^{-1}], is the maximum rate of nitrate dependent siderite oxidation, $K_{Fe(II)}$ [mM] and K_{NO_3}[mM] are the half-saturation constants for Fe(II)-siderite and nitrate, respectively, C_{NO_3}[mM] is the concentration of dissolved nitrate and C_{Sid}^{bio} is the concentration of bioavailable Fe(II)-siderite. The model considers that only a fraction of the total Fe(II) in siderite is bioavailable, based on the observation that the concentration of HCl-extractable Fe(II) plateaus at ~1 mM. Thus, bioavailable Fe(II)-siderite was computed as:

$$C_{Sid}^{bio} = C_{Sid} - NB_{syd}$$

where NB_{syd} is the non-bioavailable concentration of siderite, assumed to be equal to the observed remaining concentration of HCl-extractable Fe(II). The approach is consistent with previous considerations of bioavailable mineral fractions.(Bai *et al.* 2020) The governing processes controlling the observed bioavailability are discussed further in the Discussion section of the main manuscript.

Similarly, the rate of microbially-mediated pyrite oxidation was also parameterized based on a bio-available Fe(II)-pyrite concentration, C_{Pyr}^{bio} [mM], calculated based on the difference between the total pyrite concentration and a non-bioavailable amount, NB_{syd} [mM]. (Note: NB_{syd} is a fitting parameter, see Table S1).

$$r_{ndiox} = r_{ndiox}^{max}\left(\frac{C_{Pyr}^{bio}}{K_{Fe(II)} + C_{Pyr}^{bio}}\right)\left(\frac{C_{NO_3}}{K_{NO_3} + C_{NO_3}}\right)$$

In equation (3), r_{ndiox}^{max} [mM d^{-1}], is the maximum rate of nitrate-dependent pyrite oxidation. (Note: Identical values for the half-saturation coefficients $K_{Fe(II)}$ and K_{NO_3} were found to adequately depict the system behavior for all Fe(II)-mineral-nitrate reactive systems). As mentioned in the main manuscript, elemental sulfur, S^0, was initially present in incubations with pyrite, a direct artefact of the synthesis procedure. Because considerable sulfate production was measured throughout the experiments a contribution of S^0 oxidation coupled to NO_3^- reduction was also accounted for in the model:

$$r_{nsulf} = r_{nsulf}^{max}\left(\frac{C_{S(0)}}{K_{S(0)} + C_{S(0)}}\right)\left(\frac{C_{NO_3}}{K_{NO_3} + C_{NO_3}}\right)$$

where, r_{nsulf} and r_{sidox}^{max} [mM d^{-1}], the rate and maximum rate of S^0-dependent denitrification, $K_{S(0)}$ [mM] and K_{NO_3}[mM] are the half-saturation constants for S^0 and nitrate, respectively, and$C_{S(0)}$[mM] is the concentration S^0.

Finally, the abiotic oxidation of pyrite by Fe(III) released from siderite oxidation (in mixed siderite and pyrite incubations) was parameterized as the second order rate expression, r_{pyrox} [mM d^{-1}]:

$$r_{pyrox} = k_{pyrox} \cdot C_{Pyr} \cdot C_{Fe(III)}$$

where k_{pyrox} [L mmol^{-1} s^{-1}] is the second-order rate constant of abiotic Fe(III)-mediated pyrite oxidation, and C_{Pyr} and $C_{Fe(III)}$ [mM], are the total (without considering a bioavailable fraction) concentrations of Fe(II)-pyrite and aqueous Fe^{3+}, respectively. The free Fe(II) released from the abiotic oxidation of pyrite could then serve as an additional source of electrons for further nitrate-dependent Fe(II) oxidation. In model Scenario 2 (S2), described in detail in the main manuscript, the rate of this additional contribution to denitrification was parameterized as r_{fedint}^{free} [mM d^{-1}], dependent on the concentration of dissolved ("free") Fe(II), $C_{Fe(II)}^{free}$ [mM], and for simplicity the same kinetic rate coefficients as for r_{ndiox} were used.

$$r_{fedenit}^{free} = r_{ndiox}^{max} \left(\frac{C_{Fe(II)}^{free}}{K_{Fe(II)} + C_{Fe(II)}^{free}} \right) \left(\frac{C_{NO_3}}{K_{NO_3} + C_{NO_3}} \right)$$

Considering the above reaction rate expressions, the well-mixed reactor model yields the following system(s) of governing ordinary differential equations the (1) siderite-only, (2) pyrite-only, and (3) mixed pyrite-siderite biotic experiments:

Siderite only:

$$\frac{dC_{NO_3}}{dt} = -r_{sidox}$$

$$\frac{dC_{Sid}}{dt} = -5 \cdot r_{sidox}$$

$$\frac{dC_{Fe(III)}}{dt} = 5 \cdot r_{sidox}$$

Pyrite only:

$$\frac{dC_{NO_3}}{dt} = -3 \cdot r_{ndiox} - 1.2 \cdot r_{nsulf}$$

$$\frac{dC_{Pyr}}{dt} = -r_{ndiox}$$

$$\frac{dC_{Fe(III)}}{dt} = r_{ndiox}$$

$$\frac{dC_{S(0)}}{dt} = -r_{nsulf}$$

$$\frac{dC_{SO_4}}{dt} = 2 \cdot r_{ndiox} + r_{nsulf}$$

Mixed pyrite and siderite:

$$\frac{dC_{NO_3}}{dt} = -r_{sidox} - 3 \cdot r_{ndiox} - 1.2 \cdot r_{nsulf} - r_{fedint}^{free}$$

$$\frac{dC_{Sid}}{dt} = -5 \cdot r_{sidox}$$

$$\frac{dC_{Fe(II)}}{dt} = 14 \cdot r_{pyrox} - 5 \cdot r_{fedint}^{free}$$

$$\frac{dC_{Fe(III)}}{dt} = r_{ndiox} + 5 \cdot r_{sidox} + 5 \cdot r_{fedint}^{free} - 14 \cdot r_{pyrox}$$

$$\frac{dC_{Pyr}}{dt} = -r_{ndiox} - \boldsymbol{r_{pyrox}}$$

$$\frac{dC_{S(0)}}{dt} = -r_{nsulf}$$

$$\frac{dC_{SO_4}}{dt} = 2 \cdot r_{ndiox} + r_{nsulf} + 2 \cdot r_{pyrox}$$

The terms in bold font in equations 16, 17 and 19 mark the distinction between model versions that consider both biotic and abiotic pyrite oxidation (i.e., including all terms) versus biotic pyrite oxidation only (i.e., not including the terms in bold). The systems of ordinary differential equations were solved using ode15s in MATLAB. The model was calibrated by fitting the parameters to the experimental data of the siderite- and pyrite-only cases jointly, as these allowed to separate the reactive contributions of siderite and pyrite from one another, which were then lumped in a validation step of the "mixed" experiment. Fitting was performed on the logarithmized parameter values using the trust-region-reflective algorithm in the MATLAB least squares optimization function *lsqnonlin*(Coleman and Li 1996), minimizing the sum of squared error between measurements and model output. The calibrated parameter set yielded a root mean squared error (RMSE) of 0.01 mM, well within the standard deviation of the measurements. Model parameter values are presented in Table S1.

5.1.5. NanoSIMS

NanoSIMS analyses were performed at the Cameca NanoSIMS 50L at the Institute of Interdisciplinary Research on Environment and Materials (IPREM) (UPPA, Pau, France) with courtesy of Cameca, France. Prior to the measurements, the samples were coated with a Pd layer (~12 nm) to avoid charging during the SEM analysis. The O^- and Cs^+ primary ion beams were used with a primary ion impact energy of 16 keV. Prior to the final measurement, any potential contaminants and the coating layer were sputtered away with a high primary beam current (pre-sputtering). The primary beam (~3 pA for O^- and ~1pA for Cs^+) was focused and scanned over the sample with $^{56}Fe^+$, $^{57}Fe^+$ (O^-

beam) and $^{56}Fe^{16}O$, ^{32}S (Cs^+ beam) secondary ions collected using electron multipliers. All analyses were performed in imaging mode, on samples from the treatments containing 1) ^{NA}Fe-pyrite, ^{57}Fe-siderite and bacterial cells (biotic control), 2) ^{NA}Fe-pyrite, ^{NA}Fe-siderite and bacterial cells (control for isotopic enrichment), and 3) ^{NA}Fe-pyrite, ^{57}Fe-siderite and autoclaved bacterial cells (abiotic control). For every treatment, four representative spots were analyzed for the spatial distribution of ^{56}Fe mainly originating from pyrite and ^{57}Fe mainly derived from siderite taking advantage of the high spatial resolution of the new RF plasma O source. To follow the sulfur distribution (^{32}S), due to the pure ionization in O^- polarity, the Cs^+ primary beam of the NanoSIMS instrument was used, at similar spatial resolution (~100 nm). In this configuration iron isotopes can be measured as ^{56}FeO and ^{57}FeO. Images of 20 µm x 20 µm (O^- beam) and 25 µm x 25 µm (Cs^+ beam) field of view, 30 and 20 planes respectively with a dwell time of 1 ms/pixel, 256 pixels x 256 pixels were recorded. The NanoSIMS images were analyzed using the Open MIMS Image plugin available within ImageJ (available free-of-charge at, https:// imagej.nih.gov/ij/). All presented images were corrected for the electron multiplier dead time (44 ns), as well as drift corrected, and the planes accumulated.

5.1.6. Enrichment and cultivation of microorganisms

Briefly, 10 cm-long pieces of Teflon tubing were filled with crushed pyrite-rich Upper Muschelkalk limestone representative for the aquifer and deployed in one of groundwater monitoring wells. After 4 months of incubation, exposed rock particles were retrieved from the well and added to anoxic bicarbonate-buffered (22 mM) freshwater low phosphate medium (LPM) modified from Ehrenreich & Widdel(Ehrenreich and Widdel 1994) containing 0.6 g/L KH_2PO_4, 0.3 g/L NH_4Cl, 0.5 g/L $MgSO_4 \cdot 7H_2O$, and 0.1 g/L $CaCl_2 \cdot 2H_2O$, adjusted to pH 7.1, amended with 2 mM of $NaNO_3$ and 2 mM of $FeCl_2$. The concentration of selenite–tungstate solution (Widdel, 1980) was decreased from 1.0 mL/L to a final concentration of 0.1 mL/L to eliminate a potential inhibitory effect of tungsten on the nitrate reductase (Burke, Calder and Lascelles, 1980). The enrichment culture has a genetic potential to perform pyrite oxidation as it is dominated by a potential Fe(II)-oxidizer belonging to the *Gallionellaceae* family, among which some species also have nitrate reductases (He et al., 2016) and thiosulfate oxidases (Emerson et al., 2013), accompanied by bacteria affiliated with *Acidovorax* spp., *Dechloromonas* spp. and *Bradyrhizobium* spp., known heterotrophic nitrate-reducers (Coates *et al.*, 2001; Polcyn and Luciński, 2003; Heylen, Lebbe and de Vos, 2008; Siqueira, Minamisawa and Sánchez, 2017) and bacteria belonging to *Thiobacillus* family, having potential for sulfur oxidation. After 36 continuous transfers under autotrophic conditions (no organic carbon added) the enrichment NRFeOx culture was used as inoculum in the batch incubation experiments described below.

5.2. Supplementary discussion

5.2.1. Additional stoichiometric calculations

The culture used in our study was described to perform complete denitrification with a $nitrate_{reduced}$:$Fe(II)_{oxidized}$ ratio close to the expected stochiometric ratio of 0.2 (Jakus *et al,* 2021) following equation (1).

$$10Fe^{2+} + 2NO_3^- + 24H_2O \rightarrow 10Fe(OH)_3 + N_2 + 18H^+ \quad (1)$$

Herein, we calculated the stoichiometric ratio based on measured Fe(III) concentrations (representing $Fe(II)_{oxidized}$) because of the sorption of Fe(II) discussed in the manuscript. For setups with only ^{57}Fe-siderite and nitrate, the calculated ratio of $nitrate_{reduced}$:$Fe(III)_{formed}$ was 0.2±0.04 (Table S2). Thus, equaling the theoretical ratio for Fe(II) oxidation coupled to complete denitrification to N_2. However, in microcosms where both pyrite and ^{57}Fe-siderite or pyrite and ^{NA}Fe-siderite were present, the ratios were much higher (0.89±0.05 and 0.85±0.16, respectively), suggesting that more nitrate was reduced than expected based on the measured Fe(III) produced. This is in line with the modelled contribution of S^0-dependent denitrification, which adequately captured the trends in concentration time series. Based on equation (2) and the presence of 3.12±0.1 mass% S^0 associated with our pyrite, a maximum of 0.54 mM of sulfate could be formed and 0.7 mM of nitrate reduced in agreement the higher $nitrate_{reduced}$:$Fe(III)_{formed}$ ratio.

$$S^0 + 1.2NO_3^- + 0.4H_2O \rightarrow SO_4^{2-} + 0.6N_2 + 0.8H^+ \quad (2)$$

We also estimated the maximum amount of pyrite which could be potentially oxidized by Fe^{3+} originating from siderite oxidation coupled to nitrate reduction, assuming that all HCl-extractable siderite-Fe(II) could be oxidized by bacteria to Fe^{3+}(aq). Following equation (3) and considering the amount of HCl-extractable Fe(II) depleted in the setup with pyrite and ^{57}Fe-siderite (Table S2), up to 0.2 mM of sulfate deriving from oxidation of structural sulfur (S_2^{2-}) could be produced by Fe^{3+} driven oxidation of pyrite.

$$FeS_2 + 14Fe^{3+} + 8H_2O \rightarrow Fe^{2+} + 2SO_4^{2-} + 16H^+ \quad (3)$$

Considering this value (0.2 mM) in addition to the theoretical concentration of sulfate which could be formed as a consequence of S^0 oxidation (0.54 mM, see above), the theoretically expected value (ca. 0.74 mM sulfate coming from oxidation of S^0 and S_2^{2-} by Fe^{3+}) is higher than the range of the measured values of total sulfate (0.60±0.10 and 0.61±0.10 for setups with pyrite and ^{57}Fe-siderite or ^{NA}Fe-siderite, respectively; Figure 3H). These results, together with the model output, suggest that direct biotic oxidation of pyrite took place.

5.3. Supplementary figures and tables

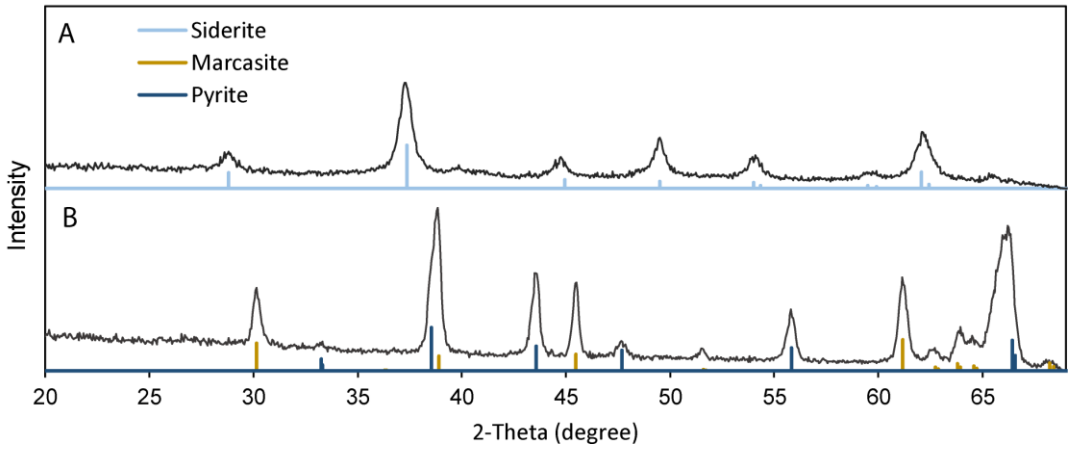

Figure S1. XRD data of synthesized Fe(II) minerals used in this study. (A) synthesized siderite ($FeCO_3$) and (B) synthesized pyrite (FeS_2) containing some marcasite (FeS_2).

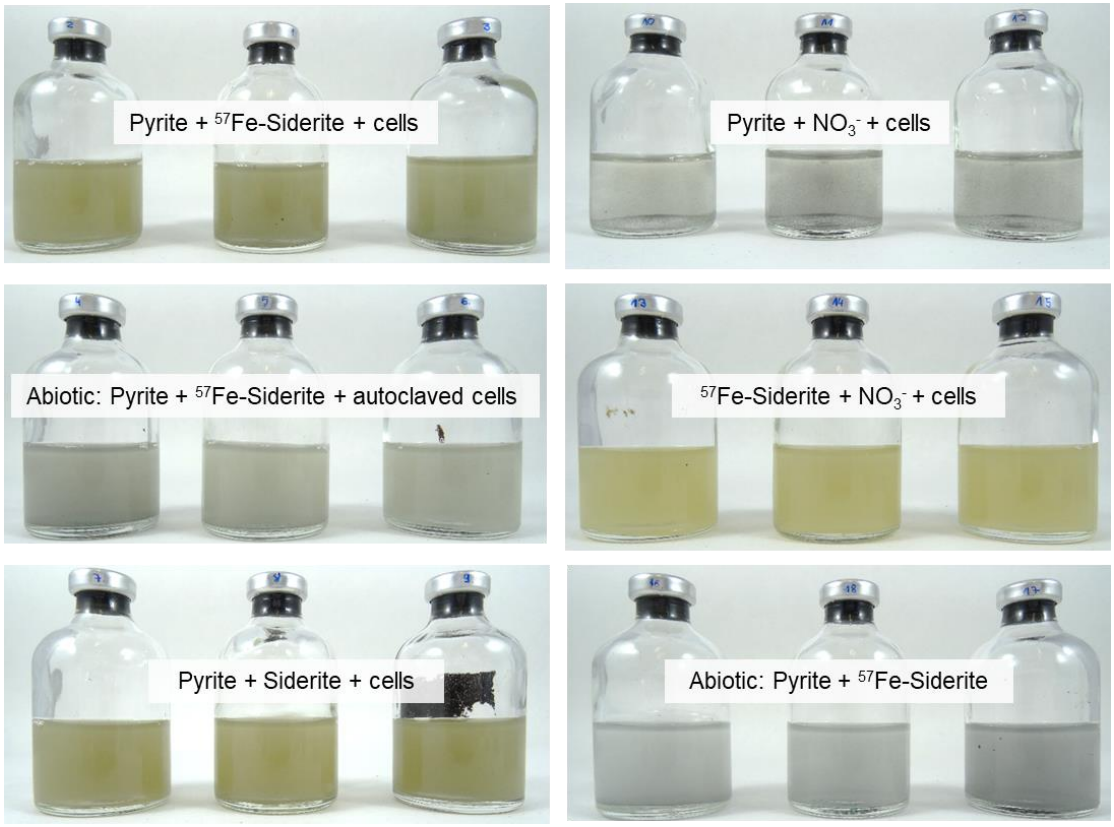

Figure S2. Photographs of experimental bottles containing various combinations of pyrite, ^{57}Fe-labelled or non-labelled siderite and cells. Photos were taken at day 8 (when the bottles were sampled for NanoSIMS analysis).

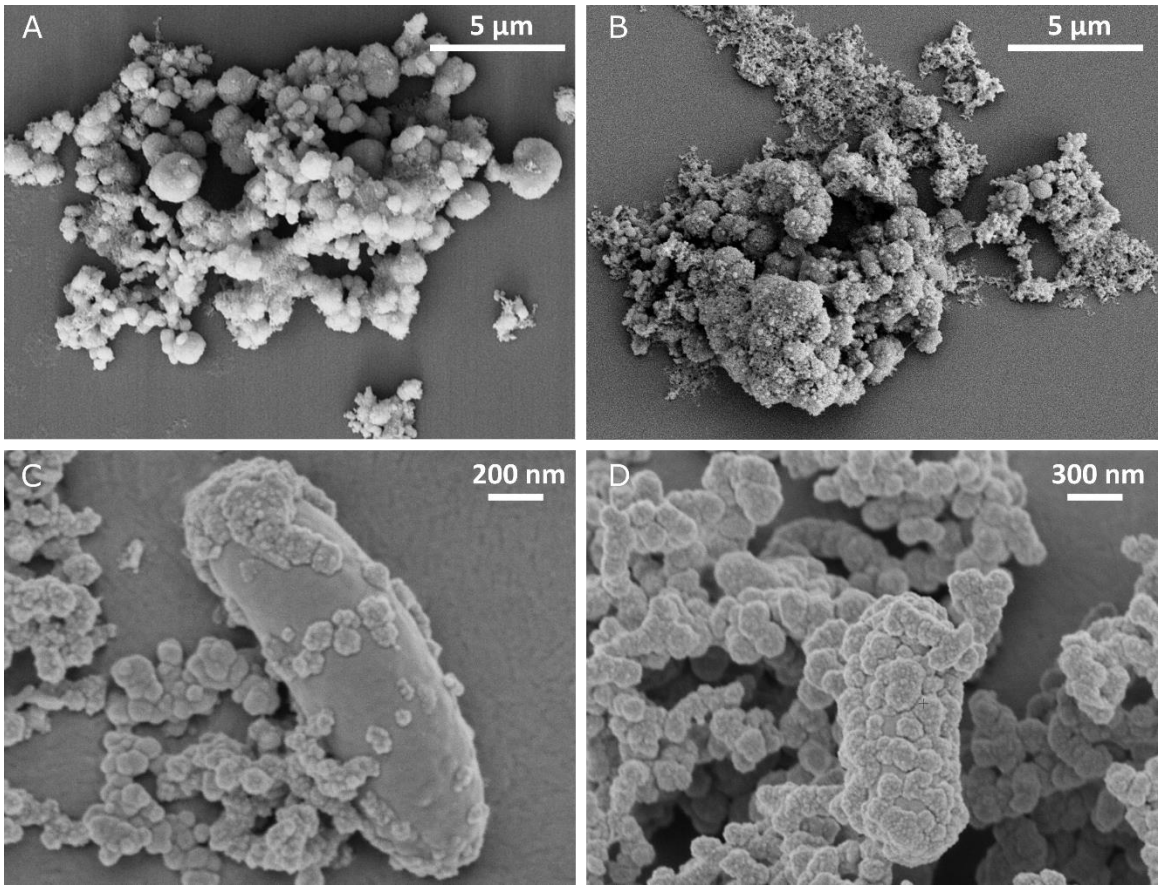

Figure S3. Scanning electron micrographs of cell-mineral aggregates from setups containing both pyrite and ^{57}Fe-siderite incubated with autoclaved bacterial cells (A) and active bacterial cells (B) at day 8 of the experiment. Images of encrusted bacterial cells (C) and (D) collected at day 8 from setups that contained both pyrite and siderite and living cells.

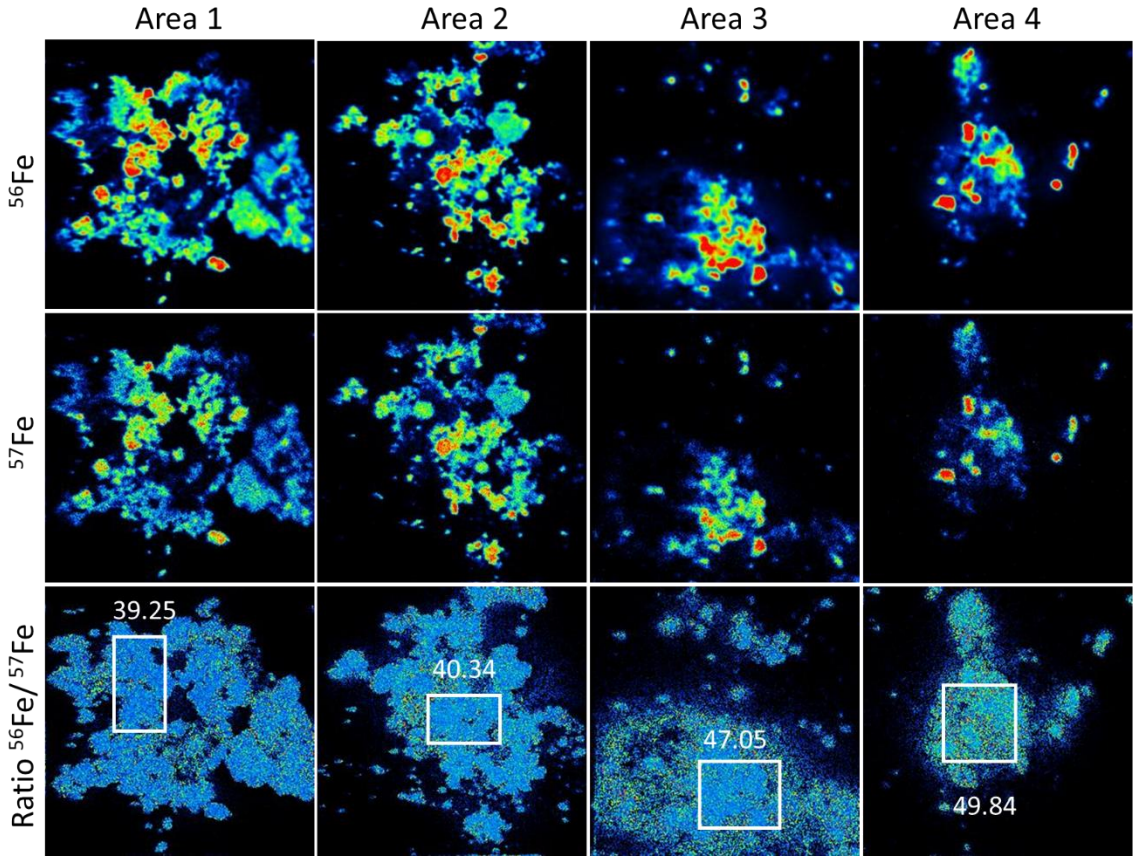

Figure S4. High spatial resolution NanoSIMS analysis of two isotopes of iron: ^{56}Fe (1st row) and ^{57}Fe (2nd row) of 4 different areas containing mineral aggregates. All images were collected at the 8th day of incubation of ^{NA}Fe-siderite and ^{NA}Fe-pyrite with NRFeOx culture. The homogenous distribution iron isotopes is demonstrated by ratio image ^{56}Fe/^{57}Fe (3rd row). White boxes are indicating areas in which particular ratio was calculated while the numbers are showing the calculated value. All ratios exhibit a close value to theoretical ^{56}Fe/^{57}Fe ratio for natural abundance of iron isotopes (91.75/2.21 = 43.28).

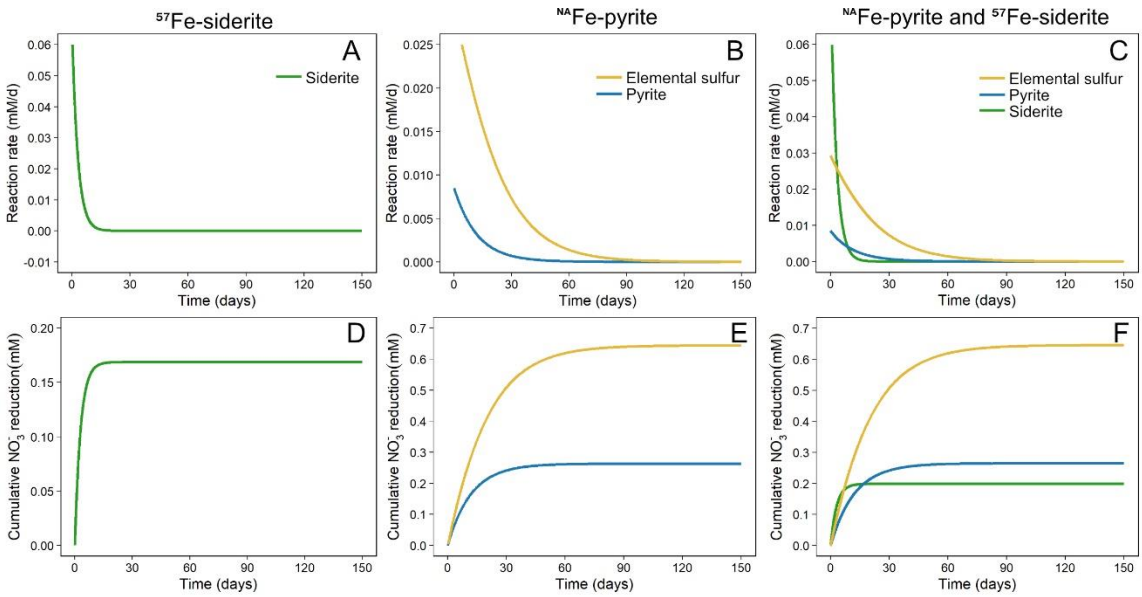

Figure S5. Reaction rates of microbially-mediated siderite oxidation (green), elemental sulfur oxidation (yellow) and pyrite oxidation (blue). Cumulative nitrate reduction (mM) coupled to siderite oxidation (green), elemental sulfur oxidation (yellow) and pyrite oxidation (blue).

Table S1. Calibrated parameter values for the reaction model versions described above.

Parameter	Unit	Value	Fitted
r_{sidox}^{max}	[mM s^{-1}]	1.82e-5	*
r_{ndiox}^{max}	[mM s^{-1}]	1.65e-6	*
r_{nsulf}^{max}	[mM s^{-1}]	1.32e-6	*
$K_{Fe(II)}^{sid}$	[mM]	20	*
$K_{Fe(II)}^{pyr}$	[mM]	1.43	*
$K_{NO_3}^{Fe}$	[mM]	0.25	*
$K_{NO_3}^{S}$	[mM]	0.15	*
$K_{S(0)}$	[mM]	1.73	*
k_{pyrox}	[L mmol s^{-1}]	1e-8	[a]
NB_{sid}	[mM]	1 – 1.15	[b]
NB_{pyr}	[mM]	4.91	*

*Fitted. [a]Not fitted, taken as the HCl-extractable iron remaining in each treatment. [b]Arbitrary value to illustrate that even a small contribution of abiotic pyrite oxidation would over-predict nitrate reduction.

Table S2. Mass balance of substrates and products of the reaction in setups initially containing 2 mM NO_3^- and 5 mM of Fe(II) in form of FeS_2 together with 0.54 mM S^0 and/or 2 mM of Fe(II) in form of $FeCO_3$ incubated with our lithoautotrophic NRFeOx enrichment culture under anoxic, pH-neutral conditions.

	NO_3^- reduced (mM)	HCl-extractable Fe(II) remaining the in solids (mM)	Final Fe^{2+} (aq)	Fe(II) absorbed to glass walls (mM)	HCl-extractable Fe(II) depleted (mM)*	Fe(III) formed (mM)	SO_4^{2-} formed (mM)	Ratio $NO_3^-{}_{reduced}/ SO_4^{2-}{}_{formed}$	Ratio $NO_3^-{}_{reduced}/ Fe(III)_{formed}$
^{57}Fe-Siderite	0.16 ± 0.13	1.11 ± 0.08	0.01 ± 0.00	0.02 ± 0.00	0.78 ± 0.1	1.28 ± 0.2	0.11 ± 0.15	-	0.2 ± 0.04
Pyrite	0.79 ± 0.19	0.00 ± 0.00	0.01 ± 0.00	0 .00 ± 0.00	0.00 ± 0.01	0.01 ± 0.04	0.72 ± 0.2	1.11 ± 0.04	-
Pyrite and ^{57}Fe-Siderite	0.84 ± 0.04	0.89 ± 0.04	0.04 ± 0.01	0.01 ± 0.00	1.11 ± 0.08	0.94 ± 0.07	0.60 ± 0.08	1.41 ± 0.12	0.89 ± 0.05
Pyrite ^{NA}Fe-Siderite	0.90 ± 0.06	0.78 ± 0.12	0.02 ± 0.01	0.01 ± 0.00	1.40 ± 0.14	1.09 ± 0.14	0.61 ± 0.07	1.49 ± 0.17	0.85 ± 0.16
Abiotic control	0.00 ± 0.01	1.67 ± 0.16	0.21 ± 0.02	0.31 ± 0.06	0.31 ± 0.29	0.03 ± 0.07	0.1 ± 0.03	-	-

*Calculated as final concentration of Fe(II) extracted from solids subtracted from initial concentration of Fe(II) extracted from solids. This fraction represents the amount of Fe(II) removed by oxidation and dissolution from the Fe(II) solids at the beginning of experiment.

Table S3. Overview on Mössbauer spectra fitting parameters. Temp. – temperature during measurement; Phase – fitted compound, Db: doublet, center shift (CS in mm/s); quadrupole splitting (ΔEQ in mm/s); sigma – deviation/broadening of the quadrupole splitting fit. quadrupole shift (ε in mm/s); hyperfine field (Bhf in T), Pop – relative abundance (in %), χ2 as goodness of fit and identified (iron) mineral phases.

Sample	**Temp. K**	**Phase**	**CS mm/s**	**ΔE_Q mm/s**	**sigma mm/s**	**Pop (±) %**	**χ^2**	**Fe phase**
^{NA}Fe-Pyrite	77	Db1	0.34	0.52	0.18	100 (0.3)	0.61	Pyr
	5	Db1	0.36	0.52	0.08	100 (0.2)	0.54	Pyr
^{NA}Fe-Pyrite + ^{57}Fe-Siderite + cells (day 0)	77	Db1	0.34	0.52	0.19	5.2 (1.3)	0.62	Pyr
	77	Db2	1.34	2.40	0.81	94.2 (1.2)		Sid
	77	Db3	0.43	0.74	0.20	0.6 (0.2)		Fe(III)
^{NA}Fe-Pyrite + ^{57}Fe-Siderite + cells (day 8)	77	Db1	0.34	0.52	0.25	13.8 (1.5)	3.65	Pyr
	77	Db2	1.33	2.36	0.49	53.1 (1.3)		Sid
	77	Db3	0.50	0.80	0.39	33.1 (1.6)		Fe(III)
^{NA}Fe-Pyrite + ^{57}Fe-Siderite + cells (day 146)	77	Db1	0.34	0.52	0.24	12.0 (1.5)	3.78	Pyr
		Db2	1.23	2.24	0.48	46.6 (1.9)		Sid
		Db3	0.50	0.79	0.36	43.4 (1.4)		F(III)
Abiotic (no cells) ^{NA}Fe-Pyrite + ^{57}Fe-Siderite (day 0)	77	Db1	0.34	0.52	0.21	5.4 (0.14)	0.65	Pyr
		Db2	1.22	2.39	0.41	94.6 (0.81)		Sid
Abiotic (no cells) ^{NA}Fe-Pyrite +^{57}Fe-Siderite (day 8)	77	Db1	0.34	0.52	0.19	5.6 (0.21)	0.64	Pyr
		Db2	1.21	2.36	0.39	94.4 (0.48)		Sid

References

Bai Y, Mellage A, Cirpka OA *et al.* AQDS and redox-active NOM enables microbial Fe(III)-mineral reduction at cm-scales. *Environ Sci Technol* 2020;**54**:4131–9.

Berner RA. Sedimentary pyrite formation. *Am J Sci* 1970;**268**:1–23.

Coleman TF, Li Y. An interior trust region approach for nonlinear minimization subject to bounds. *SIAM J Optim* 1996;**6**:418–45.

Ehrenreich A, Widdel F. Anaerobic oxidation of ferrous iron by purple bacteria, a new type of phototrophic metabolism. *Appl Environ Microbiol* 1994;**60**:4517–26.

Evans BJ, Johnson RG, Senftle FE *et al.* The 57Fe Mössbauer parameters of pyrite and marcasite with different provenances. *Geochim Cosmochim Acta* 1982;**46**:761–75.

Jakus N, Blackwell N, Osenbrück K et al. Nitrate removal by a novel lithoautotrophic nitrate-reducing iron(II)-oxidizing culture enriched from a pyrite-rich limestone aquifer. *Appl Environ Microbiol* 2021a, DOI: 10.1128/AEM.00460-21.

Peiffer S, Stubert I. The oxidation of pyrite at pH 7 in the presence of reducing and nonreducing Fe(III)-chelators. *Geochim Cosmochim Acta* 1999;**63**:3171–82.

Stookey LL. Ferrozine-A New Spectrophotometric Reagent for Iron. *Anal Chem* 1970;**42**:779–81.

Yan R, Kappler A, Muehe EM *et al.* Effect of reduced sulfur species on chemolithoautotrophic pyrite oxidation with Nitrate. *Geomicrobiol J* 2019;**36**:19–29.

6. Presence of Fe(II) and nitrate shapes aquifer-originating denitrifying communities leading to an enrichment of autotrophic Fe(II)-oxidizing *Gallionellaceae* sp. under organic carbon limitation

Natalia Jakus[a,b], Nia Blackwell[b], Daniel Straub[b,c], Andreas Kappler[a,d] and Sara Kleindienst[b,#]

[a]Geomicrobiology, Center for Applied Geoscience, University of Tuebingen, Germany

[b]Microbial Ecology, Center for Applied Geoscience, University of Tuebingen, Germany

[c]Quantitative Biology Center (QBiC), University of Tuebingen, Germany

[d]Cluster of Excellence: EXC 2124: Controlling Microbes to Fight Infection, Tübingen, Germany

Abstract

Autotrophic nitrate reduction coupled to Fe(II) oxidation is an important nitrate removal process in anoxic aquifers. However, it remains unknown how changes of O_2 and carbon availability influence the community structure of nitrate-reducing Fe(II)-oxidizing (NRFeOx) microbial assemblages and what the genomic traits of these NRFeOx key players are. We compared three metabolically distinct denitrifying assemblages, supplemented with acetate, acetate/Fe(II), or Fe(II), enriched from an organic-poor, pyrite-rich aquifer. The presence of Fe(II) promoted the growth of denitrifying *Burkholderiaceae* spp. and an unclassified *Gallionellaceae* sp. This *Gallionellaceae* sp. was related to microaerophilic Fe(II) oxidizers, however, it did not grow under microoxic conditions. Furthermore, we explored a metagenome and 15 metagenome-assembled genomes from an aquifer-originating, autotrophic NRFeOx culture. The dominant *Gallionellaceae* sp. revealed the potential to oxidize Fe(II) (e.g. *cyc2*), fix CO_2 (e.g. *rbcL*), and perform near complete denitrification leading to N_2O formation (e.g. *narGHJI*, *nirK/S*, and *norBC*). In addition, *Curvibacter* spp., *Methyloversatilis* sp., and Thermomonas spp. were identified as novel putative NRFeOx taxa. Our findings provide first insights into the genetic traits of the so far only known autotrophic NRFeOx culture originating from an organic-poor aquifer, providing the genomic basis to study mechanisms of nitrate removal in organic-poor subsurface ecosystems.

6.1. Introduction

Nitrate (NO_3^-) pollution in groundwater is one of the major worldwide environmental issues as many aquifers exhibit values exceeding the maximum regulatory concentration of nitrate in drinking water (50 mg L^{-1}) (European Union 2006; European Commission 2018; Kazakis *et al.* 2020). Only two biological pathways are known that lead to nitrate attenuation: dissimilatory nitrate reduction to ammonium (DNRA) and denitrification (Kuypers, Marchant and Kartal 2018). Denitrification is an anaerobic respiratory process in which dissolved nitrate is reduced to nitrite (NO_2^-) and further to gaseous nitric oxide (NO), nitrous oxide (N_2O) and dinitrogen (N_2) via a series of enzymatic steps, mediated by a wide range of bacterial and archaeal taxa (Kuypers, Marchant and Kartal 2018). Denitrifying bacteria can be divided into three different groups: heterotrophs, autotrophs or mixotrophs, depending on whether they gain energy from the oxidation of organic compounds, inorganic compounds, or both, respectively (Bryce *et al.* 2018). In many subsurface ecosystems including aquifers, organic carbon is limited and as such, autotrophic denitrifiers utilizing inorganic electron donors like Fe(II), reduced sulfur, or H_2 were suggested to play important roles in nitrate removal (Postma *et al.* 1991; Pauwels et al. 1998; Schwientek *et al.* 2008; Jørgensen *et al.* 2009; Zhang *et al.* 2012; Visser *et al.* 2020). However, the influence of the availability of alternative electron acceptors (e.g. O2) as well as electron donors (e.g. organic compounds) when compared to nitrate and Fe(II) on autotrophic nitrate-reducing Fe(II)-oxidizing (NRFeOx) groundwater assemblages remains poorly understood.

Most prominent candidates for NRFeOx microorganisms are Fe(II)-oxidizing bacteria (FeOB) belonging to the family Gallionellaceae, typically inhabiting microoxic pH-neutral environments, which were also reported to have the potential to reduce nitrogen species under anoxic conditions (He et al. 2016; Huang et al. 2021b). Metagenome-assembled genomes (MAGs) of *Gallionellaceae* spp. were shown to harbor several denitrification genes (e.g. *narG*, *nirK*, *nirS*, *norB*, or *nosZ*), co-occurring with at least one of the candidate Fe(II)-oxidase genes encoding for example cytochrome c Cyc2 or a MtoAB complex (He *et al.* 2016; Huang *et al.* 2021b, 2021a). Additionally, *Gallionellaceae* spp. were demonstrated to fix CO_2 (Tominski et al. 2018), utilizing the Calvin–Benson–Bassham (CBB) Cycle encoded by *cbbL*, *cbbM* or *rbcS* genes (Huang *et al.* 2021a). Since several *Gallionellaceae* spp. MAGs in field studies and cultivation experiments were found to have incomplete gene sets encoding denitrification (Jewell et al. 2016; Bethencourt et al. 2020; Huang et al. 2021a, 2021b), complete autotrophic denitrification coupled to Fe(II) oxidation was suggested to be achieved via metabolic handoffs between *Gallionellaceae* spp. and other community members rather than by *Gallionellaceae* sp. alone (He et al. 2016; Huang *et al.* 2021a, 2021b). However, our knowledge about this process and the underlying complex interdependencies in organic-poor aquifers is limited.

To fill this gap, a novel autotrophic NRFeOx culture was recently obtained from a nitrate polluted, pyrite-rich (4.1±1.4 mg (g rock)-1) limestone aquifer, and it is to date the only autotrophic NRFeOx culture originating from an organic-poor environment (dissolved organic carbon <2.0 mg L-1) (Jakus *et al.* 2021a). This culture is composed of a mixed community with diverse bacterial taxa, dominated

by *Gallionellaceae* sp., and was demonstrated to oxidize 1-3 mM of dissolved Fe^{2+} or Fe(II) minerals such as siderite and pyrite under anoxic conditions using nitrate as an electron acceptor (Jakus *et al.* 2021b). Yet, the genomic traits that enable the uncultured *Gallionellaceae* sp. in the aquifer-originating culture to grow under anoxic conditions, the role of other microbial members, and the mechanism(s) of Fe(II) oxidation remain unknown.

We therefore compared the microbial community composition of the autotrophic NRFeOx culture originating from the pyrite-rich organic-poor limestone aquifer with two other metabolically distinct enrichment cultures, originating from the same groundwater monitoring well, growing in the same medium but supplemented with either acetate (heterotrophic culture), or acetate and Fe(II) (mixotrophic culture), i.) to investigate how the availability of organic carbon and Fe(II) shapes the community structure of denitrifiers at this habitat. We further subjected the autotrophic culture to microoxic conditions to simulate potential fluxes of oxygen that may occur in the aquifer and ii.) to test the response of the microbial community to the change of electron acceptor. Next, we investigated the metagenome of the autotrophic NRFeOx culture that was considered to represent a microbial key assemblage responsible for nitrate removal in the organic-poor aquifer, and retrieved 15 MAGs. We analyzed the genetic traits encoded in the MAGs (iii.) to predict the metabolism of the most abundant microorganisms growing in the enrichment culture including the Gallionellaceae sp. and (iv.) to search for putative electron transfer pathways involved in NRFeOx organisms. We furthermore compared our results to the so far best studied autotrophic NRFeOx enrichment culture KS (Straub *et al.* 1996) and the recently obtained autotrophic NRFeOx enrichment culture BP (Huang *et al.* 2021b) that are both dominated by *Gallionellaceae* spp. as well but are stemming from organic-rich freshwater sediments, which is in stark contrast to the origin of our enrichment culture, the pyrite-rich and organic-poor limestone aquifer.

6.2. Materials and methods

6.2.1. Enrichment and cultivation

The field site location, the conditions, and the procedure of enrichment was the same for all three types of nitrate-reducing cultures (autotrophic, mixotrophic and heterotrophic) as described previously for the autotrophic NRFeOx enrichment, Culture AG (Altingen Groundwater, named after the source of the culture; Jakus *et al.* 2021a). Briefly, denitrifying communities were enriched using passive samplers filled with crushed, pyrite-rich limestone particles and incubated in an anoxic (dissolved O_2 of 0.1±0.1 mg L^{-1}) low-nitrate (1.5±0.6 mg L^{-1}) monitoring well. After incubation, rock particles with attached microbial cells were retrieved and transferred to sterile serum bottles (58 mL) filled with 25 mL of anoxic bicarbonate-buffered (22 mM), modified low phosphate freshwater medium (LPM) (Jakus *et al.* 2021), adjusted to pH 7.1 and amended with 2 mM of $NaNO_3$. Next, either 2 mM of $FeCl_2$, 1 mM of acetate, or 1 mM of acetate plus 2 mM of $FeCl_2$ were added to the medium for autotrophic, heterotrophic and mixotrophic cultivation conditions, respectively. For cultures growing under microaerophilic conditions, gradient tubes and zero-valent iron (ZVI) plates were used. Gradient tubes with opposing gradients of Fe^{2+} and O_2were prepared following Emerson

and Floyd (2005). Cultures in ZVI plates were established using petri dishes (55 mm diameter) containing 8 ml of modified Wolfe's mineral medium (Emerson and Floyd 2005) and approximately 0.5 g of ZVI powder (200 mesh; metal basis; Alfa Aesar, Ward Hill, MA). ZVI plates were inoculated by adding 100 µl of inoculum from a gradient tube and incubated in an acrylic jar (Merck, Germany) with a gas pack (BD GasPack EZ Campy; Becton, Dickinson and Co., NJ) to form microoxic conditions (6-10% atmospheric O_2).

6.2.2. Experimental setup and DNA extraction for 16S rRNA gene and metagenome sequencing

In order to grow a sufficient amount of cells for the experiment, a preculture of autotrophic NRFeOx enrichment culture was grown in six serum bottles containing modified LPM (25 mL of medium each) prepared as described above, supplemented with 2 mM NO_3^- and 2 mM Fe(II). After 5 days of growth, the content of all bottles was pooled into one sterile anoxic serum bottle and used as an inoculum. Immediately after obtaining the preculture, a sample for 16S rRNA gene sequencing was collected (day 0) and 53 serum bottles, containing the same modified LPM, were inoculated with 10% (vol/vol) of the preculture (*ca.* $2 \cdot 10^6$ cells mL^{-1}). To follow consumption of substrates, three inoculated bottles (biotic controls) were randomly selected and sampled daily. Additionally, abiotic controls (no cells, only modified LPM supplemented with substrates) were simultaneously run in triplicates. At days 2, 3 and 9 of the experiment, we collected DNA samples to follow changes in the relative abundance of the microbial community, by harvesting three bottles at each sampling point. After harvesting, all liquid together with microbial cells was centrifuged (20 min, 4000 rpm) to remove the supernatant. The biomass was frozen at -20°C and stored until DNA extraction. At day 3, we additionally collected a DNA sample for metagenome sequencing, for which, to have sufficient yield of DNA, 40 serum bottles were sacrificed by filtration using four (10 bottles per filter) 0.2 µm pore-size membrane filters (Isopore®, Milipore) (Figure 1). Filters were subsequently placed in 2 mL centrifuge tubes and frozen at -20°C. All DNA samples collected in this study were extracted using the FastDNA™ SPIN Kit according to the manufacturer's instructions, and DNA extracts were then pooled for shotgun metagenome library construction.

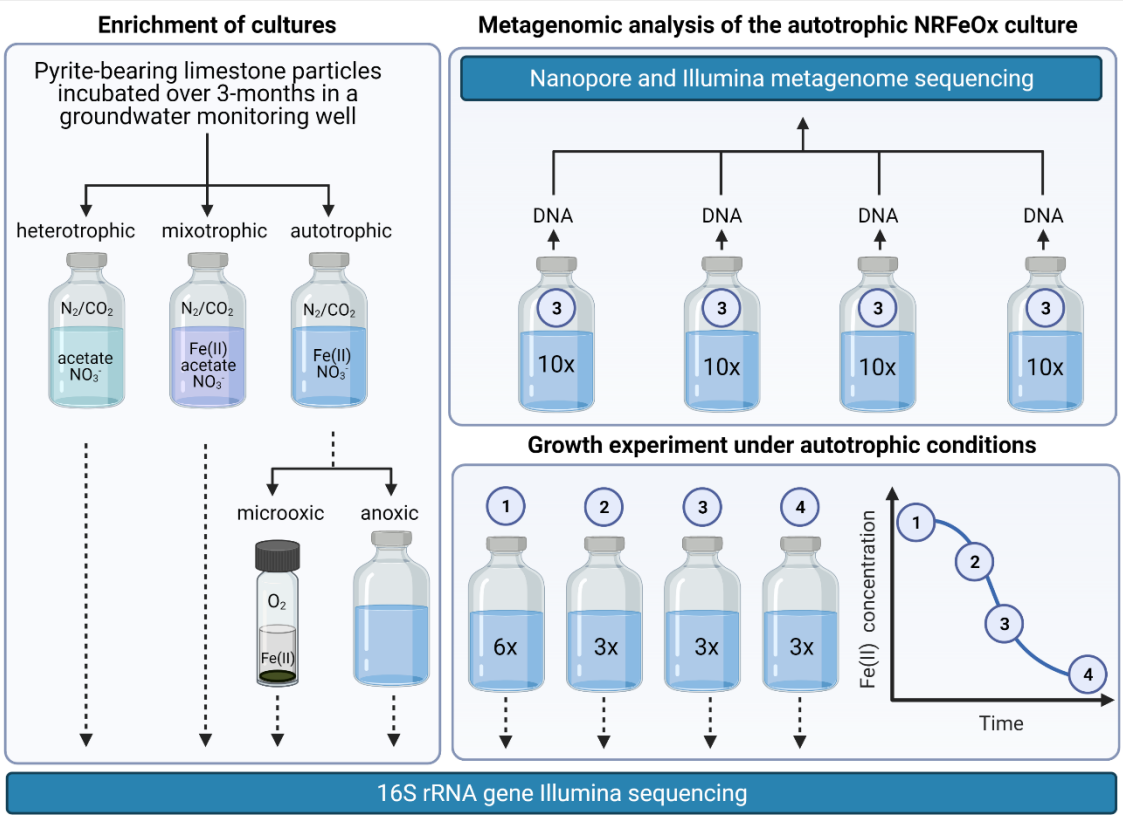

Figure 1. Schematic figure of the experimental setups. Different bottle colors represent three different setups containing growth medium used to enrich heterotrophic (pale blue), mixotrophic (purple) and autotrophic (blue) denitrifying communities using acetate and nitrate, Fe(II), acetate and nitrate, and Fe(II) and nitrate, respectively. The grey serum vial represents cultures grown under microoxic conditions in opposite gradients of oxygen (entering from the top into the solidified agar layer) and Fe^{2+} (released by dissolution of the black FeS from the bottom). Numbers on the bottles show the number of replicates used for DNA extractions followed by sequencing. Numbers in circles indicate the timepoint when samples were collected in relation to Fe(II) consumption. Dark blue boxes display sequencing method used. The figure was created with BioRender.com.

6.2.3. Chemical analyses

Samples were taken daily in an anoxic glovebox (100% N_2) using a syringe with a needle through the butyl-rubber stopper and centrifuged (14,000 x g, 10 min). For quantification of Fe(II) and Fe(III), a revised ferrozine protocol for nitrite-containing samples was used to eliminate the abiotic reaction of nitrite with Fe(II) during acidification as described in detail previously (Klueglein and Kappler 2013; Schaedler *et al.* 2018). Nitrate and nitrite were quantified following the DIN 38405/ISO 13395 standard quantification method using AA3 HR AutoAnalyzer System (Seal Analytical, Germany).

6.2.4. 16S rRNA gene sequencing and analysis

DNA extracted from the cultures was used for amplification with universal primers (515F: GTGYCAGCMGCC-GCGGTAA (Parada, Needham and Fuhrman 2016) and 806R: GGACTACNVGGGT- WTCTAAT (Apprill *et al.* 2015)) fused to Illumina adapters. The PCR, library preparation, and sequencing are detailed in the supplementary information. Quality control, reconstruction of 16S rRNA gene sequences and taxonomic annotation was performed with nf-

core/ampliseq v1.1.0 (Ewels *et al.* 2020; Straub *et al.* 2020) as described in detail in the supplementary information.

6.2.5. Quantitative PCR

Total cell numbers of bacteria were estimated by quantitative PCR (qPCR) (Bio-Rad Laboratories GmbH, Munich, Germany) based on the amplification of bacterial 16S rRNA genes following a protocol described previously (Schaedler *et al.* 2018) and described in detail in the supplementary information. Absolute abundances of taxa in the autotrophic NRFeOx culture were calculated by multiplication of 16S rRNA gene copy numbers and relative abundances of 16S rRNA gene amplicon sequences.

6.2.6. Metagenome sequencing, assembly and annotation

Metagenome library preparation and shotgun Illumina sequencing was conducted by CeGaT, Tuebingen, Germany. Short- and long-read quality control, hybrid assembly, metagenome assembled genome binning and taxonomic annotation was performed with nf-core/mag v1.0.0 (https://nf-co.re/mag, DOI: 10.5281/zenodo.3589528) as described in detail in the supplementary information. The assembled metagenome and eight high quality MAGs (≥89.9% completeness, <10% contamination) were uploaded to the Joint Genome Institute's Integrated Microbial Genome and Microbiome Expert Review (IMG/MER) pipeline for annotation, and subsequent analysis was performed using tools available through the pipeline IMGAP v5.0.19 (Chen *et al.* 2019). Putative Fe(II) oxidation genes were identified using the blast function in IMG (10^{-5} E value cutoff). For the remaining seven MAGs with completeness between 89.9% and 56.1%, gene annotations were subset from the whole metagenome annotation. The genes of interest present in these MAGs where then identified by their KEGG Orthology (KO) numbers and analyzed manually. In addition, all 15 assembled MAGs were analyzed using the FeGenie tool (Garber *et al.* 2020) installed using Python 3.6 (Python Software Foundation, https://www.python.org/) to search for genes related to Fe cycling.

6.3. Results and discussion

6.3.1. Microbial community composition under autotrophic NRFeOx growth conditions

Using 16S rRNA gene sequencing of the V4 region (*ca.* 250 bp) in combination with quantification of 16S rRNA gene copy numbers and substrate concentrations over time during a 10-day incubation of the autotrophic NRFeOx culture, we determined microbial community changes linked with nitrate and Fe(II) consumption (Figure 2).

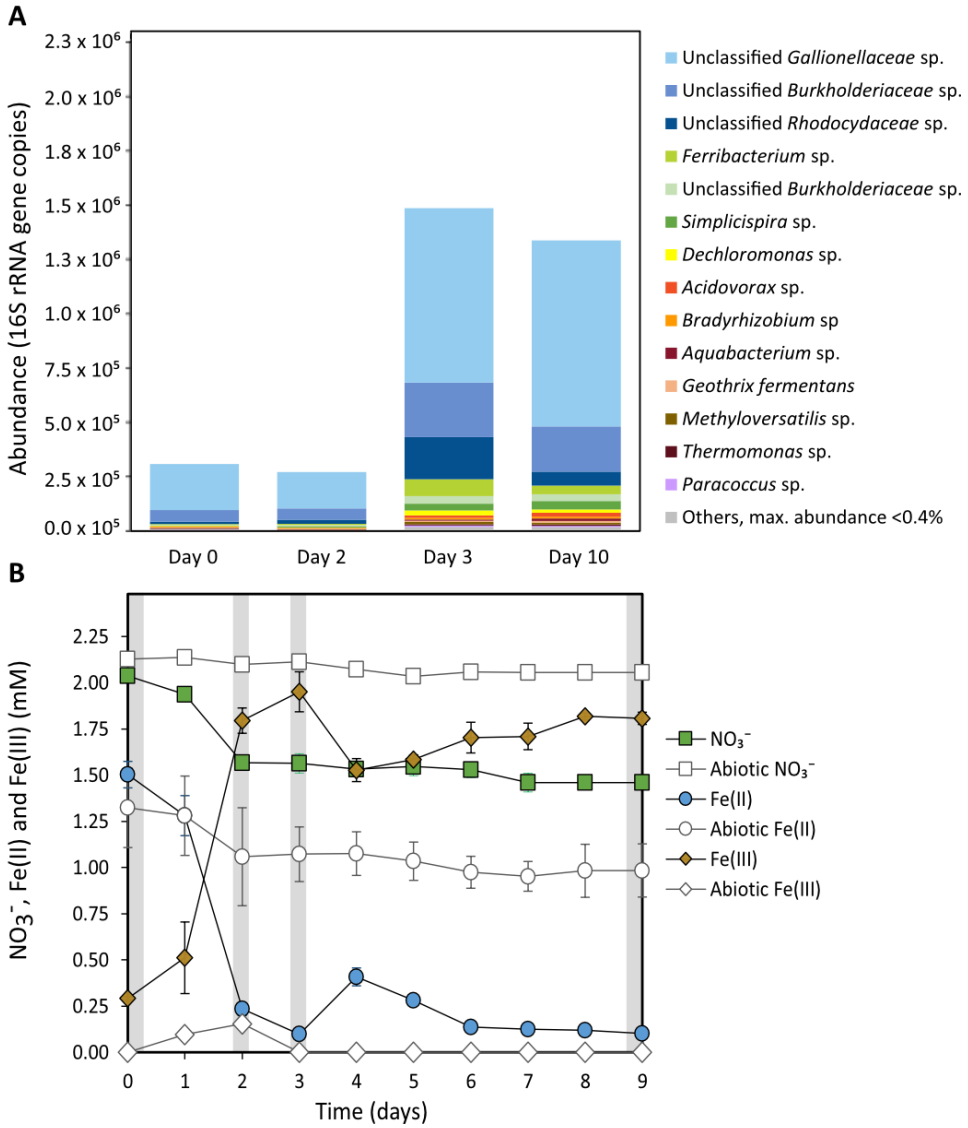

Figure 2. Changes in microbial community composition based on 16S rRNA gene amplicon sequencing (A) and concentrations of NO3- (green), total Fe(II) (blue) and total Fe(III) (brown) (B) in a 10-day incubation experiment using the autotrophic nitrate-reducing Fe(II)-oxidizing enrichment culture. All data points are mean values of samples collected from three biological replicate bottles, error bars represent standard deviations.

Overall, the microbial community structure was stable as we did not observe any major changes over 10 days (Figure 2A). Minor changes in the microbial community occurred between day 2 and day 3, where the largest increase in 16S rRNA gene copy numbers occurred (Figure 2A). After a total consumption of 0.49±0.07 mM of NO_3^- and 1.22±0.07 mM of Fe(II), the relative abundance of the unclassified *Gallionellaceae* sp. decreased from 61.8% (day 2) to 54% (day 3), while 16S rRNA gene sequence abundances of both *Dechloromonas* sp. and *Ferribacterium* sp. nearly doubled between these two timepoints (from 7.0% to 13.1% and from 2.1% to 5.2%, respectively). The overall increase in absolute 16S rRNA gene copies over time from $3.08 \cdot 10^5$ (day 0) to $1.36 \cdot 10^6$ (day 10) suggests the ability of this culture (or at least some of its members) to fix inorganic carbon for biomass production coupled to Fe(II) oxidation. This is in agreement with our previous study, where the culture was shown to produce more cells while incubated in medium containing nitrate and 1-3 mM

of Fe(II) vs. nitrate alone (no Fe(II)) (Jakus *et al.* 2021). Interestingly, our growth experiment results presented here, point to a slight delay between substrate consumption and cell growth at the beginning of the experiment. The largest increase in the 16S rRNA gene copy numbers between day 2 and day 3 did not correlate with the largest decrease in Fe(II) and NO_3^- concentrations between day 0 and day 2 (Figure 2), which may indicate that uptake of substrates took place ahead of CO_2 fixation and subsequent cell production. Alternatively, the discrepancy between cell growth and consumption of substrates, could result from oxidation of either electron donors carried over from the inoculum, or MQ-water derived organics as discussed previously (Jakus *et al.* 2021).

6.3.2. Oxygen as potential electron acceptor for autotrophic growth of Fe(II) oxidizers

To examine the capability of the autotrophic NRFeOx culture to perform microaerophilic Fe(II) oxidation that may occur in the aquifer due to the presence of microoxic niches (Visser *et al.* 2020), the culture was transferred to gradient tubes and plates containing FeS and zero valent iron (ZVI), respectively. With this approach, we intended to test the community's response to O_2 and to promote growth and ultimately isolate the uncultured *Gallionellaceae* sp., as these bacteria are typically known to be microaerophilic Fe(II)-oxidizers and some of the cultured members of this family were isolated using one of the applied techniques (Hallbeck, Ståhl and Pedersen 1993; Emerson and Moyer 1997). However, none of these *Gallionellaceae* sp. isolates were reported to perform Fe(II) oxidation under anoxic conditions, i.e. coupled to (partial) denitrification. After inoculation into a gradient tube, our culture was observed to oxidize Fe(II), evidenced by the appearance of a bacterial layer above the bottom FeS-containing layer. In contrast, after inoculating ZVI plates, we did not observe an increase in cell numbers under the microscope and no notable difference in Fe(II) oxidation was observed compared to the abiotic control, therefore further transfers were only done in gradient tubes. After three continuous transfers in gradient tubes, the initially very diverse bacterial community was reduced to four taxa: the unclassified *Burkholderiaceae* sp. (56.2%), *Rhizobium* sp. (36.5%), *Bradyrhizobium* sp. (5.2%) and *Paracoccus* sp. (1.8%) (Figure 3). Surprisingly, the uncultured *Gallionellaceae* sp. was not identified among the sampled microbial community, suggesting its adaptation to strictly anoxic conditions or its dependence on other community members which could not thrive under microoxic conditions.

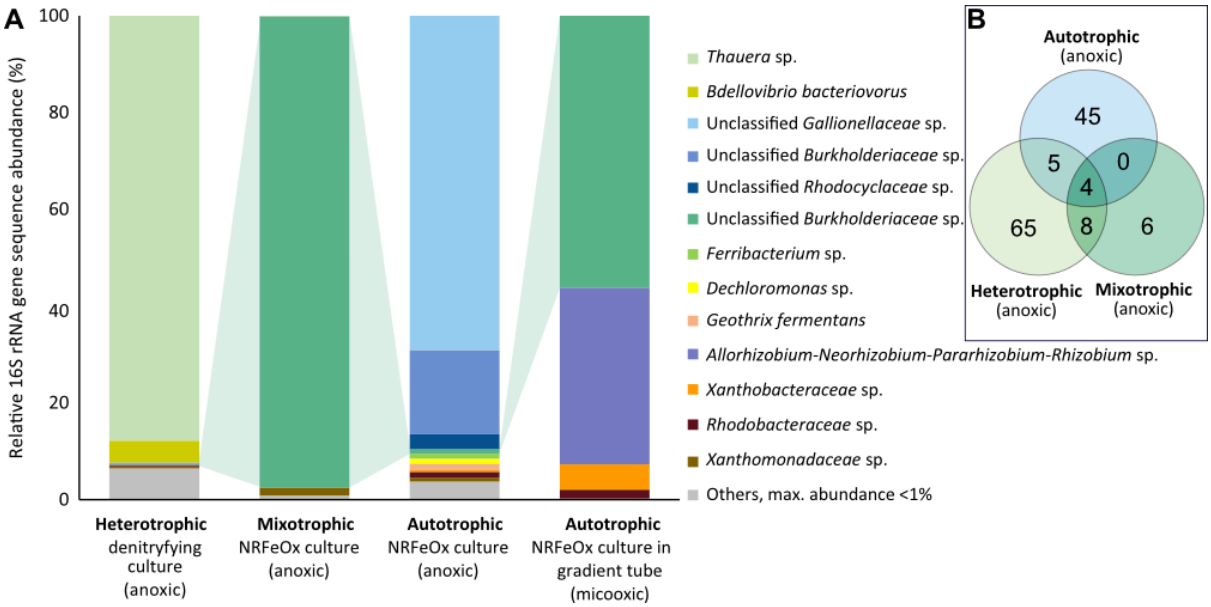

Figure 3. Microbial community composition based on 16S rRNA gene amplicon sequencing of three enrichment cultures (A) incubated under heterotrophic denitrifying, mixotrophic nitrate-reducing iron(II)-oxidizing (NRFeOx), and autotrophic NRFeOx (anoxic) conditions using nitrate-containing freshwater medium supplemented with either 1 mM acetate, 1 mM acetate and 2 mM Fe(II), or 2 mM Fe(II), respectively. The fourth bar chart represents the community composition of the autotrophic NRFeOx culture growing under microoxic conditions in a gradient tube with FeS as Fe(II) source and air (with O_2) in the headspace. The unclassified *Burkholderiaceae* sp. (100% identity to both *Curvibacter delicatus*, MN684217.1, and *Acidovorax* sp., MK402969.2) was present in all cultures and dominated communities growing under mixotrophic and microoxic conditions (gradient tube). Venn diagram (B) depicting the shared and distinct ASVs (Supplemental data) of the three metabolically different enrichment cultures. Autotrophic culture stands here for the culture grown under anoxic conditions.

6.3.3. Organic carbon as substrate for the aquifer-originating enrichment cultures

To evaluate the impact of inorganic versus organic electron donors that could both serve for microbial growth at the field site (though organotrophic denitrification was suggested to play a rather minor role when compared to other metabolic pathways at this field site (Visser *et al.* 2020)), the community composition of denitrifying cultures supplemented with organic carbon (i.e. acetate), simultaneously enriched from the same field site, were compared to the autotrophic NRFeOx culture (Figure 3). The 16S rRNA gene sequencing revealed that the heterotrophic nitrate-reducing culture grown on acetate was dominated by known denitrifying bacteria belonging to the genus *Thauera* (Etchebehere and Tiedje 2005; Wang *et al.* 2017), yielding 84.8% relative sequence abundance. Interestingly, the second most dominant (4.6% relative 16S rRNA gene sequence abundance) bacterial taxon in the heterotrophic culture shares 100% 16S rRNA gene sequence identity (based on the ASV region) with the predatory bacterium *Bdellovibrio bacteriovorus*, probably preying on heterotrophic cells living in this culture.

6.3.4. Effect of Fe(II) on the community structure of denitrifiers

We further analyzed the composition of the culture supplemented with both acetate and Fe(II) (mimicking fluxes of organic carbon compounds in iron-rich fractures in the aquifer). Surprisingly, despite being supplied with two different electron donors (i.e. acetate and Fe(II) at the same time), this culture had the least complex, i.e. the least diverse microbial community composition (Shannon's diversity index for heterotrophic and mixotrophic cultures were 1.03 and 0.23, respectively). This suggests that the addition of Fe(II) acted as a stressor, strongly inhibiting the growth and probably activity of most of the heterotrophic and autotrophic denitrifiers. In general, the culture grown under mixotrophic conditions was dominated by the unclassified *Burkholderiaceae* sp., which accounted for up to 97.3% relative 16S rRNA gene sequence abundance. In general, *Burkholderiaceae* spp. were present in all cultures ranging from 1.4% (heterotrophic culture) to 97.5% (mixotrophic culture) of relative abundance, represented by a wide range of genera, including those which were previously found to directly and/or indirectly, i.e. via chemodenitrification (Bryce *et al.* 2018), catalyze Fe(II) oxidation such as *Acidovorax* spp. (Muehe *et al.* 2009; Carlson *et al.* 2013; Chakraborty and Picardal 2013) and *Curvibacter* spp. (Gülay *et al.* 2018). Our observation based on the microbial community changes among the different treatments leading to the enrichment of *Burkholderiaceae* spp. in Fe(II)-containing media further confirmed that these microbes play an important role in Fe cycling, especially in environments where redox conditions and supply of nutrients are changing.

A comparison of the microbial communities of all three cultures revealed that the unclassified *Burkholderiaceae* sp., together with three other taxa identified as *Thiobacillus denitrificans*, a *Thermomonas* sp., and another less abundant unclassified *Gallionellaceae* sp. were identified in all three cultures, being able to survive under heterotrophic, mixotrophic or autotrophic conditions (Figure 3). The less abundant unclassified *Gallionellaceae* sp. from this study was only 98.03% identical to *Gallionella* sp. JA52 (KC677661.1) and 96.84% identical to the most dominant *Gallionellaceae* sp. in this study. Interestingly, besides these four ASVs there was no further overlap detected for the microbial community composition in autotrophic and mixotrophic cultures.

6.3.5. Recovery of MAGs of the autotrophic NRFeOx community

Since autotrophic communities are hypothesized to play a key role of nitrate removal at the field site (Visser *et al.* 2020), the metabolic potential of the autotrophic NRFeOx community was furthermore assessed using metagenome sequencing, assembly and genome binning methods and yielded in the recovery of 15 MAGs with a minimum of 56.1% estimated completeness and a maximum of 1.4% estimated contamination (Table 1). Most (ten out of fifteen) MAGs were assigned to the class *Betaproteobacteria* as expected from 16S rRNA gene amplicon sequencing which showed *Betaproteobacteria* spp. to be the most dominant class (96.3%, based on estimated coverage). The MAG with the highest estimated coverage (AG 11) was identified as unclassified member of the order *Nitrosomonadales* (Table 1). The 16S rRNA gene sequence retrieved from this MAG was compared with 16S rRNA gene amplicon sequences and showed 100% identity to the most dominant *Gallionellaceae* sp. identified in our cultivation experiments. The MAG was then compared with other genomes of *Gallionellaceae* spp. using Average Nucleotide Identity (ANI) and Average Amino

Acid Identity (AAI) analyses, confirming that the MAG belongs to the family *Gallionellaceae* (Figure S1, S3). Therefore, the *Nitrosomondales* sp. MAG (AG11) will be further referred to as the unclassified *Gallionellaceae* sp. MAG (AG11). In addition, four other MAGs were identified using pairwise comparison of MAG-recovered 16S gene sequences and 16S rRNA gene amplicon sequencing data obtained from the culture (Table 1).

Table 1. Overview of taxonomic classification, completeness and contamination of MAGs, contig numbers, contig and MAG sizes, GC content together with number of ORFs and estimated coverage of MAGs retrieved in this study from an autotrophic NRFeOx culture. A complete table with NCBI and IMG identifiers is provided in the supplementary information (Table S1).

MAG ID	Taxonomy classification (Last common ancestor of a majority of genes)	Top BLASTN hit to 16S rRNA gene amplicon sequences	Complete-ness (%)	Contami-nation (%)	Number of contigs	Largest contig (Mbp)	Genome size (Mbp)	GC (%)	Number of ORFs in MAG	Estimated coverage
AG16	*Rhodobacteraceae sp.* QY30	-	97.3	0	2	2.5	3.6	65.0	3484	63.2
AG20	Unclassified *Betaproteobacteria sp.*	*Thermomonas* sp.	95.9	0.7	12	1.0	3.8	65.0	3421	37.8
AG27	*Thermomonas fusca*	-	95.3	0	6	1.3	3.0	68.4	2722	31.4
AGun1	Unclassified *Bradyrhizobiaceae* sp.	*Bradyrhizobium* sp.	93.2	0	1	4.1	4.1	65.0	3828	64.7
AG31	*Methylotenera* sp. G11	-	93.2	0	53	0.2	2.5	45.4	2434	4.6
AG5	*Geothrix fermentans*	*Geothrix fermentans*	89.9	0.7	2	2.0	3.3	67.1	3081	27.2
AG29	*Curvibacter delicatus*	-	89.9	1.4	6	1.6	3.8	63.3	3586	229.5
AG11	Unclassified *Nitrosomonadales*	*Gallionellaceae* sp.	89.9	0	9	0.8	2.2	58.0	2038	3617.9
AG26	*Acidovorax* sp.	-	84.5	0.7	63	0.2	3.6	63.9	3349	631.9
AG17	Unclassified *Burkholderiales*	-	83.8	0	42	0.3	3.0	64.5	2710	13.6
AG1	*Curvibacter* sp. PAE-UM	-	70.9	0.7	82	0.2	3.0	67.0	3106	11.4
AG28	Unclassified *Betaproteobacteria*	-	68.2	0.7	17	0.5	2.9	62.1	2737	199.9
AG14	*Thiobacillus denitrificans*	-	66.2	1.4	14	0.7	2.5	63.5	2496	10.0
AG22	*Burkholderiales* sp.	-	56.8	1.4	322	0.1	4.1	69.6	4331	3.7
AG18	*Rhizobium* sp.	*Rhizobium* sp.	56.1	0.7	455	0.1	4.4	64.1	4963	3.4

6.3.6. Nitrate reduction by the autotrophic NRFeOx community

Among all of the genes associated with nitrogen cycling, genes involved in nitrate reduction were the most abundant genes identified in the metagenome (Figure 4). The first step of denitrification and DNRA is performed by the periplasmic or membrane-bound nitrate reductases encoded by *napAB* or *narKGHJI* genes, respectively, that were detected in twelve of the fifteen MAGs (Figure 4). Only one copy of *nrf*, a functional gene specific for DNRA, was identified in the whole metagenome, while genes encoding nitrite reductases (*nirK* and *nirS*) and/or nitric oxide reductase (*norBC*), and/or nitrous oxide reductase (*nosZ*) were annotated in all fifteen MAGs. In general, all analyzed MAGs harbored at least one of the functional genes involved in the denitrification pathway, but only five MAGs revealed all the genes necessary to complete the entire process, starting from reduction of NO_3^- to N_2 formation. MAGs encoding genes for the complete pathway were identified as an unclassified *Rhodobacteraceae* sp., *Methylotenera* sp., *Acidovorax* sp., *Thiobacillus denitrificans*, and a *Rhizobium* sp., all previously described to be members of heterotrophic and/or autotrophic denitrifying communities (Bellini *et al.* 2013; Mustakhimov *et al.* 2013; Chu and Wang 2017; Li *et al.* 2017; Kumar *et al.* 2018). In contrast, the *Gallionellaceae* sp. MAG (AG11) was found to harbor all genes required to reduce NO_3^-, NO_2^- and transform toxic NO to N_2O, but the last step was missing due to the lack of the *nosZ* gene in the genome. However, the lack of *nosZ* in this MAG might be attributed to the relatively low completeness (89.9%). Alternatively, the organism may simply not possess the full set of enzymes and rely on other microbial community members to complete denitrification as suggested previously for *Gallionellaceae* spp. from cultures KS and BP (He *et al.* 2016; Huang *et al.* 2021a, 2021b). Since the autotrophic NRFeOx culture presented in this study is expected to also produce N_2 resulting from denitrification based on the previously determined stoichiometric ratio of oxidized Fe(II) and reduced nitrate as well as gas measurements (Jakus *et al.* 2021), microbial community members likely have to cooperate to complete the process via a series of metabolic handoffs.

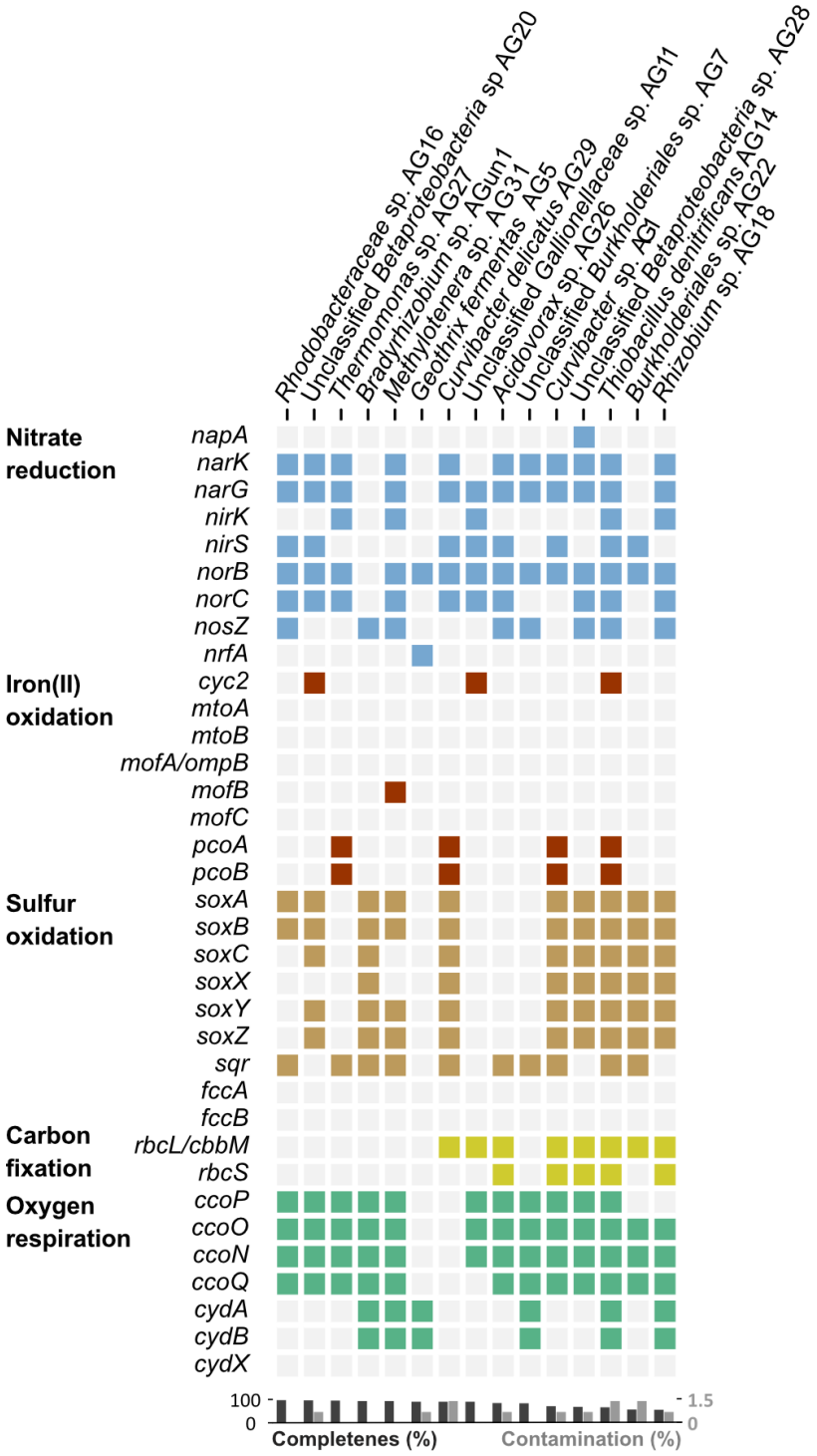

Figure 4. Summary of key genes involved in putative energy generation pathways. Colored squares indicate presence of genes involved in nitrate reduction (blue), Fe(II) oxidation (red), sulfur oxidation (brown), inorganic carbon fixation (bright green) and oxygen respiration (dark green). MAGs are ordered according to the genome completeness, starting from the most complete (97.3%) to the least complete (56.1%) MAG. Bar plot underneath the table shows completeness (0-100%, dark grey) and contamination (0-1.5%, bright grey) of each individual MAG.

6.3.7. Iron oxidation by the autotrophic NRFeOx community

The mechanisms for autotrophic Fe(II) oxidation in neutrophilic Fe(II)-oxidizing bacteria remain largely unknown and are hypothesized to be facilitated by extracellular electron transfer (EET) (Ilbert and Bonnefoy 2013; He *et al.* 2017). Using the FeGenie software (Garber *et al.* 2020), we searched for putative genes involved in Fe(II) oxidation (i.e. *cyc1, cyc2, foxABC, foxEYZ, sulfocyanin, pioABC* and *mtoAB*) which resulted in the detection of the genes in three out of all fifteen MAGs: the *Gallionellaceae* sp. (AG11), *Thiobacillus denitrificans* (AG14) and unclassified *Betaproteobacteria* sp. (AG20). All three MAGs possessed homologs of the gene encoding an outer membrane cytochrome *c*, *cyc2* (Figure 4, 5A). However, it was previously found that Fe(II) oxidation in *Thiobacillus denitrificans* is not catalyzed by any *c*-type cytochrome (Beller *et al.* 2013), and we therefore conclude that the identified homolog in *Thiobacillus denitrificans* of our study might rather be a heme-containing protein which may participate in a yet-to-be defined electron transfer pathway rather than Fe(II) oxidation. For further discussion, we thus consider only the dominant *Gallionellaceae* sp. and unclassified *Betaproteobacteria* MAGs to contain a *cyc2* gene potentially involved in Fe(II) oxidation. The *cyc2* homolog recovered from the unclassified *Gallionellaceae* sp. grouped phylogenetically with the putative *cyc2* of other known neutrophilic Fe(II)-oxidizers (Figure 5A), indicating that this microbe may also use Cyc2 to facilitate Fe(II) oxidation. A homolog of the *cyc2* gene identified in the MAG of the unclassified *Betaproteobacteria* (AG20) in our enrichment culture was found to be more phylogenetically similar to cytochromes present in *Dechloromonas* sp. and *Methylotenera* sp. genomes and other microbes not commonly classified as typical Fe(II)-oxidizers (Figure 5A). The 16S rRNA gene retrieved from this MAG is incomplete (954 bp), and we therefore performed additional comparative genomic analyses (Multilocus sequence analysis (MLSA), see Figure S3) which revealed that the unclassified *Betaproteobacteria* MAG (AG20) containing a *cyc2* gene can be affiliated with so far unclassified *Methyloversatilis* spp. Interestingly, in previously published genome analysis of methylotrophic nitrate-reducing *Methyloversatilis* sp. growing in a presence of Fe(II), no potential Fe(II) oxidase was identified, instead, a nitrate reductase (*nar*) was proposed to be potentially involved in Fe(II) oxidation (Liu *et al.* 2018), i.e. via chemodenitrification (enzymatic production of nitrite leading to abiotic Fe(II) oxidation by the nitrite; Klueglein and Kappler 2013). Using annotations of the MAGs and metagenome produced by the IMG/MER pipeline, we further searched for putative Fe(II) oxidation genes and detected the presence of homologs of three more putative oxidases: a homolog of a gene encoding MofB in the MAG of *Methylotenera* sp. (AG31), and PcoAB in MAGs of both *Curvibacter* sp. (AG29) and *Thiobacillus denitrificans* (AG14) (further discussed in the supplementary information). Since we were unable to retrieve a 16S rRNA gene sequence of the *Curvibacter* sp. MAG (AG29), we compared 16S rRNA gene amplicon sequence-based relative abundances of ASVs in the autotrophic NRFeOx culture with estimated coverages of the MAGs (Table 1), revealing that the *Curvibacter* sp. MAG (AG29) most likely represents the unclassified *Burkholderiaceae* sp. (accounting for 3% relative abundance). The same ASV was additionally identified in the culture growing in the gradient tube and in the culture growing under mixotrophic conditions (Figure 3), which further supports the hypothesis that this taxon has the ability to oxidize Fe(II). Although *Curvibacter* spp. were recently recognized as FeOB (Gülay et al. 2018a), the genes encoding proteins involved in this process have not yet been identified; in addition, the electron transfer pathway has not yet been proposed. Therefore, we suggest that

Fe(II)-oxidizing *Curvibacter* spp., closely related to the organism identified in this study, are likely to use the putative Fe(II) oxidase PcoAB to promote Fe(II) oxidation.

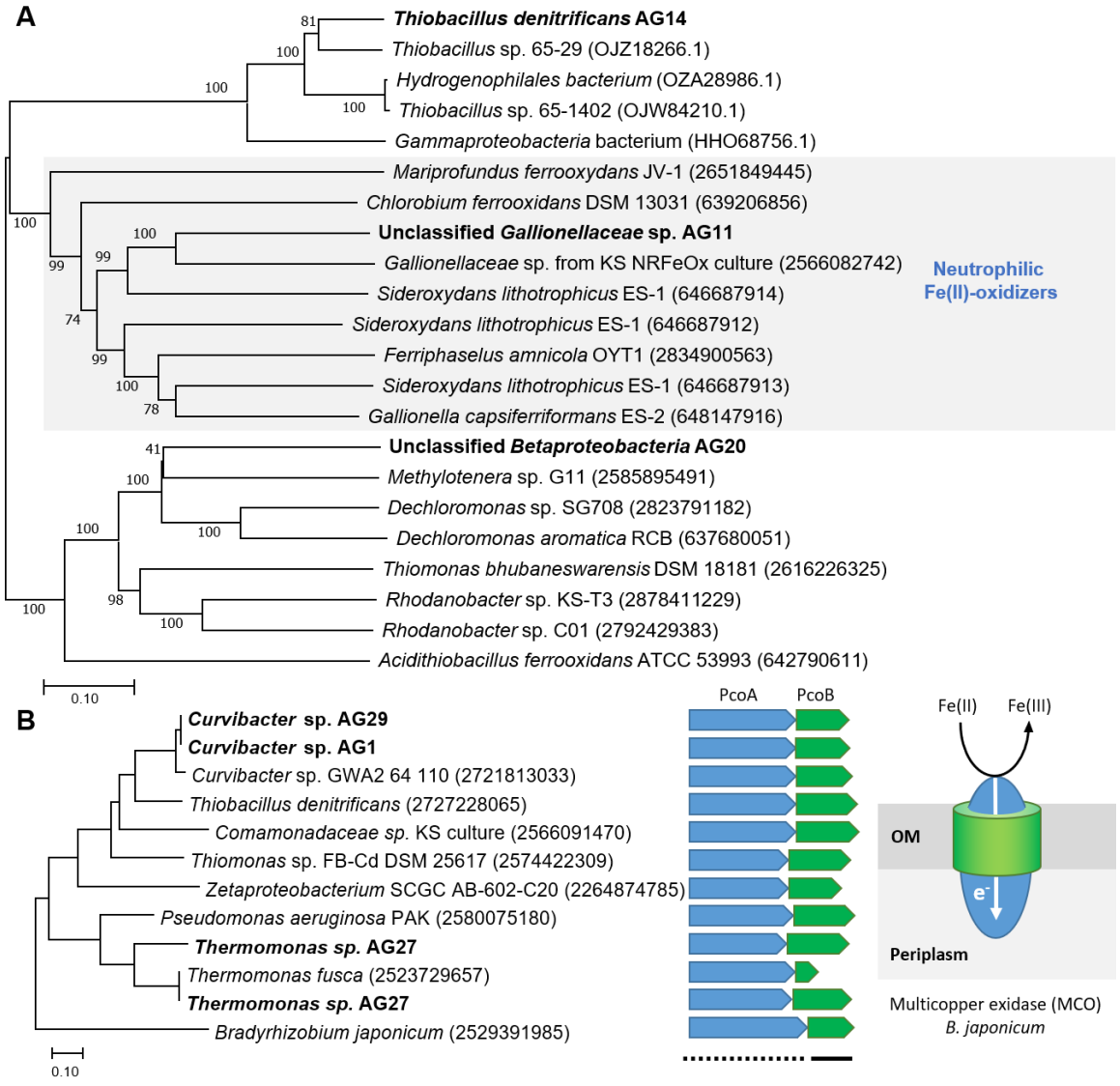

Figure 5. Phylogenetic trees of putative Fe(II)-oxidase homologs: Cyc2 (A), and PcoAB (B) identified from MAGs recovered in this study (**bold font**). Sequences of *Thiobacillus denitrificans* sp. (AG14), unclassified *Gallionellaceae* sp. (AG11) and unclassified *Betaproteobacteria* sp. (AG20) are shown in relation to other homologs of Cyc2, including protein sequences of commonly known neutrophilic Fe(II)-oxidizers (grey background). *Curvibacter* spp. (AG29 and AG1) and *Thermomonas* sp. (AG27) are shown in relation to homologous sequences of PcoAB. Predicted cellular locations of encoded PcoAB are shown by different line types under the genes, with dashed lines and thick lines indicating periplasm and outer membrane, respectively. The trees were produced by Neighbor–Joining in the MEGAX software suite using the *p*-distance model and pairwise gap deletion. Bootstrap values are the percentage of 1000 trials in which a given node was present. Numbers in brackets are IMG gene ID accession numbers. The scale bar corresponds to 0.1 nucleotide substitutions per site.

6.3.8. Sulfur oxidation by the autotrophic NRFeOx community

Pyrite present in the aquifer is a potential source of both Fe(II) and reduced sulfur. Since the complete oxidation of sulfur involves multiple electron transfer steps, we searched for genes involved in the first and the last oxidation step to identify potential microbial key players in this process. Ten out of fifteen most complete MAGs, contained sulfide:quinone oxidoreductase (*sqr*) genes providing the potential for oxidation of sulfide (S^{2-}) to zero-valent sulfur (S^0) (Berben *et al.* 2019). This oxidation step can be also mediated by the flavocytochrome *c* sulfide dehydrogenase (*fccAB*) genes (Berben *et al.* 2019) which were not detected in the metagenome (Table S1). Genes needed for thiosulfate ($S_2O_3^{2-}$) oxidation (*sox* cluster) leading to sulfate (SO_4^{2-}) formation were present in most of the MAGs, including those identified as *Thiobacillus denitrificans* (AG14), *Methylotenera* sp. (AG31) and both *Curvibacter* spp. (AG29 and AG1). Similarly, homologs of sulfur-oxidizing *sox* genes were recovered in all of the MAGs in our study, which cover a diverse range of community members, except for the *Chitinophagaceae* sp. In a previous study, *Chitinophagaceae* were members of an enrichment culture that demonstrated to accelerate pyrite oxidation under microoxic conditions (Percak-Dennett *et al.* 2017). The genome of the dominant *Gallionellaceae* sp. (AG11) assembled in our study possessed neither *sqr* nor *sox* genes, and is most probably unable to participate in steps initiating and completing the sulfur oxidation pathway. This implies that the most dominant *Gallionellaceae* sp. of our study is likely better adapted for growth with Fe(II) than reduced S-compounds, even though the ability to grow on these compounds would give it a competitive advantage during pyrite oxidation after all available Fe(II) is oxidized. The lack of the *sqr* gene in this MAG (if not missing due to MAG incompleteness) differentiates it from *Gallionellaceae* spp. reported in groundwater and microbial mats, thriving across a redox transition zone (Bethencourt *et al.* 2020). In this previous study, all MAGs contained *sqr* genes with a few possessing additionally *fccAB* genes. In contrast, possession *of sox* genes seems to be more heterogeneous among the *Gallionellaceae* family. For example, in the previous study only four out of fourteen MAGs had *sox* clusters (Bethencourt *et al.* 2020). Other examples are two *Gallionellaceae* spp. described previously (Emerson *et al.* 2013) where it was shown that one of them, *Sideroxydans* ES-1, had a *soxXYZAB* gene cluster, while the other one, *Gallionella* ES-2, did not possess S-oxidation pathway genes, nor did it show evidence for growth on reduced S compounds.

6.3.9. Autotrophic carbon fixation by the NRFeOx community

Even though the NRFeOx culture enriched from the aquifer is able to continuously grow under autotrophic conditions, with CO_2 being the sole carbon source (Jakus *et al.* 2021), only eight MAGs were found to contain the ribulose-1,5-bisphosphate carboxylase/oxygenase gene, encoding the key enzyme of the CBB cycle, used for CO_2 fixation. In total, 19 copies of this gene were annotated in the whole metagenome but seven of them were excluded from further analysis due to short sequence length (<150 bp, Table S2). Four copies of the gene belonging to the MAGs of the *Thiobacillus denitrificans* (AG14), *Acidovorax* sp. (AG26), *Rhizobium* sp. (AG18), as well as an unbinned sequence, were identified as *rbcS* genes. The *rbcS* gene encodes RuBisCO Form I (Figure S4), a key protein participating in CO_2 fixation particularly in environments with elevated levels of O_2 (Badger and Bek 2008). The unbinned sequence of the *rbcS* gene showed the highest similarity to *rbcS* found

in the genome of *Acidovorax* sp. SD340 (WP_055394172.1, 100% query cover, 100% identity). The other gene encoding RuBisCO, *rbcL/cbbM* (Form II, Figure S4), was identified in the MAGs of *Gallionellaceae* sp. (AG11), unclassified *Betaproteobacteria* sp. (AG28), *Curvibacter delicatus* (AG29) and two more sequences which were not affiliated to any genome bins but had the highest similarity to *rbcL*/*cbbM* sequences identified in *Dechloromonas aromatica* (WP_011289362.1, 100% query cover, 96.51% and 91.72% identity). Additionally, the *Thiobacillus denitrificans* MAG (AG17) was found to also possess genes encoding Form II RuBisCO alongside the Form I, which was expected for this organism based on a previous study (English *et al.* 1992). We also found that two MAGs contained genes encoding RuBisCO Form IV (Figure S4) that is unable to catalyze CO_2 fixation because of key substitutions of many essential active-site residues, but it was found to play a role in sulfur metabolism (thiosulfate oxidation) (Hanson and Tabita 2001, 2003; Tabita *et al.* 2008).

6.3.10. Potential oxygen reduction by the autotrophic NRFeOx community

Conventional biological denitrification requires hypoxic conditions with dissolved oxygen (DO) concentrations lower than 0.2 mg L^{-1} (Seitzinger *et al.* 2006). However in the studied aquifer, structural discontinuities such as bedding planes or fractures produce preferential flow paths, which can transport oxygen (Osenbrück *et al.* 2021). Microbes living in such environments are often adapted to take an advantage of local redox changes and respire oxygen when it is present at low concentrations. Genes encoding for the *cbb3*-type cytochrome *c* (*ccoGPONQ*) were identified in all fifteen MAGs with the exception of *Curvibacter delicatus* (AG29) and *Geothrix fermentans* (AG5). The lack of the genes encoding *cbb3*-type cytochrome *c* in the *Curvibacter delicatus* MAG is particularly surprising and might be linked to the MAG incompleteness (89.9% completeness) since this taxon was found to dominate the community growing under microoxic conditions. The majority of the MAGs, including the *Gallionellaceae* sp. (AG11) was also missing genes *cydABX* coding for another terminal oxidase: the cytochrome *bd* oxidase. As expected from our culture originating from an anoxic aquifer, none of the genomes was found to possess *aa3*-type cytochrome oxidases, which is a gene involved in oxygen reduction and therefore would require elevated oxygen levels (Castelle *et al.* 2008).

6.3.11. Candidates of NRFeOx bacteria

The unclassified *Gallionellaceae* sp. dominating the autotrophic NRFeOx culture most likely is a truly autotrophic NRFeOx organism, performing Fe(II) oxidation via Cyc2 coupled to near complete denitrification since it probably lacks the NosZ reductase. Other potential autotrophic NRFeOx candidates were *Curvibacter* spp. Similar to the *Gallionellaceae* sp., both MAGs of *Curvibacter* spp. recovered in this study possessed almost all genes required for complete denitrification except for the *nosZ* gene. Fe(II) oxidation by this organism could potentially be facilitated by the putative Fe(II) oxidase PcoAB. Another potential autotrophic NRFeOx bacterium is *Thiobacillus denitrificans*, previously reported to be able to couple nitrate reduction to Fe(II) and pyrite oxidation (Bosch and Meckenstock 2012; Bosch *et al.* 2012), however it has never been shown to maintain Fe(II) oxidation over several transfers without organic carbon addition (Bryce *et al.* 2018). Furthermore, we classified

Methyloversatilis sp., and *Thermomonas* sp. as an additional two candidates for NRFeOx bacteria, since both possessed all genes required to facilitate almost complete denitrification, except for the *nosZ* gene. The MAGs of the *Methyloversatilis* sp., and *Thermomonas* sp. revealed genes putatively involved in Fe(II) oxidation, i.e. *cyc2* and *pcoAB*, respectively, but neither of them were found to possess genes required for carbon fixation. The lack of these genes can be associated with the incompleteness of MAGs or reflect the lack of ability to fix CO_2 by these bacteria, which can be supported by the fact that known cultivated strains of these organisms are heterotrophs capable of methanol and ethanol consumption (Kalyuzhnaya *et al.* 2006; Lu, Kalyuzhnaya and Chandran 2012). This further indicates that *Methyloversatilis* sp. and *Thermomonas* sp., enriched in the culture supplemented with nitrate and Fe(II) (only) are most probably facultative mixotrophic NRFeOx bacteria, able to survive under autotrophic conditions. Interestingly, the MAG of the second most abundant species in the autotrophic NRFeOx culture, *Acidovorax* sp. (16.4%), was found to have a complete set of genes to reduce NO_3^- to N_2 together with genes encoding CO_2 fixation but none of the putative Fe(II) oxidation genes was present. The lack of the enzymatic component of Fe(II) oxidation was previously reported in a draft genome of the NRFeOx *Acidovorax* sp. BoFeN1 (Price *et al.* 2018). Fe(II) oxidation catalyzed by this taxon was therefore interpreted to be a result of a chemodenitrification (Klueglein and Kappler 2013; Bryce *et al.* 2018). Thus, the *Acidovorax* sp. present in the NRFeOx culture is therefore most likely a "chemodenitrifier", catalyzing nitrate reduction (coupled to organic carbon consumption) and indirectly contributing to Fe(II) oxidation, although an enzymatic contribution to Fe(II) oxidation cannot be ruled out.

6.3.12. Fe(II) and organic carbon availability changes the composition of subsurface denitrifying communities

The availability of Fe(II) selects for a subset of denitrifying microbial assemblages that in the presence of organic substrates are able to tolerate, resist or transform Fe(II) by chemodenitrification or by enzymatic oxidation, to gain energy from simultaneous utilization of Fe(II) and organic compounds (mixotrophy). Alternatively, when the readily-degradable organic carbon is limited (which often is the case in deeper aquifers; Griebler and Lueders 2009), microbes able to perform denitrification coupled to Fe(II) oxidation, and fixation of CO_2 for energy and biomass production (autotrophy) may become predominant. Here we observed major differences in the composition of the denitrifying communities stemming from the same low-organic carbon, anoxic groundwater monitoring well in the aquifer, in three different treatments supplemented with Fe(II) and/or acetate. We found that only four taxa were shared between the different enrichment cultures taking an advantage of metabolic adaptation to exploit various electron donors and acceptors, which indicates that the supply of Fe(II) and in/organic carbon shapes very specialized and distinct assemblages. Among these organisms, the most metabolically flexible were bacteria related to *Burkholderiaceae* sp. identified as *Curvibacter delicatus,* shown to dominate mixotrophic communities and a bacterial culture subjected to microoxic conditions, outcompeting the *Gallionellaceae* sp. which are typically known as microaerophiles (Emerson, Fleming and McBeth 2010). The metabolic flexibility of *Curvibacter* spp. was further supported by the metabolic potential for complete denitrification, Fe(II) oxidation, CO_2 fixation and additionally sulfur oxidation pathways. This flexibility is especially

advantageous in an aquifer, where fluxes of recent groundwater transported along the horizontal, karstified bedding planes or fractures, may carry oxygen, nitrate and organic compounds and mix with anoxic, electron donor-depleted groundwater (Hofmann *et al.* 2020; Osenbrück *et al.* 2021) (Figure 6).

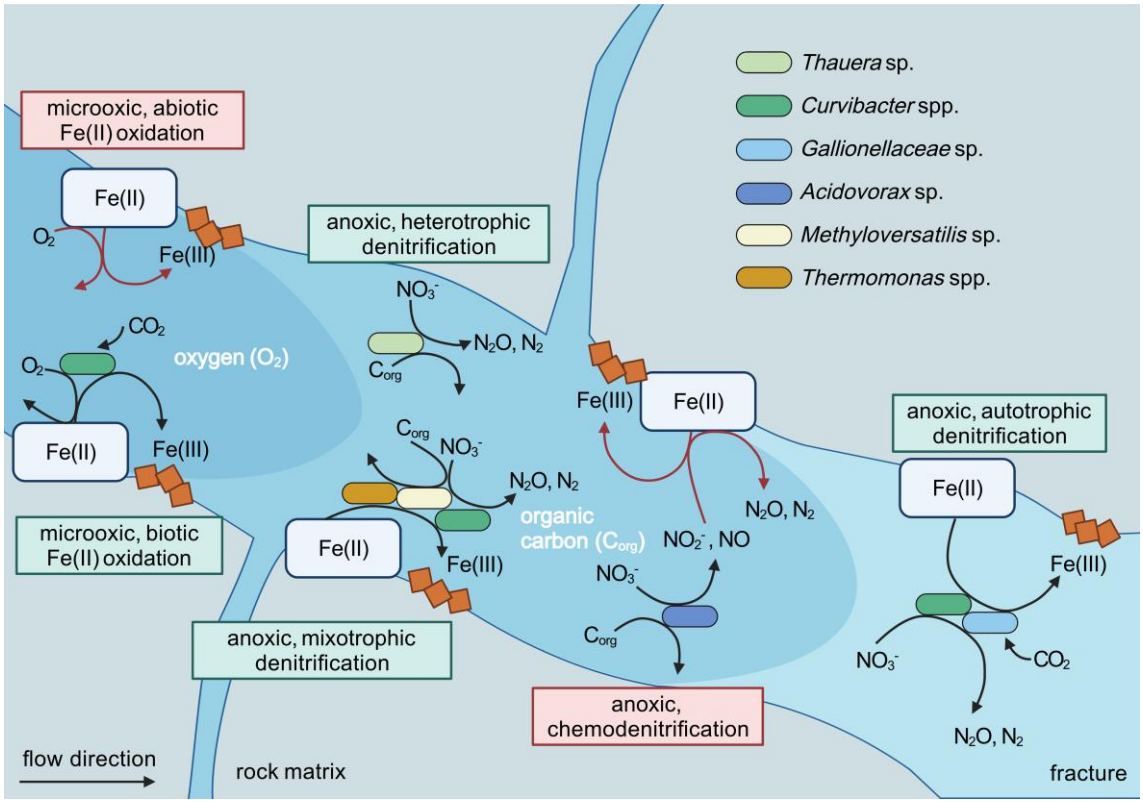

Figure 6. A conceptual model of biogeochemical reactions and microbial key players controlling the fate of Fe(II) and NO_3^- in response to fluxes of O_2 and bioavailable organic carbon (C_{org}) along the groundwater flow through fractures in the studied aquifer. First, oxygen entering the aquifer reacts either abiotically with Fe(II) phases or is oxidized by microaerophilic FeOB (e.g. *Curvibacter* spp.) leading to precipitation of Fe(III) (oxhyhydr)oxides. Once all O_2 is exhausted, NO_3^- reduction coupled to C_{org} oxidation via heterotrophic denitrification (e.g. *Thauera* sp.), and mixotrophic denitrification (with Fe(II) as a co-substrate, e.g. *Thermomonas* spp., *Methyloversatilis* sp., *Curvibacter* spp.) commences, likely leading to the formation of N_2O or N_2. Additionally, heterotrophic denitrification leading to the formation of reactive N-species (NO_2^-, NO) (e.g. by *Acidovorax* sp.) may trigger abiotic oxidation of Fe(II) and, as a consequence, further reduce the reactive N-species (chemodenitrification). Finally, after all bioavailable C_{org} is consumed, NO_3^- can be reduced via Fe(II) oxidation by autotrophic denitrifiers (e.g. *Gallionellaceae* sp., *Curvibacter* spp.). Note, that white rectangles represent all forms of Fe(II) available for microbes in the studied aquifer, including pyrite, Fe(II)-bearing carbonates, and aqueous Fe^{2+}. Red arrows and boxes indicate abiotic reactions.

The culture represents one of a few known existing autotrophic NRFeOx cultures that is continuously grown for a span of several years without the addition of organic carbon, and fulfilling the criteria for truly NRFeOx cultures defined by Bryce et al. (2018). Additionally, the capability of the CO_2 uptake was now confirmed by the presence of genes encoding RuBisCO in eight out of fifteen recovered MAGs. The culture contains several so far uncultured taxa and potential candidates for autotrophic NRFeOx bacteria, including the most dominant, unclassified *Gallionellaceae* sp. The physiology of these taxa remains rather speculative, and thus, our experiments provide novel insights into the potential lifestyles of uncultivated organisms relevant for nitrate-contaminated aquifer sites. Our findings have implications for assessing the denitrification potential of microbial communities

thriving in subsurface ecosystems like many aquifers, where the host rock contains Fe(II) minerals, which can serve as electron donor, supporting chemolithotrophic microbial metabolisms and nitrate removal even under organic carbon limitation.

6.4. Conflict of interest

The authors declare that the research was conducted in the absence of any commercial or financial relationships that could be construed as a potential conflict of interest.

6.5. Author contributions

N.J., N.B. and S.K. designed the study. N.J. and D.S. analyzed the data. N.J., N.B. and S.K. interpreted the data and N.J. wrote the manuscript with the help of N.B., D.S., S.K. and A.K. All authors commented and approved the final manuscript.

6.6. Funding

This work was funded by the Institutional Strategy of the University of Tübingen [German Research Foundation; Deutsche Forschungsgemeinschaft (DFG), ZUK 63] and by the Collaborative Research Center 1253 CAMPOS (Project 5: Fractured Aquifers), funded by the German Research Foundation [DFG, Grant Agreement SFB 1253/1 2017]. S.K. is supported by an Emmy-Noether fellowship [DFG Grant 326028733].

6.7. Acknowledgements

We would like to thank Stefanie Becker, Caroline Schlaiss and Jonah Schooss for the maintenance of cultures and help with DNA extractions. A.K. acknowledges infrastructural support by the DFG under Germany's Excellence Strategy, cluster of Excellence [EXC2124, project ID 390838134].

6.8. Data availability

The datasets generated for this study can be found in the GenBank/Sequence Read Archive under BioProject accession number PRJNA678222 (access link only for the review process: https://dataview.ncbi.nlm.nih.gov/object/PRJNA678222?reviewer=1vbkrk6f1m91id17vlhoi9c693).

References

Apprill A, Mcnally S, Parsons R *et al.* Minor revision to V4 region SSU rRNA 806R gene primer greatly increases detection of SAR11 bacterioplankton. *Aquat Microb Ecol* 2015;**75**:129–37.

Badger MR, Bek EJ. Multiple Rubisco forms in proteobacteria: Their functional significance in relation to CO_2 acquisition by the CBB cycle. *J Exp Bot* 2008;**59**:1525–41.

Beller HR, Zhou P, Legler TC *et al.* Genome-enabled studies of anaerobic, nitrate-dependent oxidation in the chemolithoautotrophic bacterium Thiobacillus denitrificans. *Front Microbiol* 2013;**4**:1–16.

Bellini MI, Gutiérrez L, Tarlera S *et al.* Isolation and functional analysis of denitrifiers in an aquifer with high potential for denitrification. *Syst Appl Microbiol* 2013;**36**:505–16.

Berben T, Overmars L, Sorokin DY *et al.* Diversity and distribution of sulfur oxidation-related genes in *Thioalkalivibrio*, a genus of chemolithoautotrophic and haloalkaliphilic sulfur-oxidizing bacteria. *Front Microbiol* 2019;**10**:1–15.

Bethencourt L, Bochet O, Farasin J *et al.* Genome reconstruction reveals distinct assemblages of *Gallionellaceae* in surface and subsurface redox transition zones. *FEMS Microbiol Ecol* 2020;**96**:1–13.

Bosch J, Lee KY, Jordan G *et al.* Anaerobic, nitrate-dependent oxidation of pyrite nanoparticles by *Thiobacillus denitrificans*. *Environ Sci Technol* 2012;**46**:2095–101.

Bosch J, Meckenstock RU. Rates and potential mechanism of anaerobic nitrate-dependent microbial pyrite oxidation. *Biochem Soc Trans* 2012;**40**:1280–3.

Bryce C, Blackwell N, Schmidt C *et al.* Microbial anaerobic Fe(II) oxidation - ecology, mechanisms and environmental implications. *Environ Microbiol* 2018;**20**:3462–83.

Carlson HK, Clark IC, Blazewicz SJ *et al.* Fe(II) oxidation is an innate capability of nitrate-reducing bacteria that involves abiotic and biotic reactions. *J Bacteriol* 2013;**195**:3260–8.

Castelle C, Guiral M, Malarte G *et al.* A new iron-oxidizing/O_2-reducing supercomplex spanning both inner and outer membranes, isolated from the extreme acidophile *Acidithiobacillus ferrooxidans*. *J Biol Chem* 2008;**283**:25803–11.

Chakraborty A, Picardal F. Induction of nitrate-dependent Fe(II) oxidation by Fe(II) in *Dechloromonas* sp. strain UWNR4 and *Acidovorax* sp. strain 2AN. *Appl Environ Microbiol* 2013;**79**:748–52.

Chen IMA, Chu K, Palaniappan K *et al.* IMG/M v.5.0: An integrated data management and comparative analysis system for microbial genomes and microbiomes. *Nucleic Acids Res* 2019;**47**:D666–77.

Chu L, Wang J. Denitrification of groundwater using a biodegradable polymer as a carbon source: Long-term performance and microbial diversity. *RSC Adv* 2017;**7**:53454–62.

Emerson D, Field EK, Chertkov O *et al.* Comparative genomics of freshwater Fe-oxidizing bacteria: Implications for physiology, ecology, and systematics. *Front Microbiol* 2013;**4**:1–17.

Emerson D, Fleming EJ, McBeth JM. Iron-oxidizing bacteria: An environmental and genomic perspective. *Annu Rev Microbiol* 2010;**64**:561–83.

Emerson D, Floyd MM. Enrichment and isolation of iron-oxidizing bacteria at neutral pH. *Methods Enzymol* 2005;**397**:112–23.

Emerson D, Moyer C. Isolation and characterization of novel iron-oxidizing bacteria that grow at circumneutral pH. *Appl Environ Microbiol* 1997;**63**:4784–92.

English RS, Williams CA, Lorbach SC *et al.* Two forms of ribulose-l,5-bisphosphate carboxylase/oxygenase from *Thiobacillus denitrificans* . 1992;**94**.

Etchebehere C, Tiedje J. Presence of two different active nirS nitrite reductase genes in a denitrifying *Thauera* sp. from a high-nitrate-removal-rate reactor. *Appl Environ Microbiol* 2005;**71**:5642–5.

European Commission. Report from the commission to the council and the European Parliament on the implementation of Council Directive 91/676/EEC. *Eur Comm* 2018:14.

European Union. Directive 2006/118/EC of the European Parliament and of the council of 12 December 2006 on the protection of groundwater against pollution and deterioration. *Off J Eur Union* 2006;**19**:19–31.

Ewels PA, Peltzer A, Fillinger S *et al.* The nf-core framework for community-curated bioinformatics pipelines. *Nat Biotechnol* 2020;**38**:271.

Garber AI, Nealson KH, Okamoto A *et al.* FeGenie: A comprehensive tool for the identification of iron genes and iron gene neighborhoods in genome and metagenome assemblies. *Front Microbiol* 2020;**11**:1–23.

Griebler C, Lueders T. Microbial biodiversity in groundwater ecosystems. *Freshw Biol* 2009;**54**:649–77.

Gülay A, Çekiç Y, Musovic S *et al.* Diversity of iron oxidizers in groundwater-fed rapid sand filters: Evidence of Fe(II)-dependent growth by *Curvibacter* and *Undibacterium* spp. *Front Microbiol* 2018;**9**:1–14.

Hallbeck L, Ståhl F, Pedersen K. Phylogeny and phenotypic characterization of the stalk-forming and iron-oxidizing bacterium *Gallionella ferruginea*. *J Gen Microbiol* 1993;**139**:1531–5.

Hanson TE, Tabita FR. A ribulose-1,5-bisphosphate carboxylase/oxygenase (RubisCO)-like protein from *Chlorobium tepidum* that is involved with sulfur metabolism and the response to oxidative stress. *Proc Natl Acad Sci U S A* 2001;**98**:4397–402.

Hanson TE, Tabita FR. Insights into the stress response and sulfur metabolism revealed by proteome analysis of a Chlorobium tepidum mutant lacking the Rubisco-like protein. *Photosynth Res* 2003;**78**:231–48.
He S, Barco RA, Emerson D *et al.* Comparative genomic analysis of neutrophilic iron(II) oxidizer genomes for candidate genes in extracellular electron transfer. *Front Microbiol* 2017;**8**:1–17.
He S, Tominski C, Kappler A *et al.* Metagenomic analyses of the autotrophic Fe(II)-oxidizing, nitrate-reducing enrichment culture KS. *Appl Environ Microbiol* 2016;**82**:2656–68.
Hofmann R, Uhl J, Hertkorn N *et al.* Linkage between dissolved organic matter transformation, bacterial carbon production, and diversity in a shallow oligotrophic aquifer: results from flow-through sediment microcosm experiments .*Front Microbiol* 2020;**11**:2425.
Huang Y-M, Straub D, Blackwell N *et al.* Meta-omics reveal *Gallionellaceae* and *Rhodanobacter* as interdependent key players for Fe(II) oxidation and nitrate reduction in the autotrophic enrichment culture KS. *Revis* 2021a, DOI: 10.1128/aem.00496-21.
Huang Y-M, Straub D, Kappler A *et al.* A novel enrichment culture highlights core features of microbial networks contributing to autotrophic Fe(II) oxidation coupled to nitrate reduction. *Microb Physiol* 2021b;**In press**.
Ilbert M, Bonnefoy V. Insight into the evolution of the iron oxidation pathways. *Biochim Biophys Acta - Bioenerg* 2013;**1827**:161–75.
Jakus N, Blackwell N, Osenbrück K *et al.* Nitrate removal by a novel lithoautotrophic nitrate-reducing iron(II)-oxidizing culture enriched from a pyrite-rich limestone aquifer. *Appl Environ Microbiol* 2021a, DOI: 10.1128/AEM.00460-21.
Jakus N, Mellage A, Hoeschen C *et al.* Anaerobic neutrophilic pyrite oxidation by a chemolithoautotrophic nitrate-reducing iron(II)-oxidizing culture enriched from a fractured aquifer. *Environ Sci Technol* 2021b.
Jewell TNM, Karaoz U, Brodie EL *et al.* Metatranscriptomic evidence of pervasive and diverse chemolithoautotrophy relevant to C, S, N and Fe cycling in a shallow alluvial aquifer. *ISME J* 2016;**10**:2106–17.
Jørgensen CJ, Jacobsen OS, Elberling B *et al.* Microbial oxidation of pyrite coupled to nitrate reduction in anoxic groundwater sediment. *Environ Sci Technol* 2009;**43**:4851–7.
Kalyuzhnaya MG, De Marco P, Bowerman S *et al. Methyloversatilis universalis* gen. nov., sp. nov., a novel taxon within the *Betaproteobacteria* represented by three methylotrophic isolates. *Int J Syst Evol Microbiol* 2006;**56**:2517–22.
Kazakis N, Matiatos I, Ntona MM *et al.* Origin, implications and management strategies for nitrate pollution in surface and ground waters of Anthemountas basin based on a $\delta^{15}N\text{-}NO_3^-$ and $\delta^{18}O\text{-}NO_3^-$ isotope approach. *Sci Total Environ* 2020;**724**:138211.
Klueglein N, Kappler A. Abiotic oxidation of Fe(II) by reactive nitrogen species in cultures of the nitrate-reducing Fe(II) oxidizer *Acidovorax* sp. BoFeN1 – questioning the existence of enzymatic Fe(II) oxidation. *Geobiology* 2013;**11**:180–90.
Kumar S, Herrmann M, Blohm A *et al.* Thiosulfate- and hydrogen-driven autotrophic denitrification by a microbial consortium enriched from groundwater of an oligotrophic limestone aquifer. *FEMS Microbiol Ecol* 2018;**94**:1–13.
Kuypers MMM, Marchant HK, Kartal B. The microbial nitrogen-cycling network. *Nat Rev Microbiol* 2018;**16**:263–76.
Li J, Hao H, Cheng G *et al.* Enhancing nitrate removal from freshwater pond by regulating carbon/nitrogen ratio. *Front Microbiol* 2017;**8**:1–9.
Liu Y, Feng C, Sheng Y *et al.* Effect of Fe(II) on reactivity of heterotrophic denitrifiers in the remediation of nitrate- and Fe(II)-contaminated groundwater. *Ecotoxicol Environ Saf* 2018;**166**:437–45.
Lu H, Kalyuzhnaya M, Chandran K pd. Comparative proteomic analysis reveals insights into anoxic growth of *Methyloversatilis universalis* FAM5 on methanol and ethanol. *Environ Microbiol* 2012;**14**:2935–45.
Muehe EM, Gerhardt S, Schink B *et al.* Ecophysiology and the energetic benefit of mixotrophic Fe(II) oxidation by various strains of nitrate-reducing bacteria. *FEMS Microbiol Ecol* 2009;**70**:335–43.
Mustakhimov I, Kalyuzhnaya MG, Lidstrom ME *et al.* Insights into denitrification in methylotenera mobilis from denitrification pathway and methanol metabolism mutants. *J Bacteriol* 2013;**195**:2207–11.
Osenbrück K, Blendinger E, Leven C *et al.* Nitrate reduction potential of a fractured Middle Triassic carbonate aquifer in southwest Germany. *Submitted* 2021.
Parada AE, Needham DM, Fuhrman JA. Every base matters: Assessing small subunit rRNA primers for marine microbiomes with mock communities, time series and global field samples. *Environ Microbiol* 2016;**18**:1403–14.
Pauwels H, Kloppmann W, Foucher JC *et al.* Field tracer test for denitrification in a pyrite-bearing schist aquifer. *Appl Geochemistry* 1998;**13**:767–78.
Percak-Dennett E, He S, Converse B *et al.* Microbial acceleration of aerobic pyrite oxidation at circumneutral pH. *Geobiology* 2017;**15**:690–703.

Postma D, Boesen C, Kristiansen H *et al.* Nitrate reduction in an unconfined sandy aquifer: water chemistry, reduction processes, and geochemical modeling. *Water Resour Res* 1991;**27**:2027–45.

Price A, Macey MC, Miot J *et al.* Draft Genome Sequences of the Nitrate-Dependent Iron- Oxidizing Proteobacteria *Acidovorax sp.* Strain BoFeN1 and *Paracoccus pantotrophus* Strain KS1. *Microbiol Resour Annoucements* 2018;**5**:17–8.

Schaedler F, Lockwood C, Lueder U *et al.* Microbially mediated coupling of Fe and N cycles by nitrate-reducing Fe(II)-oxidizing bacteria in littoral freshwater sediments. 2018;**84**:1–14.

Schwientek M, Einsiedl F, Stichler W *et al.* Evidence for denitrification regulated by pyrite oxidation in a heterogeneous porous groundwater system. *Chem Geol* 2008;**255**:60–7.

Seitzinger S, Harrison JA, Böhlke JK *et al.* Denitrification across landscapes and waterscapes: A synthesis. *Ecol Appl* 2006;**16**:2064–90.

Straub D, Blackwell N, Langarica-Fuentes A *et al.* Interpretations of environmental microbial community studies are biased by the selected 16S rRNA (Gene) amplicon sequencing pipeline. *Front Microbiol* 2020;**11**:1–18.

Straub KL, Benz M, Schink B *et al.* Anaerobic, nitrate-dependent oxidation of ferrous iron. *Appl Environ Microbiol* 1996;**62**:1458–60.

Tabita FR, Satagopan S, Hanson TE *et al.* Distinct form I, II, III, and IV Rubisco proteins from the three kingdoms of life provide clues about Rubisco evolution and structure/function relationships. *J Exp Bot* 2008;**59**:1515–24.

Tominski C, Lösekann-Behrens T, Ruecker A *et al.* Insights into carbon metabolism provided by fluorescence *in situ* hybridization-secondary ion mass spectrometry imaging of an autotrophic, nitrate-reducing, Fe(II)-oxidizing enrichment culture. *Appl Environ Microbiol* 2018;**84**:1–19.

Visser AN, Lehmann MF, Rügner H *et al.* Fate of nitrate during groundwater recharge in a fractured karst aquifer in Southwest Germany. *Hydrogeol J* 2020;**29**:1153–71.

Wang Y, Tian H, Huang F *et al.* Time-resolved analysis of a denitrifying bacterial community revealed a core microbiome responsible for the anaerobic degradation of quinoline. *Sci Rep* 2017;**7**:1–11.

Zhang Y-C, Slomp CP, Broers HP *et al.* Isotopic and microbiological signatures of pyrite-driven denitrification in a sandy aquifer. *Chem Geol* 2012;**300**–**301**:123–32.

7. **Supplementary information on**: Presence of Fe(II) and nitrate shapes aquifer-originating denitrifying communities leading to an enrichment of autotrophic Fe(II)-oxidizing *Gallionellaceae* sp. under organic carbon limitation

7.1. Supplemental materials and methods

7.1.1. 16S rRNA gene sequence analysis

Quality control, reconstruction of 16S rRNA gene sequences and taxonomic annotation was performed with nf-core/ampliseq v1.1.0 (Ewels *et al.* 2020; Straub *et al.* 2020) with Nextflow v20.04.1 (Di Tommaso *et al.* 2017) using containerized software with singularity v3.0.3 (Kurtzer, Sochat and Bauer 2017). Primers were trimmed, and untrimmed sequences were discarded (< 5%) with Cutadapt v1.16 (Martin 2011). Adapter and primer-free sequences were imported into QIIME2 version 2018.06 (Bolyen *et al.* 2019), their quality was checked with demux (https://github.com/qiime2/q2-demux), and they were processed with DADA2 version 1.6.0 (Callahan *et al.* 2016) to eliminate PhiX contamination, trim reads (before the mean quality score falls below 35, i.e. position 230 in forward reads and 176 in reverse reads), correct errors, merge read pairs, and remove PCR chimeras; ultimately, 241 amplicon sequencing variants (ASVs) were obtained across all samples. Alpha rarefaction curves were produced with the QIIME2 diversity alpha-rarefaction plugin, which indicated that the richness of the samples had been fully observed. A Naive Bayes classifier was fitted with 16S rRNA gene sequences extracted with the PCR primer sequences from the QIIME compatible, 99%-identity clustered SILVA v132 database (Pruesse *et al.* 2007). ASVs were classified by taxon using the fitted classifier (Bokulich *et al.* 2018). Three ASVs that classified as chloroplasts or mitochondria were removed, totaling to < 0.1% relative abundance per sample, and the remaining ASVs had their abundances extracted by feature-table (https://github.com/qiime2/q2-feature-table).

7.1.2. Quantitative PCR

Quantitative PCRs (qPCRs) were performed on DNA extracts from samples collected at day 0, 2, 3 and 9 using the SybrGreen® Supermix (Bio-Rad Laboratories GmbH, Munich, Germany) on an iQ5 real-time PCR detection system (iQ5 optical system software, version 2.0, Bio-Rad) with primers targeting the 16S rRNA gene: 341f (CCTACGGGAGGCAGCAG), 534r (ATTACCGCGGCTGCTGG). Each reaction mixture contained 5 µl SsoAdvanced Universal SYBR, 1 µl 341f (5 µM), 1 µl 534r (5 µl), 2 µl PCR water, 1 µl template, and the qPCRs were conducted using the following thermal profile: 5 s at 98°C, 12 s at 60°C, 1 min at 95°C for 40 cycles. Plasmid vectors (pCR2.1®, Invitrogen, Darmstadt, Germany) containing a cloned 16S rRNA gene fragment from *Thiomonas* sp. were used as standards for the quantification of total bacteria. Each qPCR assay was repeated in triplicates. Data analysis was done using the iQ5 optical system software, version 2.0 (Bio-Rad, 2006).

7.1.3. Metagenome sequencing, assembly and annotation

Metagenome library preparation and shotgun Illumina sequencing was conducted by CeGaT, Tuebingen, Germany. 1 µg of DNA was used for library preparation with the TruSeq DNA PCR-Free Kit (Illumina). Libraries were sequenced on the Illumina NovaSeq 6000 platform to generate 157 million paired-end (2 × 150-bp) (short-) reads (23.8 Gbp). 3.20 µg DNA was send for long-read sequencing with PromethION (Oxford Nanopore Technologies) to GenXone Inc, Suchy Las, Poland, that yielded 13 Gbp in 2.5 million reads.

Short- and long-read quality control, hybrid assembly, metagenome assembled genome binning and taxonomic annotation was performed with nf-core/mag v1.0.0 (https://nf-co.re/mag, DOI: 10.5281/zenodo.3589528) with Nextflow v 19.10.0 (Di Tommaso *et al.* 2017) using containerized software with singularity v3.0.3 (Kurtzer, Sochat and Bauer 2017). Short-read quality was assessed with FastQC v0.11.8 (Andrews 2010), quality filtering and Illumina adapter removal was performed with fastp v0.20.0 (Chen *et al.* 2018), and reads mapped with Bowtie2 v2.3.5 (Langmead and Salzberg 2012) to the PhiX genome (Enterobacteria phage WA11, GCA_002596845.1, ASM259684v1) were removed. Long-read quality was assessed with NanoPlot v1.26.3 (De Coster *et al.* 2018), adapter trimming was done with Porechop v0.2.3_seqan2.1.1 (https://github.com/rrwick/Porechop), *Escherichia virus Lambda* (PRJNA485481, GCA_000840245.1) contamination was removed with Nanolyse v1.1.0 (De Coster *et al.* 2018), and quality filtering was performed with Filtlong v0.2.0 (https://github.com/rrwick/Filtlong). Finally, processed short and long reads were assembled with metaSPAdes v3.13.1 (Nurk *et al.* 2017) and the assembly was evaluated with QUAST v5.0.2 (Gurevich *et al.* 2013). Metagenome-assembled genomes (MAGs) were binned with MetaBAT2 v2.13 (Kang *et al.* 2019) and checked for their completeness and contamination with BUSCO v3.0.2 (Waterhouse *et al.* 2018) using 148 near-universal single-copy orthologs (http://busco.ezlab.org/v3/datasets/bacteria_odb9.tar.gz) selected from OrthoDB v9 (Zdobnov *et al.* 2017), summary statistics were obtained with QUAST for each MAG, and finally MAGs were taxonomically annotated with CAT v4.6 (Von Meijenfeldt *et al.* 2019)

using a reference database created 8 January 2019 from NCBI nr using the command "CAT prepare --fresh".

7.1.4. Average Nucleotide Identity (ANI) and Average Amino Acid Identity (AAI) analysis

Nitrosomodales genomes and MAGs were downloaded from NCBI microbial genome resources. Average Nucleotide Identity (ANI) analysis was performed by using pyani.py (https://github.com/widdowquinn/pyani).
CheckM v1.0.11 (https://github.com/Ecogenomics/CheckM) was used to calculate Average Amino Acid Identity (AAI) between input sequences. The ANI and AAI matrixes were visualized using R (https://www.r-project.org/).

7.2. Supplemental discussion

7.2.1. Iron oxidation by the autotrophic NRFeOx community:

To evaluate the metabolic potential of the autotrophic NRFeOx community to perform Fe(II) oxidation, we searched for genes encoding putative Fe(II) oxidases in the MAGs. Besides the *cyc2* gene, the following homologs of putative Fe(II) oxidases were identified: a homolog of *mofB* was found in MAG of *Methylotenera* sp. (AG31), homologs of *pcoAB* were found in MAGs of both *Curvibacter* sp. (AG29) and *Thiobacillus denitrificans* (AG14). MofB functions as a protein-folding chaperone and activates MofA, a putative manganese oxidase, which together with MofC form a protein homologous to OmpBC, which is an outer membrane-associated multicopper oxidase (MCO) (Brouwers *et al.* 2000). The *ompBC* gene was recently proposed as candidate EET gene, facilitating Fe(II) oxidation (He *et al.* 2016). However, the MAG of the *Methylotenera* sp. (AG31) did not reveal *mofA*, possibly due to the incompleteness of the reconstructed genome (93.2%). Alternatively, *mofA* might be not present in the *Methylotenera* sp. MAG (AG31) at all, since other genomes of *Methylotenera* spp. currently available through the IMG/MER platform did not reveal any homologs to *mofA*. The *pcoAB* genes which were identified in the MAGs of the *Curvibacter* sp. (AG29) and *Thiobacillus denitrificans* (AG14) (Figure 5B), are genes predicted to encode an outer-membrane protein forming a beta-barrel structure. In this gene cluster, the *pcoA* gene encodes a protein that allows access to the outer surface for EET to occur, and could potentially facilitate the export of oxidized Fe(II) in the periplasm across the outer membrane.

7.3. Supplemental figures and tables

Table S1. A full list of MAG identifiers in NCBI and IMG JGI platforms. Note that only MAGs with completeness >90% could be uploaded to the IMG Gold database.

MAG identifier	NCBI name	NCBI genome accession	IMG identifier
AG16	*Rhodobacteraceae* bacterium AG16	JAHRYM000000000	2886187112
AG20	*Betaproteobacteria* bacterium AG20	JAHRYN000000000	2860365763
AG27	Thermomonas sp. AG27	JAHRYO000000000	2886184315
AGun1*	*Bradyrhizobiaceae* bacterium AGun1	CP078014	2860369277
AG31	*Methylotenera* sp. AG31	JAHRYP000000000	2886181812
AG5	*Geothrix* sp. AG5	JAHRYQ000000000	2886178660
AG29	*Curvibacter* sp. AG29	JAHRYR000000000	2886174954
AG11	*Nitrosomonadales* bacterium AG11	JAHRYS000000000	2860363623
AG26	*Acidovorax* sp. AG26	JAHRYT000000000	-
AG17	*Burkholderiales* bacterium AG17	JAHRYU000000000	-
AG1	*Curvibacter* sp. AG1	JAHRYV000000000	-
AG28	*Betaproteobacteria* bacterium AG28	JAHRYW000000000	-
AG14	*Thiobacillus denitrificans* AG14	JAHRYX000000000	-
AG22	*Burkholderiales* bacterium AG22	JAHRYY000000000	-
AG18	*Rhizobium* sp. AG18	JAHRYZ000000000	-

*un = unbinned. The MAG AGun1 consists only of one contig, therefore the binning software MetaBAT2 did not bin it. However, due to high quality assembly of this contig (4.1 Mbp length, which corresponds to 93.2% MAG completeness; Table 1) we used it in further analysis as a MAG even though it was not reported by MetaBAT2.

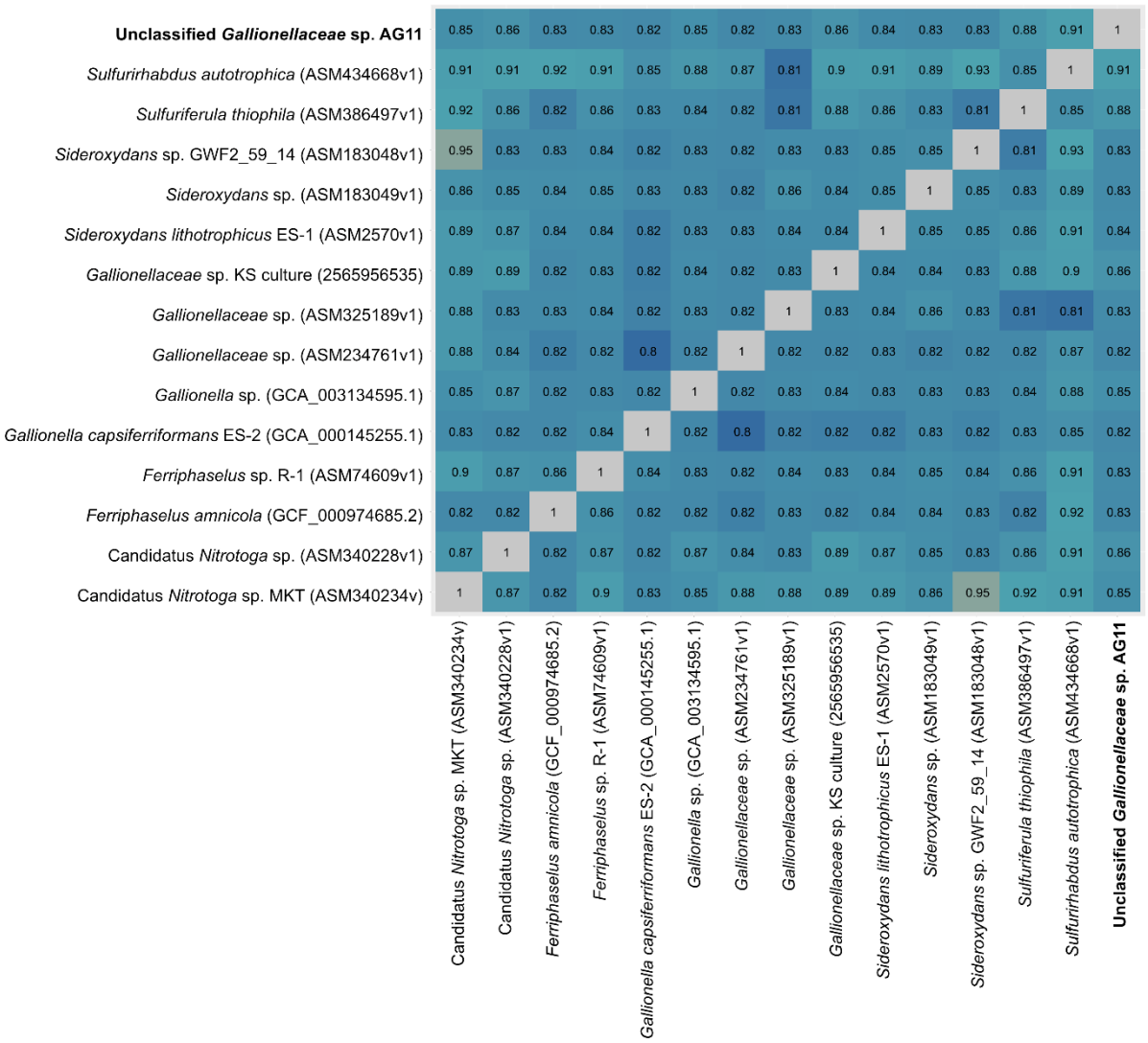

Figure S1. Heat map of the average nucleotide identity (ANI) among the 15 strains belonging to the family Gallionellaceae along with the unclassified *Gallionellaceae* sp. (AG11) (**bold font**) enriched in the NRFeOx culture. The percentages are listed in the figure. Numbers in brackets are IMG and NCBI databases ID accession numbers.

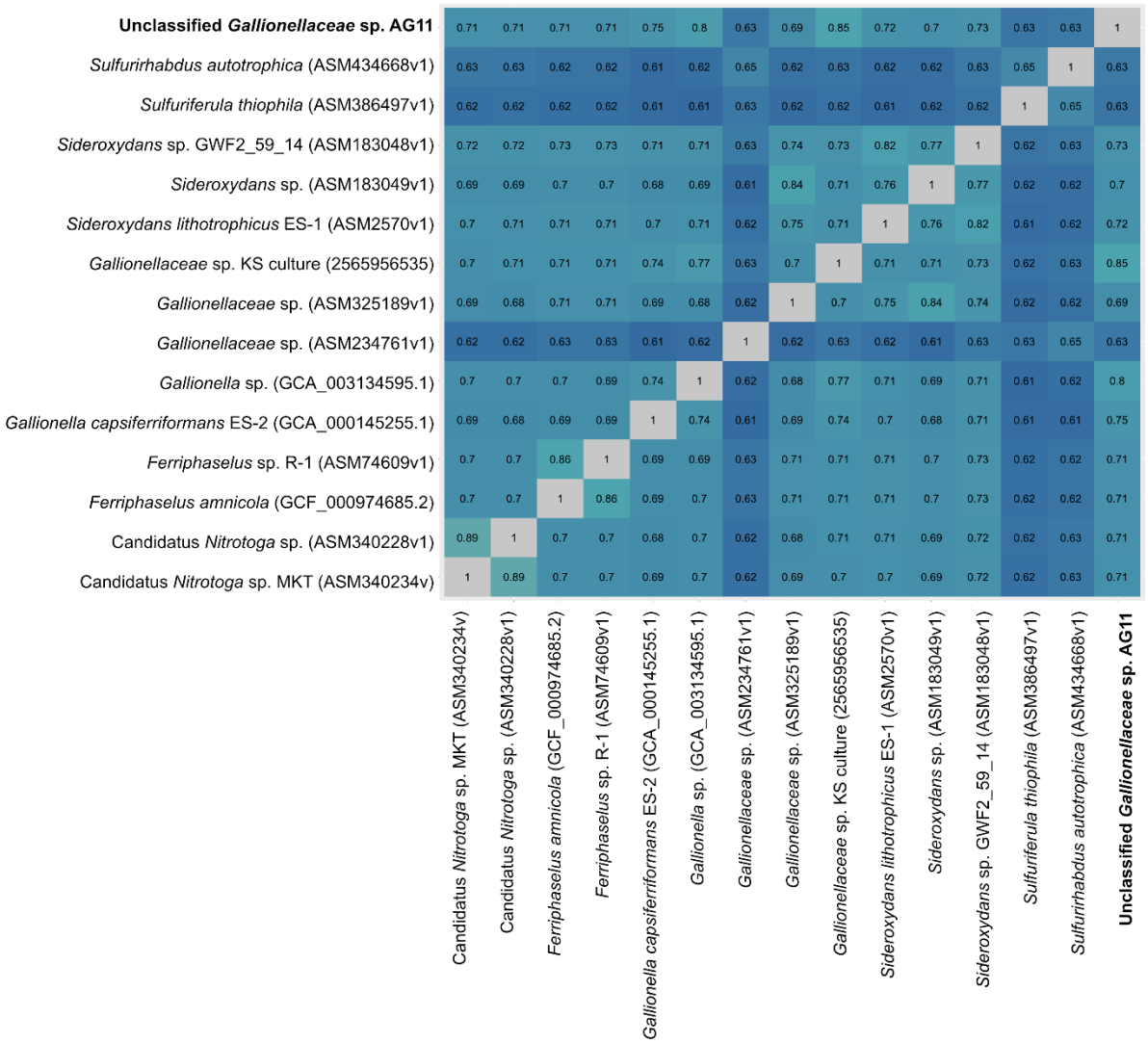

Figure S2. Heat map of the average amino acid identity (AAI) among the 15 strains belonging to the Gallionellaceae family along with the unclassified *Gallionellaceae* sp. (AG11) (**bold font**) enriched in the NRFeOx culture. The percentages are listed in the figure. Numbers in brackets are IMG and NCBI databases ID accession numbers.

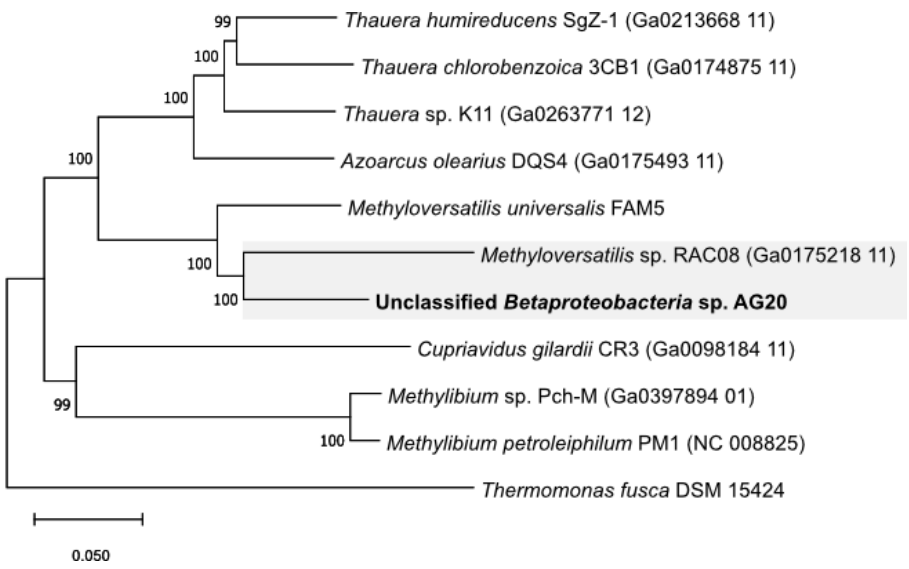

Figure S3. Concatenated phylogenetic tree of *dnaK, gryB, ileS, pnp, recA, thrC, gltA,* and *rpoB* genes. The tree was produced by Neighbor–Joining in the MEGAX software suite using the p-distance model and pairwise gap deletion. Bootstrap values are the percentage of 1000 trials in which a given node was present. The scale bar corresponds to 0.05 nucleotide substitutions per site.

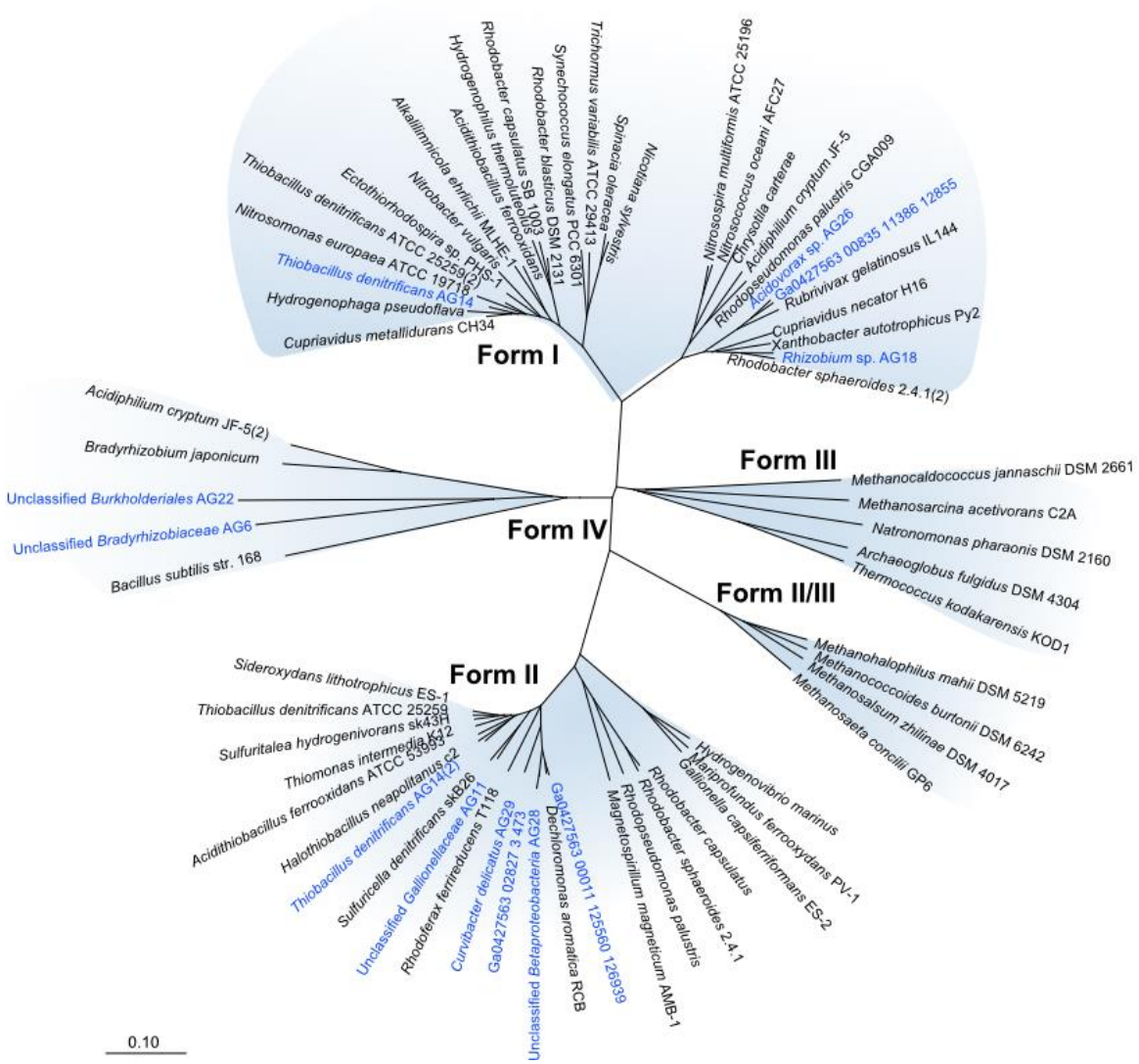

Figure S4. Phylogenetic tree of four forms of RuBisCO including RuBisCO-like proteins (RLP, form IV). The tree was constructed from a CLUSTALW alignment of RuBisCO and RLP sequences annotated from the metagenome of the autotrophic NRFeOx culture (blue font) together with sequences downloaded from the publicly accessible GeneBank database (black font). GenBank accession numbers are shown in Table S3. The tree was produced by Neighbor–Joining in the MEGAX software suite using the *p*-distance model and pairwise gap deletion. The scale bar corresponds to 0.1 nucleotide substitutions per site.

Table S2. RubisCO sequences annotated in the metagenome mapped to metagenomic bins which were used for constructing the RuBisCO large subunit amino acid tree. Sequences <150 amino acids were excluded from analysis due to the short length.

IMG JGI Locus Tag	Protein sequence length (aa)	Sequence identity (metagenomic bin)	Form
Ga0427563_00835_11386_12855	489	Unbinned	I
Ga0427563_00108_70768_72234	488	*Acidovorax* sp. (AG26)	I
Ga0427563_00798_6086_7546	486	*Rhizobium* sp. (AG18)	I
Ga0427563_00065_49250_50671	473	*Thiobacillus denitrificans* (AG14)	I
Ga0427563_00011_125560_126939	459	Unbinned	II
Ga0427563_00014_394589_395968	459	*Curvibacter delicatus* (AG29)	II
Ga0427563_00023_219767_221146	459	Unclassified *Gallionellaceae* sp. (AG11)	II
Ga0427563_00063_176984_178363	459	Unclassified *Betaproteobacteria* (AG28)	II
Ga0427563_00065_30808_32187	459	*Thiobacillus denitrificans* (AG14)	II
Ga0427563_03289_3_1118	372	Unclassified *Burkholderiales* (AG22)	IV
Ga0427563_00547_11661_12593	310	Unclassified *Bradyrhizobiaceae* (AG6)	IV
Ga0427563_02827_3_473	157	Unbinned	II
Ga0427563_02708_2209_2541	111	-	-
Ga0427563_17265_1_276	92	-	-
Ga0427563_19258_26_265	80	-	-
Ga0427563_00146_83665_83901	79	-	-
Ga0427563_24161_2_235	78	-	-
Ga0427563_15615_171_317	48	-	-
Ga0427563_08431_476_556	26	-	-

Table S3. Reference organism RubisCO sequences and accession numbers used for constructing the RuBisCO large subunit amino acid tree.

Accession number	Sequence identity	Form
P00880	*Synechococcus elongatus* PCC6301	I
Q59613	*Nitrobacter vulgaris*	I
Q56259	*Thiobacillus denitrificans* ATCC 25259	I
AAD10331	*Hydrogenophaga pseudoflava*	I
P0C916	*Acidithiobacillus ferrooxidans*	I
Q1LN92	*Cupriavidus metallidurans* CH34	I
Q82TG6	*Nitrosomonas europaea* ATCC 19718	I
BAA06437	*Hydrogenophilus thermoluteolus*	I
CAA23473	*Spinacia oleracea*	I
Q3M674	*Anabaena variabilis* ATCC 29413	I
YP_358684	*Nicotiana sylvestris*	I
Q6N9J0	*Rhodopseudomonas palustris* CGA009	I
YP_354363	*Rhodobacter sphaeroides* 2.4.1	I
BAA39175	*Pleurochrysis carterae*	I
A7IGM0	*Xanthobacter autotrophicus* Py2	I
Q2YB78	*Nitrosospira multiformis* ATCC 25196	I
BAC54025	*Rhodobacter blasticus* DSM 2131	I
EDZ66308	*Nitrosococcus oceani* AFC27	I
BAL96945	*Rubrivivax gelatinosus* IL144	I
BAO28567	*Sulfuritalea hydrogenivorans* sk43H	II
AAB82048	*Rhodobacter capsulatus* SB 1003	II
Q479W5	*Dechloromonas aromatica* RCB	II
YP_354780	*Rhodobacter sphaeroides* 2.4.1	II
Q9ZHZ4	*Halothiobacillus neapolitanus* c2	II
Q60028.3	*Thiobacillus denitrificans* ATCC 25259	II
Q2W3S5.1	*Magnetospirillum magneticum* AMB-1	II
Q21YM9	*Rhodoferax ferrireducens* T118	II
ACH84035	*Acidithiobacillus ferrooxidans* ATCC 53993	II
ADE10264	*Sideroxydans lithotrophicus* ES-1	II
BAN36649	*Sulfuricella denitrificans* skB26	II

AAN52766	*Rhodopseudomonas palustris*	II
O84917	*Thiomonas intermedia* K12	II
BAA05677	*Hydrogenovibrio marinus*	II
EAU56143	*Mariprofundus ferrooxydans* PV-1	II
ADL54079	*Gallionella capsiferriformans* ES-2	II
YP_003542093	*Methanohalophilus mahii* DSM 5219	II/III
YP_566926	*Methanococcoides burtonii* DSM 6242	II/III
YP_004385218	*Methanosaeta concilii* GP6	II/III
YP_004615354	*Methanosalsum zhilinae* DSM 4017	II/III
NP_248230	*Methanocaldococcus jannaschii* DSM 2661	III
NP_619414	*Methanosarcina acetivorans* C2A	III
YP_327035	*Natronomonas pharaonis* DSM 2160	III
NP_070466	*Archaeoglobus fulgidus* DSM 4304	III
YP_184703	*Thermococcus kodakarensis* KOD1	III
NP_389242	*Bacillus subtilis* str. 168	IV
ABQ30283	*Acidiphilium cryptum* JF-5	IV
AHY51744	*Bradyrhizobium japonicum* SEMIA 5079	IV

References

Andrews S. A Quality Control Tool for High Throughput Sequence Data [Online]. Available online at: http://www.bioinformatics.babraham.ac.uk/projects/fastqc/ 2010.

Bokulich NA, Kaehler BD, Rideout JR *et al*. Optimizing taxonomic classification of marker-gene amplicon sequences with QIIME 2's q2-feature-classifier plugin. *Microbiome* 2018;**6**:1–17.

Bolyen E, Rideout JR, Dillon MR *et al.* Reproducible, interactive, scalable and extensible microbiome data science using QIIME 2. *Nat Biotechnol* 2019;**37**:852–7.

Brouwers GJ, Corstjens PLAM, De Vrind JPM et al. Stimulation of Mn^{2+} oxidation in leptothrix discophora SS-1 by Cu^{2+} and sequence analysis of the region flanking the gene encoding putative multicopper oxidase *mofA*. *Geomicrobiol J* 2000;**17**:25–33.

Callahan BJ, McMurdie PJ, Rosen MJ et al. DADA2: High-resolution sample inference from Illumina amplicon data. *Nat Methods* 2016;**13**:581–3.

Chen S, Zhou Y, Chen Y et al. Fastp: An ultra-fast all-in-one FASTQ preprocessor. *Bioinformatics* 2018;**34**:i884–90.

De Coster W, D'Hert S, Schultz DT et al. NanoPack: Visualizing and processing long-read sequencing data. *Bioinformatics* 2018;**34**:2666–9.

Ewels PA, Peltzer A, Fillinger S et al. The nf-core framework for community-curated bioinformatics pipelines. *Nat Biotechnol* 2020;**38**:271.

Gurevich A, Saveliev V, Vyahhi N et al. QUAST: Quality assessment tool for genome assemblies. *Bioinformatics* 2013;**29**:1072–5.

He S, Tominski C, Kappler A et al. Metagenomic analyses of the autotrophic Fe(II)-oxidizing, nitrate-reducing enrichment culture KS. *Appl Environ Microbiol* 2016;**82**:2656–68.

Kang DD, Li F, Kirton E et al. MetaBAT 2: An adaptive binning algorithm for robust and efficient genome reconstruction from metagenome assemblies. PeerJ 2019;**2019**:1–13.

Kurtzer GM, Sochat V, Bauer MW. Singularity: Scientific containers for mobility of compute. *PLoS One* 2017;**12**:1–20.

Langmead B, Salzberg SL. Fast gapped-read alignment with Bowtie 2. Nat Methods 2012;**9**:357–9.

Martin M. Cutadapt removes adapter sequences from high-throughput sequencing reads. *EMBnetJournal* 2011;**17**:10–2.

Von Meijenfeldt FAB, Arkhipova K, Cambuy DD et al. Robust taxonomic classification of uncharted microbial sequences and bins with CAT and BAT. *Genome Biol* 2019;**20**:1–14.

Nurk S, Meleshko D, Korobeynikov A et al. MetaSPAdes: A new versatile metagenomic assembler. Genome Res 2017;**27**:824–34.

Pruesse E, Quast C, Knittel K et al. SILVA: A comprehensive online resource for quality checked and aligned ribosomal RNA sequence data compatible with ARB. *Nucleic Acids Res* 2007;**35**:7188–96.

Straub D, Blackwell N, Langarica-Fuentes A et al. Interpretations of Environmental Microbial Community Studies Are Biased by the Selected 16S rRNA (Gene) Amplicon Sequencing Pipeline. *Front Microbiol* 2020;**11**:1–18.

Di Tommaso P, Chatzou M, Floden EW et al. Nextflow enables reproducible computational workflows. *Nat Biotechnol* 2017;**35**:316–9.

Waterhouse RM, Seppey M, Simao FA et al. BUSCO applications from quality assessments to gene prediction and phylogenomics. *Mol Biol Evol* 2018;**35**:543–8.

Zdobnov EM, Tegenfeldt F, Kuznetsov D et al. OrthoDB v9.1: Cataloging evolutionary and functional annotations for animal, fungal, plant, archaeal, bacterial and viral orthologs. *Nucleic Acids Res* 2017;**45**:D744–9.

Contribution to other works

8. ‘*Candidatus* Ferrigenium straubiae’ sp. nov., ‘*Candidatus* Ferrigenium bremense’ sp. nov., ‘*Candidatus* Ferrigenium altingense’ sp. nov., are autotrophic Fe(II)-oxidizing bacteria of the family *Gallionellaceae*

Yu-Ming Huang[a,b], **Natalia Jakus**[a,b], Daniel Straub[a,c], Konstantinos T. Konstantinidis[d], Nia Blackwell[a], Andreas Kappler[b,e] and Sara Kleindienst[a]

[a]Microbial Ecology, Center for Applied Geoscience, University of Tuebingen, Germany

[b]Geomicrobiology, Center for Applied Geoscience, University of Tuebingen, Germany

[c]Quantitative Biology Center (QBiC), University of Tuebingen, Germany

[d]School of Civil and Environmental Engineering, School of Biological Sciences, and Center for Bioinformatics and Computational Genomics, Georgia Institute of Technology, USA

[e]Cluster of Excellence: EXC 2124: Controlling Microbes to Fight Infections, Germany

Abstract

Autotrophic iron(II) [Fe(II)] oxidation coupled to denitrification is recognized as an environmentally important process in many ecosystems. However, the Fe(II)-oxidizing bacteria (FeOB) dominating autotrophic nitrate-reducing Fe(II)-oxidizing enrichment cultures, affiliated with the family *Gallionellaceae*, remain poorly taxonomically defined due to lack of representative isolates. We describe the taxonomic classification of three novel FeOB in the autotrophic nitrate-reducing enrichment cultures KS, BP and AG. Phylogenetic analysis of nearly full-length 16S rRNA gene sequences demonstrated that these three FeOB were most closely affiliated to the genera *Ferrigenium*, *Sideroxydans* and *Gallionella*, with up to 96.5%, 95.4% and 96.2% 16S rRNA gene sequence identities to representative isolates of these genera, respectively. In addition, average amino acid identities (AAI) of the genomes compared to the most closely related genera revealed highest AAI with *Ferrigenium kumadai* An22 (76.35-76.74%), suggesting that the three FeOB are members of this genus. Phylogenetic analysis of conserved functional genes further supported that these FeOB represent three novel species of the genus *Ferrigenium*. Physiological observations of the FeOB revealed unique features, such as the ability to perform partial denitrification coupled to Fe(II) oxidation and carbon fixation. Scanning electron microscopy of the enrichment cultures showed

slightly curved rod-shaped cells, ranging from 0.2-0.7 μm in width and 0.5-2.3 μm in length. Based on the phylogenetic, genomic, and physiological characteristics, we propose that these FeOB represent three novel species, '*Candidatus* Ferrigenium straubiae' sp. nov., '*Candidatus* Ferrigenium bremense' sp. nov. and '*Candidatus* Ferrigenium altingense' sp. nov. that might have unique metabolic features among the genus Ferrigenium.

8.1. Introduction

Ferrous iron [Fe(II)] oxidation can be mediated by specific microorganisms and plays a crucial role in biogeochemical nitrogen, carbon, oxygen and sulfur cycles of natural and engineered ecosystems (Kappler *et al.*, 2021), such as freshwater sediment (Straub *et al.*, 1996; Straub and Buchholz-Cleven, 1998; Straub *et al.*, 2004), marine coastal sediment (Laufer *et al.*, 2015; Laufer *et al.*, 2016) and constructed wetlands (Zhimiao *et al.*, 2020). Fe(II)-oxidizing bacteria (FeOB) are capable of oxidizing both solid and dissolved Fe(II) as electron donors. Studies of FeOB living at circumneutral pH have demonstrated that these organisms flourish within the zone in which ferrous ions are stable, i.e. at microoxic to anoxic conditions at which abiotic Fe(II) oxidation is limited enough for microorganisms to compete (Rentz *et al.*, 2007; Jewell *et al.*, 2016). Most known FeOB are members of *Proteobacteria* and are grouped into three physiological types, depending on the electron acceptor and energy source used for Fe(II) oxidation: light-dependent (photoferrotrophs), O_2-dependent (microaerophiles), and nitrate-reducing (Ehrenberg, 1838; Widdel *et al.*, 1993; Straub *et al.*, 1996).

Many of the common neutrophilic Fe(II)-oxidizing bacteria belong to the family *Gallionellaceae*, which are divided into eight defined genera. Four of these are represented entirely by FeOB: *Ferrigenium, Ferriphaselus, Gallionella* and *Sideroxydans.* These bacteria typically oxidize Fe(II) under microoxic conditions (Hallbeck and Pedersen, 1991; Emerson and Moyer, 1997; Emerson and Merrill Floyd, 2005; Weiss *et al.*, 2007; Krepski *et al.*, 2012; Emerson *et al.*, 2013; Kato *et al.*, 2013; Kato *et al.*, 2015; Kadnikov *et al.*, 2016; Khalifa *et al.*, 2018) and a few of them, unclassified *Gallionellaceae* spp., were suggested to couple Fe(II) oxidation to partial denitrification under anoxic conditions (Straub *et al.*, 1996; He *et al.*, 2016; Jewell *et al.*, 2016; Huang *et al.*, 2021a; Huang *et al.*, 2021b; Jakus *et al.*, 2021). Additionally, some of the FeOB in the *Gallionellaceae* family were reported to perform carbon fixation (Hallbeck and Pedersen, 1991; Emerson and Moyer, 1997; Emerson and Merrill Floyd, 2005; Weiss *et al.*, 2007; Krepski *et al.*, 2012; Emerson *et al.*, 2013; Kato *et al.*, 2013; Kato *et al.*, 2015; Jewell *et al.*, 2016; Kadnikov *et al.*, 2016; Khalifa *et al.*, 2018), as they are very often inhabiting C-depleted environments such as aquifers (Jewell *et al.*, 2016), geysers and high-CO_2 subsurface wetland soils (Emerson *et al.*, 2016), inactive seafloor hydrothermal sulfide chimneys (Li *et al.*, 2017), as well as mine water discharges (Fabisch *et al.*, 2016). Despite the genetic potential of these bacteria and the broad variety of habitats that members of the family *Gallionellaceae* occupy, there is no reported isolate of neutrophilic autotrophic nitrate-reducing Fe(II)-oxidizing (NRFeOx) bacteria. However, members of the family *Gallionellaceae* were found to dominate microbial communities of known neutrophilic autotrophic NRFeOx enrichment cultures (Straub *et al.*, 1996; Huang *et al.*, 2021b; Jakus *et al.*, 2021).

So far there are only three published examples of stable autotrophic NRFeOx enrichment cultures. Two of the cultures were obtained from freshwater sediments in Bremen, northern Germany (cultures KS and BP) (Straub *et al.*, 1996; Huang *et al.*, 2021b), and one was obtained from an anoxic groundwater monitoring well in Altingen, southern Germany (culture AG) (Jakus *et al.*, 2021). Recent metagenomic analysis revealed that all of these unclassified *Gallionellaceae* spp. in the three enrichment cultures share many common features. They possess the genes encoding putative Fe(II) oxidases such as Cyc2 and/or MtoAB, and genes involved in denitrification such as nitrate reductase (*narGHI*), nitrite reductase (*nirK/S*) and/or nitric oxide reductase (*norBC*) (He *et al.*, 2016; Huang *et al.*, 2021a; Huang *et al.*, 2021b; Jakus *et al.*, (under review; and provided to the reviewers with this submission).). The bacteria were also found to possess *rbcL*, a key gene for carbon dioxide fixation during the Calvin–Benson–Bassham (CBB) cycle (He *et al.*, 2016; Tominski *et al.*, 2018a; Huang *et al.*, 2021a; Huang *et al.*, 2021b; Jakus *et al.*, (under review; and provided to the reviewers with this submission).). Thus, they likely have the ability to perform autotrophic Fe(II) oxidation coupled to partial denitrification. Based on nearly full-length 16S rRNA gene sequence (~1460 bp) analysis, most closely related isolated species of the dominating *Gallionellaceae* spp. present in these cultures are *Ferrigenium kumadai* An22, *Sideroxydans lithotrophicus* ES-1 and *Gallionella capsiferriformans* ES-2. Despite elaborate cultivation attempts, these three FeOB *Gallionellaceae* spp. have so far not been isolated (He *et al.*, 2016; Tominski *et al.*, 2018a; Huang *et al.*, 2021b; Jakus *et al.*, 2021). Furthermore, the exact phylogenetic placement and taxonomic description for these FeOB in the *Gallionellaceae* family remains unresolved.

An increasing number of available genomes derived from metagenomics studies of so far uncultured members of the family *Gallionellaceae*, sharing the potential of coupling Fe(II) oxidation to partial denitrification, shows the importance of classifying these new taxa of FeOB (Jewell *et al.*, 2016; Kadnikov *et al.*, 2016; Bethencourt *et al.*, 2020). In addition, the key FeOB of the only stable NRFeOx cultures that exist to date (i.e. cultures KS, BP and AG) and that are currently frequently used as model systems to study autotrophic nitrate reduction coupled to Fe(II) oxidation remain to be classified. Moreover, the advancement of methods in (meta)genomics complement traditional approaches and promote the assessment of the existing taxonomic system (Konstantinidis and Tiedje, 2007; Murray *et al.*, 2020). For example, a widely applied approach is to use the category of '*Candidatus*' to propose putative taxa (Stackebrandt *et al.*, 2002). These yet-to-be isolated microorganisms do not meet all requirements of the International Code of Nomenclature of Prokaryotes (2019); however, there is sufficient evidence to justify their classification through (meta)genomic data (Murray and Stackebrandt, 1995; Konstantinidis and Rosselló-Móra, 2015; Konstantinidis *et al.*, 2017; 2019; Murray *et al.*, 2020). Here, we describe phylogenetic, genomic, and phenotypic analyses to suggest the designation of the three novel FeOB species within the family *Gallionellaceae*.

8.2. Materials and methods

8.2.1. Cultivation and isolation strategies

Culture KS, named after Kristina Straub who reported the first study on this culture (Straub *et al.*, 1996) (dominated by '*Ca.* Ferrigenium straubiae' strain KS) originated from a freshwater ditch in Bremen, Germany. Since then, culture KS has been transferred for more than 20 years under autotrophic conditions with 1-10% (v/v) inoculum (He *et al.*, 2016; Tominski *et al.*, 2018a; Huang *et al.*, 2021a). Several cultivation and isolation techniques have been used, e.g. cultivation under microoxic conditions in gradient tubes and zero-valent iron (ZVI) plates (Tominski *et al.*, 2018a), or growth with different substrates under anoxic conditions in serum bottles, such as $FeCl_2$, Fe(II)-EDTA, and $FeSO_4$ as the electron donor with nitrate as the electron acceptor (Straub *et al.*, 1996; Blöthe and Roden, 2009; Tominski *et al.*, 2018a).

Culture BP, named after Bremen Pond, (dominated by '*Ca.* Ferrigenium bremense' strain BP) originated from a freshwater pond in the backyard of the Max Planck Institute for Marine Microbiology, Bremen, Germany in 2015 (Huang *et al.*, 2021b). Since then, culture BP has been transferred for more than 2 years (>20 times/year since 2018) under autotrophic conditions with 4-10% (v/v) inoculum. Both culture KS and BP were stored and transferred continuously in 25 mL mineral medium (Hegler *et al.*, 2008; Blöthe and Roden, 2009), pH 6.9-7.2, with 10 mM $FeCl_2$ and 4 mM $NaNO_3$ in 58 mL serum bottles and incubated in the dark at 28°C.

Culture AG, named after Altingen Groundwater, (dominated by '*Ca.* Ferrigenium altingense' strain AG) originated from an anoxic groundwater monitoring well in Altingen, southern Germany (Jakus *et al.*, 2021). Since then, culture AG has been transferred for more than 3 years (>20 times/year since 2018) under autotrophic conditions with 2 mM $FeCl_2$ and 2 mM $NaNO_3$ in 58 mL serum bottles containing 25 mL of medium and with 10% (v/v) inoculum (Jakus *et al.*, 2021).

8.2.2. PacBio long-read 16S rRNA gene amplicon sequencing

DNA extraction for culture KS, culture BP and culture AG was reported previously (Huang *et al.*, 2021b; Jakus *et al.*, 2021). PacBio Sequel SMRT long-read amplicon sequencing was performed at the Helmholtz Zentrum München, Germany. DNA amplification was conducted twice using two rounds of PCR with primers universal for bacterial 16S rRNA genes, tailed with PacBio universal sequencing adapters (universal tags) and 5' amino modifiers (27F gcagtcgaacatgtagctgactcaggtcacAGRGTTYGATYMTGGCTCAG, 1492R tggatcacttgtgcaagcatcacatcgtagRGYTACCTTGTTACGACTT) (Biomers.net, Ulm, Germany) to amplify the nearly full-length 16S rRNA genes from the genomic DNA extracted of all three cultures, respectively (Huang *et al.*, 2021b; Jakus *et al.*, 2021). The PCR amplification protocol was described in detail previously (Huang *et al.*, 2021b; Jakus *et al.*, 2021). For the SMRTbell library preparation (Franzen *et al.*, 2015), the SMRTbell Template Prep Kit (PacBio biosciences, California, USA) was applied according to the user's manual instructions.

Subsequently, 11,688 circular consensus sequencing reads were analyzed with DADA2 v1.10.0 (Callahan *et al.*, 2016; Callahan *et al.*, 2019) in R v3.5.1 (Team, 2018) by sequentially orienting reads and removing primers, filtering (no ambiguous nucleotides and maximum 2 expected errors) and trimming (1000 bp to 1600 bp read length; leading to 7,475 sequences), dereplicating sequences (4,138 unique sequences), learning error rates, removing chimera de novo and finally assigning taxonomy to the detected sequences based on SILVA v132 (Callahan, 2018). Lastly, 8 ASVs with 5,543 total counts were obtained.

8.2.3. Phylogenetic tree construction

The evolutionary history was inferred by using the Maximum Likelihood method and the Tamura-Nei model (Tamura and Nei, 1993). This analysis involved 14 nearly full-length 16S rRNA gene nucleotide sequences and 9 concatenated house-keeping, protein-coding, amino acid gene sequences. There were a total of 1622 and 4529 positions in the final dataset, respectively. The tree with the highest log likelihood was selected with 1000 bootstraps of nucleotide and amino acid sequences. The percentage of trees in which the associated taxa clustered together was indicated next to the branches. Initial trees for the heuristic search were obtained automatically by applying Neighbor-Join and BioNJ algorithms to a matrix of pairwise distances estimated using the Tamura-Nei model, and then selecting the topology with superior log likelihood value. The tree was drawn to scale, with branch lengths measured in the number of substitutions per site. Evolutionary analyses were conducted in MEGA X (Kumar *et al.*, 2018). The house-keeping genes, i.e. RNA polymerase α subunit (*rpoA*), DNA gyrase α subunit (*gyrA*), protein translocase subunit (*secA*), isoleucyl-tRNA synthetase (*ileS*), rho termination factor (*rho*) and translation initiation factor IF-2 (*infB*), were selected via the gene sequence availability of the top three closest related isolated genomes and other physiological related species (i.e. FeOB of the family *Gallionellaceae* and NRFeOx bacteria), to generate a concatenated maximum likelihood phylogenetic tree (Holmes *et al.*, 2004; Emerson *et al.*, 2013; Glaeser and Kämpfer, 2015; Rocha *et al.*, 2015).

8.2.4. Average nucleotide identity (ANI) and Average amino acid identity (AAI)

The average nucleotide identity (ANI) and alignment fraction (AF) was analyzed via the online tool IMG/MER Pairwise ANI (https://img.jgi.doe.gov/cgi-bin/mer/main.cgi?section=ANI&page=pairwise) (Varghese *et al.*, 2015; Chen *et al.*, 2017; Chen *et al.*, 2019). Average amino acid identity (AAI) was conducted via the online tool AAI calculator, developed by the Environmental Microbial Genomics Laboratory (enve-omics lab) at the Georgia Institute of Technology (Kostas lab) (http://enve-omics.ce.gatech.edu/) (Rodriguez-R and Konstantinidis, 2016).

8.2.5. Metagenome assembly genome (MAGs) analysis

Three metagenome-assembled genomes (MAGs) of strain KS, strain BP and strain AG were obtained from the Joint Genome Institute's Integrated Microbial Genome and Microbiome Expert Review

(IMG/MER) database (https://img.jgi.doe.gov/; (Chen *et al.*, 2019)). FeGenie (Garber *et al.*, 2020) was used to search for potential Fe(II) oxidation genes, e.g. *cyc2, mtoAB, mofA* (He *et al.*, 2017), and the IMG (Chen *et al.*, 2019) and the National Center for Biotechnology Information (NCBI) (https://www.ncbi.nlm.nih.gov/) (Coordinators, 2016; Schoch *et al.*, 2020) databases were used for obtaining genomes and 16S rRNA gene sequences of closely related taxa. The basic local alignment search tool (BLAST) (Altschul *et al.*, 1990) was used to compare the nearly full-length 16S rRNA gene sequences of the *Gallionellaceae* spp. of cultures KS, BP and AG to those gene sequences of *Gallionellaceae* spp. that were isolated or identified in environmental samples.

8.2.6. Scanning electron microscopy

For scanning electron microscopy (SEM) analysis, samples of the enrichment cultures KS, BP and AG were taken during the mid Fe(II)-oxidizing phase (after 3 days of incubation under autotrophic conditions) and at the end of the Fe(II) oxidation phase (after 6 days of incubation under autotrophic conditions). SEM samples were fixed in 2.5% glutaraldehyde for three hours on ice, by adding 100 µl of a 25% glutaraldehyde solution directly to 900 µl of centrifuged cell suspension in culture medium. After fixation, the samples were centrifuged (1 min, 2348x g) to concentrate the cells and approximately 900 µl of supernatant was removed and replaced by MQ H_2O to wash out the glutaraldehyde from the sample. This procedure was repeated twice. Then, 25 µl of each sample was dropped onto Poly-l-Lysine coated cover glass slides [coated each with 75 µl 0.1% Poly-L-Lysine solution (PLANO, Wetzlar, item number 18026) and air dried over night before usage], placed in a 12-well plate. The plate was then covered with the plate lid and left for 15 minutes for the samples to settle. In the following, the samples were dehydrated by a graded ethanol series (30%, 70%, 95% for 5 min each; 2 x 100% for 30 min). In a final step, the samples were dipped into hexamethyldisilazane (HMDS) in two separated continuous-flow analysis vials in sequence for 30 seconds each and left to dry on filter paper afterwards. The cover glass slides were then fixed onto aluminum stubs with carbon tape (PLANO, Wetzlar, item numbers G301 & G3347) and sputter-coated with ~ 8 nm Pt by use of a BAL-TEC SCD 005. The SEM examination was performed at a Crossbeam 550L FIB-SEM (Zeiss, Oberkochen, Germany) using the InLens or SESI detector at an acceleration voltage of 2 kV and working distances of 4.0–5.3 mm.

8.2.7. Data availability and figure illustration

The heat maps were constructed via R v3.6.1 and its working interface RStudio (https://www.R-project.org/ and http://www.rstudio.com/) (Team, 2019; Team, 2020).

The datasets presented in this study can be found in online repositories: SRR14879643 for culture KS including '*Ca*. Ferrigenium straubiae' strain KS, SRR13504099 for culture BP including '*Ca*. Ferrigenium bremense' strain BP, and SRR10568922 for culture AG including '*Ca*. Ferrigenium altingense' strain AG (Table 1). The three nearly full-length 16S rRNA sequences of strain KS, strain BP and strain AG are provided in the supplementary file. The IMG metagenome IDs for cultures KS, BP and AG are 3300040739, 3300036710, and 3300041015 and the corresponding accession numbers of the MAGs of '*Ca.* Ferrigenium straubiae', '*Ca.* Ferrigenium bremense', and '*Ca.* Ferrigenium

altingense' in IMG are 2878407288, 2831290873, and 2860363623, respectively (Table 1). The NCBI genome acc. nos. for '*Ca.* Ferrigenium straubiae', '*Ca.* Ferrigenium bremense', and '*Ca.* Ferrigenium altingense' are JAHQXD000000000, JAGRPI000000000 and JAHRYS000000000, respectively (Table 1).

8.3. Results and discussion

8.3.1. The novel strains represent dominant taxa of autotrophic NRFeOx enrichment cultures

Based on the near full-length 16S rRNA gene sequences analysis all three *Gallionellaceae* spp., strain KS, strain BP and strain AG, dominated the autotrophic NRFeOx enrichment cultures KS, BP and AG, with ≥95%, ≥71% and ≥50% relative sequence abundance, respectively (He *et al.*, 2016; Huang *et al.*, 2021a; Huang *et al.*, 2021b; Jakus *et al.*, 2021). Highest abundance of these strains was observed during the exponential phase of growth, i.e. during the most active Fe(II) oxidation and nitrate reduction phase. All three NRFeOx cultures were cultivated under anoxic autotrophic conditions with $FeCl_2$ and $NaNO_3$ (Straub *et al.*, 1996; Huang *et al.*, 2021b; Jakus *et al.*, 2021) as electron donor and acceptor (Figure 1), respectively. The average $Fe(II)_{oxidized}/nitrate_{reduced}$ stoichiometric ratio was 4.28 in culture KS, 3.4 in culture BP and 5.0 in culture AG (Tominski *et al.*, 2018a; Huang *et al.*, 2021a; Huang *et al.*, 2021b; Jakus *et al.*, 2021).

Both culture KS and culture BP originate from freshwater sediments collected in Bremen from a ditch (Straub *et al.*, 1996) and a pond (Huang *et al.*, 2021b), respectively, while culture AG was obtained from an aquifer (Jakus *et al.*, 2021). The geochemistry at the habitat of enrichment culture KS's origin was neither stated in the first publication (Straub *et al.*, 1996) nor in subsequent publications. However, since the ditch of culture KS's origin is close by and connected to the pond of culture BP's origin, the geochemistry might be similar. The physiochemical conditions at the area of the sampling site, where culture BP was obtained, were measured in 2017 as follows; temperature: 11.7-11.9°C, pH: 6.0-6.3, oxygen saturation: 8.5-74.3%, conductivity: 32.5-36.8 µS/m, $Fe(II)_{pore\ water}$: 0.324-4.85 µM, $Fe(III)_{pore\ water}$: 2.51-1 µM, nitrate: 0.714 µM, total organic carbon (TOC) in sediment: 0.16-0.45% (wt%), and dissolved organic carbon (DOC) in pond water: 0.6-0.7 mg/L (Sauter, 2018). The physico-chemical parameters of the groundwater accessed via the monitoring well in Altingen were continuously monitored during observation periods (2004-2018) and the average values were calculated as follows; temperature: 12.5±1.6°C, pH: 7.1±0.1, dissolved O_2: 0.1±0.1 mg/L, conductivity: 885.1±75.1 µS/cm, nitrate concentration: 0.02±0.01 mM and DOC: 1.2±0.3 mg/L (Jakus *et al.*, 2021).

Despite the different isolation habitats of the three cultures, all three FeOB unite a unique feature within the family *Gallionellaceae*, i.e. the ability to grow under autotrophic anoxic conditions and perform partial denitrification coupled to Fe(II) oxidation (Straub *et al.*, 1996; Huang *et al.*, 2021b; Jakus *et al.*, 2021). This unique capability differentiates them from all the isolated strains of the family *Gallionellaceae*, which typically perform microaerophilic Fe(II) oxidation using oxygen as

electron acceptor (Kucera and Wolfe, 1957; Straub *et al.*, 1996; Emerson and Moyer, 1997; Krepski *et al.*, 2012; Kato *et al.*, 2014; Khalifa *et al.*, 2018; Huang *et al.*, 2021b; Jakus *et al.*, 2021).

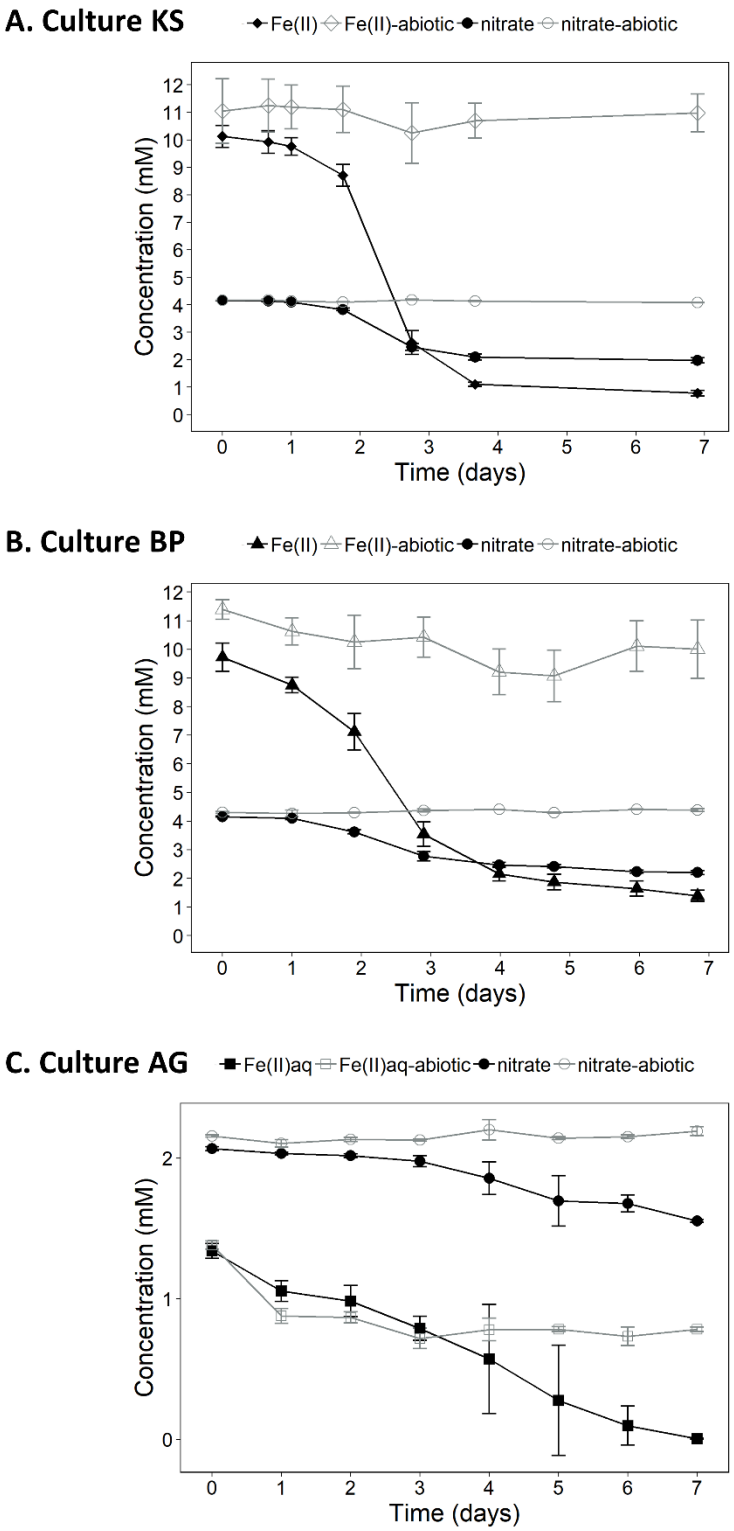

Figure 1. Average Fe(II) and nitrate concentration over time for the enrichment cultures (A) KS, (B) BP and (C) AG. The chemistry data of culture KS and culture AG were replotted from publications by Huang *et al.*, 2021 and Jakus *et al.*, 2021, respectively.

8.3.2. Phylogenetic and genome (MAG) identity analysis of FeOB within the *Gallionellaceae*

In order to classify the three *Gallionellaceae* spp., strain KS, strain BP and strain AG, we performed phylogenetic analysis, using nearly full-length 16S rRNA gene sequences and available MAGs in the family *Gallionellaceae* (Figure 2 and Figure 3). Strain KS, strain BP and strain AG were closely related to each other and formed a novel clade within the phylogenetic tree (Figure 2). The most closely related isolated species was *Ferrigenium kumadai*, which is a microaerophilic Fe(II)-oxidizing bacterium and was cultivated using gradient tubes (Khalifa *et al.*, 2018). *Ferrigenium kumadai* has 96.45%, 96.17% and 96.24% of nearly full-length 16S rRNA gene sequence identity with strain KS, strain BP and strain AG, respectively (Figure 3) (Huang *et al.*, 2021a; Huang *et al.*, 2021b; Jakus *et al.*, 2021). The second most closely related isolated species of strain KS and strain BP was *Sideroxydans lithotrophicus* ES-1, with 95.9% and 95.30% identity of nearly full-length 16S rRNA gene sequences, respectively (Figure 3) (Huang *et al.*, 2021a; Huang *et al.*, 2021b). The second most closely related isolated species of strain AG was *Gallionella capsiferriformans* ES-2, sharing 96.17% of nearly full-length 16S rRNA gene sequence identity (Figure 3) (Jakus *et al.*, 2021). As with *Ferrigenium kumadai*, both *Sideroxydans lithotrophicus* ES-1 and *Gallionella capsiferriformans* ES-2 are microaerophilic Fe(II)-oxidizing bacteria (Emerson and Moyer, 1997) and have been cultivated using gradient tubes. While *Ferrigenium kumadai* An22 originated from rice paddy soil (Khalifa *et al.*, 2018; Watanabe *et al.*, 2021), *Sideroxydans lithotrophicus* ES-1 and *Gallionella capsiferriformans* ES-2 were both from a groundwater-fed iron seep (Emerson and Moyer, 1997). The three *Gallionellaceae* spp., strain KS, strain BP and strain AG, revealed 16S rRNA gene similarities of 97.06-97.88% among each other indicating that they represent distinct species within the same genus (Figure 3).

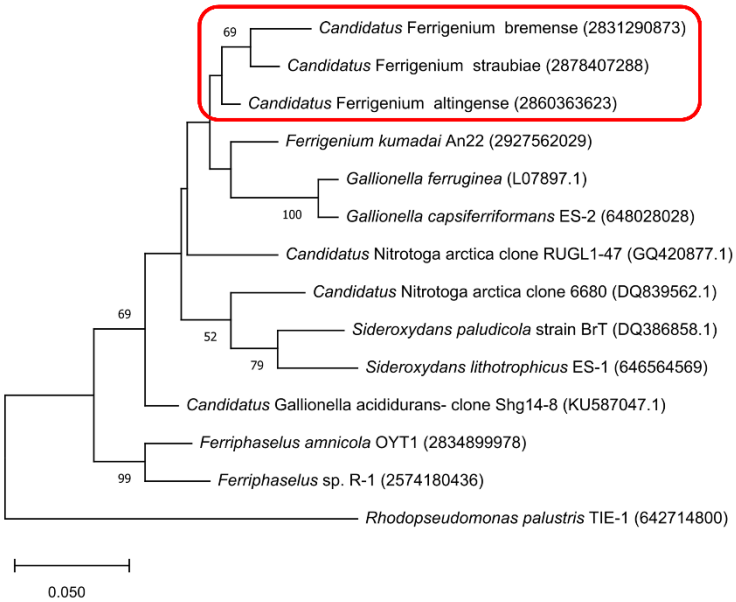

Figure 2. Phylogenetic tree of seven isolated Gallionellaceae spp. and six metagenome-assembled genomes (*Candidatus* species), using available full or nearly full-length 16S rRNA gene sequences and calculated on 1000 replicates using the Maximum Likelihood method. The red box highlights the species classified in this study. The scale bar represents branch lengths measured by the number of substitutions per site. The numbers in brackets show the identifier of each gene in the IMG or NCBI databases.

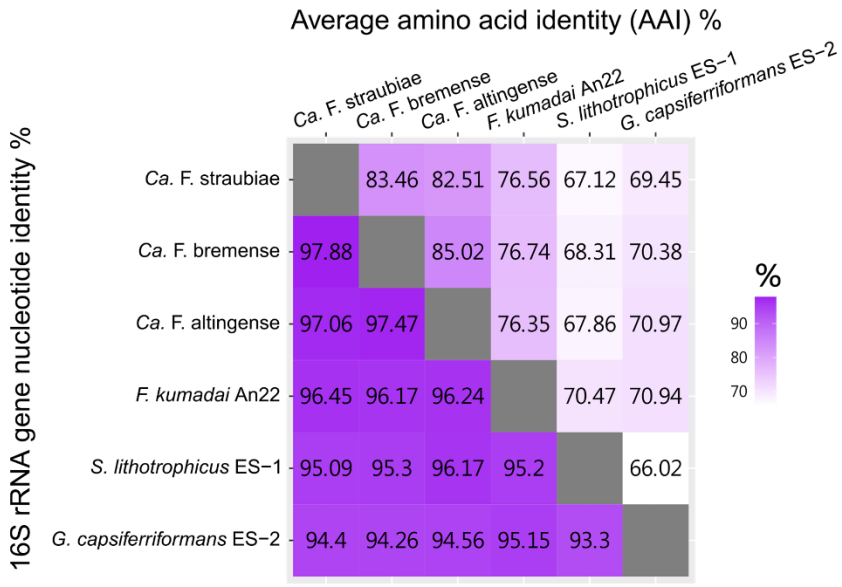

Figure 3. Nearly full-length 16S rRNA gene identity, average amino acid identity (AAI) of strains from '*Candidatus* Ferrigenium straubiae' (strain KS) sp. nov., '*Candidatus* Ferrigenium bremense' (strain BP) sp. nov. and '*Candidatus* Ferrigenium altingense' (strain AG) sp. nov. compared to their top three closely related isolated strains affiliating with the genera *Ferrigenium*, *Sideroxydans* and *Gallionella*. Recommended thresholds: nearly full-length 16S rRNA gene sequence identity: genus >95%, species >98.6%; AAI: genus 65–95%, species ≥95%.

In addition, using metagenome binning methods, nearly complete and high-quality genomes (MAGs) were obtained for the *Gallionellaceae* spp. strain KS, strain BP and strain AG, with a completeness of 99.3%, 93.2% and 89.9%, respectively (Table 1) (Huang *et al.*, 2021a; Huang *et al.*, 2021b; Jakus *et al.*, 2021). Further, we compared the AAI and ANI of all five isolated *Gallionellaceae* spp. to the MAGs of strain KS, strain BP and strain AG. Based on the AAI and ANI results, the closest related, isolated strains affiliated with the genera *Ferrigenium*, *Sideroxydans* and *Gallionella* (Figure 3, Figure S1). All three of the novel *Gallionellaceae* spp., i.e. strain KS, strain BP and strain AG, displayed AAI values in the range between 76.35% to 76.74% for *Ferrigenium kumadai* as well as 67.12% to 70.97% for *Sideroxydans lithotrophicus* ES-1 and *Gallionella capsiferriformans* ES-2 (Figure 3). The AAI alignment fraction coverages of the three novel *Gallionellaceae* spp. and closest related strains were all higher than 48% (Table S1). As the AAI of the three novel *Gallionellaceae* spp. compared to *Ferrigenium kumadai* were higher in comparison to *Sideroxydans lithotrophicus* ES-1 and *Gallionella capsiferriformans* ES-2, this indicates that all three strains (i.e. strain KS, strain BP and strain AG) belong to the same genus (AAI threshold >65%), postulated as genus *Ferrigenium*, but represent different species (AAI threshold <95%) (Rodriguez-R and Konstantinidis, 2016). Notably, these results are consistent with the 16S rRNA gene-based results mentioned above. Moreover, these novel species, i.e. strain KS, strain BP and strain AG, have AAI values in the range of 82.51% to 85.02% compared to each other (Figure 3), suggesting that they are more closely related to each other than to any described isolate. This result suggests that they should be designated as distinct species of the same genus. As for ANI, a threshold of ANI ≥ 96.5% (alignment fraction: AF ≥ 60%) was proposed for the same species (Varghese *et al.*, 2015; Barco *et al.*, 2020). Our results showed that the ANI values between the three novel *Gallionellaceae* spp. and the most closely related isolate, *Ferrigenium kumadai*, range between 81.12% to 81.38% (Figure S1), while the ANI to *Sideroxydans*

lithotrophicus ES-1 and *Gallionella capsiferriformans* ES-2 are in the range of 75.05% to 79.47% (Figure S1).

For more evidence of the genealogical position, the amino acid sequences of house-keeping genes, which encode the RNA polymerase α subunit (*rpoA*), DNA gyrase α subunit (*gyrA*), protein translocase subunit (*secA*), isoleucyl-tRNA synthetase (*ileS*), rho termination factor (*rho*), and translation initiation factor IF-2 (*infB*), were selected to generate a concatenated maximum likelihood phylogenetic tree (Figure 4) (Holmes *et al.*, 2004; Emerson *et al.*, 2013; Glaeser and Kämpfer, 2015; Rocha *et al.*, 2015). The phylogenetic analysis of concatenated house-keeping genes indicated that strain KS, strain BP and strain AG were closely affiliated to *Ferrigenium kumadai* An22, and were more distantly related to other isolated members of *Gallionellaceae* genera, a proposed neutrophilic mixotrophic nitrate-reducing FeOB, i.e. *Thiobacillus denitrificans* (Beller *et al.*, 2006) and an acidophilic aerobic FeOB, i.e. *Acidithiobacillus ferrooxidans* (Figure 4) (Valdés *et al.*, 2008).

Taken together the results of nearly full-length 16S rRNA gene identity and phylogeny as well as AAI, ANI and house-keeping gene phylogenetic analyses indicated strain KS, strain BP and strain AG, belong to the same genus, postulated as *Ferrigenium*, but represent different species.

Table 1. Description table of '*Candidatus* Ferrigenium straubiae' sp. nov., '*Candidatus* Ferrigenium bremense' sp. nov. and '*Candidatus* Ferrigenium altingense' sp. nov.

Genus name	***Candidatus* Ferrigenium**	***Candidatus* Ferrigenium**	***Candidatus* Ferrigenium**
Species name	*straubiae*	*bremense*	*altingense*
Genus status	-	-	-
Genus etymology	-	-	-
Type species of the genus	*Ferrigenium kumadai* An22	*Ferrigenium kumadai* An22	*Ferrigenium kumadai* An22
Specific epithet	*straubiae*	*bremense*	*altingense*
Species status	sp. nov.	sp. nov.	sp. nov.
Species etymology	kris.ti'nae. N.L. gen. n. *straubiae*, of Straub, honouring Dr. Kristina Straub who enriched, cultured and studied the culture KS in 1993-1996.	bre.men'se. M.L. neut. adj. *bremense*, the enrichment sample originating from Bremen, Germany.	al.tin.gen'se. N.L. neut. adj. *altingense*, the enrichment sample originating from Altingen, Germany.
Description of the new taxon and diagnostic traits	Found in freshwater habitats. Cells are rod shaped. Fimbriae and flagella were not observed. Cells are 0.8–2.2 µm long and 0.2–0.7 µm wide. *In silico* genome analysis indicated that the species possesses potential Fe(II) oxidation genes: *cyc2, mtoAB, mofABC*; denitrification genes: *narGHIJ, nirK/S*; and the carbon fixation gene: *rbcL*.	Found in freshwater habitats. Cells are rod shaped. Fimbriae and flagella were not observed. Cells are 1.1–2.3 µm long and 0.2–0.6 µm wide. *In silico* genome analysis indicated that the species possesses potential Fe(II) oxidation genes: *cyc2*; denitrification genes: *narGHIJ, nirK/S*; and the carbon fixation gene: *rbcL*.	Found in freshwater habitats. Cells are rod shaped. Fimbriae and flagella were not observed. Cells are 0.5–1.8 µm long and 0.2–0.6 µm wide. *In silico* genome analysis indicated that the species possesses potential Fe(II) oxidation genes: *cyc2, mofAB (distant homologs)*; denitrification genes: *narGHIJ, nirK/S, norBC*; and the carbon fixation gene: *rbcL*.

Country of origin	Germany	Germany	Germany
Region of origin	Bremen, Bremen	Bremen, Bremen	Altingen, Baden-Wuerttemberg
Source of isolation	freshwater sediment	freshwater sediment	aquifer, groundwater monitoring well
Sampling date (dd/mm/yyyy)	1993	25/09/2015	12/09/2017
Latitude (xx°xx′xx″N/S)	-	53°06'36.7"N	48° 33' 47.52"N
Longitude (xx°xx′xx″E/W)	-	8°50'48.6"E	8° 53' 59.28"W
Altitude (meters above sea level)	N/A	N/A	378.5
16S rRNA gene accession nr.	IMG gene ID: 2878408845	Sequence listed in supplementary file	IMG gene ID: 2860363887
IMG Genome ID	2878407288	2831290873	2860363623
NCBI Genome accession number	JAHQXD000000000	JAGRPI000000000	JAHRYS000000000
Genome status	incomplete (MAG) completeness: 99.3%	incomplete (MAG) completeness: 93.2%	incomplete (MAG) completeness: 89.9%
Genome size (bp)	2,659,708	2,446,084	2,180,025
GC mol%	60.13%	58.92%	57.97%
Number of strains in study	1	1	1
Source of isolation of non-type strains	N/A	N/A	N/A
Information related to the Nagoya Protocol	N/A	N/A	N/A
Designation of the Type Strain	strain KS	strain BP	strain AG
Strain Collection Numbers	N/A	N/A	N/A

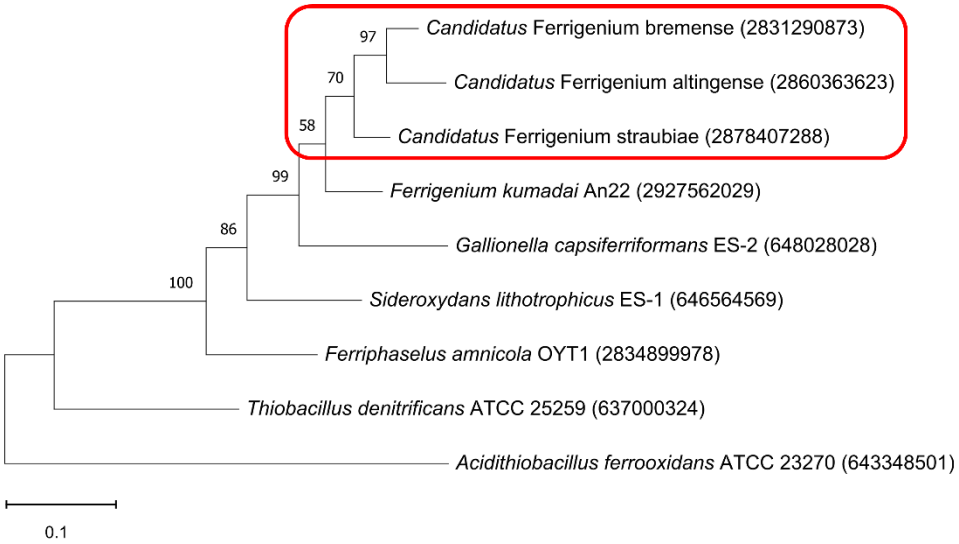

Figure 4. Phylogenetic tree of nine concatenated house-keeping genes amino acid sequences of *rpoA*, *gyrA*, *secA*, *ileS*, *rho* and *infB* of isolated and *Candidatus* members of the *Gallionellaceae* family and other FeOB, calculated on 1000 replicates using the Maximum Likelihood method. The red box highlights the species classified in this study. The scale bar represents branch lengths measured by the number of substitutions per site. The numbers in brackets show the identifier of each gene in IMG.

8.3.3. Putative metabolic and physiological features

The metagenomic results showed that all three *Gallionellaceae* MAGs of strain KS, strain BP and strain AG have at least one putative Fe(II) oxidation gene, which could accept the electrons from the Fe(II) substrate, i.e. *cyc2* and *mofA* for all three MAGs and *mtoA* in the MAG of strain KS (Figure 5) (He *et al.*, 2016; He *et al.*, 2017; Huang *et al.*, 2021b; Jakus *et al.*, (under review; and provided to the reviewers with this submission).). Among these genes, *cyc2*, *mtoA* and *mofA* were detected at transcript level and MofA was detected at protein level in culture KS (Huang *et al.*, 2021a). On the other hand, both transcript and protein of *cyc2* were detected in culture BP (Huang *et al.*, 2021b). To date, a metagenome was constructed and analyzed for culture AG (Jakus *et al.*, (under review; and provided to the reviewers with this submission).), while metatranscriptomic and metaproteomic analysis for culture AG have not yet been done.

As for the electron acceptor, the genes for a partial denitrification pathway detected in MAGs of the strain KS, strain BP and strain AG were different. For strain KS, the genes, transcripts and proteins encoding nitrate reductase (NarGHI) and nitrite reductase (NirK/S) were detected under autotrophic conditions (Figure 5) (Huang *et al.*, 2021a). For strain BP, the genes, transcripts and proteins encoding NirK/S were detected and the genes and transcripts encoding nitric oxide reductase (NorBC) were detected under autotrophic conditions (Figure 5) (Huang *et al.*, 2021b). The genes encoding NarGHI, NirK/S and NorBC were all detected in strain AG (Figure 5) (Jakus *et al.*, (under review; and provided to the reviewers with this submission).). These results indicated that strain KS, strain BP and strain AG probably have the ability to perform only partial denitrification. As previously suggested (Huang *et al.*, 2021a; Huang *et al.*, 2021b; Jakus *et al.*, (under review; and provided to the reviewers with this submission).), they might require other denitrifiers to complete the denitrification pathways.

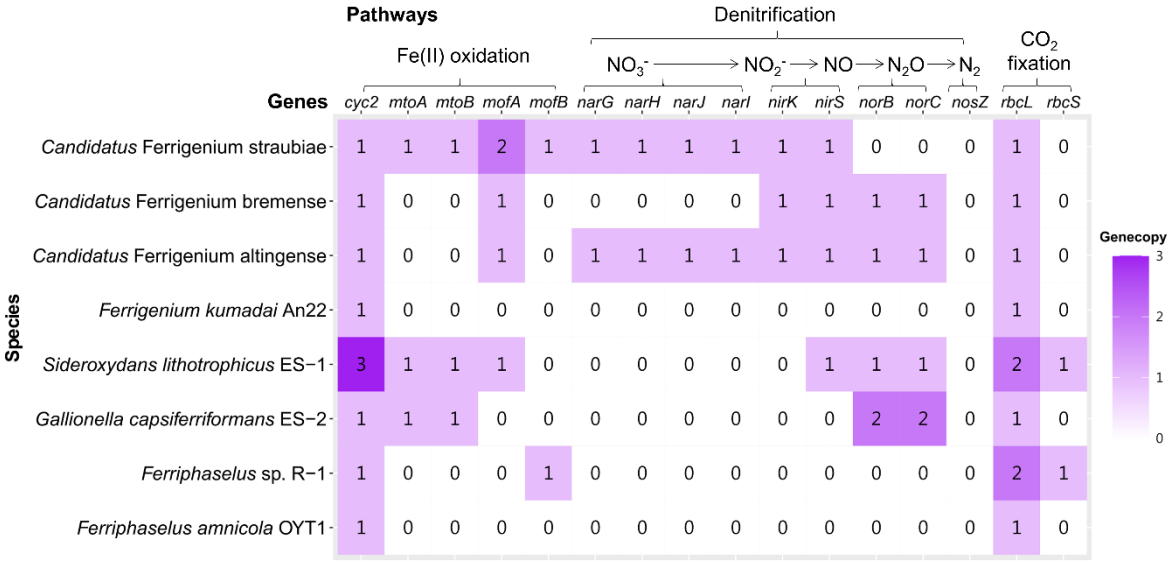

Figure 5. Summary of key gene copy numbers involved in putative Fe(II)-oxidation, denitrification and carbon fixation of '*Ca.* Ferrigenium straubiae', '*Ca.* Ferrigenium bremense' and '*Ca.* Ferrigenium altingense', *Ferrigenium kumadai* An22, *Sideroxydans lithotrophicus* ES-1, *Gallionella capsiferriformans* ES-2, *Ferriphaselus* sp. R-1, and *Ferriphaselus amnicola* OYT1.

An alternative electron accepting pathway was speculated to be oxidative phosphorylation (e.g., via respiratory chain complexes I-V) (Mitchell, 1961; Kalckar, 1991; He *et al.*, 2016). The genetic potential for energy generation via respiratory chain complexes I-V were detected in strain KS, strain BP and strain AG (He *et al.*, 2016; Huang *et al.*, 2021b; Jakus *et al.*, (under review; and provided to the reviewers with this submission).). Interestingly, the detection of homologous genes encoding the cbb_3- and aa_3- type cytochrome *c* oxidases of complex IV indicates that strain KS, strain BP and strain AG could have the ability to respire oxygen (Huang *et al.*, 2021a; Huang *et al.*, 2021b; Jakus *et al.*, (under review; and provided to the reviewers with this submission).). Some microoxic growth conditions were tested for culture KS (Tominski *et al.*, 2018a), as well as culture AG (Jakus *et al.*, 2021), i.e. in gradient tubes or zero valent iron plates, but a stable growth was not yet observed.

Moreover, due to the detection of the essential gene of carbon fixation, i.e. the large subunit ribulose-1,5-bisphosphate carboxylase-oxygenase gene (*rbcL*), it was proposed that strain KS, strain BP and strain AG have the ability to fix carbon to grow under autotrophic conditions (He *et al.*, 2016; Tominski *et al.*, 2018b; Huang *et al.*, 2021a; Huang *et al.*, 2021b; Jakus *et al.*, (under review; and provided to the reviewers with this submission).). The dominance of strain KS, strain BP and strain AG in the different NRFeOx enrichment cultures, i.e. culture KS, culture BP and culture AG, respectively, was likely caused by the ability to fix carbon by these three strains. In culture KS, carbon fixation by strain KS was additionally reported using nanoscale secondary ion mass spectrometry (NanoSIMS) to monitor the incorporation of ^{13}C-labeled bicarbonate (Tominski *et al.*, 2018b) and the transcript and protein encoding the essential carbon fixation enzyme, RbcL, were detected for strain KS under autotrophic conditions (Huang *et al.*, 2021a). For strain BP, the transcript of *rbcL* was also detected (Huang *et al.*, 2021b), while there are currently no transcript and protein data available for culture AG .

8.3.4. Morphology of the three *Gallionellaceae* spp.

In this study, we analyzed the cell morphology by scanning electron microscopy (SEM) (Figure 6). It should be noted, however, that the timepoint for SEM sampling was determined based on relative nearly full-length 16S rRNA gene sequence abundance to capture the most dominant strains (i.e. Fe(II) oxidizers); the relative abundance of strain KS, strain BP, and strain AG in the three cultures KS, BP and AG were ≥95%, ≥71% and ≥50% (Huang *et al.*, 2021b; Jakus *et al.*, 2021). For strain KS, the cell sizes (averaged for 17 cells) ranged from 0.8-2.2 µm in length and 0.2-0.7 µm in width (Table 2). For strain BP, the cell sizes (averaged for 27 cells) ranged from 1.1-2.3 µm in length and 0.2-0.6 µm in width (Table 2). As for strain AG, the cell sizes (averaged for 15 cells) ranged from 0.5-1.8 µm in length and 0.2-0.6 µm in width (Table 2). In the SEM images of the three enrichment cultures, the observed cells were either rod shaped or they revealed a slightly curved rod shape (Figure 6). Given the fact that strain KS, strain BP and strain AG dominate the enrichment cultures KS, BP and AG, respectively, we estimated the morphology of strain KS, strain BP and strain AG based on the dominating morphological type of the culture, i.e. the rod or slightly curved rod shaped cells. For culture KS, there were in addition several different imaging analyses performed in previous studies: 4',6-diamidino-2-phenylindole (DAPI) staining (Tominski *et al.*, 2018a; Tominski *et al.*, 2018b) and fluorescence *in-situ* hybridization (FISH) in combination with fluorescence microscopy, and helium ion microscopy (HIM) (Nordhoff *et al.*, 2017). The results for cell sizes and cell morphology of these imaging analyses corresponded to the SEM observations for strain KS in this study. Most of the cells we observed in all three cultures (i.e. 16 out of 17 cells analyzed for culture KS, 25 out of 27 cells for culture BP and 15 out of 15 cells for culture AG) were closely associated with minerals and in a few cases, cells even seemed to be partly or completely encrusted in Fe minerals, although it remains unknown whether these cells were still alive or whether such encrustation only happened with dead or inactive cells. Additionally, although the genes for flagellar assembly were detected in the three MAGs of strain KS, strain BP and strain AG, the fimbriae and flagella were not observed under SEM. However, during the chemical preparation, the fimbriae and flagella might have been destroyed and, thus, we cannot rule out the existence of fimbriae and flagella.

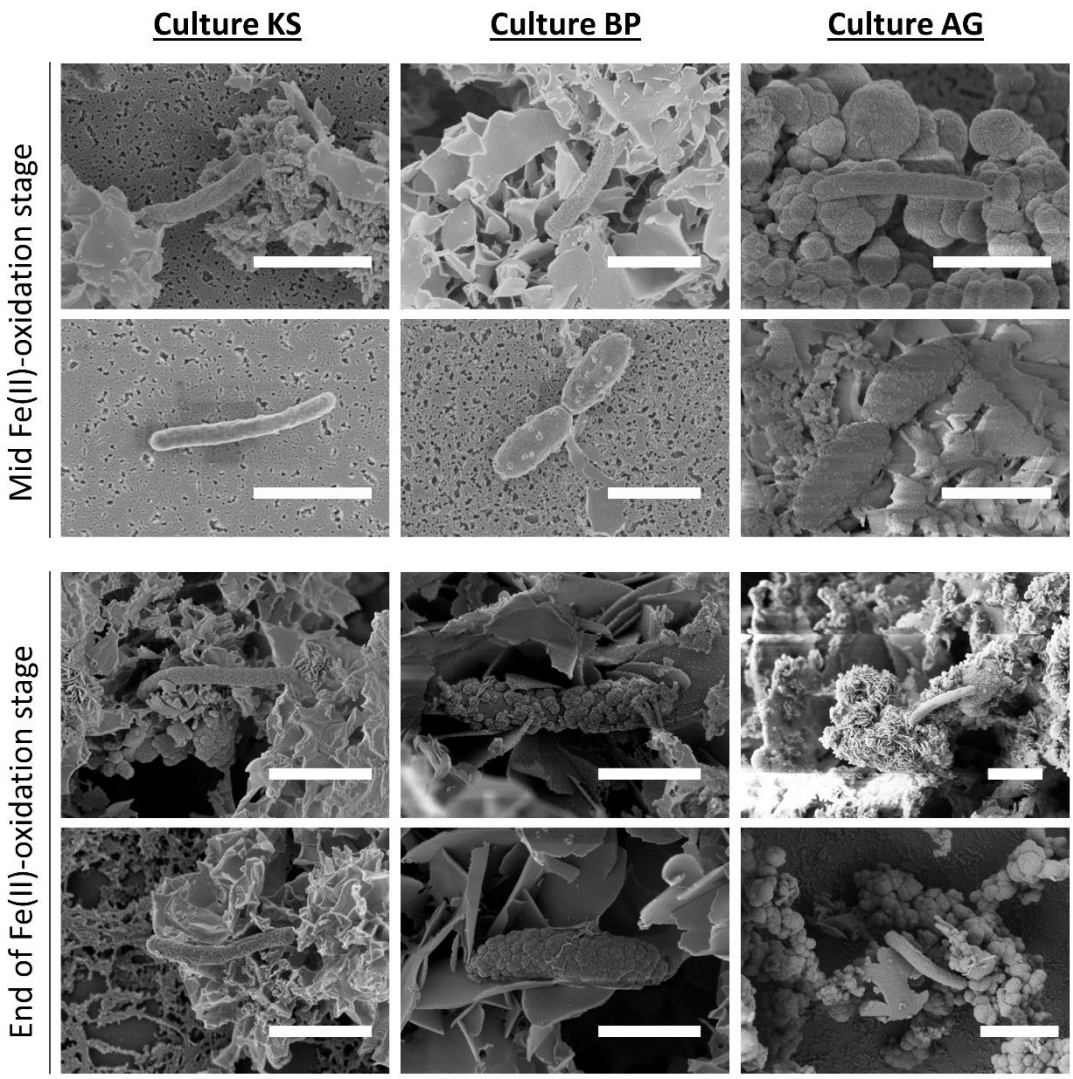

Figure 6. Scanning electron microscopy (SEM) pictures of culture KS, culture BP and culture AG during the mid Fe(II)-oxidation stage (exponential growth phase) and at the end of the Fe(II)-oxidation stage (lag phase). The scale bars represent 1 µm. Cells were slightly curved rod shaped and partly encrusted with putative Fe(III) minerals in cultures BP and AG (and to a minor extent in culture KS; not shown), especially at end of the Fe(II)-oxidation stage.

Table 2. Phenotypic and genotypic information of '*Candidatus* Ferrigenium straubiae' sp. nov., '*Candidatus* Ferrigenium bremense' sp. nov. and '*Candidatus* Ferrigenium altingense' sp. nov. compared with closely related strains of different genera in the family *Gallionellaceae.*

Characteristics	***Candidatus* Ferrigenium straubiae**	***Candidatus* Ferrigenium bremense**	***Candidatus* Ferrigenium altingense**	***Ferrigenium kumadai* An22**	***Sideroxydans lithotrophicus* ES-1**	***Gallionella capsiferrifor mans* ES-2**
Isolation source	Sediment	Sediment	Aquifer	Rice paddy soil	Groundwater	Groundwate r
Geographic location	Bremen, Germany	Bremen, Germany	Altingen, Germany	Anjo, Japan	Michigan, USA	Michigan, USA
Cell morphology	curved rod	curved rod	curved rod	curved rod	helical rod	curved rod
Cell size (LxW, in μm)	0.8–2.2 x 0.2–0.7	1.1–2.3 x 0.2–0.6	0.5–1.8 x 0.2–0.6	0.9–2.0 x 0.2–0.4	0.3 diameter	0.7 diameter
Stalk formation	N/O	N/O	N/O	-	-	-
Motile/Flagella	N/O	N/O	N/O	+	+	+
Doubling time (h)	9.4±2.9	46.11#	34.98#	6.2	8	12.5
highest relative abundance in the culture	98%	86%	68%	N/A	N/A	N/A
Genome size (bp)	2,659,708	2,446,084	2,180,025	2,572,603	3,003,656	3,162,471
G + C content (mol %)	60.13	58.92	57.97	61.4	57.5	52.8
16S rRNA gene copies	2	1	1	2	2	3
Fe(II) oxidation	+	+	+	+	+	+
Carbon fixation	+	+	+	+	+	+
Growth temperature	28°C*	28°C*	25°C*	12 - 37°C	10 - 35°C	4 - 30°C
Growth pH	6.8-7.2*	6.9-7.2*	6.0-7.0*	5.2–6.8	5.5-7.0	5.5-7.0
Reference	(Straub *et al.*, 1996; He *et al.*, 2016; Tominski *et al.*, 2018b; Huang *et al.*, 2021a)	(Huang *et al.*, 2021b)	(Jakus *et al.*, 2021; Jakus *et al.*, submitted)	(Khalifa *et al.*, 2018; Watanabe *et al.*, 2021)	(Emerson *et al.*, 2013)	(Emerson *et al.*, 2013)

N/A: not applicable; N/O: not observed
the doubling time of '*Ca.* Ferrigenium bremense' and '*Ca.* Ferrigenium altingense' was estimated by multiplying total cell counts of the enrichment culture obtained by flow cytometry with relative abundance data determined by V4 region 16S rRNA gene amplicon sequencing, respectively, as reported previously (Huang *et al.*, 2021b; Jakus *et al.*, 2021).
* the temperature and pH of the whole enrichment culture KS, BP and AG was measured.

8.3.5. Ecological relevance

To estimate the environmental occurrence, i.e. potential niches and preferred habitats, of the three FeOB and closely related organisms that affiliate with the same species (and the same strain), nearly full-length 16S rRNA gene sequences that showed a similarity >98.6% (and >99.5%) compared to strain KS, strain BP or strain AG were identified using the BLAST function and the NCBI database (Table S2). For strain KS, the highest similarity (nearly full-length 16S rRNA gene identity 99.52-99.93%) was found for sequences originating from a parallel culture to culture KS cultivated at the University of Wisconsin - Madison and identified as uncultured betaproteobacterium sp. (acc. nos. FN430662.1, FN430666.1, FN430669.1, FN430668.1, FN430670.1, FN430663.1 and FN430659.1; clones F25F63, F29F67, F32F70, F31F69, F33F71, F26F64 and F21F59) (Blöthe and Roden, 2009). In addition, an uncultured bacterial sequence from an iron-rich microbial mat revealed 99.43% nearly full-length 16S rRNA gene identity (acc. no. LN870688.1; clone Hoffnungsstollen_#4-1A_D09) (Zeitvogel et al., unpublished). For strain BP, the most closely related sequence (nearly full-length 16S rRNA gene identity of 99.26%) was identified as an uncultured bacterium from a polycyclic aromatic hydrocarbon (PAH) degrading bacterial community of a PAH-contaminated soil (acc. no. FQ659636.1; clone I1AB101) (Martin *et al.*, 2012). For strain AG, closely related sequences (nearly full-length 16S rRNA gene identity of 100% and 99.93%) were retrieved from a stratified freshwater lake, Lake Mizugaki, in Japan (acc. nos. AB754138.1 and AB754154.1; clones rS43m_43 and rS43m_63) (Kojima *et al.*, 2014). Additional closely related sequences were identified as an uncultured *Gallionella* sp. (99.93% nearly full-length 16S rRNA gene sequence identity; acc. no. AM167950.1; clone BB03) from spring water consisting mostly of groundwater (Wagner *et al.*, 2007), an uncultured betaproteobacterium sp. (99.80%, 99.53% and 99.53% nearly full-length 16S rRNA gene sequence identity; acc. nos. JQ278897.1, JQ278948.1 and JQ279049.1; clones hmx-114, sf-34 and sz-131) from groundwater (Guan *et al.*, 2013), and an uncultured bacterium sp. (99.67% nearly full-length 16S rRNA gene sequence identity; acc. no. AY662038.1; clone 015C-C11) from nitric acid-bearing uranium waste contaminated groundwater (Fields *et al.*, 2005). The uncultured bacterial sequence from the iron-rich microbial mat (acc. no. LN870688.1; clone Hoffnungsstollen_#4-1A_D09) had 99.79% nearly full-length 16S rRNA gene identity compared to strain AG (Zeitvogel et al., unpublished). In summary, closely related sequences of strain KS, strain BP and strain AG were mainly identified in freshwater ecosystems, e.g. groundwater, pond or ditch sediments, as well as aquifer and wetland soils that probably represent preferred habitats of the three novel FeOB.

8.4. Conclusion

Overall, from the ecological traits, unique metabolic and physiological features, phylogenetic and MAG identity analyses comparing to closest related isolated species (Table 2), we propose the name of these three FeOB species as '*Candidatus* Ferrigenium straubiae' sp. nov., '*Candidatus* Ferrigenium bremense' sp. nov. and '*Candidatus* Ferrigenium altingense' sp. nov., named after 'Kristina Straub' who originally isolated culture KS, 'Bremen Pond' the location of culture BP's isolation and 'Altingen Groundwater' the location of culture AG's isolation. The detailed description of the

proposed species is shown in table 1 and the phenotypic and genotypic information compared to closely related isolates of the proposed species are described in table 2.

8.5. Funding

This work was supported by the German Research Foundation (Deutsche Forschungsgemeinschaft, DFG)-funded research training group [grant number RTG 1708] “Molecular principles of bacterial survival strategies”. Natalia Jakus was funded by the Collaborative Research Center 1253 CAMPOS (Project 5: Fractured Aquifers) from the DFG [grant number SFB 1253/1 2017]. Daniel Straub was funded by the Institutional Strategy of the University of Tuebingen (DFG, ZUK63). Nia Blackwell was funded by the Collaborative Research Center 1253 CAMPOS (project 5: fractured aquifers) from the DFG [grant number SFB 1253/1 2017]. Andreas Kappler is funded by the cluster of Excellence: EXC 2124: Controlling Microbes to Fight Infections, Tübingen, Germany [project ID 390838134]. Sara Kleindienst is funded by an Emmy-Noether fellowship from the DFG [grant number 326028733].

8.6. Acknowledgements

The authors gratefully acknowledge the infrastructural support by the DFG under Germany’s Excellence Strategy, cluster of Excellence EXC2124, project ID 390838134 and the Tübingen Structural Microscopy Core Facility (funded by the Excellence Strategy of the German Federal and State Governments) for their support & assistance in this work. We also thank the German Research Foundation DFG (INST 37/1027-1 FUGG) for financial support provided for the acquisition of the cryogenic focused ion beam scanning electron microscope. We thank Tillmann Lueders and Zhe Wang for PacBio library preparation and sequencing as well as Bernhard Schink for the recommendation of the nomenclature.

References

(2019) International code of nomenclature of prokaryotes. *Int J Syst Evol Microbiol* **69**: S1-S111.

Altschul, S.F., Gish, W., Miller, W., Myers, E.W., and Lipman, D.J. (1990) Basic local alignment search tool. *J Mol Biol* **215**: 403-410.

Barco, R.A., Garrity, G.M., Scott, J.J., Amend, J.P., Nealson, K.H., and Emerson, D. (2020) A genus definition for Bacteria and Archaea based on a standard genome relatedness Index. *mBio* **11**.

Beller, H.R., Chain, P.S., Letain, T.E., Chakicherla, A., Larimer, F.W., Richardson, P.M. *et al.* (2006) The genome sequence of the obligately chemolithoautotrophic, facultatively anaerobic bacterium *Thiobacillus denitrificans*. *J Bacteriol* **188**: 1473-1488.

Bethencourt, L., Bochet, O., Farasin, J., Aquilina, L., Borgne, T.L., Quaiser, A. *et al.* (2020) Genome reconstruction reveals distinct assemblages of *Gallionellaceae* in surface and subsurface redox transition zones. *FEMS Microbiol Ecol* **96**.

Blöthe, M., and Roden, E.E. (2009) Composition and activity of an autotrophic Fe(II)-oxidizing, nitrate-reducing enrichment culture. *Appl Environ Microbiol* **75**: 6937-6940.

Callahan, B. (2018) *Silva taxonomic training data formatted for DADA2 (Silva version 132)*.

Callahan, B.J., McMurdie, P.J., Rosen, M.J., Han, A.W., Johnson, A.J., and Holmes, S.P. (2016) DADA2: High-resolution sample inference from Illumina amplicon data. *Nat Methods* **13**: 581-583.

Callahan, B.J., Wong, J., Heiner, C., Oh, S., Theriot, C.M., Gulati, A.S. *et al.* (2019) High-throughput amplicon sequencing of the full-length 16S rRNA gene with single-nucleotide resolution. *Nucleic Acids Res* **47**: e103.

Chen, I.A., Markowitz, V.M., Chu, K., Palaniappan, K., Szeto, E., Pillay, M. *et al.* (2017) IMG/M: integrated genome and metagenome comparative data analysis system. *Nucleic Acids Res* **45**: D507-D516.

Chen, I.A., Chu, K., Palaniappan, K., Pillay, M., Ratner, A., Huang, J. *et al.* (2019) IMG/M v.5.0: an integrated data management and comparative analysis system for microbial genomes and microbiomes. *Nucleic Acids Res* **47**: D666-D677.

Coordinators, N.R. (2016) Database resources of the National Center for Biotechnology Information. *Nucleic acids research* **44**: D7-D19.

Ehrenberg, C.G. (1838) *Die infusionsthierchen als vollkommene organismen: Ein blick in das tiefere organische leben der natur*: L. Voss.

Emerson, D., and Moyer, C. (1997) Isolation and characterization of novel iron-oxidizing bacteria that grow at circumneutral pH. *Appl Environ Microbiol* **63**: 4784-4792.

Emerson, D., and Merrill Floyd, M. (2005) Enrichment and Isolation of Iron-Oxidizing Bacteria at Neutral pH. In *Environ Microbiol*, pp. 112-123.

Emerson, D., Field, E.K., Chertkov, O., Davenport, K.W., Goodwin, L., Munk, C. *et al.* (2013) Comparative genomics of freshwater Fe-oxidizing bacteria: implications for physiology, ecology, and systematics. *Front Microbiol* **4**: 254.

Emerson, J.B., Thomas, B.C., Alvarez, W., and Banfield, J.F. (2016) Metagenomic analysis of a high carbon dioxide subsurface microbial community populated by chemolithoautotrophs and bacteria and archaea from candidate phyla. *Environ Microbiol* **18**: 1686-1703.

Fabisch, M., Freyer, G., Johnson, C.A., Büchel, G., Akob, D.M., Neu, T.R., and Küsel, K. (2016) Dominance of '*Gallionella capsiferriformans*' and heavy metal association with *Gallionella*-like stalks in metal-rich pH 6 mine water discharge. *Geobiology* **14**: 68-90.

Fields, M.W., Yan, T., Rhee, S.K., Carroll, S.L., Jardine, P.M., Watson, D.B. *et al.* (2005) Impacts on microbial communities and cultivable isolates from groundwater contaminated with high levels of nitric acid-uranium waste. *FEMS Microbiol Ecol* **53**: 417-428.

Franzen, O., Hu, J., Bao, X., Itzkowitz, S.H., Peter, I., and Bashir, A. (2015) Improved OTU-picking using long-read 16S rRNA gene amplicon sequencing and generic hierarchical clustering. *Microbiome* **3**: 43.

Garber, A.I., Nealson, K.H., Okamoto, A., McAllister, S.M., Chan, C.S., Barco, R.A., and Merino, N. (2020) FeGenie: A comprehensive tool for the identification of iron genes and iron gene neighborhoods in genome and metagenome assemblies. *Front Microbiol* **11**: 37.

Glaeser, S.P., and Kämpfer, P. (2015) Multilocus sequence analysis (MLSA) in prokaryotic taxonomy. *Syst Appl Microbiol* **38**: 237-245.

Guan, X., Liu, F., Xie, Y., Zhu, L., and Han, B. (2013) Microbiota associated with the migration and transformation of chlorinated aliphatic hydrocarbons in groundwater. *Environmental Geochemistry and Health* **35**: 535-549.

Hallbeck, L., and Pedersen, K. (1991) Autotrophic and mixotrophic growth of Gallionella ferruginea. *Microbiology* **137**: 2657-2661.

He, S., Barco, R.A., Emerson, D., and Roden, E.E. (2017) Comparative genomic analysis of neutrophilic iron(II) oxidizer genomes for candidate genes in extracellular electron transfer. *Front Microbiol* **8**: 1584.

He, S., Tominski, C., Kappler, A., Behrens, S., and Roden, E.E. (2016) Metagenomic analyses of the autotrophic Fe(II)-oxidizing, nitrate-reducing enrichment culture KS. *Appl Environ Microbiol* **82**: 2656-2668.

Hegler, F., Posth, N.R., Jiang, J., and Kappler, A. (2008) Physiology of phototrophic iron(II)-oxidizing bacteria: implications for modern and ancient environments. *FEMS Microbiol Ecol* **66**: 250-260.

Holmes, D.E., Nevin, K.P., and Lovley, D.R. (2004) Comparison of 16S rRNA, *nifD*, *recA*, *gyrB*, *rpoB* and *fusA* genes within the family *Geobacteraceae* fam. nov. *Int J Syst Evol Microbiol* **54**: 1591-1599.

Huang, Y., Straub, D., Blackwell, N., Kappler, A., and Kleindienst, S. (2021a) Meta-omics reveal *Gallionellaceae* and *Rhodanobacter* as interdependent key players for Fe(II) oxidation and nitrate reduction in the autotrophic enrichment culture KS. *Appl Environ Microbiol*: AEM.00496-00421.

Huang, Y., Straub, D., Kappler, A., Smith, N., Blackwell, N., and Kleindienst, S. (2021b) A novel enrichment culture highlights core features of microbial networks contributing to autotrophic Fe(II) oxidation coupled to nitrate reduction. *Microbial Physiol*.

Jakus, N., Blackwell, N., Straub, D., Kappler, A., and Kleindienst, S. (under review) Metagenomics reveal the potential role of *Gallionellaceae* sp. to perform near-complete denitrification coupled to Fe(II) oxidation under autotrophic conditions. *FEMS Microbiol Ecol*.

Jakus, N., Blackwell, N., Osenbrück, K., Straub, D., Byrne, J.M., Wang, Z. *et al.* (2021) Nitrate removal by a novel lithoautotrophic nitrate-reducing iron(II)-oxidizing culture enriched from a pyrite-rich limestone aquifer. *Appl Environ Microbiol*: DOI: 10.1128/AEM.00460-21

Jewell, T.N.M., Karaoz, U., Brodie, E.L., Williams, K.H., and Beller, H.R. (2016) Metatranscriptomic evidence of pervasive and diverse chemolithoautotrophy relevant to C, S, N and Fe cycling in a shallow alluvial aquifer. *ISME J* **10**: 2106-2117.

Kadnikov, V.V., Ivasenko, D.A., Beletskii, A.V., Mardanov, A.V., Danilova, E.V., Pimenov, N.V. *et al.* (2016) A novel uncultured bacterium of the family *Gallionellaceae*: description and genome reconstruction based on metagenomic analysis of microbial community in acid mine drainage. *Microbiology* **85**: 449-461.

Kalckar, H.M. (1991) 50 years of biological research--from oxidative phosphorylation to energy requiring transport regulation. *Annu Rev Biochem* **60**: 1-38.

Kappler, A., Bryce, C., Mansor, M., Lueder, U., Byrne, J.M., and Swanner, E.D. (2021) An evolving view on biogeochemical cycling of iron. *Nat Rev Microbiol* **19**: 360-374.

Kato, S., Chan, C., Itoh, T., and Ohkuma, M. (2013) Functional gene analysis of freshwater iron-rich flocs at circumneutral pH and isolation of a stalk-forming microaerophilic iron-oxidizing bacterium. *Appl Environ Microbiol* **79**: 5283-5290.

Kato, S., Krepski, S., Chan, C., Itoh, T., and Ohkuma, M. (2014) *Ferriphaselus amnicola* gen. nov., sp. nov., a neutrophilic, stalk-forming, iron-oxidizing bacterium isolated from an iron-rich groundwater seep. *Int J Syst Evol Microbiol* **64**: 921-925.

Kato, S., Ohkuma, M., Powell, D.H., Krepski, S.T., Oshima, K., Hattori, M. *et al.* (2015) Comparative genomic insights into ecophysiology of neutrophilic, microaerophilic iron oxidizing bacteria. *Front Microbiol* **6**: 1265.

Khalifa, A., Nakasuji, Y., Saka, N., Honjo, H., Asakawa, S., and Watanabe, T. (2018) *Ferrigenium kumadai* gen. nov., sp. nov., a microaerophilic iron-oxidizing bacterium isolated from a paddy field soil. *Int J Syst Evol Microbiol* **68**: 2587-2592.

Kojima, H., Watanabe, T., Iwata, T., and Fukui, M. (2014) Identification of major planktonic sulfur oxidizers in stratified freshwater lake. *PLoS One* **9**: e93877.

Konstantinidis, K.T., and Tiedje, J.M. (2007) Prokaryotic taxonomy and phylogeny in the genomic era: advancements and challenges ahead. *Curr Opin Microbiol* **10**: 504-509.

Konstantinidis, K.T., and Rosselló-Móra, R. (2015) Classifying the uncultivated microbial majority: A place for metagenomic data in the *Candidatus* proposal. *Syst Appl Microbiol* **38**: 223-230.

Konstantinidis, K.T., Rosselló-Móra, R., and Amann, R. (2017) Uncultivated microbes in need of their own taxonomy. *ISME J* **11**: 2399-2406.

Krepski, S.T., Hanson, T.E., and Chan, C.S. (2012) Isolation and characterization of a novel biomineral stalk-forming iron-oxidizing bacterium from a circumneutral groundwater seep. *Environ Microbiol* **14**: 1671-1680.

Kucera, S., and Wolfe, R.S. (1957) A selective enrichment method for *Gallionella ferruginea*. *J Bacteriol* **74**: 344-349.

Kumar, S., Stecher, G., Li, M., Knyaz, C., and Tamura, K. (2018) MEGA X: molecular evolutionary genetics analysis across computing platforms. *Mol Biol Evol* **35**: 1547-1549.

Laufer, K., Røy, H., Jørgensen, B.B., and Kappler, A. (2016) Evidence for the existence of autotrophic nitrate-reducing Fe(II)-oxidizing bacteria in marine coastal sediment. *Appl Environ Microbiol* **82**: 6120-6131.

Laufer, K., Nordhoff, M., Røy, H., Schmidt, C., Behrens, S., Jørgensen, B.B., and Kappler, A. (2015) Coexistence of microaerophilic, nitrate-reducing, and phototrophic Fe(II) Oxidizers and Fe(III) reducers in coastal marine sediment. *Appl Environ Microbiol* **82**: 1433-1447.

Li, J., Cui, J., Yang, Q., Cui, G., Wei, B., Wu, Z. *et al.* (2017) Oxidative weathering and microbial diversity of an inactive seafloor hydrothermal sulfide chimney. *Front Microbiol* **8**.
Martin, F., Torelli, S., Le Paslier, D., Barbance, A., Martin-Laurent, F., Bru, D. *et al.* (2012) *Betaproteobacteria* dominance and diversity shifts in the bacterial community of a PAH-contaminated soil exposed to phenanthrene. *Environmental Pollution* **162**: 345-353.
Mitchell, P. (1961) Coupling of phosphorylation to electron and hydrogen transfer by a chemi-osmotic type of mechanism. *Nature* **191**: 144-148.
Murray, A.E., Freudenstein, J., Gribaldo, S., Hatzenpichler, R., Hugenholtz, P., Kämpfer, P. *et al.* (2020) Roadmap for naming uncultivated Archaea and Bacteria. *Nat Microbiol* **5**: 987-994.
Murray, R.G., and Stackebrandt, E. (1995) Taxonomic note: implementation of the provisional status *Candidatus* for incompletely described procaryotes. *Int J Syst Bacteriol* **45**: 186-187.
Nordhoff, M., Tominski, C., Halama, M., Byrne, J.M., Obst, M., Kleindienst, S. *et al.* (2017) Insights into nitrate-reducing Fe(II) oxidation mechanisms through analysis of cell-mineral associations, cell encrustation, and mineralogy in the chemolithoautotrophic enrichment culture KS. *Appl Environ Microbiol* **83**: e00752-00717.
Rentz, J.A., Kraiya, C., Luther, G.W., 3rd, and Emerson, D. (2007) Control of ferrous iron oxidation within circumneutral microbial iron mats by cellular activity and autocatalysis. *Environ Sci Technol* **41**: 6084-6089.
Rocha, D.J., Santos, C.S., and Pacheco, L.G. (2015) Bacterial reference genes for gene expression studies by RT-qPCR: survey and analysis. *Antonie Van Leeuwenhoek* **108**: 685-693.
Rodriguez-R, L.M., and Konstantinidis, K.T. (2016) The enveomics collection: a toolbox for specialized analyses of microbial genomes and metagenomes. *PeerJ Prepr* **4**: e1900v1901.
Sauter, L. (2018) The competition between nitrate-reducing Fe(II)-oxidizing and photoferrotrophic microorganisms in the environment. In *Center for Applied Geoscience*: Eberhard-Karls-University Tübingen, pp. 12-13, 25.
Schoch, C.L., Ciufo, S., Domrachev, M., Hotton, C.L., Kannan, S., Khovanskaya, R. *et al.* (2020) NCBI Taxonomy: a comprehensive update on curation, resources and tools. *Database (Oxford)* **2020**.
Stackebrandt, E., Frederiksen, W., Garrity, G.M., Grimont, P.A.D., Kämpfer, P., Maiden, M.C.J. *et al.* (2002) Report of the ad hoc committee for the re-evaluation of the species definition in bacteriology. *Int J Syst Evol Microbiol* **52**: 1043-1047.
Straub, K.L., and Buchholz-Cleven, B.E. (1998) Enumeration and detection of anaerobic ferrous iron-oxidizing, nitrate-reducing bacteria from diverse European sediments. *Appl Environ Microbiol* **64**: 4846–4856.
Straub, K.L., Benz, M., Schink, B., and Widdel, F. (1996) Anaerobic, nitrate-dependent microbial oxidation of ferrous iron. *Appl Environ Microbiol* **62**: 1458.
Straub, K.L., Schönhuber, W.A., Buchholz-Cleven, B.E.E., and Schink, B. (2004) Diversity of ferrous iron-oxidizing, nitrate-reducing bacteria and their involvement in oxygen-independent iron cycling. *Geomicrobiol J* **21**: 371-378.
Tamura, K., and Nei, M. (1993) Estimation of the number of nucleotide substitutions in the control region of mitochondrial DNA in humans and chimpanzees. *Mol Biol Evol* **10**: 512-526.
Team, R. (2019) RStudio: Integrated Development for R. *RStudio, Inc Boston, MA*
Team, R.C. (2020) R: A language and environment for statistical computing. *R Foundation for Statistical Computing, Vienna, Austria*.
Team, R.D.C. (2018) R: A language and environment for statistical computing. *Generic*.
Tominski, C., Heyer, H., Lösekann-Behrens, T., Behrens, S., and Kappler, A. (2018a) Growth and population dynamics of the anaerobic Fe(II)-oxidizing and nitrate-reducing enrichment culture KS. *Appl Environ Microbiol* **84**: e02173-02117.
Tominski, C., Lösekann-Behrens, T., Ruecker, A., Hagemann, N., Kleindienst, S., Mueller, C.W. *et al.* (2018b) Insights into carbon metabolism provided by fluorescence *in situ* hybridization-secondary ion mass spectrometry imaging of an autotrophic, nitrate-reducing, Fe(II)-oxidizing enrichment culture. *Appl Environ Microbiol* **84**: 19.
Valdés, J., Pedroso, I., Quatrini, R., Dodson, R.J., Tettelin, H., Blake, R., 2nd *et al.* (2008) *Acidithiobacillus ferrooxidans* metabolism: from genome sequence to industrial applications. *BMC Genomics* **9**: 597.
Varghese, N.J., Mukherjee, S., Ivanova, N., Konstantinidis, K.T., Mavrommatis, K., Kyrpides, N.C., and Pati, A. (2015) Microbial species delineation using whole genome sequences. *Nucleic Acids Res* **43**: 6761-6771.
Wagner, C., Mau, M., Schlömann, M., Heinicke, J., and Koch, U. (2007) Characterization of the bacterial flora in mineral waters in upstreaming fluids of deep igneous rock aquifers. *J Geophys Res Biogeosci* **112**.
Watanabe, T., Khalifa, A., Asakawa, S., and Thrash, J.C. (2021) Complete genome sequence of *Ferrigenium kumadai* An22, a microaerophilic iron-oxidizing bacterium isolated from a paddy field soil. *Microbiology Resource Announcements* **10**: e00346-00321.
Weiss, J.V., Rentz, J.A., Plaia, T., Neubauer, S.C., Merrill-Floyd, M., Lilburn, T. *et al.* (2007) Characterization of neutrophilic Fe(II)-oxidizing bacteria isolated from the rhizosphere of wetland plants and

description of *Ferritrophicum radicicola* gen. nov. sp. nov., and *Sideroxydans paludicola* sp. nov. *Geomicrobiol J* **24**: 559-570.

Widdel, F., Schnell, S., Heising, S., Ehrenreich, A., Assmus, B., and Schink, B. (1993) Ferrous iron oxidation by anoxygenic phototrophic bacteria. *Nature* **362**: 834-836.

Zhimiao, Z., Zhufang, W., Mengyu, C., Xinshan, S., Mengqi, C., and Yinjiang, Z. (2020) Adding ferrous ions improved the performance of contaminant removal from low C/N coastal wastewater in constructed wetlands. *Environ Sci: Water Res Technol* **6**: 3351-3360.

9. Supplementary information on: ‘*Candidatus* Ferrigenium straubiae’ sp. nov., ‘*Candidatus* Ferrigenium bremense’ sp. nov., ‘*Candidatus* Ferrigenium altingense’ sp. nov., are autotrophic Fe(II)-oxidizing bacteria of the family *Gallionellaceae*

9.1. Supplementary figures and tables

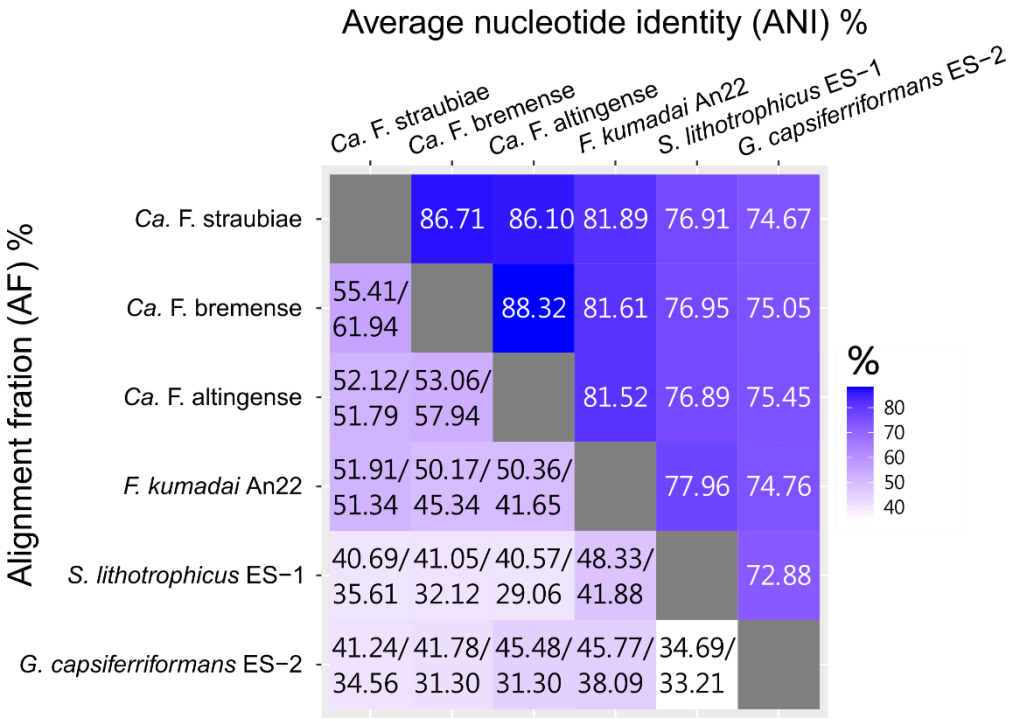

Figure S1. Average nucleotide identity (ANI) and alignment fraction (AF; genome x aligned to genome y [upper no.], genome y aligned to genome x [lower no.]) of strains from ‘*Candidatus* Ferrigenium straubiae’ (strain KS) sp. nov., ‘*Candidatus* Ferrigenium bremense’ (strain BP) sp. nov. and ‘*Candidatus* Ferrigenium altingense’ (strain AG) sp. nov. compared to their top three closely related isolated strains affiliating with the genera *Ferrigenium*, *Sideroxydans* and *Gallionella*. Recommended thresholds: ANI: species >96.5%; AF: species ≥60% [53, 65].

Table S1. AAI alignment fraction coverages from '*Candidatus* Ferrigenium straubiae' (strain KS) sp. nov., '*Candidatus* Ferrigenium bremense' (strain BP) sp. nov. and '*Candidatus* Ferrigenium altingense' (strain AG) sp. nov. compared to their top three closely related isolated strains affiliating with the genera *Ferrigenium*, *Sideroxydans* and *Gallionella*.

	***Ca.* F. straubiae**	***Ca.* F. bremense**	***Ca.* F. altingense**	***F. kumadai* An22**	***S. lithotrophicus* ES-1**	***G. capsiferriformans* ES-2**
***Ca.* F. straubiae**	-	67.23%	67.02%	62.03%	51.33%	50.33%
***Ca.* F. bremense**	71.63%	-	73.59%	66.93%	55.96%	56.15%
***Ca.* F. altingense**	64.07%	66.02%	-	58.32%	48.12%	50.47%
***F. kumadai* An22**	69.02%	69.89%	67.88%	-	61.91%	59.20%
***S. lithotrophicus* ES-1**	69.62%	71.23%	68.26%	75.45%	-	61.37%
***G. capsiferriformans* ES-2**	65.81%	68.90%	69.03%	69.56%	59.18%	-
Total protein number in the MAG	2182	2325	2068	2428	2959	2853

Table S2. Standard nucleotide BLAST search results to NCBI nucleotide collection (nr/nt) (June 8, 2021) of closely related sequences (>98.6% nearly full-length 16S rRNA gene identity) of strain KS, strain BP and strain AG.

Description	Query Cover	Identity (%)	Length (bp)	Accession No.	Habitat	Location	Refernce
Sequences >98.6% identical to strain KS							
Uncultured beta proteobacterium 16S rRNA gene, clone F25F63	100%	100	1464	FN430662.1	autotrophic Fe(II)-oxidizing, nitrate-reducing enrichment culture KS	Bremen, Germany	Blöthe and Roden, 2009
Uncultured beta proteobacterium 16S rRNA gene, clone F29F67	100%	99.93	1464	FN430666.1	autotrophic Fe(II)-oxidizing, nitrate-reducing enrichment culture KS	Bremen, Germany	Blöthe and Roden, 2009
Uncultured beta proteobacterium 16S rRNA gene, clone F32F70	100%	99.86	1464	FN430669.1	autotrophic Fe(II)-oxidizing, nitrate-reducing enrichment culture KS	Bremen, Germany	Blöthe and Roden, 2009
Uncultured beta proteobacterium 16S rRNA gene, clone F31F69	100%	99.73	1464	FN430668.1	autotrophic Fe(II)-oxidizing, nitrate-reducing enrichment culture KS	Bremen, Germany	Blöthe and Roden, 2009
Uncultured beta proteobacterium 16S rRNA gene, clone F33F71	100%	99.59	1464	FN430670.1	autotrophic Fe(II)-oxidizing, nitrate-reducing enrichment culture KS	Bremen, Germany	Blöthe and Roden, 2009
Uncultured beta proteobacterium 16S rRNA gene, clone F26F64	100%	99.59	1464	FN430663.1	autotrophic Fe(II)-oxidizing, nitrate-reducing enrichment culture KS	Bremen, Germany	Blöthe and Roden, 2009
Uncultured bacterium partial 16S rRNA gene, clone Iron-rich microbial mat clone Hoffnungsstollen_#4-1A_D09	94%	99.56	1396	LN870688.1	environmental Fe-rich microbial mats, abandoned pyrrhotite mine Hoffnungsstollen	Black Forest, Germany	Zeitvogel et al, unpublished
Uncultured beta proteobacterium 16S rRNA gene, clone F21F59	100%	99.52	1464	FN430659.1	autotrophic Fe(II)-oxidizing, nitrate-reducing enrichment culture KS	Bremen, Germany	Blöthe and Roden, 2009
Uncultured beta proteobacterium 16S rRNA gene, clone F28F66	100%	99.38	1464	FN430665.1	autotrophic Fe(II)-oxidizing, nitrate-reducing enrichment culture KS	Bremen, Germany	Blöthe and Roden, 2009
Uncultured beta proteobacterium 16S rRNA gene, clone F22F60	100%	99.38	1464	FN430660.1	autotrophic Fe(II)-oxidizing, nitrate-reducing enrichment culture KS	Bremen, Germany	Blöthe and Roden, 2009

Sequences >98.6% identical to strain BP							
Uncultured bacterium 16S ribosomal RNA gene clone I1AB101, partial sequence	93%	99.26	1359	FQ659636.1	PAH degrading bacterial community of a contaminate soil	Chambéry, France	Martin et al, 2012
Uncultured bacterium clone VE08-104-BAC 16S ribosomal RNA gene, partial sequence	94%	98.77	1398	GQ340331.1	Drinking water reservoir	Marathonas, Greece	Lymperopoulou et al, 2012
Uncultured bacterium gene for 16S rRNA, partial sequence, clone: RB112	97%	98.74	1444	AB240306.1	rhizosphere of Phragmites	Sapporo, Japan	Okabe et al, unpublished
Sequences >98.6% identical to strain AG							
Uncultured bacterium gene for 16S ribosomal RNA, partial sequence, clone: rS43m_43	94%	100	1460	AB754138.1	stratified freshwater lake	Yamanashi, Japan	Kojima et al, 2014
Uncultured *Gallionella* sp. partial 16S rRNA gene, clone BB03	96%	99.93	1491	AM167950.1	deep igneous rock aquifers	Bad Brambach, Germany	Wagner et al, 2007
Uncultured bacterium gene for 16S ribosomal RNA, partial sequence, clone: rS43m_63	94%	99.93	1460	AB754154.1	stratified freshwater lake	Yamanashi, Japan	Kojima et al, 2014
Uncultured beta proteobacterium clone hmx-114 16S ribosomal RNA gene, partial sequence	97%	99.8	1497	JQ278897.1	groundwater	China	Guan et al, 2013
Uncultured bacterium partial 16S rRNA gene, clone Iron-rich microbial mat clone Hoffnungsstollen_#5-1B_E10	90%	99.79	1396	LN870871.1	environmental Fe-rich microbial mats	Black Forest, Germany	Zeitvogel et al, unpublished
Uncultured bacterium clone 015C-C11 small subunit ribosomal RNA gene, partial sequence	99%	99.67	1529	AY662038.1	groundwater	USA	Fields et al, 2005
Uncultured beta proteobacterium clone sf-34 16S ribosomal RNA gene, partial sequence	97%	99.53	1498	JQ278948.1	groundwater	China	Guan et al, 2013
Uncultured beta proteobacterium clone sz-131 16S ribosomal RNA gene, partial sequence	97%	99.53	1497	JQ279049.1	groundwater	China	Guan et al, 2013
Uncultured *Gallionella* sp. partial 16S rRNA gene, clone BB49	99%	99.22	1529	AM167944.1	deep igneous rock aquifers	Bad Brambach, Germany	Wagner et al, 2007
Uncultured *Gallionella* sp. partial 16S rRNA gene, clone BB28	96%	99.13	1491	AM167970.1	deep igneous rock aquifers	Bad Brambach, Germany	Wagner et al, 2007
Uncultured beta proteobacterium clone sf-73 16S ribosomal RNA gene, partial sequence	97%	99.06	1494	JQ278969.1	groundwater	China	Guan et al, 2013

Uncultured bacterium clone EMIRGE_OTU_s5t4a_5708 16S ribosomal RNA gene, partial sequence	97%	99.06	1499	JX223560.1	subsurface aquifer sediment	Rifle, USA	Handley et al, unpublished
Uncultured beta proteobacterium clone fjc-85 16S ribosomal RNA gene, partial sequence	97%	99	1495	JQ278828.1	groundwater	China	Guan et al, 2013
Uncultured bacterium clone EMIRGE_OTU_s3t2d_3118 16S ribosomal RNA gene, partial sequence	97%	99	1500	JX222776.1	subsurface aquifer sediment	Rifle, USA	Handley et al, unpublished
Uncultured *Gallionella* sp. partial 16S rRNA gene, clone BB46	99%	98.95	1528	AM167953.1	deep igneous rock aquifers	Bad Brambach, Germany	Wagner et al, 2007
Uncultured *Gallionella* sp. partial 16S rRNA gene, clone BB59	99%	98.89	1530	AM167946.1	deep igneous rock aquifers	Bad Brambach, Germany	Wagner et al, 2007

10. Nitrate reduction potential of a fractured Middle Triassic carbonate aquifer in southwest Germany

Karsten Osenbrück[a], Eva Blendinger[a], Carsten Leven[b], Hermann Rügner[a], Michael Finkel[b],

Natalia Jakus[c,d], Hartmut Schulz[e], Peter Grathwohl[a]

[a]Hydrogeochemistry, Center for Applied Geoscience, University of Tuebingen, Germany

[b]Hydrogeology, Center for Applied Geoscience, University of Tuebingen, Germany

[c]Geomicrobiology, Center for Applied Geoscience, University of Tuebingen, Germany

[d]Microbial Ecology, Center for Applied Geoscience, University of Tuebingen, Germany

[e]Micropaleontology, Center for Applied Geoscience, University of Tuebingen, Germany

Abstract

Nitrate reduction constitutes an important natural mechanism to mitigate the widespread and persistent nitrate contamination of groundwater resources. In fractured aquifers, however, the abundance and accessibility of electron donors and their spatial correlation with groundwater flow paths are often poorly known. In this study, the nitrate reduction potential of a fractured carbonate aquifer in the Upper Muschelkalk of SW Germany was investigated where denitrification is due to the oxidation of ferrous iron and reduced sulfur. Petrographical analyses of rock samples revealed concentrations of syn-sedimentary and diagenetically formed pyrite ranging from 1–4 wt.% with only small differences between different facies types. Additional ferrous iron is available in saddle dolomites (up to 2.6 wt.%), which probably were formed by tectonically induced percolation of low-temperature hydrothermal fluids. Borehole logging at groundwater wells (flowmeter, video, gamma) indicate that most groundwater flow occurs along karstified bedding planes partly located within dolomites of the shoal and backshoal facies. The high porosity of 15–30% of these facies facilitates molecular diffusive exchange of solutes between flow paths and the reactive minerals in the pore matrix. The high porosity facies together with hydraulically effective fractures featuring pyrite or saddle dolomite precipitates constitute the zones of highest nitrate reduction potential within the aquifer. Model-based estimates of electron acceptor/donor balances indicate that the nitrate reduction potential protecting water supply wells increases with increasing porosity of the rock matrix and

decreases with increasing hydraulic conductivity (or effective fracture aperture) and spacing of the fracture network.

10.1. Introduction

Fractured and karstified carbonate aquifers constitute major drinking water resources worldwide (Goldscheider *et al.* 2020). As with other groundwater resources, carbonate aquifers are at risk of pollution by anthropogenic compounds such as nitrate (Vías *et al.* 2006; Husic *et al.* 2019). Nitrate contamination evolved to a global environmental and health problem (Ward *et al.* 2018) due to continuing expansion of agricultural production over the last decades (Morris *et al.* 2003; OECD 2008). Under oxic conditions, nitrate (NO_3^-) is usually transported conservatively with percolating water or along groundwater flow paths. In the absence of oxygen, NO_3^- may be degraded by microbially-mediated processes, which lead to the formation of more reduced compounds such as N_2 (by denitrification) or NH_4^+ (by dissimilatory nitrate reduction to ammonium) (Korom 1992; Kuypers, Marchant and Kartal 2018). The reduction of nitrate constitutes an important natural mechanism for the attenuation of high NO_3^- concentrations in groundwater in general (Rivett *et al.* 2008) and specifically in carbonate rock aquifers (Einsiedl and Mayer 2006; Heffernan *et al.* 2012). Therefore, a better understanding and estimation of the nitrate reduction potential is imperative for safeguarding groundwater quality and the supply of drinking water.

The nitrate reduction potential is mainly governed by the occurrence of suitable redox conditions (e.g., low oxygen concentrations), a sufficient amount of electron donors near groundwater flow paths, and the presence and activity of microbial communities capable of coupling nitrate reduction to the oxidation of bioavailable electron donors. While natural organic matter (NOM) is the most common electron donor for (heterotrophic) denitrification in shallow alluvial aquifers (Smith and Duff 1988; Zarnetske *et al.* 2011), ferrous iron (Fe(II)) and reduced sulfur (S(-I)) bearing minerals such as pyrite were found to dominate (autotrophic) denitrification in aquifers with low amounts and limited bioavailability of NOM. This includes fractured aquifers in carbonate rocks (Baker *et al.* 2012; Kim *et al.* 2016; Opazo, Aravena and Parker 2016), crystalline bedrocks (Pauwels, Foucher and Kloppmann 2000; Orr *et al.* 2016), but also porous aquifers (Schwientek *et al.* 2008; Zhang *et al.* 2013). The presence of denitrifying microorganisms within fractured carbonate aquifers was confirmed by studies investigating microbial communities in the major conduit and fracture network (Farnleitner *et al.* 2005; Jakus *et al.* 2021) or attached to the limestone rock matrix (Herrmann *et al.* 2017; Starke *et al.* 2017). However, only few studies provided sound estimates of the amount of electron donors available in the aquifer matrix for the observed nitrate reduction processes (e.g., Kludt *et al.* 2016). Particularly for fractured aquifers, detailed information on the extent of nitrate turnover and the inventory of available electron donors are usually sparse, which often limits the estimation of the nitrate reduction potential to geostatistical or stochastic modeling approaches (Rivas *et al.* 2017; Loschko *et al.* 2019).

The Middle Triassic carbonates of the Upper Muschelkalk form an important regional fractured aquifer in southwest Germany, which is used for drinking water supply. Despite high nitrate

concentrations in the recharge area, groundwater extracted by the water suppliers from the same aquifer does often reveal relatively low nitrate concentrations. Evidence that this decrease in nitrate is due to microbially-mediated nitrate reduction coupled to oxidation of Fe(II) or S(-I) was provided by geochemical and isotopic investigations (Visser *et al.* 2020) and by microbial enrichment cultures (Jakus *et al.* 2021) from the aquifer. While it is well known that Fe(II) or S(-I)-bearing minerals often occur in carbonate rocks such as the Upper Muschelkalk, their source and distribution and their interrelationship with advective transport of nitrate along groundwater flow paths remain unclear. It was thus the main purpose of this study to characterize the rock matrix of the Middle Triassic carbonate aquifer in terms of (1) major sedimentological facies types, (2) pore spaces and porosities as well as their connection with major hydraulically effective fractures and bedding planes, and (3) presence and origin of Fe(II) and S(-I)-bearing minerals in order to assess and estimate the available nitrate reduction potential protecting drinking water produced from the aquifer's wells or springs.

10.2. Methodical approach

To assess the nitrate reduction potential of the Upper Muschelkalk aquifer, petrographical analyses of the rock matrix were combined with hydraulic and geophysical borehole logging and model simulations of electron donor/acceptor mass balances. The inventory of electron donors available for nitrate reduction within the aquifer was determined by analyzing the abundance of Fe(II) and S(-I) together with the porosity of the rock matrix using thin sections microscopy and EDX spectra of rock samples from the main sedimentological facies types. Since nitrate (and oxygen) transport in the aquifer is mainly linked to groundwater flow along fractures, the rock matrix adjacent to these flow paths form the major zones contributing electron donors for the potential redox processes. The location and distribution of the predominant flow paths were derived from flowmeter logs in three wells extracting groundwater from the Upper Muschelkalk. Gamma logs were used to relate the observed groundwater flow paths with the known lithological and facies profiles from quarries and drilling cores. This allowed to interrelate the hydraulically effective fractures with the measured porosity and Fe(II) and S(-I) concentrations of the respective facies and to identify potential zones of high nitrate turnover within the aquifer. Finally, the impact of the occurring nitrate degradation processes was evaluated using model simulations of the electron donor/acceptor mass balance along groundwater flow paths for the different facies types. Based on the observed porosity and Fe(II) and S(-I) concentration, this provided estimates of the remaining nitrate reduction potential for an assumed groundwater extraction well as function of nitrate input concentrations and the time over which this nitrate input might persist.

10.3. Study area

The study area "Oberes Gäu" is an intensively agriculturally used region located in Baden-Württemberg, Southwest Germany. It is located near the town of Herrenberg, approximately 25 km SW of the city of Stuttgart and 20 km east of the city of Tübingen (Figure 1).

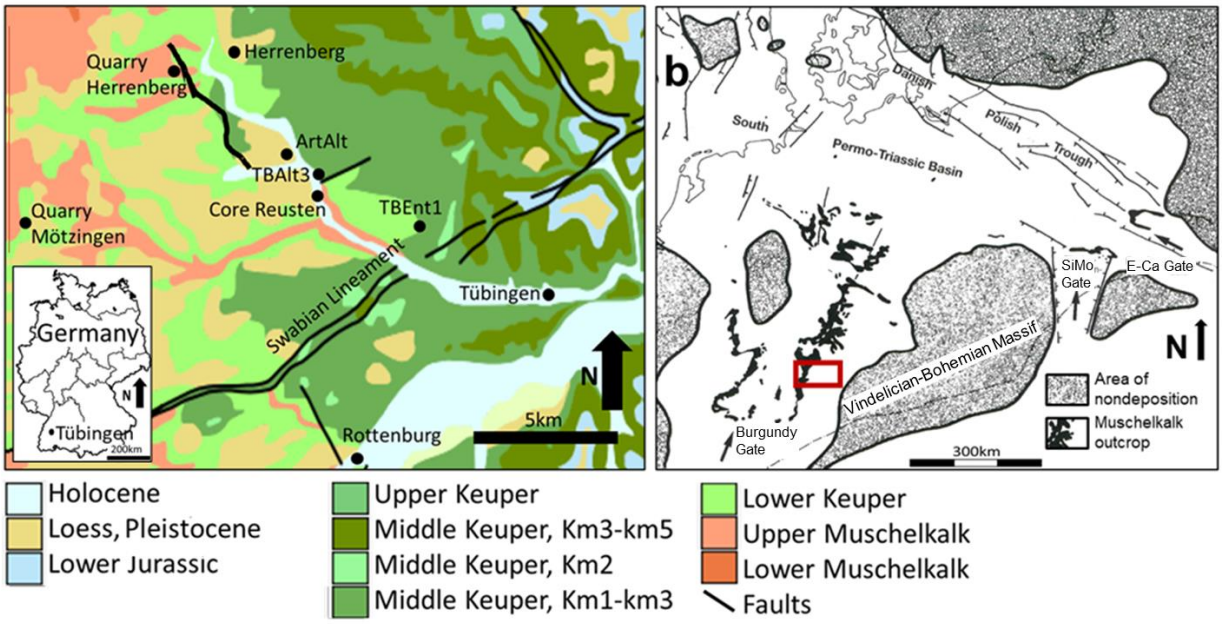

Figure 1. a Geologic map of the study area (LGRB 2019) with major tectonic elements and location of sampling sites; **b** Paleogeography of the Muschelkalk (Middle Triassic; white area) in central Europe (after Hagdorn 1991) . The red frame indicates the study area.

10.3.1. Geological setting

The up to 90 m thick carbonates of the Upper Muschelkalk (Middle Triassic; Figure S1 of the electronic supplementary material (ESM)) have been extensively investigated with respect to sedimentology (e.g., Koehrer *et al.* 2010; Palermo *et al.* 2012; Warnecke and Aigner 2019). The sedimentation area of the Middle Triassic limestones of southwest Germany is interpreted as a shallow marine storm-dominated carbonate ramp (Aigner 1985). It developed on the NW margin of the Vindelician-Bohemian Massif in the semi-enclosed intracratonic Germanic Basin, which was sporadically linked to the Tethys ocean in the south via the Silesian-Moravian (SiMo), East Carpathian (E-Ca), and the Burgundy seaways or "gates" (Ziegler 1990; Figure 1b). The gently inclined paleoslope was dipping at less than 1° to the NW into the basin. On a section from SE to NW different facies zones from the shallow marine to the deep basin can be observed. Due to changes in sea level a transgressive/regressive cycle or composite third-order sequence evolved (Aigner and Bachmann 1992). The succession of the Upper Muschelkalk starts with the shallow marine Zwergfauna-Schichten and the Haßmersheim-Schichten, which are characterized by a prominent clay horizon. They are followed by the ramp deposits of the Trochitenkalk-Formation, an alternation of more basinal marlstones, mudstones, and crinoidal limestone beds forming an overall fining-upward sequence (Palermo *et al.* 2012) of stacked meter-scale stratigraphic cycles. The Meißner-Formation forms an overall coarsening upward sequence (Palermo *et al.* 2012) made up of marlstones, fine grained limestones, and shoal carbonates. The peritidal dolomites of the Rottweil-Formation ("Trigonodusdolomit") are overlain with a sequence boundary (Aigner and Bachmann 1992) by the clastic and gypsum deposits of the Keuper Group (Upper Triassic).

10.3.2. Tectonic setting

Concerning tectonics, the study area is situated in the western part of the South German Triangle (Carlé 1955; Ring and Bolhar 2020), a major structural element of south Germany. The sedimentary cover of the South German Triangle consists of up to 1000 m clastic sediments, evaporates, and carbonates of Permian to Jurassic age, which overlay the crystalline basement (Gwinner and Geyer 2011). As a consequence of tectonic events, such as the rifting of the Atlantic in the Jurassic-Early Cretaceous and the formation of the Upper Rhine Graben in Late Eocene-Quaternary, the area was affected by intense fracturing and brittle deformation of the sedimentary cover resulting in the gently (1 to 3°) dipping of the lithostratigraphic units to the SE. Faults with horizontal and often lateral displacements up to several tens of meters, e.g. the Swabian Lineament, are trending mainly NW-SE, ENE-WSW and NNE-SSW (Reicherter *et al.* 2008; Hegler *et al.* 2010). Extensional tectonics, erosional unroofing, and decrease of the overburden pressure might have caused decompression in the subsurface, which enabled the rise of pore fluids (Staude, Bons and Markl 2009; Bons *et al.* 2014) and the formation of ore deposits and hydrothermal veins along the Upper Rhine Graben and in the Black Forest (Baatartsogt *et al.* 2007; Staude, Bons and Markl 2009). In the study area, escaping mantle-born CO_2 (Lübben and Leven 2018), which was used by D'Affonseca et al. (2020) to verify the existence of unmapped faults, might be related to these processes.

10.3.3. Hydrogeological setting

The limestone and dolomite rocks of the Upper Muschelkalk constitute a fractured aquifer, which outcrops in the NW of the study area over a distance of 2–4 km and gently dips to the SE, where it is increasingly covered by low permeable sedimentary Upper Triassic rocks (Figure 1a). The uncovered part of the study area constitutes the main recharge area and karstification of the limestone rocks caused numerous dolines and other karstic structures (sinkholes and karstic springs) in this area. Towards the SE the fractured carbonate aquifer becomes confined or even artesian. Generally, the groundwater flow direction is from NW to SE following the dipping of the Triassic formations. In addition to karstic features, regional groundwater flow is influenced by numerous tectonic structures and their associated fault systems (D'Affonseca, Finkel and Cirpka 2020). Most fractures visible in quarries or boreholes follow the ENE-WSW and NW-SE directions of the fault zones. Spacing of the mainly subvertical fractures typically range between 1.5 and 5.0 m. No reliable data on fracture apertures were available because of weathering or mechanical stress of the rock faces at quarries. Dominating agricultural land use (about 67%; Visser *et al.* 2020) leads to the release of NO_3^- into the karstic aquifer. Groundwater nitrate concentrations decline with increasing distance from the recharge area from elevated values (approximately 35 mg/L at average) to low concentrations in the range of 0–2 mg/L in the confined part of the aquifer. Access to the groundwater is provided by an artesian monitoring well (ArtAlt) and two production wells (TBEnt1, TBAlt3), which were used for flowmeter logging and chemical monitoring.

10.4. Data collection and experimental methods

10.4.1. Petrographical analyses

To investigate the occurrence, amount, and origin of reactive, iron- and sulfur-containing minerals in rocks of the Upper Muschelkalk, rock samples from different locations within the study area were collected from quarries near Herrenberg and Mötzingen and from a recently drilled Muschelkalk core near Reusten (Figure1). Special care was taken during sampling to consider lithologies that vary in facies type and visible porosity and to select samples from areas with different degrees of tectonic stress. From the samples, about 30 uncovered thin sections mounted on glass-slides 26×48 mm and 50×50 mm and polished on grinding powder of grit size 100–1200 to a final thickness of 35 µm have been prepared. Thin sections were analyzed with a polarizing light microscope (Leitz Laborlux 12 Pol S) using transmitted and reflected light at a magnification of 50–200 according to lithology and Dunham texture (Dunham, 1962), in order to (1) identify type and content of iron-bearing minerals, (2) to estimate macro-porosity and (3) to evaluate sedimentary features of the selected rock samples and identify the facies type. For porosity determination, thin sections were pre-treated with blue dyed resin. Thin sections selected for energy dispersive X-ray spectroscopy (EDX) were polished with diamond suspensions of 6–15 µm and 3 µm grain diameter. To prevent the electrically non-conductive samples from becoming charged during electron beam bombardment, the samples were cleaned with acetone, dried and coated with a thin layer of carbon using a Sputter Coater (BAL-TEC Model SCD 005/CEA 035). Analyses of the iron minerals and matrix composition were carried out using a Scanning Electron Microscope (LEO 1450 VP) and EDX-system (OXFORD Instruments INCA Energy300).

10.4.2. Fraction of organic carbon in rock samples

To quantify the organic carbon content, f_{oc}, rock samples were crushed using a jaw crusher, dried at 60°C in an oven, pulverized (ZrO_2 ball mill), decarbonized (HCl 16%), purged with deionized water and re-dried (60 °C). Measurements were performed with an elemental analyzer (Elementar Vario EL; thermal oxidation at 950 °C and CO_2 quantification using a heat conductivity detector). Results are reported in wt.%; LOQ = 0.003 wt.%.

10.4.3. Chemical analyses of sulfur as proxy for pyrite concentrations

The determination of pyrite concentrations in rock samples according to the AVS/CRS method was done at Aarhus University. The inorganic sulfur was divided into two fractions, acid volatile sulfides (AVS): H_2S, FeS, and chromium reducible sulfides (CRS): S^0, FeS_2. Their digestions were performed following a two-step procedure. In a first step, AVS were distilled from a weighed amount of homogenized rock powder. In a second step, the CRS were determined in the sediment slurry remaining after AVS distillation as described by Fossing and Jorgensen (1989). The total concentration of pyrite was calculated from the total concentration of CRS assuming that pyrite was the only source of chromium-reducible inorganic sulfur in the sample.

10.4.4. Flowmeter and video logging

Flowmeter logging was used to identify groundwater inflow horizons and quantify the corresponding water fluxes at three groundwater wells completed in the Upper Muschelkalk aquifer (see Figure 1 for their locations). A flowmeter with a hot wire sensor (Berghof Analytik & Umweltengineering GmbH, Tübingen, Germany) using the principle of anemometry (Agarwal and Olin 2014) was used to measure vertical flow rates in the 45 m deep water supply well TBEnt1 and in the artesian well ArtAlt in April and July 2014, respectively. The 60 m deep ArtAlt has a completed well casing down to 19 m below ground surface (bgs) corresponding to the base of the Upper Triassic (Lower Keuper) sediments. The remaining 41 m within the Upper Muschelkalk are left unscreened as open borehole with a diameter of 330 mm (from 19 to 28 m bgs) and 220 mm (from 28 to 60 m bgs). At the 60 m deep water supply well TBAlt3, an impeller flowmeter (Mount Sopris Instruments, Denver, USA) was used to measure vertical flow rates in Jan 2019. Details on the construction of the wells TBEnt1 and TBAlt3 are provided in Figs. S3 and S4 of ESM. In total, four flowmeter logs were conducted at each well, at ArtAlt under natural artesian outflow conditions of about 6 L/s, at TBEnt1 and TBAlt3 during groundwater extraction by a submersible pump (Grundfos GmbH, Erkrath, Germany) installed in the well casing a few meters below the groundwater table with a rate of 6.0 and 6.6 L/s, respectively. Each log consisted of continuous measurements with data recording every 5–10 cm starting at least 2 m above and ending 2 m below the screened sections or open borehole. Prior to groundwater extraction, baseline flowmeter logs were measured at TBEnt1 and TBAlt3 under ambient conditions without pumping. At ArtAlt, a video log (Wiggerich Video-Inspektionssysteme, Arnsberg, Germany) was additionally performed in March 2014, which in combination with the results of the flowmeter logging, allowed to visualize the horizons of groundwater inflow.

10.4.5. Depth oriented groundwater sampling

Groundwater samples for hydrochemical analysis were taken from the artesian well ArtAlt in July 2014, directly after the flowmeter logging. Groundwater was collected from three different depths (17.5 m, 30.5 m, 46.0 m bgs) to capture the changes caused by inflowing groundwater from the major fractures. The samples were taken from all three depths simultaneously with a flow rate of about 0.1 L/min using a set of custom-made pneumatically-controlled, miniaturized double valve pumps. For the pneumatic activation of the pumps, nitrogen gas with a purity of 99.999% was used. Dissolved ions were quantified in the lab by ion chromatography (Thermo Scientific Dionex DX-120; Anions: Dionex IonPac A523 analytical column with a Dionex IonPac AG23 guard column; Cations: Dionex IonPac CS12A-5µm analytical column with a Dionex IonPac CG12A-5 µm guard column; LOQ = 0.1 mg/L).

The concentration C_s of an ion (e.g., NO_3^-, SO_4^{2-}) in the collected water samples from depth s represent a mixture of groundwater from the inflow Q_n, directly at the sampling depth (with concentration C_n), and the cumulated vertical groundwater flux from other inflow horizons:

$$C_s\, Q_s = C_n Q_n + \sum_{i=1}^{n-1} C_i\, Q_i \qquad (1)$$

where Q_s is the cumulative groundwater flux corresponding to the value measured by the flowmeter log at depth s. The concentrations C_i were derived by rearranging Eq. (1) for each inflow horizon i and solving the system of linear equations for the unknown concentrations.

10.4.6. Gamma logging

Logging of the natural gamma radiation was applied for assessment and assignment of the lithological and stratigraphic setting at the artesian well ArtAlt using a slim gamma probe (Mount Sopris Instruments, Denver, USA). Logging was performed over the entire depth of the well with the smallest possible logging speed of approximately 1.8 m/min and a depth resolution of approximately 5 cm. For the analysis four logs were averaged for improving the signal-to-noise ratio of the log.

10.5. Modeling approach

10.5.1. Conceptional setup of geometry and reaction fronts

Due to reactions between electron donor-bearing minerals in the rock matrix and electron acceptors (O_2 or NO_3^-) entering the porous matrix by diffusion, a moving reaction front will develop along the hydraulically effective fractures (Sidborn and Neretnieks 2007, 2008). The extent of rock matrix contributing to the reduction capacity of the aquifer is growing with time and increasing electron acceptor/donor ratio. On time scales of decades or at low electron donor concentration, it is restricted to a narrow zone around the fractures and usually substantially smaller than the total extent of the aquifer (Figure 2).

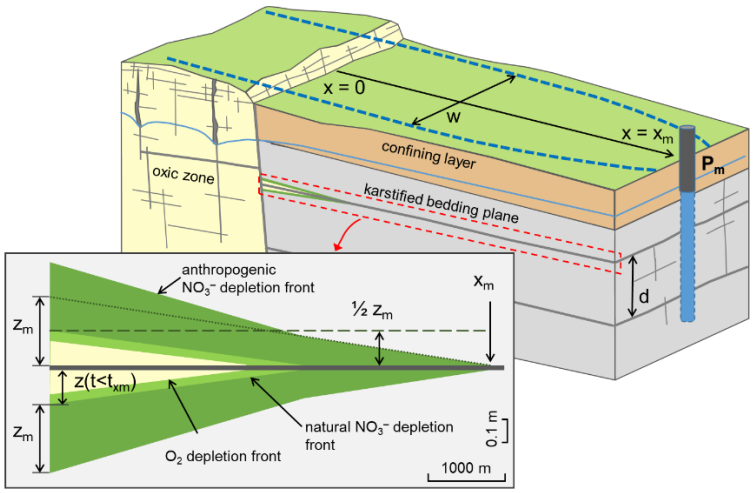

Figure. 2 Schematic display of a typical section across the oxic and the confined part of the fractured carbonate aquifer. The oxic zone is characterized by continuous replenishment of oxygen due to karstic features across the

vadose zone. The dashed blue line represents the capture zone of a hypothetical well P_m. Lower panel: Location of electron donor depletion fronts in the rock matrix along a fracture/bedding plane as assumed in the electron acceptor/donor balance model (vertical scale exaggerated). The fronts are due to reactions of O_2 and NO_3^- with electron donor-bearing minerals in the rock matrix. The sketch shows the situation when the front has just reached the location x_m of the well. Note that the depths of the fronts within the rock matrix are additive, i.e. the depletion due to NO_3^- degradation only would form a triangular depletion area, as indicated by the dotted line. Note further that the size of this depletion area is ½ $z_m x_m$.

In general, the penetration depth z of a solute or a reaction front into the rock matrix after time t can be expressed based on the mean square displacement (e.g., Grathwohl 1998; Sidborn and Neretnieks 2007):

$$z = \sqrt{2\,D_a\,\mathrm{t}} = \sqrt{2D_e\frac{C_a}{C_d}\,t} \tag{2}$$

$$D_e = D_{aq}\frac{\varepsilon}{\tau} \approx D_{aq}\,\varepsilon^{\,2} \tag{3}$$

where D_a and D_e are an apparent and the effective diffusion coefficient, respectively. The reciprocal of the acceptor/donor ratio $C_a/\,C_d$ accounts for retardation of the electron donor depletion front in the rock matrix. D_e is derived from the aqueous diffusion coefficient D_{aq} by accounting for the porosity ε and tortuosity τ of the rock matrix (Rügner et al. 1999; Boving and Grathwohl 2001). After onset of the current hydrological cycle, the oxidation of electron donors by O_2 followed by the reduction of natural (non-anthropogenic) NO_3^- formed a sequence of depletion fronts in the rock matrix along fractures. Due to high concentrations, the recently added anthropogenic NO_3^- lead to an accelerated penetration of the nitrate depletion front into the matrix as depicted in Fig 2. The thickness of the rock matrix contributing to nitrate reduction is considered to reach a maximum value z_m at time t_{xm} when the depletion front along the fracture reaches a hypothetical well P_m at x_m. Given that the reaction front can be approximated by a linear decrease of z with increasing distance along the fracture as shown in Figure 2 (see also Sidborn and Neretnieks 2007), the total area of NO_3^- depletion in the rock matrix may be represented by half of the depth z_m (hence the factor ½ in Eq. (5)). The prolonged exposure of reactive minerals to O_2 and natural NO_3^- since the onset of the current groundwater flow regime resulted in the depletion of electron donors in parts of rock matrix along the fractures. The degradation of anthropogenic NO_3^- leads to the depletion of minerals further inside the rock matrix and is additive to the previous mineral depletion. Correspondingly, the depth of the depletion front z_m in the rock matrix is calculated independently of any previous mineral depletion (see Figure 2). This approach is justified by the relatively fast non-reactive diffusion of NO_3^- across the depleted porous matrix with a pore diffusion coefficient of D_e/ε (Grathwohl 1998).

10.5.2. Electron acceptor/ donor mole balance

The nitrate reduction potential of the fractured carbonate aquifer is assessed by quantifying the moles of electron donors in the rock matrix along hydraulically effective fractures, which allow the transport of known quantities of the electron acceptors dissolved oxygen (O_2) and nitrate (NO_3^-). A mole balance is applied to groundwater extracted or discharging naturally from a typical aquifer section

forming the capture zone of a hypothetical well P_m (or other discharge point) as shown in Figure 2. The number of moles of NO_3^- (or of any other electron acceptor) N_a that are transformed in the aquifer section over time *t* can be derived by:

$$N_a = C_a\, Q\, t \tag{4}$$

where C_a is the concentration of NO_3^- in mol/L in the groundwater entering the fractures (nitrate input). The discharge Q (in L/yr) constitutes the groundwater flux emerging from the fracture network at x_m. Note that in Eq. (4) the nitrate input C_a and discharge Q are assumed to remain constant over time or to represent time averaged values. The nitrate reduction potential protecting the well P_m is governed by the volumetric molar concentration of electron donor equivalents C_d in mol NO_3^-/L, which comprises the concentration C_i of all electron donors in the rock matrix next to the effective fractures and the stoichiometric factors γ_i of each reaction (moles of NO_3^- that can be reduced by one mole of donor i): $C_d = \sum C_i \gamma_i$. The number of moles of electron donor equivalents N_d that is available for nitrate reduction before the nitrate front reaches the well at P_m can be expressed as:

$$N_d = 2\, C_d\, w\, x_m \frac{z_m}{2} n_f \tag{5}$$

where w denotes the width of the cross section providing Q (perpendicular to flow but parallel to fracture planes), x_m is the distance (parallel to flow) between the well P_m and the boundary to the oxic zone at $x = 0$ (see Figure 2), z_m is the penetration depth of the nitrate reduction front into the rock matrix at $x = 0$ for the time when the reaction front reaches the well at P_m, and n_f is the number of hydraulically effective fractures. The width w of the capture zone of well P_m is related to discharge Q by Darcy's law:

$$Q = A\, K\, I = d\, n_f\, w\, K\, I \tag{6}$$

where A is the cross section of the capture zone of P_m, K is the hydraulic conductivity of the fractured aquifer, d the mean fracture spacing, and I the hydraulic gradient along the capture zone. Under the assumption of a network of (parallel) fractures with laminar flow and a mean effective aperture b, the hydraulic conductivity of the fractured aquifer is given by:

$$K = \frac{g}{12\,\vartheta} \frac{b^3}{d} \tag{7}$$

where g is the gravitational acceleration and ϑ the kinematic viscosity of water at 10°C.

Assuming a quasi-steady state where the nitrate input concentration, groundwater discharge rate, and groundwater flow paths stay constant over the considered time *t*, the remaining fraction of protection potential $r_{PP} = 1 - N_a/N_d$ along all groundwater flow paths contributing to Q can be quantified by combining Eqs. (4–6):

$$r_{PP} = 1 - \frac{C_a}{C_d} \frac{Q\ t}{n_f\ w\ x_m\ z_m} = 1 - \frac{C_a}{C_d} \frac{d\ K\ I\ t}{x_m\ z_m} \quad (8)$$

By definition, the well protection potential is depleted (i.e. nitrate concentration ≥ 0) when the reaction front has arrived at x_m after time $t = t_{xm}$. For this situation, r_{PP} in Eq. (8) becomes zero and thus can be used to determine t_{xm} after inserting Eqs. (2) and (3) for $z_m = z(t_{xm})$ into Eq. (8):

$$t_{xm} = 2\ D_{aq} \frac{C_d}{C_a} \left(\frac{\varepsilon\ x_m}{d\ K\ I}\right)^2 \quad (9)$$

Inserting this expression into Eq. (2), the average penetration depth of the reaction front z_m can also be written as:

$$z_m = \frac{2\ x_m\ \varepsilon^2\ D_{aq}}{d\ K\ I} \quad (10)$$

Now z_m is independent of C_a/C_d for a given value of x_m. Provided that the different fractures contributing to discharge Q can be represented by "averaged fractures" with an effective aperture and flow velocity, z_m constitutes a representative mean of the considered aquifer section. Note that the derivation of Eqs. (9) and (10) is based on the assumption that the reaction with minerals is instantaneous and that the NO_3^- concentration in the pore water of the rock matrix is much smaller than the concentration of electron donors in the rock. As such it represents an optimal case for nitrate reduction. Inserting Eq. (10) into Eq. (8), the remaining well protection potential r_{PP} becomes:

$$r_{PP} = 1 - \frac{C_a}{C_d} \left(\frac{d\ K\ I}{\varepsilon\ x_m}\right)^2 \frac{t}{2\ D_{aq}} \quad (11)$$

10.5.3. Parameter assignment and model scenarios

The parameters required to calculate r_{PP} can usually be obtained from basic hydrogeological studies or monitoring programs. In this work, r_{PP} was determined for the aquifer matrix of a typical well catchment situated in the confined part of the aquifer. Modeling was performed for the geological and geochemical conditions determined for three of the four investigated facies (aggregating shoal and backshoal facies). In addition, for each facies two different nitrate input scenarios were considered: (1) low natural nitrate concentrations (~1.0 mg/L) that presumably prevailed during onset of the current groundwater flow regime, and (2) high anthropogenic nitrate concentrations (>10 mg/L) that started about 60 years ago. Regional groundwater flow is assumed to take place mainly in horizontal fractures that developed along bedding planes. A spacing of flow effective fracture/bedding planes d of 10 m was used, corresponding to a mean value determined from flowmeter logs at the three studied wells. Hydraulic conductivity of the fractured aquifer was set to 1.5×10^{-5} m/s, which is in the upper range of values reported for the confined part of the aquifer (D'Affonseca, Finkel and Cirpka 2020). The length of the effective bedding planes x_m was taken to be about 5000 m corresponding to the

average distance of the production wells from the start of the confining layers preventing oxygen replenishment along karstic features. The hydraulic gradient I of 1.0% was derived from groundwater table contours (D'Affonseca, Finkel and Cirpka 2020).

The depth of the rock matrix potentially contributing to nitrate reduction was determined using Eq. (10). The effective diffusion coefficient D_e has been estimated as 0.004–1.0×10^{-10} m²/s for a nitrate diffusion coefficient D_{aq} of 1.5×10^{-9} m²/s (in pure water at 10°C; e.g., (Picioreanu C, van Loosdrecht and Heijnen 1997) and mean porosities ε of 23%, 5%, and 1% of the shoal/backshoal, tempestite, and basinal facies, respectively. Similar values for D_e were reported by Hill (1984) for the British chalk aquifer. The concentration of electron donor equivalents C_d was determined from measured concentrations of reactive minerals by assuming that nitrate reduction is coupled to the oxidation of reduced iron Fe(II) and sulfur S(-I) contained in pyrite (FeS_2) and iron-rich dolomites $Ca(Fe,Mg)(CO_3)_2$ according to the following reactions (Straub *et al.* 1996; Appelo and Postma 2004):

$$5FeS_2 + 14NO_3 + 4H^+ \rightarrow 10SO_4 + 7N_2 + 5Fe^{2+} + 2H_2O \quad (12)$$

$$10Fe^{2+} + 2NO_3 + 24H_2O \rightarrow 10Fe(OH)_3 + N_2 + 18H^+ \quad (13)$$

Based on the stoichiometry of these reactions, C_d in mol/L can be calculated from the average abundance of reactive minerals C_{pyr} and C_{dol} (in wt.%) as follows:

$$C_d = \left(C_{Fe(II)} \cdot \frac{1}{5} + C_{S(-I)} \cdot \frac{7}{5}\right) \rho_r (1 - \varepsilon) \quad (14)$$

with:

$$C_{Fe(II)} = \left(C_{pyr} \cdot 0.465 + C_{dol} \cdot 0.059\right) \cdot \frac{1000}{55.845} \quad (15)$$

$$C_{S(-I)} = \left(C_{pyr} \cdot 0.535\right) \cdot \frac{1000}{32.065} \quad (16)$$

here $C_{Fe(II)}$ and $C_{S(-I)}$ are the molar concentrations (in mol/g) of reduced iron and sulfur, respectively. The mean density of the carbonate minerals was set to ρ_r = 2.7 g/cm³.

10.6. Results and discussion

10.6.1. Type, occurrence, and characterization of reactive minerals

Concentrations of organic carbon f_{oc} in the Upper Muschelkalk rock matrix are rather low with values in the range of 0.04–0.31 wt.% (three samples from quarry Herrenberg) and 0.2–1.8 wt.% (six samples from quarry Mötzingen). (Kleineidam *et al.* 1999; Kleineidam, Rügner and Grathwohl 1999) reported f_{oc} values in Muschelkalk rock fragments from the same region in the range of 0.03–0.09 wt.%. They also showed that organic matter in sedimentary rocks of substantial burial (e.g., the carbonates of the Muschelkalk) is composed mainly of inert kerogen and of limited bioavailability.

Results from pyrite (FeS_2) quantification via sulfur measurements performed in four rock samples from the quarry Herrenberg indicate that considerable amounts of pyrite are present in the rock matrix. The concentration ranges between 0.6 and 1.6 wt.%. Bivalent iron (Fe^{2+}) might also be present as substitute of Mg^{2+} in the crystal lattice of dolomites, particularly in the Rottweil Formation (Schauer and Aigner 1997). However, iron concentrations were too low to be quantified (Figure S2 of ESM), suggesting that these dolomites may not significantly contribute as electron donors. In addition to pyrite, marcasite, a metastable form of FeS_2, and saddle dolomite, an iron-bearing dolomite characterized by a higher Fe^{2+} content, are considered to constitute the main reactive minerals in the Upper Muschelkalk of the study area.

10.6.2. Syn-depositional and diagenetic pyrite

Pyrite (FeS_2) occurs as finely distributed crystals of 1–40 µm in size, or as framboidal pyrite in the micritic matrix of dark grey mudstones (see also Dunham 1962). Subhedral to euhedral, mostly uncorroded pyrite minerals are precipitated in anoxic to sub-oxic marine sediments at the water-sediment interface and during shallow burial. Sulfate reducing anaerobic bacteria consuming organic matter in the fresh sediments produce elemental sulfur and FeS, which is transformed to FeS_2 (Berner *et al.* 1985) (Figure 3a, b). Pyrite also occurs in the cross-bedded grainstones and in graded packstones in fecal pellets or along C-rich layers in shell fragments. This type of pyrite is interpreted to be of early diagenetic origin, precipitating within organic components in reducing microenvironments protected from the surrounding aerated water as described in (Hudson 1982) (Figure 3c). Together with coarse calcite cement, pyrite has been observed as subhedral crystals in the pore space in grainstones and in packstones together with coarse calcite cement (Figure 3d). Also, Hofmann (1989) reported pyrite and marcasite in the Upper Muschelkalk from the southeastern Black Forest area. Their origin during advanced diagenesis was related to processes of release and transport of metal ions by redox reactions (Hofmann 1989).

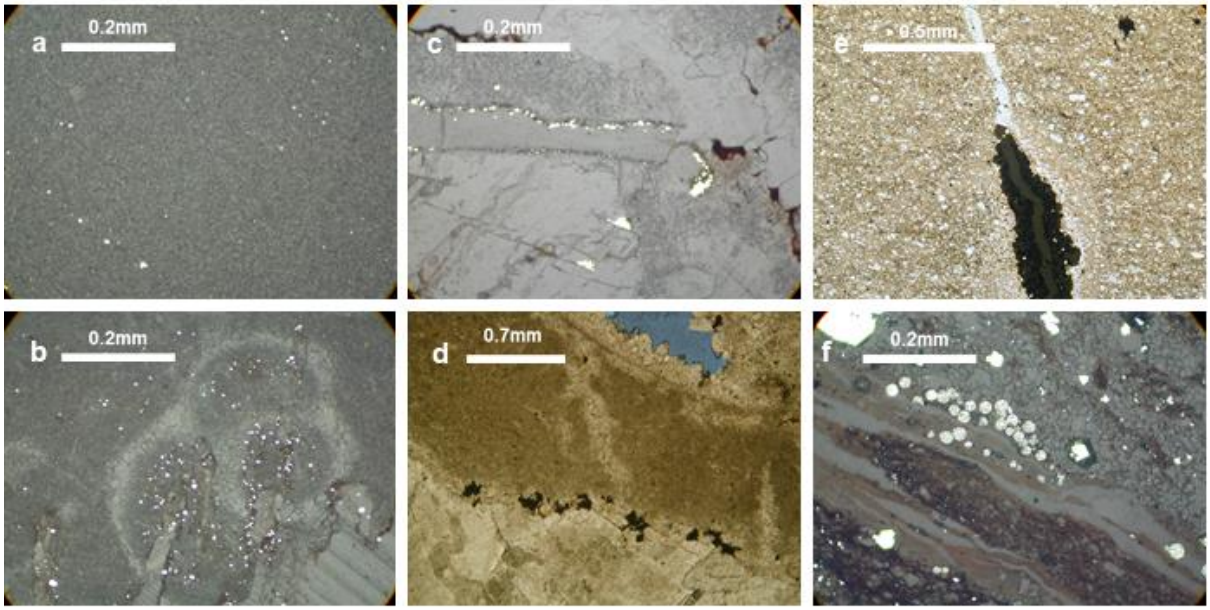

Figure. 3 Thin section photomicrographs of pyrite and marcasite appearing as white-yellow spots in reflected light and black spots in transmitted light. **a** Syn-depositional pyrite in basinal facies from quarry Mötzingen (reflected light, oil). **b** Syn-depositional pyrite in basinal facies from quarry Mötzingen (reflected light, oil). **c** Thin layer of syn-depositional pyrite lining rim of shell component in shoal facies from drill core Reusten (reflected light, oil). **d** Pyrite and blocky calcite cement in tempestite facies from quarry Herrenberg (transmitted light). **e** Post-depositional pyrite/marcasite in fracture of basinal facies from drill core Reusten (transmitted light). **f** Post-depositional framboidal pyrite/marcasite in fracture fill from drill core Reusten (reflected light, oil).

10.6.3. Post-depositional pyrite and ferrous iron bearing dolomite

Pyrite in fractures (Figs. 3e, f) has been observed in carbonates of various facies types. Pyrite precipitated as fracture fill occurs as aggregates, sometimes together with framboids and often in the orthorhombic metastable form of marcasite (FeS_2). The occurrence in fractures and veins point to a post-sedimentary transport of iron along tectonic pathways and is interpreted to be of hydrothermal origin. Similar ore mineralizations in Middle Triassic limestones have been described from other fault related settings near the Upper Rhine Graben and were interpreted as having formed by mixing of ascending fluids from the hot basement with saline formation water (Pfaff *et al.* 2010; Staude *et al.* 2010).

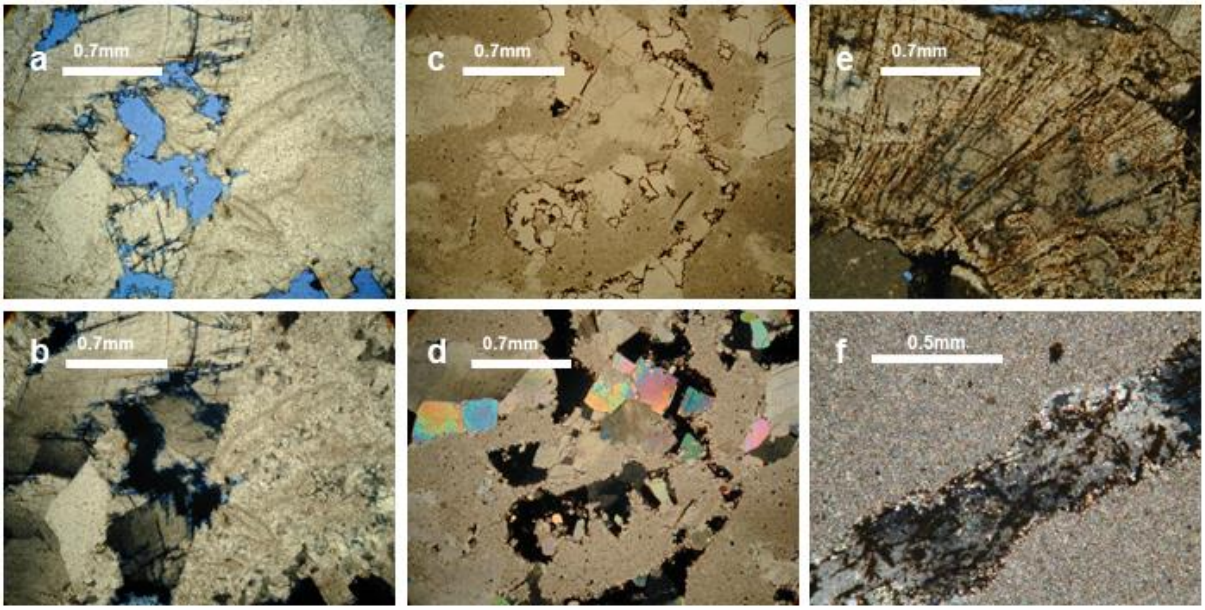

Figure. 4 Thin section photomicrographs (transmitted light) of saddle dolomite in different facies types and fractures. **a** Shoal facies from quarry Mötzingen using plane polarized light and **b** crossed polarized light. **c** Tempestite facies from drill core Reusten in plane polarized light **d** and crossed polarized light. **e** Fracture fill from quarry Mötzingen (plane polarized light). **f** Fracture fill from quarry Mötzingen (crossed polarized light).

Ferroan saddle dolomite can be found in fractures in various lithologies and as pore filling cement in moldic and vuggy pore spaces in grainstones and packstones (Figs. 4a - f) in an amount of up to 2 wt.% all over the study area. In thin sections saddle dolomite shows the typical oscillatory extinction in x-polarized light. Characteristic are large mm-sized crystals, which can be cloudy due to fluid inclusions and which show curved cleavage plains and crystal faces due to incorporation of additional lattice layers at the crystal edges (Searl 1989). Iron contents of 1.7–2.6 wt.% of the saddle dolomite were obtained from EDX analyses (Figure S2 of ESM). Oxidation to limonite results in yellow-brown colored covers along the cleavage plains and dark brown limonite coatings around the edges of the vugs (Koehrer *et al.* 2010) (Figure 4c).

Saddle dolomite forms from hypersaline fluids at elevated temperatures. Previous studies report precipitation at temperatures from 60° up to 180°C (Radke and Mathis 1980; Jay M. Gregg 1990; Spötl and Pitman 1998; Davies and Smith 2006), which can be caused by burial diagenesis, a higher geothermal gradient, or by upward movement of hydrothermal fluids (Machel and Lonnee 2002). Throughout SW-Germany, saddle dolomite is frequently known in the Lower and Upper Muschelkalk (Zeeh and Geng 2001; Koehrer *et al.* 2010; Pfaff *et al.* 2010; Palermo *et al.* 2012) and in Upper Jurassic carbonates (Reinhold 1998) where it precipitated at temperatures of 82–110° (Zeeh and Geng 2001). In the study area, however, only temperatures of about 60°C were reached during burial by the maximal 1000 m thick sedimentary overload of the Keuper and Jurassic formations (Gwinner and Geyer 2011) at an expected geothermal gradient of 30–40°C/1000 m. As already suggested by Zeeh and Geng (2001), it has therefore to be assumed that in the region “Oberes Gäu” percolating hydrothermal fluids supported the precipitation of the saddle dolomite as well as the pyrite/marcasite precipitation in fractures and veins of the Upper Muschelkalk. Similarly, Pfaff et al. (2010) related

saddle dolomite in the Upper Muschelkalk of the Upper Rhine Graben to an ascending metal-bearing hot fluid mixing with meteoric or sedimentary formation waters.

10.6.4. Distribution of reactive minerals within major facies types

The facies types may exert a major influence on the occurrence of the different types of iron minerals, which have been precipitated during early or late diagenesis or supported by hydrothermal events. In order to describe the reactivity of the Upper Muschelkalk with respect to nitrate reduction only a limited number of lithological, hydrogeological and geochemical distinct facies types were considered. By regrouping and merging the originally 21 facies types (Warnecke 2018) their number was significantly reduced to only four major petrophysical facies types categorizing the complete sequence of the Upper Muschelkalk in the study area. The four major petrophysical facies types are as follows (Table 1): (a) backshoal facies, (b) shoal facies, (c) tempestite facies, and (d) basinal facies. These differ mainly by the depositional environment but also by porosity and type and content of Fe(II) minerals.

10.6.5. Backshoal facies

The low energy backshoal facies is represented by the dolomites of the Rottweil-Formation, which were deposited in a peritidal and lagoonal setting. It is made up of dolomitic mud- to packstones with laminated or nodular bedding or intensive bioturbation. Porosity is high due to inter-crystalline porosity. Analysis of thin sections from the study area revealed a porosity value of 15–28 % for this facies type (Figure 5a). Values from previous published studies ranged from 0.1–32% documenting a high variability caused by a complex dolomitization history with early and late diagenetic dolomitization phases (Schauer and Aigner 1997, Köhrer et al. 2010). Pyrite was observed in thin sections in amounts of up to 1 wt.% as small anhedral pyrite crystals in the matrix. Saddle dolomite sometimes is present in pore space originating from bioturbation or anhydride solution and in fissures and fractures in an amount of up to 1 wt.%. Zeeh and Geng (2001) give iron content values in the Rottweil-Formation of 0.6–0.7 wt.%.

Table 1 Typical ranges of porosity, pore size, abundance of pyrite (Pyr) and saddle dolomite (sDol) as well as grain sizes of reactive minerals for the main facies types of the Middle Triassic carbonate rocks in the study area.

Facies type	Sedimentary environment	Abundance of facies[1] (%)	Porosity (%)	Pore size (µm)	Pyr (wt.%)	sDol (wt.%)	Size of minerals[2] (µm)
Backshoal facies	coastal to lagoonal setting	11	15–28	<1–280	up to 1.0	<0.1–1	n.d.
Shoal facies	shoal body	2*	15–30	<1–1700	1.0–2.0	<0.1–2	sDol: <100–1500
Tempestite facies	storm deposits of the mid to deeper ramp	12	0.5–10	<1–1500	1.0–2.0	<0.1–2	sDol: <100–1280
Basinal facies	basinal setting below storm wave base	75	0.5–5.0	n.d.	up to 4.0	<0.1–0.5	Pyr: <1–40

n.d.: not detected; [1]: based on data from quarry Mötzingen. [2]: sizes below the lower bound could not be quantified; *: in this study, shoal facies only refers to high-porosity horizons.

10.6.6. Shoal facies

Basinward follows the high energy shoal facies (Figure5b), which consists of bioclastic dolomites and limestones with brachiopod and bivalve shells, crinoidal columnar plates and lithoclasts with occasional trough cross bedding. Porosity is due to interparticle and moldic pores. Visual inspection of thin sections suggests a porosity of 15–30%. In previously published studies these grainstones have been interpreted as deposits of an energy absorbing shoal body. Mud was mostly washed out due to constant wave agitation in shallow water. Previously published studies give porosity values ranging from 4–30% (Braun 2003; Kostic and Aigner 2004; Koehrer *et al.* 2010; Palermo *et al.* 2012). Pyrite was observed in thin sections in amounts of 1–2 wt.% as early diagenetic pyrite in organic carbon-rich, reducing micro-environments of shell debris or in fecal pellets, or together with coarse calcite cement in or along the rim of vuggy and moldic pore spaces. This points to a precipitation of the two minerals at later diagenetic stages as described by Hofmann (1989). Saddle dolomite precipitated in the high porosity shoal facies presumably from percolating hydrothermal fluids and can be observed in fractures and as pore fillings in amounts of up to 2 wt.%.

10.6.7. Tempestite facies

The poorly sorted to graded bioclastic packstones to wackestones of the tempestite facies in the studied rock samples (Figure 5c) contain abundant skeletal debris of brachiopod and bivalve shells, crinoidal columnar plates and lithoclasts. Umbrella structures and bioturbation has been often observed. Moldic and vuggy porosity is the most common pore type. The tempestite facies consist of proximal to distal storm deposits of the mid to deeper ramp sedimented below the fair weather wave base. Fining upward layers showing an erosive base and hummocky cross stratification indicate sedimentation as tempestite around the storm wave base (Aigner 1985; Koehrer *et al.* 2010). Thin section examination suggests a porosity value of 0.5–10%. Porosity values from previous published studies range from 0.5–20% (Braun 2003; Kostic and Aigner 2004; Koehrer *et al.* 2010). Pyrite concentrations of 1–2 wt.% were observed in the tempestite facies in reducing micro-environments as early diagenetic pyrite and in vuggy and moldic pore space precipitated at later diagenetic stages as well as in fractures as pyrite/marcasite aggregates and framboids. Saddle dolomite occurs in pore space and in fissures in an amount of 0–2 wt.%.

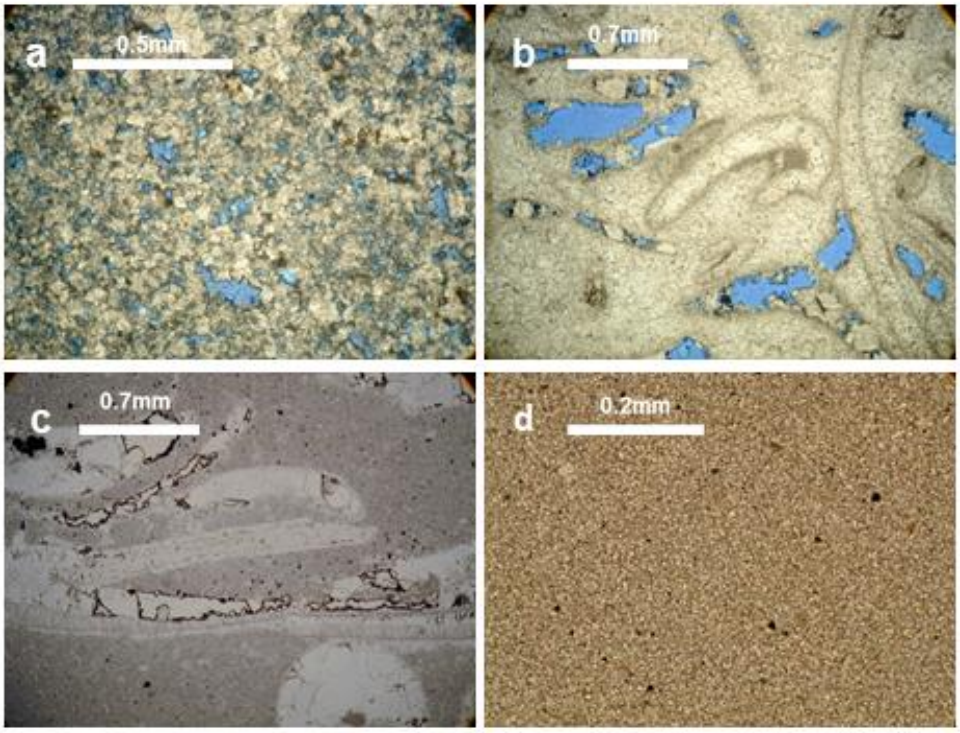

Figure. 5 Thin section photomicrographs (transmitted light) of main facies types. **a** Backshoal facies: dolomudstone with intercrystalline porosity (blue), quarry Herrenberg. **b** Shoal facies: bioclastic grainstone with vuggy porosity (blue), quarry Mötzingen. **c** Tempestite facies: bioclastic pack- to wackestone with shell debris and crinoids in micritic matrix, drilling core Reusten. **d** Basinal facies: micritic limestone, quarry Mötzingen.

10.6.8. Basinal facies

The mud dominated sediments of the basinal facies are suspension deposits of the low-energy deeper ramp below the storm wave base. They consist of dark grey well bedded or nodular, occasionally laminated limestones and marlstones and intercalations of thin claystone layers. Porosity is low with values of 0.5–5%, which corresponds to values from previous published studies range (Braun 2003; Kostic and Aigner 2004). However, values in the very low range could not precisely be determined from thin sections. Pyrite occurs as early diagenetic, finely dispersed subhedral to euhedral crystals of 1–40 µm in size (up to 4 wt.%) and indicates weakly to sub-oxygenated conditions, while bioturbation point to aerobic conditions (Figure 5d). Pyrite was not altered inside the rocks and showed no oxidation. Saddle dolomite was rare but can occur in fissures and fractures and rarely in cavities from bioturbation in an amount of up to 0.5 wt.%.

10.6.9. Evidence of reactivity

In rock fragments and thin sections of the shoal and the tempestite facies, alteration of the saddle dolomite resulted in dark, brown limonite rims in the moulds and vugs due to oxidation processes. Fresh limestones of the Upper Muschelkalk usually show a medium to dark grey colour of the rock matrix, but after some weathering, the colour turns to light brown on parts of the surfaces. The brown staining is believed to be caused by ferric oxyhydroxide accumulating in the outermost zone in

clusters and along fissures, which developed at pre-existing cracks or zones of weakness caused by discontinuity in sedimentation or by shear stress during tectonic movements. Brown weathering surfaces are commonly described, e.g., from the Jurassic Lincolnshire limestone by Baker et al. (2012), and usually attributed the oxidation of sulfide and ferrous iron in pyrite. Sulfide is converted to aqueous sulfate and removed from the rock matrix whilst ferrous iron is converted to a solid ferric oxyhydroxide phase (Baker *et al.* 2012). On the fracture surfaces a pyrite-depleted high porosity coating with brown staining will develop. The contribution of denitrification is difficult to assess and the observed coatings most likely resulted from long-term exposure to atmospheric or dissolved oxygen during the present and past hydrological cycles.

10.6.10. Groundwater flow paths with advective nitrate transport

Advective flow in the carbonate aquifer is restricted to the connected fracture and fissure network of the carbonate rocks. Assuming an average hydraulic aquifer conductivity between 3×10^{-6} and 4×10^{-5} m/s (D'Affonseca, Finkel and Cirpka 2020) and following Eq. (7), groundwater flow can be expected to mainly occur in fractures with apertures in the range of 0.2–2.0 mm given that spacing of the effective fractures is between 1.5 and 100 m, respectively. The lower value corresponds to the observed (vertical) fracture spacing at outcrops but would imply all fractures to be hydraulically effective which most likely is not the case. The upper value represents a single effective (horizontal) fracture over the total extend of the Upper Muschelkalk.

Depth profiles of groundwater inflow and nitrate concentrations at the artesian well ArtAlt, located in the confined part of the aquifer, confirm that only a few fractures significantly contribute to groundwater flow (Figure 6b). Based on flowmeter logging, four major active fractures were identified (Table 2), which under artesian conditions produced a natural groundwater discharge of 5–50 L/s (2014–2019).

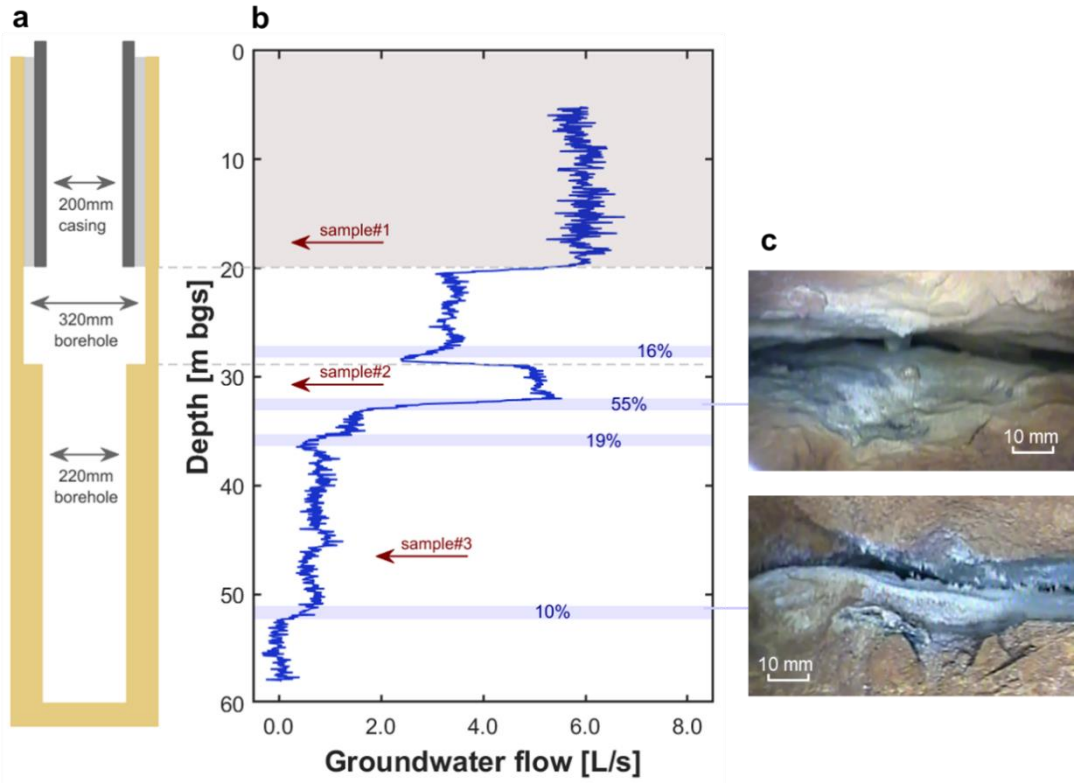

Figure. 6 a Schematic borehole profile of the artesian well ArtAlt. **b** Flowmeter log at ArtAlt at natural outflow conditions. Zones of significant groundwater inflow are characterized by steep increases in (vertical) groundwater flux and indicated by blue-shaded areas. The percentages represent the relative increase of the flow rate in relation to the total outflow of about 6 L/s. Variability of the baseline limits the detection of inflows with a contribution of >5%. The sharp drop at 28.5 m as well as the sharp increase in vertical flux at 20 m (dashed lines) are solely caused by changes in borehole diameter at these depths (see left panel). Red arrows indicate the depths where three groundwater samples for chemical analyses were taken directly after flowmeter logging. **c** Pictures of the fractures at 26.5-28.0 m and 32.0-33.5 m bgs taken from video log.

The video-logging revealed that depths of high inflow correspond with horizontal, partly karstified open bedding planes (Figure 6c). These “fractures” most probably evolved above thin interbeddings of low permeable marl or clay layers within the carbonate rocks. This is confirmed by a gamma profile of the borehole at ArtAlt. A correlation with the gamma profile measured at the quarry in Mötzingen (Koehrer *et al.* 2010; Figure 7) indicates that the two uppermost flow paths are located within the dolomite rocks of the Rottweil-Formation mainly consisting of high-porosity backshoal facies.

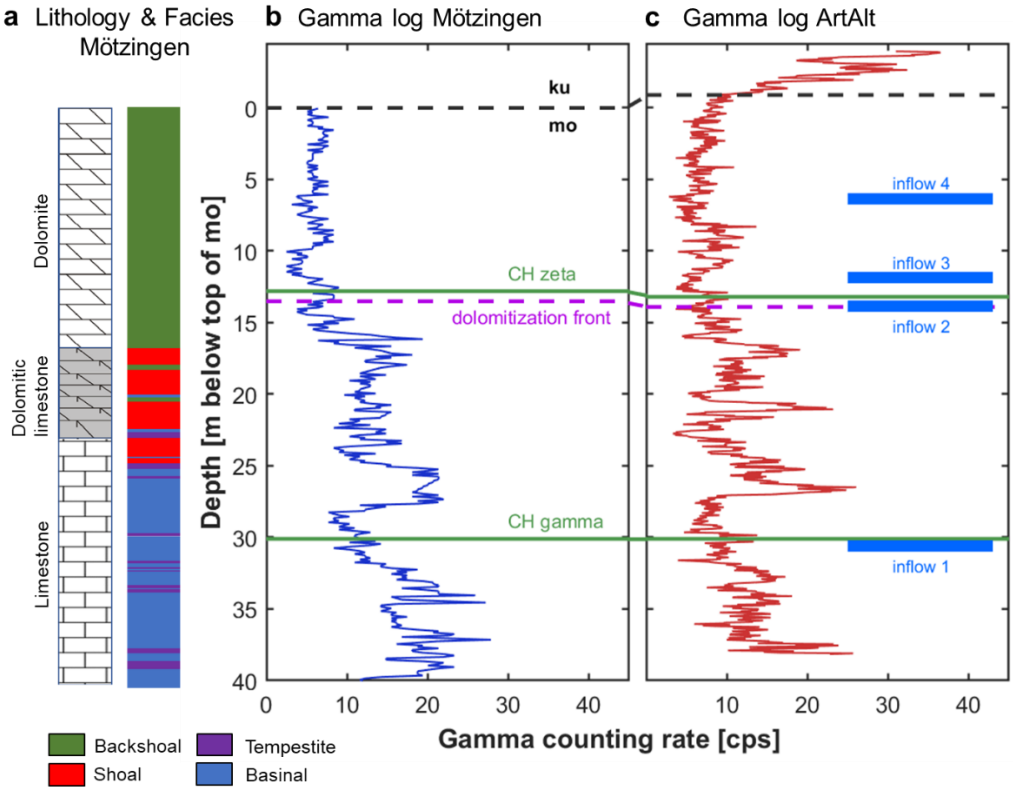

Figure 7 a Facies distribution at quarry Mötzingen (lower part not shown here); **b** Gamma log at quarry Mötzingen; and **c** Gamma log at groundwater well ArtAlt. Indicator clay horizons (CH) are shown as green lines for orientation. Blue bars indicate the locations of the observed groundwater inflows at ArtAlt. The depth scale is related to the boundary between Upper Muschelkalk (mo) and Lower Keuper (ku). The Mötzingen data was modified after Koehrer *et al.* (2010).

Besides the four active bedding planes, the video logging shows ten additional open bedding planes, which did not produce a clear signal in the flowmeter logs and apparently do not contribute (or only to a minor extent) to groundwater inflows. According to the gamma profile, most of these structures are also associated with bedding planes of carbonate rock overlying clay horizons, as indicated by peaks in gamma counting rates near the bottom of the fractures. However, the data at ArtAlt do not provide evidence if the active bedding planes below the top of the dolomite rocks, including the two lower flow paths have contact to high-porosity tempestite or low-porosity micritic (basinal) facies.

Nitrate concentrations were low (1–3 mg/L) for all groundwater inflows (see Table 2). The trend to slightly higher nitrate concentrations in the upper inflow horizons could be due to the higher relative discharge (and hence flow velocity) within these active bedding planes resulting in a deeper propagation of the nitrate plume into the aquifer along these flow horizons. Low nitrate concentrations in all inflows suggest that conditions for nitrate retardation by reactive processes and matrix diffusion are similar at all groundwater flow paths. Moreover, the rather constant sulfate concentrations (agreement within analytical uncertainties) in all sampled groundwater inflows indicate that nitrate reduction is coupled to oxidation of a similar amount (or absence) of pyrite along the different flow horizons.

Table 2 Summary of vertical fluxes representing groundwater inflow Q_{in}, relative contribution of fractures f_{in}, and concentrations of nitrate (NO_3^-) and sulfate (SO_4^-) in water samples or calculated for the individual groundwater inflows using Eq. (1) at different depths of the artesian well ArtAlt.

Depth [m bgs]	Type	Facies	Q_{in} [L/s]	f_{in} [%]	NO_3 [mg/L]	SO_4 [mg/L]
17.5	water sample 3	-	-	-	2.2 ± 0.1	93 ± 8
26.5–28.0	inflow 4	SHF/BSF	0.96	16.0	2.7 ± 1.2	91 ± 24
30.5	water sample 2	-	-	-	2.0 ± 0.1	93 ± 8
32.0–33.5	inflow 3	SHF/BSF	3.33	55.5	2.2 ± 0.2	94 ± 12
34.5–36.0	inflow 2	SHF/BSF/BAF	1.11	18.5		
46.0	water sample 1	-	-	-	1.2 ± 0.1	89 ± 8
51.0–52.0	inflow 1	BAF/TEF	0.61	10.1	1.2 ± 0.1	89 ± 8

SHF: shoal facies; BSH: backshoal facies; TEF: tempestite facies; BAF: basinal facies
Given errors are due to analytical uncertainties and uncertainties resulting from the mixing calculations

The findings in ArtAlt with respect to number and properties of flow paths as well as their position within the Upper Muschelkalk were confirmed at two other locations (production wells TBAlt3, TBEnt1) in about 1.5 and 5.5 km distance from ArtAlt (Figure 1). In both wells three to four effective horizontal flow paths were identified by the flowmeter logging (Figs. S3 and S4 of ESM). Main groundwater inflow again was observed in or close to the high-porosity dolomites of the backshoal facies at the top of the Upper Muschelkalk (Rottweil Formation). These findings suggest, that a few partly karstified bedding planes control horizontal flow in the Muschelkalk aquifer at a regional scale. Similar primary flow and transport along major horizontal fractures was inferred from tracer tests and flow logs in a limestone aquifer in Denmark (Mosthaf *et al.* 2018). Although no vertical fractures were observed at the well, such fractures, when roughly aligned with the general flow direction, may additionally contribute to regional groundwater flow. Moreover, due to the tectonic block structure at the study site (D'Affonseca, Finkel and Cirpka 2020), the horizontal flow is possibly intercepted on the 1–10 km-scale by vertical flow and mixing at fault zones with significant vertical displacements.

10.6.11. Zones of high nitrate turnover in the aquifer

While oxic conditions usually prevail in the uncovered part of karstic or fractured groundwater systems, conditions favourable for denitrification (e.g., low dissolved oxygen) are restricted to the anoxic zone, which is often situated within the confined parts of an aquifer (Rivett *et al.* 2008; Henson *et al.* 2017). This is also the case at the study site where high concentrations of dissolved oxygen (3–9 mg/L) and of nitrate (up to 60 mg/L) were measured in groundwater samples from the uncovered part of the Muschelkalk aquifer (Visser *et al.* 2020). Although Visser *et al.* (2021) found evidence for potential denitrification in niches where (near) anoxic conditions might develop, e.g., beyond the O_2 depletion front in the pore matrix along fractures of the phreatic zone or epikarst, a strong decline in groundwater O_2 and NO_3^- concentrations to values close to the detection limit were only found in the confined part of the aquifer (e.g., well ArtAlt). In this part, the replenishment of oxygen due to fast transport along karstic features or vertical fractures across the vadose zone is prevented by the covering sediments.

High absolute nitrate turnover rates can be expected to occur at those locations where flow in fractures coincides with high abundance of reactive minerals in the rock matrix. Most likely, ferrous iron and reduced sulfur bearing minerals in the rock matrix (Table 1) are the main electron donors in the carbonate aquifer. Particularly, the divalent iron minerals pyrite/marcasite and saddle dolomite provide a considerable electron donor capacity for nitrate reduction. Therefore, zones of oxygen consumption and subsequent nitrate reduction in the fractured aquifer are attributed to the occurrence and spatial distribution of these minerals, which can be found (1) in the porous backshoal, shoal and tempestite facies, where the saddle dolomite can be dissolved and the released Fe(II) is oxidized subsequently; the occurrence of these reactions is documented by the limonite rims in vuggy and moldic pore spaces, (2) along fractures filled with post-sedimentary saddle dolomite and pyrite/marcasite, precipitated from ascending hydrothermal fluids, and (3) in the micritic basinal carbonates along fractures and bedding planes, where exposed crystals of syn-sedimentary pyrite can be oxidized to limonite, while pyrite in the central parts of the rock matrix remains unaltered (Petrova et al. 2021; Baker et al. 2012).

For turnover processes to take place, the reactive minerals are assumed to come into contact with O_2 or NO_3^-, which are transported with groundwater along the horizontal, karstified bedding planes or vertical fractures in direction of the general flow. High diffusive fluxes and therefore high nitrate turnover can be expected for the high-porosity shoal and backshoal facies, which were found to host the largest part of groundwater flow at the investigated wells in the confined part of the aquifer. However, due to lacking knowledge of exact routing of the flow paths between recharge and the studied wells, fractures or bedding planes passing other facies types might contribute substantially to O_2 and NO_3^- depletion, particularly if associated with Fe(II)-rich hydrothermal precipitates near fault zones.

10.6.12. Remaining nitrate reduction potential of the aquifer

The temporal development of the aquifer's potential to protect wells against nitrate was calculated for the capture zone of a hypothetical water supply well in the confined part of the aquifer, 5 km distant from the uncovered oxic part (Figure 2). To this end, Eq. (11) was applied with measured porosities and concentrations of pyrite and saddle dolomite of each facies type and a fracture spacing d = 10 m observed at the investigated wells. In Figure 8, the remaining well-protective nitrate reduction potential r_{PP} of each facies is shown for two nitrate input scenarios: "long-term (~100,000 yr) natural background" and "short-term (~100 yr) anthropogenic input". The simulations show that the time required to deplete the nitrate reduction capacity strongly depends on the porosity of the facies constituting the rock matrix. By contrast, the variation of reactive mineral abundances between the facies is small (Table 1) and therefore only of minor importance for the differences in r_{PP}. For NO_3^- background concentrations below 1 mg/L, the high-porous shoal and backshoal facies retains more than 80% of the reduction capacity even for groundwater flow that started prior to the last interglacial (Figure 8a). If the background NO_3^- is transported along fractures in the low-porous basinal facies, the reduction capacity of the aquifer section becomes depleted after about ten thousand years (Figure 8c).

When high anthropogenic NO_3^- concentrations are considered, which entered the groundwater as a consequence of the increased fertilizer application since the 1960s, the reduction capacity remains nearly unaltered for the shoal/backshoal and tempestite facies (Figure 8d, e). The results for the low-porosity basinal facies indicate a decrease to about 60–70% after anthropogenic NO_3^- input of approximately 60 years (Figure 8f). The preservation of the reduction potential in the tempestite and particularly shoal/backshoal facies is a consequence of high matrix porosities (note that the effective diffusion coefficient D_e increases non-linearly with porosity in Eq. (3)). The higher the matrix porosity, the larger is the volume of the rock matrix that contributes to nitrate reduction and the larger is the quantity of available electron donors. This is indicated by the substantially larger penetration depth of the depletion front of $z_m = 38$ cm in the shoal/backshoal rock matrix as compared to the basinal facies with $z_m = 0.07$ cm.

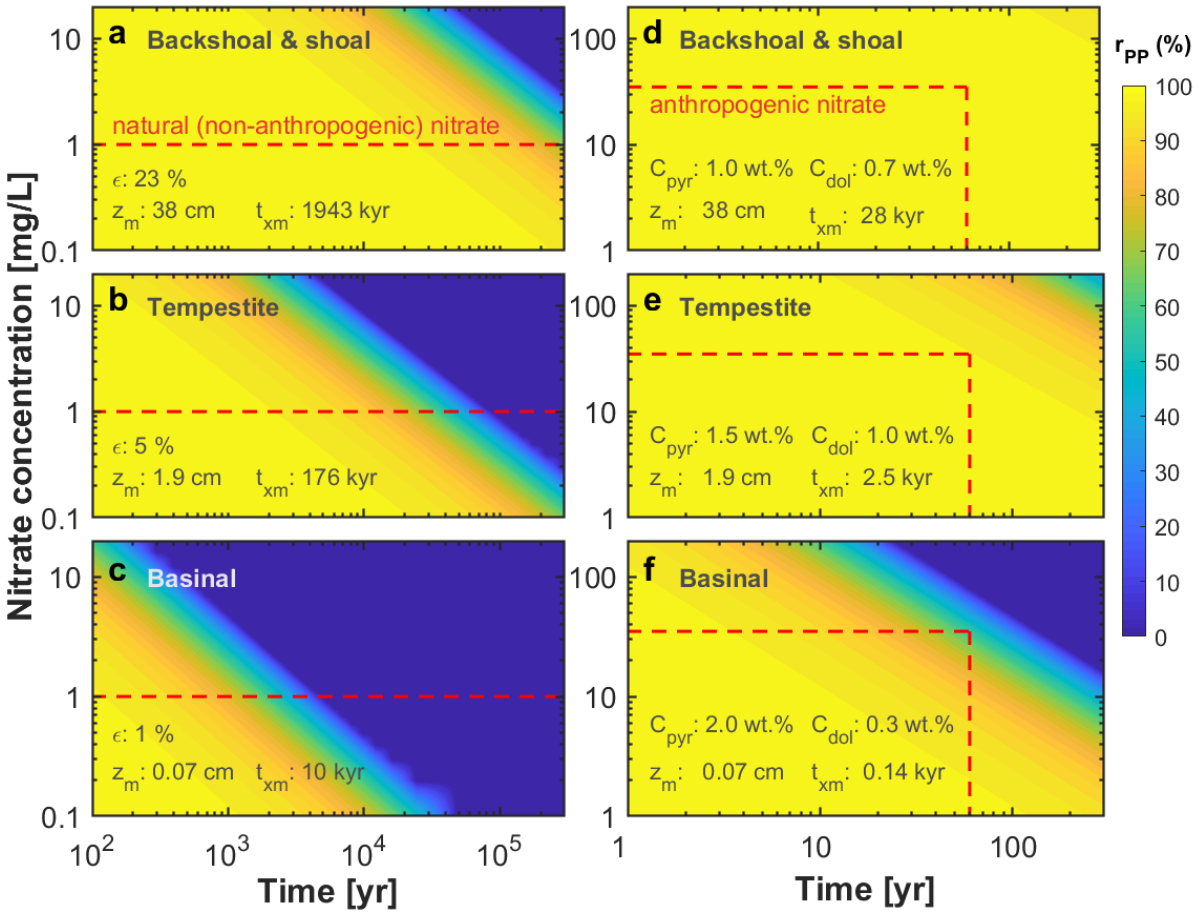

Figure 8. Remaining well-protective nitrate reduction potential r_{PP} (in %) as a function of the NO_3^- concentration (y-axis) in groundwater entering the fractures and the time with given NO_3^- loads (x-axis). **a-c** Contours for long-term natural NO_3^- input concentrations for the different facies. The dashed red line assumes low NO_3^- background values in groundwater ($C_{NO3} = 1$ mg/L) over long (but unknown) periods of time. **d-f** Contours for high NO_3^- concentrations resulting from anthropogenic N additions for the different facies. The dashed red line highlights the approximated time of high nitrate conditions ($C_{NO3} = 35$ mg/L) representing average NO_3^- concentrations in the study area. Values for t_{xm} and $z_m(x = 0)$ refer to the time when the well-protective nitrate reduction will be entirely depleted ($r_{PP} = 0$) and the depth the reaction front has propagated into the matrix at the upgradient boundary of the anoxic zone at this time.

Calculating the average mineral depletion depth in the rock matrix for different porosities at $x = 0$ yields: $z_m(O_2) + z_m(NO_3) = 0.002$ to 1.1 m, which is much smaller than the spacing of the fractures. This means that only a small part of the aquifer volume contributes to oxygen consumption and nitrate reduction and hence to the protection of the water supply well against a nitrate breakthrough.

The estimated r_{PP} values shown in Figure 8 are based on the assumption that all electron donors are used up directly in the rock matrix in instantaneous reactions. Therefore, these estimates represent optimal conditions for the considered nitrate reduction scenarios. Lower r_{PP} values are expected in case of unfavourable conditions for mineral dissolution or reactivity, or if microbial access is limited because only a fraction of the electron donors is available for the reactions. The results are sensitive to the hydraulic aquifer parameters, ε d, K, and I (r_{PP} depends on the square of these parameters). However, thanks to the well logging campaigns and previous work in the study area reported in D'Affonseca, Finkel and Cirpka (2020), these parameters could be estimated reasonably well. Against this background, we believe that the r_{PP} values presented here represent good, but optimum estimates. However, the general trends are assumed to be well represented by Figure 8, which also demonstrates the large differences between the facies types. Additional uncertainties remain due to often low accuracy of the contributing variables, such as the hydraulic conductivity K.

The flowmeter logs of three investigated wells at the study site show that a large fraction of groundwater flow takes place in the backshoal facies. Since all wells are located in the confined part of the aquifer, in about 5 to 10 km distance from the boundary of the uncovered oxic part, the modeling results indicate that for these wells the nitrate reduction potential can be expected to remain fully intact for more than hundreds of years. However, if groundwater flow towards the wells also includes bedding planes or fractures located in facies of lower porosity, the aquifer's nitrate reduction potential that can be utilized to protect the wells might diminish over a much shorter period of time. Figure 6 and Figs. S3 and S4 of ESM also show that total groundwater discharge is not distributed equally among the flow paths but is usually dominated by one of the contributing bedding planes. Under the assumption that discharge from all but one groundwater flow path is negligible, the calculation of r_{PP} using Eq. (11) has to account for an increase of the fracture spacing d (by a factor equal to $n_f = 4$), in order to maintain the average hydraulic conductivity K of the aquifer section. In this case, the reduction potential protecting a supply well in the basinal facies would be fully depleted already after 30 years of well operation for NO_3^- concentrations above 10 mg/L (Figure S5 of ESM). Although the aquifer has an almost infinite nitrate reduction potential, this again shows the large uncertainty in predicting reactive nitrate transport in such an aquifer system.

10.7. Conclusions

Catchment scale characterization of fractured carbonate aquifers requires a priori knowledge of sedimentary processes including diagenesis and tectonics in combination with hydrogeological field observations and mineralogical (e.g. thin sections, EDX), chemical (f_{oc}, Fe(II)) and physical analysis of rock samples from different facies. This is a prerequisite to assess reactive processes such as oxidation (e.g., in chemical weathering) and to describe the reactive transport of solutes such as

nitrate in groundwater. Based on investigations of the fractured Upper Muschelkalk aquifer in SW Germany, the nitrate reduction potential is mainly given by (1) the presence of Fe(II) or S(-I) bearing mineral phases such as pyrite, marcasite, or saddle dolomite formed under anaerobic conditions in shallow marine sediments or from percolating low-temperature hydrothermal fluids, (2) the diffusion coefficients and thus the matrix porosity of the different carbonate facies, and (3) the spacing of groundwater flow paths (along fractures or bedding planes) and their spatial interrelation with the different facies types. Large differences in reactive nitrate transport exist between the facies types and additional uncertainties arise due to the natural variability in matrix porosity and flow paths. The simple electron acceptor/donor balance approach presented in this study nevertheless may provide important information for water suppliers as it allows to approximately estimate the nitrate reduction potential for water supply wells or other monitoring points. Using observed data from the study site, the results of the estimation shows that concentrations of Fe(II)-minerals in the range of 1–4 wt.% represent a high nitrate reduction potential and that to date only a minor part of the nitrate reduction potential of the fractured aquifer has been consumed. Particularly, if large parts of groundwater flow take place in high-porosity facies, the nitrate reduction capacity will most likely remain high over centuries. In contrast, if matrix porosities are low and flow is restricted to one or just as few conduits, then little nitrate reduction is expected. These findings likely also apply for comparable fractured limestone aquifers which have been formed under similar conditions.

10.8. Acknowledgements

For support in the laboratory, we want to thank Bernice Nisch, Sara Cafisso, Annegret Walz. Per Jeisecke and Tatjana Miranda. Special thanks go to Andre Pellerin (Aarhus University) for sulfide analyses, to the staff of the Ammertal-Schönbuch Gruppe and the quarries Herrenberg and Mötzingen for providing access and technical support, and to the companies HydroTest Karch and Voutta Grundwasserhydraulik for support with borehole logging and sampling.

10.9. Funding

Open Access funding enabled and organized by Projekt DEAL. This study was supported by the German Research Foundation (DFG) funded Collaborative Research Centre 1253 CAMPOS (Project 5: Fractured Aquifer) (DFG Grant Agreement SFB 1253/1). On behalf of all authors, the corresponding author states that there is no conflict of interest.

References

Aigner T. *Storm Depositional Systems*. Berlin/Heidelberg: Springer-Verlag, 1985.

Aigner T, Bachmann GH. Sequence-stratigraphic framework of the German Triassic. *Sediment Geol* 1992;**80**:115–35.

Appelo CAJ, Postma D. *Geochemistry, Groundwater and Pollution*. Appelo CAJ, Postma D (eds.). CRC Press, 2004.

Baatartsogt B, Schwinn G, Wagner T *et al.* Contrasting paleofluid systems in the continental basement: a fluid inclusion and stable isotope study of hydrothermal vein mineralization, Schwarzwald district, Germany. *Geofluids* 2007;**7**:123–47.

Baker KM, Bottrell SH, Hatfield D *et al.* Reactivity of pyrite and organic carbon as electron donors for biogeochemical processes in the fractured Jurassic Lincolnshire limestone aquifer, UK. *Chem Geol* 2012;**332**–**333**:26–31.

Berner RA, De Leeuw J. W., Spiro B. *et al.* Sulphate reduction, organic matter decomposition and pyrite formation source : Philosophical Transactions of the Royal Society of London . Series A , Mathematical and Physical Sciences , Jul . 31 , 1985 , Vol . 315 , No . 1531 , Geochemistry of Published. *Philos Trans R Soc London Ser A, Math Phys Sci* 1985;**315**:25–38.

Bons PD, Fusswinkel T, Gomez-Rivas E *et al.* Fluid mixing from below in unconformity-related hydrothermal ore deposits. *Geology* 2014;**42**:1035–8.

Braun S. Quantitative analysis of carbonate sandbodies: outcrop analog study from an epicontinental basin (Triassic Germany). *Diss Univ Tübingen* 2003.

Carlé W. Bau und Entwicklung der Südwestdeutschen Großscholle. *Beih Geol Jb* 1955;**16**.

D'Affonseca FM, Finkel M, Cirpka OA. Combining implicit geological modeling, field surveys, and hydrogeological modeling to describe groundwater flow in a karst aquifer. *Hydrogeol J* 2020;**28**:2779–802.

Davies GR, Smith LB. Structurally controlled hydrothermal dolomite reservoir facies: An overview. *Am Assoc Pet Geol Bull* 2006;**90**:1641–90.

Dunham RJ. Classification of carbonate rocks according to depositional textures. In: Classification of Carbonate Rocks — A Symposium. *AAPG Mem* 1962;**1**:108–21.

Einsiedl F, Mayer B. Hydrodynamic and Microbial Processes Controlling Nitrate in a Fissured-Porous Karst Aquifer of the Franconian Alb, Southern Germany. *Environ Sci Technol* 2006;**40**:6697–702.

Farnleitner AH, Wilhartitz I, Ryzinska G *et al.* Bacterial dynamics in spring water of alpine karst aquifers indicates the presence of stable autochthonous microbial endokarst communities. *Environ Microbiol* 2005;**7**:1248–59.

Fossing H, Jorgensen BB. Measurement of bacterial sulfate reduction in sediments : Evaluation of a single-step chromium reduction method. *Biogeochemistry* 1989;**8**:205–22.

Goldscheider N, Chen Z, Auler AS *et al.* Global distribution of carbonate rocks and karst water resources. *Hydrogeol J* 2020;**28**:1661–77.

Grathwohl P. Diffusion in natural porous media: contaminant transport, sorption/desorption and dissolution kinetics. 1998.

Gwinner OF, Geyer PM. *Geologie von Baden-Württemberg*. herausgegeben von: Matthias Geyer; Edgar Nitsch; Theo Simon (ed.). Stuttgart, Germany: Schweizerbart Science Publishers, 2011.

Hagdorn H. The Muschelkalk in Germany – An introduction. In: Muschelkalk, A Field Guide. *Goldschneck Verlag, Korb* 1991.

Heffernan JB, Albertin AR, Fork ML *et al.* Denitrification and inference of nitrogen sources in the karstic Floridan Aquifer. *Biogeosciences* 2012;**9**:1671–90.

Hegler F, Schmidt C, Schwarz H *et al.* Does a low-pH microenvironment around phototrophic FeII-oxidizing bacteria prevent cell encrustation by FeIII minerals? *FEMS Microbiol Ecol* 2010;**74**:592–600.

Henson WR, Huang L, Graham WD *et al.* Nitrate reduction mechanisms and rates in an unconfined eogenetic karst aquifer in two sites with different redox potential. *J Geophys Res Biogeosciences* 2017;**122**:1062–77.

Herrmann M, Opitz S, Harzer R *et al.* Attached and suspended denitrifier communities in pristine limestone aquifers harbor high fractions of potential autotrophs oxidizing reduced iron and sulfur compounds. *Microb Ecol* 2017;**74**:264–77.

Hofmann B. Erzmineralien in paläozoischen, mesozoischen und tertiären Sedimenten der Nordschweiz und Südwestdeutschlands. *Schweizerische Mineral und Petrogr Mitteilungen* 1989;**69**:345–57.

Hudson JD. Pyrite in ammonite-bearing shales from the Jurassic of England and Germany. *Sedimentology* 1982;**29**:639–67.

Husic A, Fox J, Adams E *et al.* Nitrate pathways, processes, and timing in an agricultural karst system: development and application of a numerical model. *Water Resour Res* 2019;**55**:2079–103.

Jakus N, Blackwell N, Osenbrück K *et al.* Nitrate removal by a novel lithoautotrophic nitrate-reducing iron(II)-oxidizing culture enriched from a pyrite-rich limestone aquifer. *Appl Environ Microbiol* 2021, DOI: 10.1128/AEM.00460-21.

Jay M. Gregg KLS. Dolomitization and Dolomite Neomorphism in the Back Reef Facies of the Bonneterre and Davis Formations (Cambrian), Southeastern Missouri. *SEPM J Sediment Res* 1990;**Vol. 60**, DOI: 10.1306/212F91E2-2B24-11D7-8648000102C1865D.

Kim JJ, Comstock J, Ryan P *et al.* Denitrification and dilution along fracture flowpaths influence the recovery of a bedrock aquifer from nitrate contamination. *Sci Total Environ* 2016;**569**–**570**:450–68.

Kleineidam S, Rügner H, Grathwohl P. Influence of petrographic composition/organic matter distribution of fluvial aquifer sediments on the sorption of hydrophobic contaminants. *Sediment Geol* 1999;**129**:311–25.

Kleineidam S, Rügner H, Ligouis B *et al.* Organic matter facies and equilibrium sorption of phenanthrene. *Environ Sci Technol* 1999;**33**:1637–44.

Kludt C, Weber F, Bergmann A *et al.* Identifizierung der Nitratabbauprozesse und Prognose des Nitratabbaupotenzials in den Sedimenten des Hessischen Rieds. *Grundwasser* 2016;**21**:227–41.

Koehrer BS, Heymann C, Prousa F *et al.* Multiple-scale facies and reservoir quality variations within a dolomite body - Outcrop analog study from the Middle Triassic, SW German Basin. *Mar Pet Geol* 2010;**27**:386–411.

Korom S. Natural denitrification in the saturated zone: a review. *Water Resour Res* 1992;**28**:1657–68.

Kostic B, Aigner T. Sedimentary and poroperm anatomy of shoal-water carbonates (Muschelkalk, South-German Basin): an outcrop-analogue study of inter-well spacing scale. *Facies* 2004;**50**:113–31.

Kuypers MMM, Marchant HK, Kartal B. The microbial nitrogen-cycling network. *Nat Rev Microbiol* 2018;**16**:263–76.

Loschko M, Wöhling T, Rudolph DL *et al.* An electron-balance based approach to predict the decreasing denitrification potential of an aquifer. *Groundwater* 2019;**57**:925–39.

Lübben A, Leven C. The Starzach site in Southern Germany: a site with naturally occurring CO_2 emissions recovering from century-long gas mining as a natural analog for a leaking CCS reservoir. *Environ Earth Sci* 2018;**77**:316.

Machel HG, Lonnee J. Hydrothermal dolomite—a product of poor definition and imagination. *Sediment Geol* 2002;**152**:163–71.

Morris BL, Lawrence ARL, Chilton PJC *et al.* Groundwater and its susceptibility to degradation: A global assessment of the problem and options for management. *Early Warn Assess Rep Ser* 2003;**RS. 03-3**.

Mosthaf K, Brauns B, Fjordbøge AS *et al.* Conceptualization of flow and transport in a limestone aquifer by multiple dedicated hydraulic and tracer tests. *J Hydrol* 2018;**561**:532–46.

OECD. *Environmental Performance of Agriculture in OECD Countries Since 1990*., 2008.

Opazo T, Aravena R, Parker B. Nitrate distribution and potential attenuation mechanisms of a municipal water supply bedrock aquifer. *Appl Geochem* 2016;**73**:157–68.

Orr A, Nitsche J, Archbold M *et al.* The influence of bedrock hydrogeology on catchment-scale nitrate fate and transport in fractured aquifers. *Sci Total Environ* 2016;**569**–**570**:1040–52.

Palermo D, Aigner T, Seyfang B *et al.* Reservoir properties and petrophysical modelling of carbonate sand bodies: Outcrop analogue study in an epicontinental basin (Triassic, Germany). *Geol Soc London Spec Publ* 2012;**370**:111–38.

Pauwels H, Foucher JC, Kloppmann W. Denitrification and mixing in a schist aquifer: Influence on water chemistry and isotopes. *Chem Geol* 2000;**168**:307–24.

Pfaff K, Hildebrandt LH, Leach DL *et al.* Formation of the Wiesloch Mississippi Valley-type Zn-Pb-Ag deposit in the extensional setting of the Upper Rhinegraben, SW Germany. *Miner Depos* 2010;**45**:647–66.

Picioreanu C, van Loosdrecht MCM, Heijnen JJ. Modelling the effect of oxygen concentration on nitrite accumulation in a biofilm airlift suspension reactor. *Water Sci Technol* 1997;**36**:147–56.

Radke B, Mathis R. On the formation and occurrence of saddle dolomite. *J Sed Pet* 1980;**50**:1149–68.

Reicherter K, Froitzheim N, Jarosiński M *et al.* Alpine tectonics north of the Alps. *The Geology of Central Europe Volume 2: Mesozoic and Cenozoic*. Geological Society of London, 2008.

Reinhold C. Multiple episodes of dolomitization and dolomite recrystallization during shallow burial in Upper Jurassic shelf carbonates: eastern Swabian Alb, southern Germany. *Sediment Geol* 1998;**121**:71–95.

Ring U, Bolhar R. Tilting, uplift, volcanism and disintegration of the South German block. *Tectonophysics* 2020;**795**:228611.

Rivas A, Singh R, Horne D *et al.* Denitrification potential in the subsurface environment in the Manawatu River catchment, New Zealand: Indications from oxidation-reduction conditions, hydrogeological factors, and implications for nutrient management. *J Environ Manage* 2017;**197**:476–89.

Rivett MO, Buss SR, Morgan P *et al.* Nitrate attenuation in groundwater: A review of biogeochemical controlling processes. *Water Res* 2008;**42**:4215–32.

Schauer M, Aigner T. Cycle stacking pattern, diagenesis and reservoir geology of peritidal dolostones, Trigonodus-Dolomite, Upper Muschelkalk (Middle Triassic, SW-Germany). *Facies* 1997;**37**:99–113.

Schwientek M, Einsiedl F, Stichler W *et al.* Evidence for denitrification regulated by pyrite oxidation in a heterogeneous porous groundwater system. *Chem Geol* 2008;**255**:60–7.
Sidborn M, Neretnieks I. Long term redox evolution in granitic rocks: Modelling the redox front propagation in the rock matrix. *Appl Geochemistry* 2007;**22**:2381–96.
Sidborn M, Neretnieks I. Long-term oxygen depletion from infiltrating groundwaters: Model development and application to intra-glaciation and glaciation conditions. *J Contam Hydrol* 2008;**100**:72–89.
Smith RL, Duff JH. Denitrification in a sand and gravel aquifer. *Appl Environ Microbiol* 1988;**54**:1071–8.
Spötl C, Pitman JK. Saddle (baroque) dolomite in carbonates and sandstones: a reappraisal of a burial-diagenetic concept. *Carbonate Cem Sandstones Distrib Patterns Geochemical Evol* 1998;**26**:437–60.
Starke R, Müller M, Gaspar M *et al.* Candidate Brocadiales dominates C, N and S cycling in anoxic groundwater of a pristine limestone-fracture aquifer. *J Proteomics* 2017;**152**:153–60.
Staude S, Bons PD, Markl G. Hydrothermal vein formation by extension-driven dewatering of the middle crust: An example from SW Germany. *Earth Planet Sci Lett* 2009;**286**:387–95.
Staude S, Mordhorst T, Neumann R *et al.* Compositional variation of the tennantite–tetrahedrite solid-solution series in the Schwarzwald ore district (SW Germany): The role of mineralization processes and fluid source. *Mineral Mag* 2010;**74**:309–339.
Straub KL, Benz M, Schink B *et al.* Anaerobic, nitrate-dependent oxidation of ferrous iron. *Appl Environ Microbiol* 1996;**62**:1458–60.
Vías JM, Andreo B, Perles MJ *et al.* Proposed method for groundwater vulnerability mapping in carbonate (karstic) aquifers: The COP method. *Hydrogeol J* 2006;**14**:912–25.
Visser AN, Lehmann MF, Rügner H *et al.* Fate of nitrate during groundwater recharge in a fractured karst aquifer in Southwest Germany. *Hydrogeol J* 2020;**29**:1153–71.
Ward MH, Jones RR, Brender JD *et al.* Drinking water nitrate and human health: An updated review. *Int J Environ Res Public Health* 2018;**15**:1–31.
Warnecke M, Aigner T. Influence of subtle paleo-tectonics on facies and reservoir distribution in epeiric carbonates: Integrating stratigraphic analysis and modelling (U. Muschelkalk, SW Germany). *Sediment Geol* 2019;**383**:82–100.
Zarnetske JP, Haggerty R, Wondzell SM *et al.* Labile dissolved organic carbon supply limits hyporheic denitrification. *J Geophys Res Biogeosciences* 2011;**116**, DOI: 10.1029/2011JG001730.
Zeeh S, Geng A. Origin and diagenesis of dolomite from the Muschelkalk Group (Middle Triassic) of SW Germany. *Neues Jahrb für Geol und Paläontologie - Abhandlungen* 2001;**221**:359–95.
Zhang Y-C, Prommer H, Broers HP *et al.* Model-based integration and analysis of biogeochemical and isotopic dynamics in a nitrate-polluted pyritic aquifer. *Environ Sci & Technol* 2013;**47**:10415—10422.
Ziegler PA. Geological Atlas of Western and Central Europe. 2nd Edition. *Shell Int Pet Mij BV Geol Soc* 1990.

11. **Supplementary information on:** Nitrate reduction potential of a fractured Middle Triassic carbonate aquifer in southwest Germany

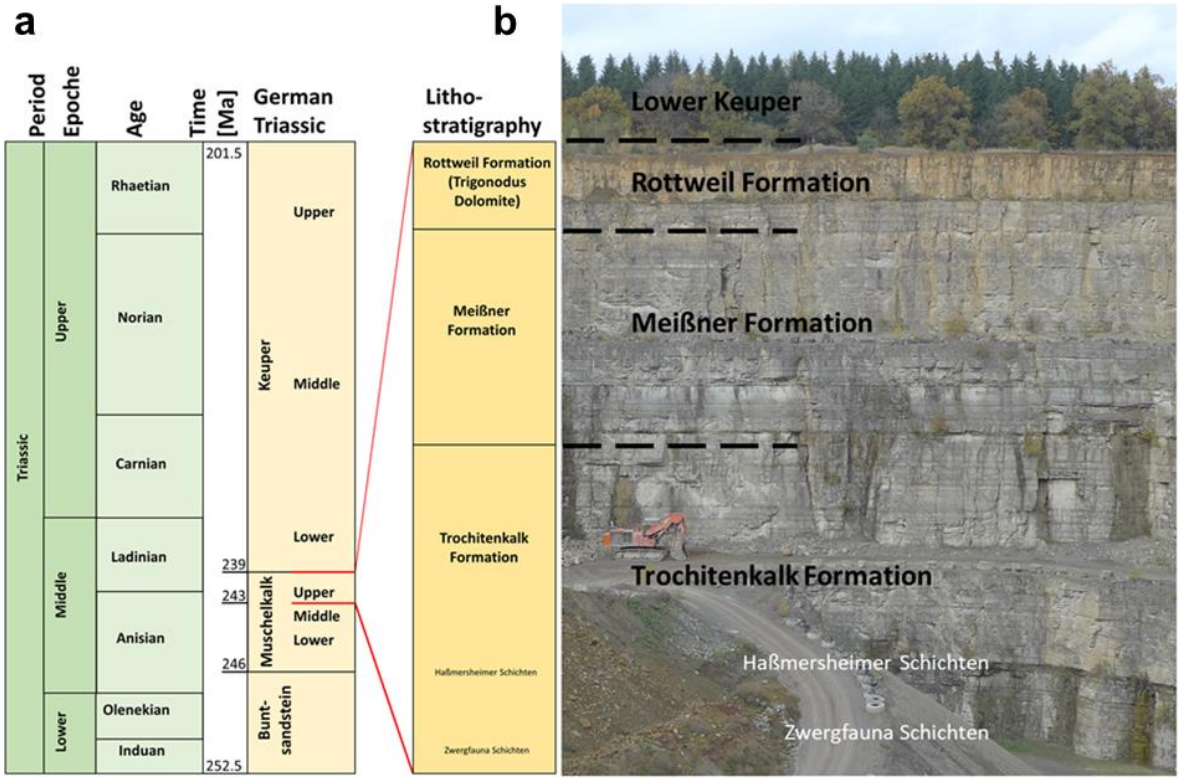

Figure S1. a Chronostratigraphic overview of the German Triassic (Menning 2018). **b** Lithostratigraphy of the Upper Muschelkalk in SW Germany during the Middle Triassic (left) with outcrop photography of the Upper Muschelkalk in the quarry of Mötzingen (right).

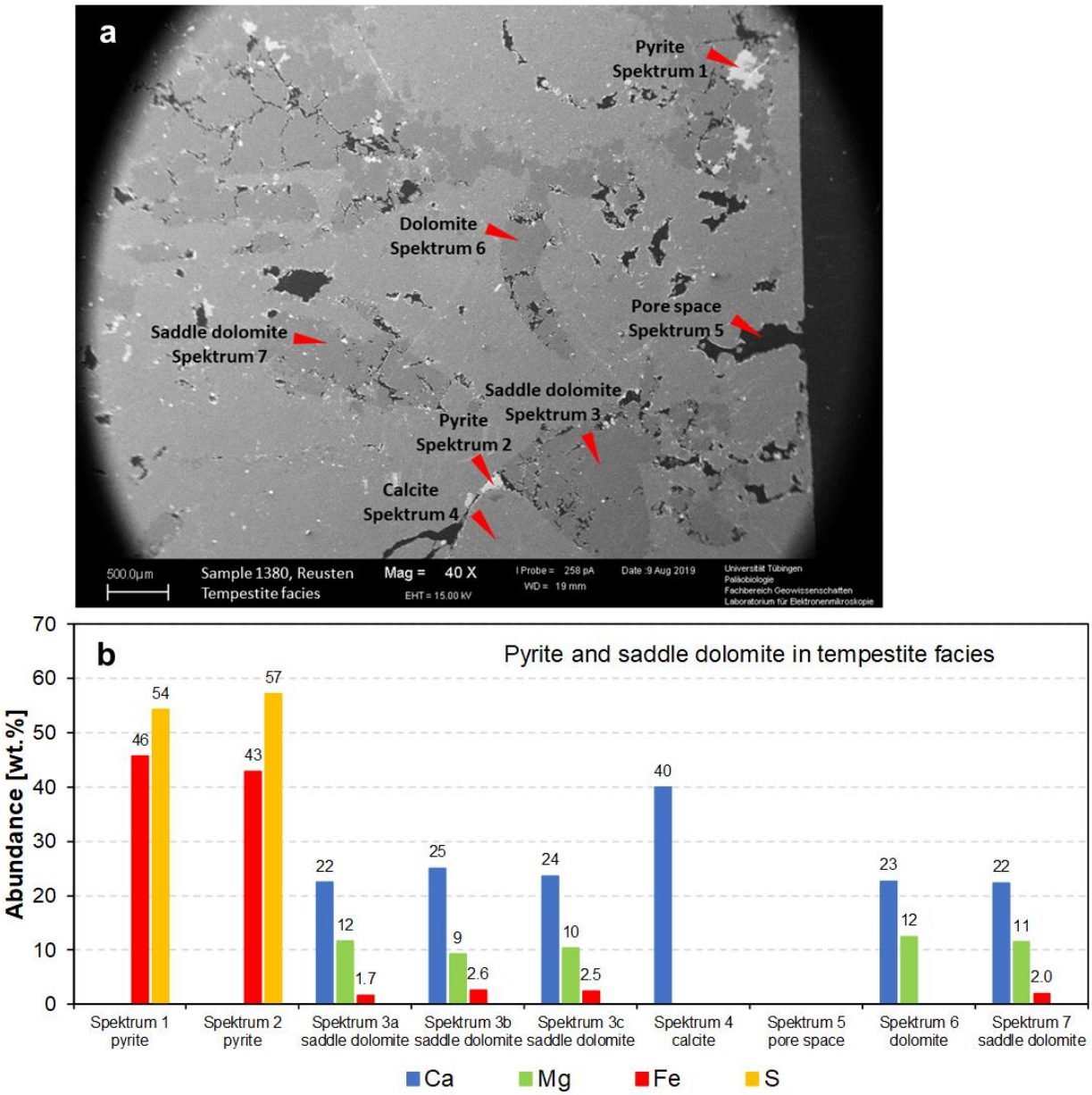

Figure S2. a Scanning electron microscope image of tempestite facies showing location of EDX spectra. **b** Abundances of main elements according to EDX spectroscopy.

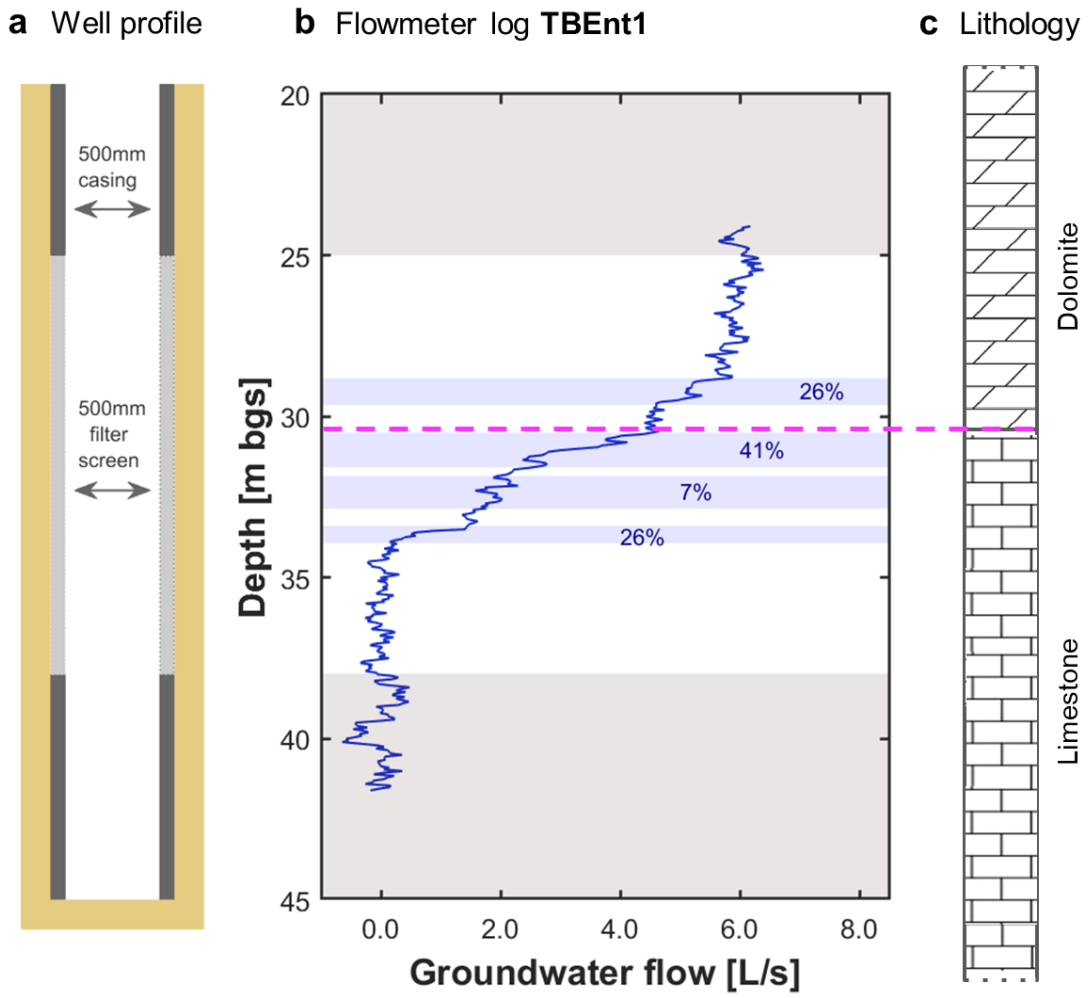

Figure S3. a Schematic well profile of the supply well TBEnt1. **b** Flowmeter log at TBEnt1 for a pumping rate of 6.0 L/s. Zones of significant groundwater inflow are characterized by steep increases in (vertical) groundwater flow indicated by blue-shaded areas. Variability of the baseline limits the detection of inflows with a contribution of >5%. **c** Lithology of the Muschelkalk according to the drilling profile and to the geological model of D'Affonseca et al. (2020). Note that the top and the base of the Muschelkalk are outside the studied well section.

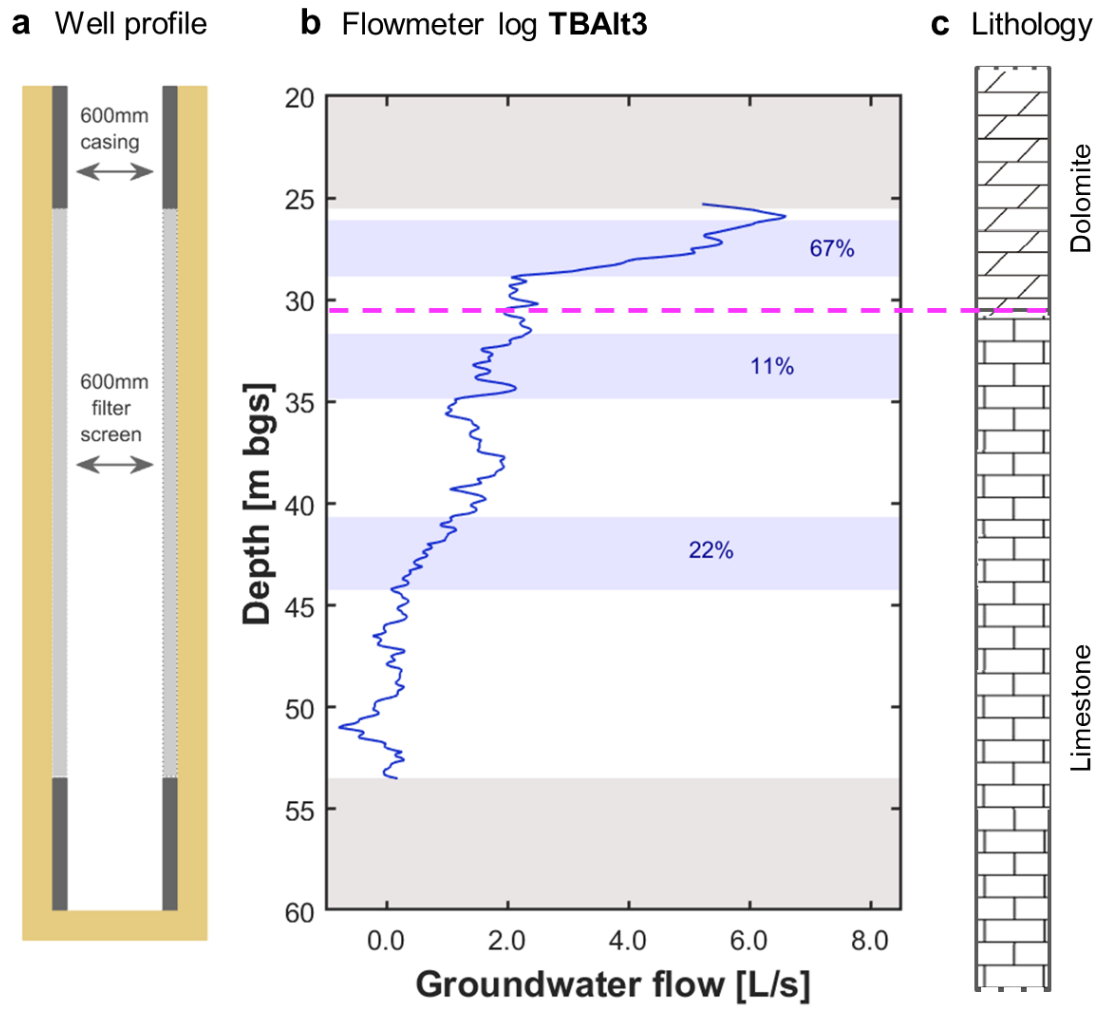

Figure S4. a Schematic well profile of the supply well TBAlt3. **b** Flowmeter log at TBAlt3 for a pumping rate of 6.6 L/s. Zones of significant groundwater inflow are characterized by steep increases in (vertical) groundwater flow indicated by blue-shaded areas. Variability of the baseline limits the detection of inflows with a contribution of >5%. **c** Lithology of the Muschelkalk according to the drilling profile and to the geological model of D'Affonseca et al. (2020). Note that the top and the base of the Muschelkalk are outside the studied well section.

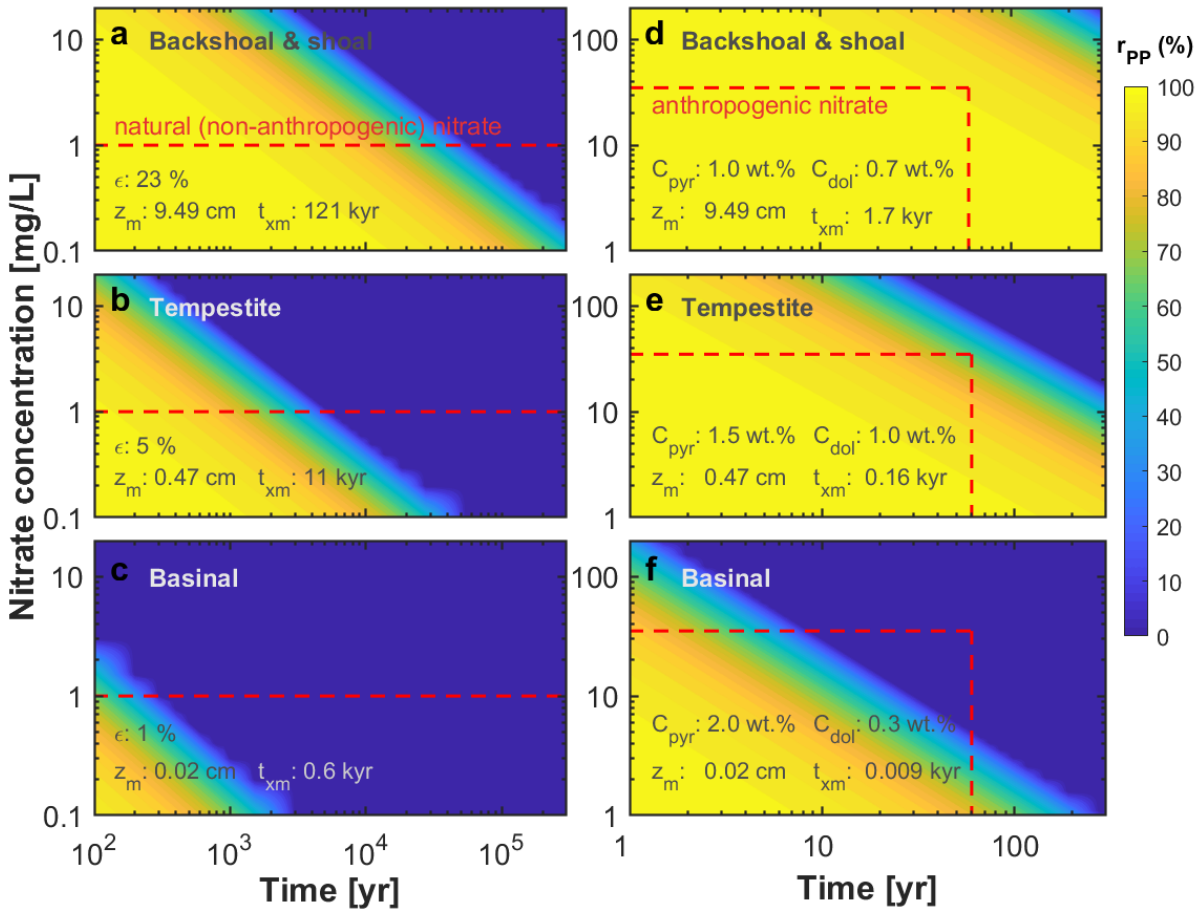

Figure S5. Remaining well-protective nitrate reduction potential r_{PP} (in %) as a function of the NO_3^- concentration and time, calculated for a larger fracture spacing of d = 40 m as compared to the base case in Figure 8 (d = 10 m). **a-c** Contours for long-term natural NO_3^- input concentrations for the different facies. The dashed red line assumes low NO_3^- background values in groundwater ($C_{NO3} = 1$ mg/L) over long (but unknown) periods of time. **d-f** Contours for high NO_3^- concentrations resulting from anthropogenic N additions for the different facies. The dashed red line highlights the approximated time of high nitrate conditions ($C_{NO3} =$ 35 mg/L) representing average NO_3^- concentrations in the study area. Values for t_{xm} and $z_m(x = 0)$ refer to the time when the well-protective nitrate reduction will be entirely depleted ($r_{PP} = 0$) and the depth the reaction front has propagated into the matrix at the upgradient boundary of the anoxic zone at this time.

12. Discussion and outlook

12.1. Novel autotrophic nitrate reducing Fe(II)-oxidizing enrichment culture from organic depleted aquifer

One of the biggest challenges in studying autotrophic nitrate reduction coupled to Fe(II) oxidation in aquifers is the lack of available NRFeOx cultures that could be used in the laboratory for mechanistic studies of this environmentally relevant process. The enrichment of these bacteria is very often unsuccessful due to limited accessibility to low-organic subsurface ecosystems, low energy yield from microbial nitrate removal coupled to Fe(II) oxidation when compared to organotrophic pathways, characteristic low cell numbers and slow growth, or carryover of organic substrates from the original habitat. In this study, the autotrophic NRFeOx bacterial culture was enriched through the *in-situ* incubation of Fe(II)-containing limestone particles in one of the groundwater monitoring wells (described in Chapters 2, 3). The long-term exposure of the aquifer water to Fe(II) allowed for sufficient growth of bacterial cells such that an aliquot could then be transferred to a liquid medium supplied with Fe(II) and nitrate, and since then (2017), maintained under these conditions. Several bacterial strains such as *Acidovorax* sp. strains BoFeN1 and 2AN, as well as, *Acidovorax ebreus* strain TPSY, *Paracoccus denitrificans* Pd 1222, and *Pseudogulbenkiania* sp. strain 2002 were previously proposed to be autotrophic NRFeOx bacteria, however, many of these strains are typically pre-grown on organic substates or organic compounds are added as co-substrates, therefore their autotrophy is questionable (Bryce *et al.* 2018). Here, the enriched community was observed to continuously perform nitrate reduction and Fe(II) oxidation with CO_2 as the only carbon source, providing evidence that the community is able to sustain cell growth under autotrophic conditions. After culture KS (Straub et al. 1996b) and culture BP (Huang et al. 2021), the novel enriched culture is only the third known autotrophic NRFeOx culture that can be continuously grown in a laboratory, and the only one originating from oligotrophic environment. The enrichment of the autotrophic NRFeOx culture demonstrates that the indigenous bacteria of the aquifer in the Ammer catchment are capable of autotrophic nitrate reduction coupled to Fe(II) oxidation, proving that this process is a feasible mechanism for nitrate removal at this field site. The relevance of this process for the Muschelkalk aquifer was further confirmed by comparing community composition between the enrichment culture and the groundwater from the monitoring well from which the bacteria were obtained. 16S rRNA gene amplicon sequencing results showed that both the enriched and the *in-situ* community are dominated by *Betaproteobacteria* with the highest relative abundance of bacteria likely belonging to the *Gallionellaceae* family (49–50% relative abundance) (Chapters 2 and 3). Members of *Gallionellaceae* family are known as obligate microaerophilic bacteria capable of autotrophic growth with Fe(II) as an electron and energy source (Emerson *et al.* 2013), and so far there is no isolated *Gallionellaceae* strain that was shown to be capable of autotrophic growth with Fe(II) under anoxic conditions. However, several recent meta'omic studies demonstrated that *Gallionellaceae* spp. have a

genetic potential to perform nitrate reduction coupled to Fe(II) oxidation (He *et al.* 2016; Jewell *et al.* 2016; Bethencourt *et al.* 2020; Huang *et al.* 2021a, 2021b). The results suggest that *Gallionellaceae* spp. may play an important role in nitrate reduction coupled to Fe(II) oxidation in environments depleted in organic compounds such as the studied aquifer. Additionally, the abundance of the most dominant ASV affiliated to *Gallionellaceae* sp. identified in the culture, reached up to 13% in one of the samples collected in the field site (Blackwell et al, unpublished data) supporting that the enriched culture is a good model to study nitrate dependent Fe(II) oxidation in aquifers as it contains the potential key taxa that live in this ecosystem. The culture can be also used in the future studies targeting development of isolation strategies and ultimately, to obtain the first isolated strain capable of autotrophic growth solely on Fe(II) and NO_3^-.

12.2. Nitrate dependent Fe(II) oxidation: a multifarious process?

The autotrophic NRFeOx enrichment culture performs nitrate reduction coupled to Fe(II) oxidation with an average $nitrate_{reduced}/Fe(II)_{oxidized}$ ratio of 0.28±0.1, this ratio is comparable to the theoretical ratio that is calculated for this process coupled to complete denitrification (nitrate reduction to N_2; Chapters 2, 3). However, the resulting ratio should be slightly lower since part of the electrons stemming from Fe(II) oxidation should be used for CO_2 fixation (Laufer, Røy and Jørgensen 2016), suggesting that nitrate removal performed by this culture cannot be explained solely by complete nitrate reduction coupled to Fe(II) oxidation. Indeed, gas measurements showed that both N_2O and N_2 were the products of the reaction. However, the measured concentrations of the gases did not close the nitrogen balance, implying that the remaining part of the nitrate must have been converted to NO (no detectable NO_2^- was produced during incubation). Alternatively, some part of the nitrate could have been converted to ammonium in a process called DNRA, however, only a few studies have suggested that DNRA can be coupled to Fe(II) oxidation (Robertson *et al.* 2016; Robertson and Thamdrup 2017) and, so far, there is no culture-based support for the existence of this process. Additionally, quantification of dissolved ammonium in the enrichment culture showed that its overall concentration decreased slightly over time, meaning that if any ammonium was produced due to nitrate reduction, its concentration was lower than the amount of ammonium that was consumed by the microbes during the incubation. Ultimately, this raises the question about a potential cryptic ammonium cycle. Next, the potential role of the organic carbon was investigated in a series of experiments, in which the culture was inoculated into medium with nitrate but without any addition of Fe(II). The experiments showed that some nitrate consumption and cell generation was observed in setups where no electron donor was supplied, albeit much lower than setups with nitrate and Fe(II). This implies that only part of nitrate is reduced by truly autotrophic nitrate reducing Fe(II) oxidizers, while the rest is likely consumed through an organotrophic pathway. Potential sources of organic carbon for nitrate reduction in the culture are internally produced organic carbon compounds/secondary metabolites derived by autotrophic NRFeOx bacteria (leading to cross-feeding), traces of organic carbon present as a carryover from inoculum (lysed cells, metabolites), internally stored carbon, or background concentrations of organic carbon in MQ water used for medium preparation. The overall nitrate removal performed by the NRFeOx bacteria both under laboratory conditions and in the natural

environment is, therefore, a complex process resulting from multiple metabolic reactions in which both Fe(II) and, most likely, organic carbon compounds are used as electron donors.

12.3. Nitrate reduction coupled to Fe(II) mineral oxidation

Since only a small fraction of total Fe(II) could be measured in the aquifer as dissolved Fe^{2+}, most of the Fe(II) available for autotrophic NRFeOx bacteria, is present in the form of solids, identified in the aquifer as Fe(II)-bearing minerals such as pyrite/marcasite and Fe(II)-carbonates (Chapter 10, 11). To evaluate the potential of Fe(II)-mineral oxidation coupled to nitrate reduction, the autotrophic NRFeOx culture was incubated in the nitrate-amended medium with batches containing pyrite, siderite, or a mix of both. All biotic treatments showed nitrate reduction, indicating that bacteria could couple denitrification to oxidation of Fe(II)-minerals (Chapters 4, 5). In addition, the computed model was used to test whether, in setups containing both pyrite and siderite, pyrite oxidation was driven by microbes directly i.e. enzymatically, or indirectly, via the oxidation of more bioavailable siderite, which could potentially produce Fe^{3+} and induce abiotic Fe^{3+}-driven pyrite oxidation. The result showed that Fe^{3+} does not contribute significantly to this process. Thus, the study provided compelling evidence for direct microbial oxidation, implying that nitrate reduction coupled to oxidation of pyrite is most likely an enzymatic process and leads to the formation of both sulfate and Fe(III) (oxhyhydr)oxides. Although, the feasibility of pyrite-based autotrophic denitrification was confirmed in the previous studies (e.g., Schwientek et al. 2008; Torrentó et al. 2010; Bosch and Meckenstock 2012), the existence of an enzymatic pathway was questioned since the mechanism bacteria use to mediate the transfer of electrons from insoluble pyrite to nitrate was (and still remains) not well understood. Additionally, some studies suggested that microbial denitrification in setups containing pyrite appears to be induced via oxidation of residual S^0 rather than via Fe(II) oxidation (Yan *et al.*, 2019). In the study presented here, the formation of Fe(III) (oxyhydr)oxides stemming from pyrite oxidation was univocally demonstrated. The exact mechanism is unknown since pyrite could be either oxidized directly by Fe(II) oxidizers or by sulfur oxidizers e.g., *Thiobacillus denitrificans* (Shao, Zhang and Fang 2010) that are present in the culture. Structural sulfur oxidation could result in liberation of Fe(II) from the pyrite, which then, in dissolved form, could have been oxidized by Fe(II) oxidizers. Direct oxidation of Fe(II) from pyrite would require a cell-mineral contact to facilitate transfer of electrons from pyrite to specific Fe(II) oxidase in the outer membrane, while oxidation of pyrite-S followed by oxidation of Fe^{2+}_{aq} would require a cooperation between nitrate dependent sulfur- and Fe(II)-oxidizing bacteria. Alternatively, pyrite-Fe oxidation coupled to nitrate reduction could be facilitated by electron shuttles or organic ligands produced by the microbial community as proposed in the two most recent studies on pyrite oxidation under anoxic conditions by Pang and Wang (2020) and Liu *et al.* (2021). Additionally, some organic acids (e.g., ethylenediaminetetraacetic acid (EDTA)) were found to maintain Fe(III) in an aqueous form, preventing cell encrustation and formation of a passivation layer of Fe(III) (oxyhydr)oxides on the surface of pyrite. This, however, was not confirmed in this study since bacterial cells and minerals surfaces were observed to be partly covered with minerals formed after Fe(II) oxidation and no evidence of Fe^{3+}-driven pyrite oxidation was found, meaning that at least the enriched microbial

community was not able to not produce a sufficient amount of organic compounds that could form aqueous Fe(III)-complexes. It was also observed that, although enough electron donor (pyrite and siderite) was available to theoretically reduce all nitrate in the setups, the reaction was limited and most of the reduction stopped after the consumption of only half of supplied nitrate. The reason for the inhibition is currently unknown, but it could be argued that the precipitation of the Fe(III) (oxyhydr)oxides formed a physical barrier between microbial cells and Fe(II) minerals, and, therefore, stopped the direct transfer of electrons to dedicated proteins involved in Fe(II) oxidation, further supporting the enzymatic character of pyrite oxidation by bacteria. However, more work needs to be done to understand this process on a molecular level.

From the ecological perspective, chemolithoautotrophic oxidation of pyrite (and other Fe(II)-containing minerals) may play a crucial role in isolated subsurface ecosystems such as deep aquifers, as it was previously demonstrated to drive primary biomass production in e.g., subglacial ecosystem, explaining how bacterial communities living there could be sustained in near-isolation from the atmosphere (Boyd *et al.* 2014). In case of the studied aquifer, *Gallionellaceae* spp. could serve as potential primary biomass producers, oxidizing pyrite, reducing nitrate and providing organic compounds for heterotrophic nitrate reduction occurring in addition to the autotrophic pathway, as discussed in the previous section.

From the environmental perspective, neutrophilic Fe(II) oxidation in aquifers may have both positive and negative consequences. For example, besides NO_3^- reduction, pyrite oxidation may result in sequestration and removal of some metals, like arsenic, from groundwater through the production of biogenic Fe(III) minerals. Numerous field and laboratory studies have shown the ability of Fe(III) (oxyhydr)oxides to act as sorbents for arsenic in circumneutral conditions (Sowers *et al.* 2017). On the other hand, pyrite oxidation can also result in the mobilization of pyrite-associated contaminants such as nickel, arsenic, or other heavy metal that are present as impurities within the structure of this mineral (Postma *et al.* 1991; Larsen and Postma 1997; Kjøller, Postma and Larsen 2004). Another negative consequence of nitrate-dependent pyrite oxidation is the potential of N_2O formation. N_2O is classified as a greenhouse gas (Wuebbles 2009), it has 300 times the global warming potential of CO_2 on a time scale of 100 years (Gray 2007) and contributes to stratospheric ozone depletion (Crutzen 1974; Ravishankara, Daniel and Portmann 2009). Studies that tracked N_2O production during denitrification in pyrite-containing systems, demonstrate that the process may result from both heterotrophic denitrification and abiotic reaction between nitrite and Fe(II), leading to the emission of this greenhouse gas (Jones et al. 2015; Pang and Wang 2020). Even though the gas products of the nitrate reduction coupled to pyrite oxidation were not measured in incubations with pyrite, the autotrophic NRFeOx enrichment culture was previously demonstrated to produce N_2O when supplemented with dissolved Fe^{2+} (Jakus *et al.* 2021a). Therefore, it cannot be excluded that enzymatic nitrate reduction coupled to pyrite oxidation performed by the community enriched from the aquifer, also results in N_2O formation. Knowing the extent of N2O production resulting from nitrate reduction coupled to pyrite oxidation is necessary to assess the overall environmental impact of this process and predict both future nitrate concentrations in groundwater and greenhouse gas emissions.

12.4. The ecological role of *Gallionellaceae* sp. in nitrate-polluted environments

The metagenomic analyses of the autotrophic NRFeOx enrichment culture, revealed that the community as a whole has the potential to mediate autotrophic nitrate reduction to N_2 and oxidize Fe(II) since genes encoding CO_2 fixation (e.g. *rbcL, rbcS*), denitrification (e.g. *narGHJI, nirK/S, norBC, nosZ*), and the Fe(II) oxidation (e.g, *cyc2, pcoAB*), were identified (Chapters 6, 7). Additionally, genes encoding oxidation of various species of sulfur (e.g. *sqr, sox*) were found, confirming the observations from the incubation experiments with pyrite that the culture has the potential to reduce nitrate coupled to S oxidation (Jakus *et al.* 2021b). Among reconstructed metagenome-assembled genomes (MAGs), the most dominant *Gallionellaceae* sp. and *Curvibacter* sp. were classified as candidates for truly autotrophic NRFeOx bacteria. Interestingly, both bacteria have the potential to catalyse the dissimilatory reduction of nitrate, nitrite, and nitric oxide, but both lack the *nosZ* reductase (responsible for final step of denitrification – converting nitrous oxide (N_2O) to N_2), most likely leading to the generation of N_2O, whose production was previously observed in the culture (Jakus *et al.* 2021a). However, if sufficient reducing equivalents are available, N_2O can be further reduced via metabolic handoffs to other organisms present in the community, leading to formation of N_2 which was also observed to be present in the incubation experiments.

Interactions between community members can include provision of cofactors, establishment of redox gradients, and turnover of key nutrients to drive biogeochemical cycles (Hug and Co 2018). Even pathways canonically conducted by isolated organisms in laboratory cultures like e.g., denitrification, are instead often the collective product of diverse and interchangeable microbes in the environment (Hug and Co 2018). Such interactions have been previously studied under laboratory conditions using co-cultures (Cooper *et al.* 2020) or mixed enrichment cultures (He *et al.* 2016; Huang *et al.* 2021b). Studies on cultures KS and BP (He *et al.* 2016; Huang *et al.* 2021b, 2021a), suggested that the interspecies interactions between *Gallionellaceae* spp. and other community members are necessary to guarantee continuous autotrophic nitrate reduction coupled to Fe(II) oxidation. *Gallionellaceae* sp. from culture KS, lacks the nitric oxide reductase gene and may partner with flanking populations capable of complete denitrification to avoid toxic metabolite accumulation (He *et al.* 2016). At the same time, the *Gallionellaceae* sp. from culture BP lacks a nitrate reductase, which is critical to initiate nitrate reduction and, therefore, it must rely on other microorganisms (Huang *et al.* 2021b). In contrast, based on the metagenomic analyses, *Gallionellaceae* sp. from the aquifer-originating autotrophic enrichment culture, theoretically does not require such interactions since it has genes that enable reduction of nitrate and removal of toxic N-species. Yet, despite many efforts, the attempts to isolate these bacteria from the culture were so far unsuccessful, suggesting that other pathways other than denitrification, e.g., essential amino acids or vitamins synthesis pathways, are critical for the *Gallionellaceae* sp.. Additionally, the *Gallionellaceae* was shown to not be able to grow under autotrophic microoxic conditions (Chapters 6, 7), suggesting its adaptation to strictly autotrophic anoxic environments.

Although denitrification is not linked to phylogeny (Jones et al., 2008), other *Gallionellaceae* sp. were found to harbour genes related to the denitrification pathway and to be active members of denitrifying

communities. For example, the abundance and activity of the *Gallionellaceae* family rapidly increased, with genes related to denitrification being expressed after artificial nitrate injection into a shallow aquifer (Jewell *et al.* 2016). Another metagenomic study focused on *Gallionellaceae* assemblages in redox transition zones reported the presence of nitrate-reductases in addition to putative genes involved in Fe(II) oxidation, and genes encoding RuBisCO in six recovered metagenome-assembled genomes (MAGs) (Bethencourt *et al.* 2020). Interestingly, none of the MAGs presented in that study possessed the entire denitrification pathway and were lacking at least one of the genes, encoding key enzymes involved in the reduction of other N species. Taken together, these results demonstrate the importance of *Gallionellaceae* spp. in linking biogeochemical cycles of C, N and Fe. Since these microbes were typically classified as microaerophilic Fe(II)-oxidizers, not denitrifiers, their role in the pollutant turnover may have been previously underestimated in environments where high concentrations of nitrate are expected. This is especially important since *Gallionellaceae* sp. were found in many environments such as aquifers (Jewell *et al.* 2016; Bethencourt *et al.* 2020; Jakus *et al.* 2021a), freshwater sediments (He *et al.* 2016), paddy soils (Khalifa *et al.* 2018; Wang *et al.* 2021), drainage waters at the metal mining areas (Kadnikov *et al.* 2016), and drinking water treatment plants (Gülay *et al.* 2018). On the other hand, the omnipresence of these bacteria and their diverse metabolic traits raises a question about their versatility and adaptation strategies in these ecosystems and, in the era of rapidly collected MAGs, calls for the revision of the existing species within the family tree of *Gallionellaceae* (Chapters 8, 9).

12.5. Controls on the fate of nitrate in the organic-poor aquifer

Taken together the results from cultivation experiments (Chapters 2, 3), geochemical analysis and numerical modelling (Chapters 4, 5) and 16S rRNA gene and metagenome sequencing (Chapters 6, 7), the following conclusions can be drawn about the microbial communities and processes impacting the nitrate fate in the studied organic-poor aquifer. (1) The aquifer-inhabiting bacteria have the capability to perform autotrophic nitrate reduction coupled to Fe(II) oxidation. (2) The overall nitrate removal performed by the community is most likely the result of several processes such as e.g., autotrophic and heterotrophic denitrification, involving complex metabolic handoffs between species, and leads to precipitation of Fe(III) (oxyhydr)oxides and formation of N_2O and N_2. (3) Both dissolved and solid Fe(II) sources such as pyrite and Fe(II)-bearing carbonates can be used as electron donors to reduce nitrate under autotrophic conditions. (4) Oxidation of these Fe(II) phases coupled to nitrate reduction is most likely enzymatic. (5) Bacteria belonging to *Gallionellaceae* family are the potential microbial key players in autotrophic denitrification in the studied aquifer.

Therefore, based on the above conclusions and results discussed in Chapters 8-11, an overview of biogeochemical reactions and potential microbial key players controlling the fate of NO_3^- can be summarized as follows: in the studied organic-poor aquifer, conditions favourable for denitrification (e.g., low dissolved oxygen), are restricted to anoxic niches that can develop along the fractures of the phretic zone or epikarst (Visser *et al.,* 2020) and the confined parts of the aquifer (Chapter 10,11). In the confined parts, the replenishment of oxygen is prevented by covering sediment supporting formation of anoxic conditions (Figure 1A, B). High nitrate turnover can be especially expected to

happen at the fractures where flow coincides with high abundance of reactive minerals (e.g., pyrite/marcasite, Fe(II)-bearing carbonate precipitates; Figure 1C) and active nitrate reducing bacteria (Figure 1D). Microbial nitrate reduction in this aquifer was evidenced using isotopes (Visser *et al.* 2020) and in cultivation-based studies (Jakus *et al.* 2021a). Bacterial enrichment cultures obtained from the aquifer were shown to be capable of performing heterotrophic, mixotrophic, and autotrophic denitrification, using organic carbon, organic carbon co-supplied with Fe(II), and Fe(II) respectively. Additionally, some of the enriched microbes were able to grow under microoxic conditions, reflecting the ability of the aquifer-inhabiting community to withstand the presence of oxygen that can be transported along the fractures. Oxygen entering the aquifer reacts either abiotically with Fe(II) phases (Figure 1E.1) or is oxidized by microaerophilic Fe(II) oxidizing bacteria (e.g., *Curvibacter* spp.; Figure 1E.2), both leading to precipitation of Fe(III) (oxhyhydr)oxides. Once all O_2 is exhausted, NO_3^- reduction coupled to organic carbon (C_{org}) oxidation via heterotrophic denitrification (e.g., *Thauera* spp.; Figure 1E.3), and mixotrophic denitrification (with Fe(II) as a co-substrate, e.g., *Methyloversatilis* sp.; Figure 1E.4) commences, likely leading to the formation of N_2O or N_2. Additionally, heterotrophic denitrification leading to the formation of reactive N-species (NO_2^-, NO) (e.g. by *Acidovorax* sp.) may trigger abiotic oxidation of Fe(II) and, as a consequence, further reduce the reactive N-species (chemodenitrification) (Figure 1E.5). Finally, after all bioavailable C_{org} is consumed, NO_3^- can be reduced via oxidation of pyrite or Fe(II)-bearing carbonates by autotrophic denitrifiers, e.g., '*Candidatus* Ferrigenium altingenase' sp. nov. a novel species proposed within the *Gallionellaceae* family, (Chapter 8, 9) enriched from the field site.

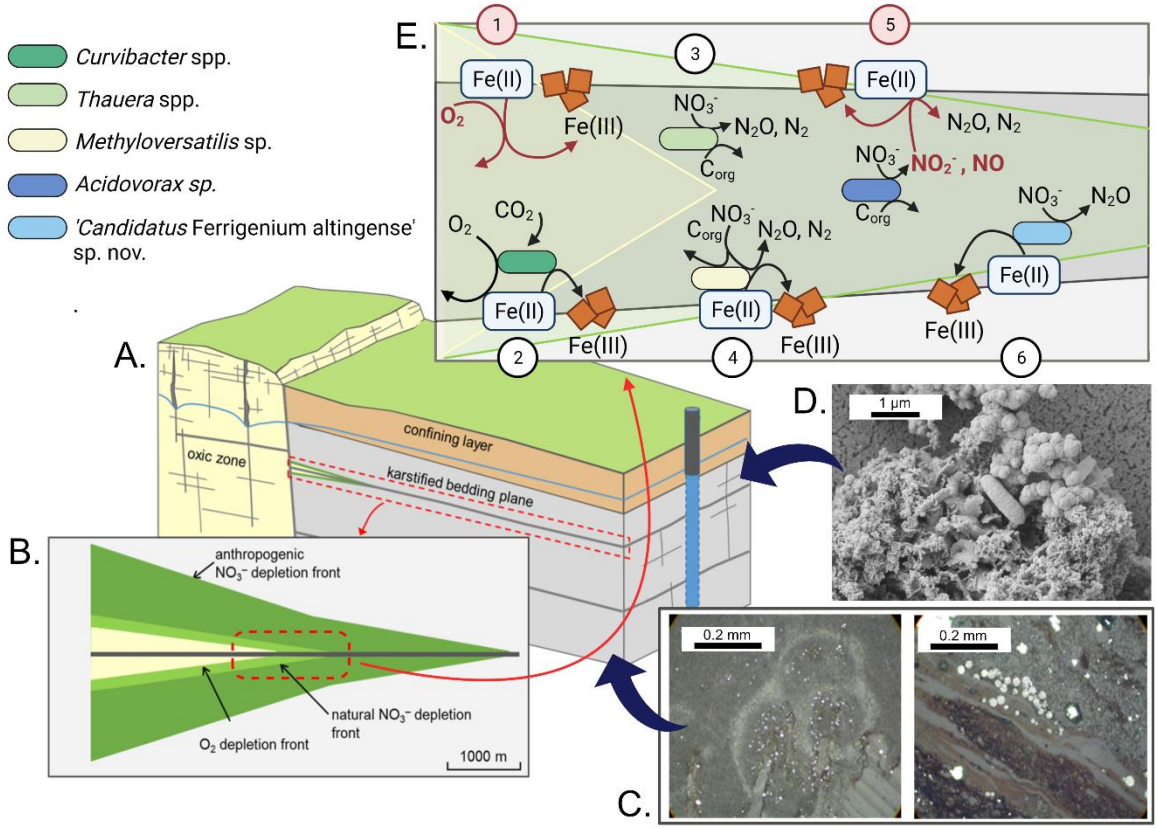

Figure 1. Schematic image of a section across the oxic and confined part of the fractured carbonate aquifer (**A**). The oxic zone is characterized by continuous replenishment of oxygen due to karstic features while confined part stays mostly anoxic and therefore has conditions favourable for nitrate reduction. The dashed red line indicates karstified bedding plane, which represents a zone with advective nitrate transport and hence potential nitrate turnover. The O_2 (yellow) and NO_3^- (green) depletion fronts formed within the bedding plane are shown on illustration **B**. The fronts are formed due to reactions with donor-bearing minerals e.g., pyrite/marcasite (**C**) featured by the plane. A series of abiotic reactions and reactions mediated by aquifer-inhabiting bacteria (**D**) is governing the fate of Fe(II), NO_3^- and O_2 in the zones with high nitrate reduction potential (**E**). The reactions include: abiotic oxidation of Fe(II) by O_2 (**E.1**), microaerophilic oxidation of Fe(II) (**E.2**), heterotrophic denitrification (**E.3**), mixotrophic denitrification (**E.4**), chemodenitrification induced by heterotrophic denitrification and formation of reactive N-species (**E.5**), autotrophic denitrification (**E.6**). Figures adapted from chapters 6 and 10. Numbers in red circles represent abiotic processes. Figure addapted from Chapters 6 and 10.

The above-discussed results have important implications for predicting the fate of nitrate in environmental systems such as freshwater bodies or sediments that are poor in organic carbon, but contain other electron donors like Fe(II)- and S-phases. Specifically, the results emphasize the need to implement direct enzymatic nitrate-dependent pyrite oxidation into reaction simulations when building field-scale models. However, future water management strategies should bear in mind that pyrite present in aquifers, especially ones built of rocks with small pore sizes, are available only in limited amounts and is, under NO_3^- reducing conditions, not renewed. Thus, as already discussed by Schwientek *et al.* (2008), for a long-term groundwater management strategy, remediation of NO_3^- concentrations in drinking water reservoirs should not only rely on autotrophic denitrification fuelled by autochthonous pyrite or Fe(II)-bearing carbonates. The results presented in this thesis likely apply to comparable fractured limestone aquifers but the transferability of the findings to other anoxic nitrate-polluted organic-poor aquifers rich in Fe(II) minerals will be controlled by many factors. For

example, (1) by the presence of alternative electron donors for nitrate reduction such as H_2, CH_4, S-species. (2) the porosity, pore sizes and microbial strategies to deal with spatial separation from substrates or (3) the specific mineral features like the presence of defects and imperfections (steps and kinks) and metal impurities that change conductive properties and make the Fe(II)-bearing minerals less or more prone to oxidation (Chandra and Gerson 2010; Renard *et al.* 2016). The limiting factors of nitrate dependent pyrite oxidation should be therefore addressed in future studies, together with other open questions identified in this study that are described in details in the next section.

12.6. Outlook

This work demonstrated that autotrophic nitrate reduction coupled to Fe(II) oxidation is a feasible nitrate removal mechanism in the fractured organic-poor aquifer consisting of rocks rich in Fe(II) phases. However, the overall contribution of autotrophic NRFeOx bacteria to nitrate reduction, when compared to other autotrophic nitrate removal pathways was not quantified. Therefore, future studies should explore the role of Fe(II) in nitrate reduction when compared to alternative electron donors such as S-compounds, H_2, CH_4 or organic compounds. Groundwater sampling at the field site showed a generally low dissolved organic carbon concentration, however, dissolved organic carbon could still be measured (<2.0 mg/L), meaning that some members of the microbial community can perform nitrate removal coupled to oxidation of organic matter. This could be confirmed by the enrichment of heterotrophic and mixotrophic bacteria using acetate as a substrate. Yet, the *in-situ* bacterial community was found to be dominated by autotrophic bacteria, suggesting that inorganic substrates were preferred over organic matter. Interestingly, the recent studies on the fate of labile organic carbon input into an oligotrophic aquifer demonstrated that the degradation of such organic matter can take days to weeks before the turnover results in a pronounced microbial growth (Hofmann et al. 2020). This raises a question about factors controlling the bioavailability of the organic carbon in aquifers that determine the selection of preferential electron donors for nitrate reduction by groundwater microbial communities. Answering this question would require characterization of organic matter dissolved in groundwater via e.g., a combination of nuclear magnetic resonance (NMR) and Fourier transform ion cyclotron resonance mass spectrometry (FT-ICR-MS). Furthermore, incubation experiments in which various organic versus inorganic substrates should be tested alongside changes of composition and activity analysis of the groundwater community. Understanding how carbon availability impacts autotrophic NRFeOx communities is especially interesting considering the two other existing autotrophic NRFeOx cultures were both isolated from organic-rich freshwater sediments.

Autotrophic NRFeOx bacteria enriched in this study have been shown to generate biomass while growing solely on nitrate and Fe(II). The potential of the culture to fix CO_2 was inferred from metagenome analyses. However, direct evidence of CO_2 fixation performed by the autotrophic members of the community is still missing. Incubation experiments with ^{14}C-labeled CO_2 could provide such evidence. Additionally, when combined with stable isotope probing (SIP) experiments or NanoSIMS and fluorescence *in-situ* hybridization (FISH) as was done previously for culture KS

(Tominski *et al.* 2018), incubation experiments could give more insights into carbon metabolism and pinpoint autotrophic bacteria living in this community.

Quantification of inorganic carbon that can be fixed by the autotrophic bacteria as a result of Fe(II) oxidation could help to estimate the amount of nitrate that was reduced by autotrophic bacteria living in the community and differentiate it from the amount of nitrate reduced heterotrophically. However, the number of electrons that autotrophic NRFeOx bacteria utilize for energy generation (i.e. nitrate reduction) versus biomass production (i.e. CO_2 fixation) is currently unknown. Additionally, the results from incubation experiments suggest that nitrate reduction coupled to Fe(II) oxidation performed by the aquifer-originating enrichment NRFeOx culture is very complex and most likely involves many metabolic processes. Therefore, a detailed mechanistic study involving the quantification of N-species: NO_3^-, NO_2^-, NO, N_2O, N_2, NH_4^+, Fe(II) and Fe(III), and biomass is necessary to learn about the extent of processes such as autotrophic and heterotrophic nitrate reduction, chemodenitrification, DNRA (if it occurs), and nitrogen assimilation from nitrate or ammonium. Moreover, since the studied culture grows under anoxic conditions and yet, dominated by bacteria related to the *Gallionellaceae* family – whose members are known as microaerophiles, intracellular production of oxygen cannot be excluded. Such intracellular production of oxygen is known to form in cultures performing nitrite dependent anaerobic methane oxidation (NDAMO) where oxygen is produced by metabolizing nitrite via nitric oxide into oxygen and dinitrogen gas (Ettwig *et al.* 2010). Internally produced oxygen, in the enrichment culture, could be used by Fe(II)-oxidizing microorganisms (e.g. the most dominant *Gallionellaceae* sp.) or cause abiotic oxidation of Fe(II), however, this theory is highly speculative and require careful investigation.

The results from the incubation experiments with pyrite and siderite indicated that nitrate reduction coupled to oxidation of the two minerals is most likely an enzymatic process. However, the exact mechanism of oxidation of these Fe(II) minerals, especially poorly soluble pyrite, is not well understood. While oxidation of siderite might have been a partly dissolution-controlled process, oxidation of pyrite must have been facilitated by extracellular electron transfer (EET). Since this culture can oxidize both aqueous and solid Fe(II), a meta'omics study aiming to compare the difference in expression of genes putatively involved in Fe(II) oxidation depending on the state of the supplied Fe(II) should be conducted. For example, a recent study performed using *Sideroxydans lithotrophicus* ES-1 demonstrated that genes encoding putative Fe(II)-oxidases like *cyc2* or *mtoB* had a different regulation pattern depending on the source of Fe(II) and Fe(II) oxidation phase (Zhou *et al.* 2021). Future studies should also investigate the potential of biofilm formation on the Fe(II) mineral surfaces by the autotrophic NRFeOx culture and the ability to create local pH microniches around the cells that could maintain Fe(III) in a dissolved state as was previously done using confocal laser scanning microscopy (CLSM) imaging of photoferrotrophic bacterial cells (Hegler et al. 2010). More focus should also be put on the role of organic compounds excreted by microorganisms that could act as electron shuttles or organic ligands and facilitate pyrite oxidation (Liu et al. 2019; Pang and Wang 2020). Understanding how (and if) such organic compounds can act as electron shuttles and facilitate pyrite oxidation coupled to nitrate reduction is especially important for answering the question of how aquifer-inhabiting microorganisms can overcome the limited accessibility to pyrite caused by the small sizes of the rock matrix pores. Identification of potential metabolites playing a key role in Fe(II)

oxidation could be achieved by applying metabolomics in addition to other meta'omic methods in a study where the impact of different sources of Fe(II) on the metatranscriptome (or metaproteome) and metabolome profiles could be compared.

Finally, metatransciptomics and metaproteomics should be applied to the autotrophic enrichment culture, in the future, to verify the potential metabolic functions and interdependencies that were proposed based on the metagenomic results in this study. The meta'omics data could then be used to design a strain-specific medium (e.g., by considering the missing ability to synthesize certain essential amino acids or vitamins) to isolate the most dominant *Gallionellaceae* sp.. In addition, methods like cell sorting could be used to increase the chance of isolation by eliminating other bacteria, that while growing under different conditions, may outcompete the *Gallionellaceae* (e.g., *Curvibacter* sp. growing under microoxic conditions in this study). The combination of novel sequencing techniques with standard isolation methods will hopefully result in successful isolation of the first truly autotrophic NRFeOx bacteria, which is a key for more detailed studies on physiology and metabolism of these enigmatic bacteria.

Filling the listed knowledge gaps will shed light on groundwater bacterial communities living under the limitation of electron donors and allow the development of effective strategies for the management of nitrate pollution in regions dominated by fractured aquifers ensuring their long-term capacity of drinking water supply.

References

Bethencourt L, Bochet O, Farasin J *et al.* Genome reconstruction reveals distinct assemblages of *Gallionellaceae* in surface and subsurface redox transition zones. *FEMS Microbiol Ecol* 2020;**96**:1–13.

Bosch J, Meckenstock RU. Rates and potential mechanism of anaerobic nitrate-dependent microbial pyrite oxidation. *Biochem Soc Trans* 2012;**40**:1280–3.

Boyd ES, Hamilton TL, Havig JR *et al.* Chemolithotrophic primary production in a subglacial ecosystem. *Appl Environ Microbiol* 2014;**80**:6146–53.

Bryce C, Blackwell N, Schmidt C *et al.* Microbial anaerobic Fe(II) oxidation - ecology, mechanisms and environmental implications. *Environ Microbiol* 2018;**20**:3462–83.

Capua F Di, Pirozzi F, Lens PNL *et al.* Electron donors for autotrophic denitrification. *Chem Eng J* 2019;**362**:922–37.

Chandra AP, Gerson AR. The mechanisms of pyrite oxidation and leaching: A fundamental perspective. *Surf Sci Rep* 2010;**65**:293–315.

Cooper RE, Wegner CE, Kügler S *et al.* Iron is not everything: unexpected complex metabolic responses between iron-cycling microorganisms. *ISME J* 2020;**14**:2675–90.

Crutzen PJ. Photochemical reactions initiated by and influencing ozone in unpolluted tropospheric air. *Tellus* 1974;**26**:47–57.

Ettwig KF, Butler MK, Le Paslier D *et al.* Nitrite-driven anaerobic methane oxidation by oxygenic bacteria. *Nature* 2010;**464**:543–8.

Gray V. Climate change 2007: The physical science basis summary for policymakers. *Energy Environ* 2007;**18**:433–40.

Gülay A, Çekiç Y, Musovic S *et al.* Diversity of iron oxidizers in groundwater-fed rapid sand filters: Evidence of Fe(II)-dependent growth by *Curvibacter* and *Undibacterium* spp. *Front Microbiol* 2018;**9**:1–14.

He S, Tominski C, Kappler A *et al.* Metagenomic analyses of the autotrophic Fe(II)-oxidizing, nitrate-reducing enrichment culture KS. *Appl Environ Microbiol* 2016;**82**:2656–68.

Hegler F, Schmidt C, Schwarz H *et al.* Does a low-pH microenvironment around phototrophic FeII-oxidizing bacteria prevent cell encrustation by FeIII minerals? *FEMS Microbiol Ecol* 2010;**74**:592–600.

Hofmann R, Uhl J, Hertkorn N *et al.* Linkage between dissolved organic matter transformation, bacterial carbon production, and diversity in a shallow oligotrophic aquifer: results from flow-through sediment microcosm experiments . *Front Microbiol* 2020;**11**:2425.

Huang Y-M, Straub D, Blackwell N *et al.* Meta-omics reveal *Gallionellaceae* and *Rhodanobacter* as interdependent key players for Fe(II) oxidation and nitrate reduction in the autotrophic enrichment culture KS. *Revis* 2021a, DOI: 10.1128/aem.00496-21.

Huang Y-M, Straub D, Kappler A *et al.* A novel enrichment culture highlights core features of microbial networks contributing to autotrophic Fe(II) oxidation coupled to nitrate reduction. *Microb Physiol* 2021b;**In press**.

Hug LA, Co R. It Takes a village: Microbial communities thrive through interactions and metabolic handoffs. *mSystems* 2018;**3**:1–5.

Jakus N, Blackwell N, Osenbrück K *et al.* Nitrate removal by a novel lithoautotrophic nitrate-reducing iron(II)-oxidizing culture enriched from a pyrite-rich limestone aquifer. *Appl Environ Microbiol* 2021a, DOI: 10.1128/AEM.00460-21.

Jakus N, Mellage A, Hoeschen C *et al.* Anaerobic neutrophilic pyrite oxidation by a chemolithoautotrophic nitrate-reducing iron(II)-oxidizing culture enriched from a fractured aquifer. *Environ Sci Technol* 2021b, DOI: https://doi.org/10.1021/acs.est.1c02049.

Jewell TNM, Karaoz U, Brodie EL *et al.* Metatranscriptomic evidence of pervasive and diverse chemolithoautotrophy relevant to C, S, N and Fe cycling in a shallow alluvial aquifer. *ISME J* 2016;**10**:2106–17.

Jones LC, Peters B, Lezama Pacheco JS *et al.* Stable isotopes and iron oxide mineral products as markers of chemodenitrification. *Environ Sci Technol* 2015;**49**:3444–52.

Kadnikov V V., Ivasenko DA, Beletskii A V. *et al.* A novel uncultured bacterium of the family *Gallionellaceae*: Description and genome reconstruction based on metagenomic analysis of microbial community in acid mine drainage. *Microbiol Russian Fed* 2016;**85**:449–61.

Khalifa A, Nakasuji Y, Saka N *et al. Ferrigenium kumadai* gen. nov., sp. nov., a microaerophilic iron-oxidizing bacterium isolated from a paddy field soil. 2018:2587–92.

Kjøller C, Postma D, Larsen F. Groundwater acidification and the mobilization of trace metals in a sandy aquifer. *Environ Sci Technol* 2004;**38**:2829–35.

Larsen F, Postma D. Nickel mobilization in a groundwater well field: Release by pyrite oxidation and desorption from manganese oxides. *Environ Sci Technol* 1997;**31**:2589–95.

Laufer K, Røy H, Jørgensen B. Evidence for the existence of autotrophic nitrate-reducing Fe(II)-oxidizing bacteria in marine coastal sediment. *Appl Environ Microbiol* 2016;**82**:6120–31.

Liu T, Chen D, Li X *et al.* Microbially mediated coupling of nitrate reduction and Fe(II) oxidation under anoxic conditions. *FEMS Microbiol Ecol* 2019;**95**:1–12.
Liu T, Hu Y, Chen N *et al.* High redox potential promotes oxidation of pyrite under neutral conditions: Implications for optimizing pyrite autotrophic denitrification. *J Hazard Mater* 2021;**416**:125844.
Osenbrück K, Blendinger E, Leven C *et al.* Nitrate reduction potential of a fractured Middle Triassic carbonate aquifer in southwest Germany. *Submitted* 2021.
Pang Y, Wang J. Insight into the mechanism of chemoautotrophic denitrification using pyrite (FeS_2) as electron donor. *Bioresour Technol* 2020;**318**:124105.
Postma D, Boesen C, Kristiansen H *et al.* Nitrate reduction in an unconfined sandy aquifer: water chemistry, reduction processes, and geochemical modeling. *Water Resour Res* 1991;**27**:2027–45.
Ravishankara AR, Daniel JS, Portmann RW. Nitrous oxide (N_2O): The dominant ozone-depleting substance emitted in the 21st century. *Science (80-)* 2009;**326**:123–5.
Renard F, Putnis C V, Montes-Hernandez G *et al.* Siderite dissolution coupled to iron oxyhydroxide precipitation in the presence of arsenic revealed by nanoscale imaging. *Chem Geol* 2016, DOI: 10.1016/j.chemgeo.2016.12.001.
Robertson EK, Roberts KL, Burdorf LDW *et al.* Dissimilatory nitrate reduction to ammonium coupled to Fe(II) oxidation in sediments of a periodically hypoxic estuary. *Limnol Oceanogr* 2016;**61**:365–81.
Robertson EK, Thamdrup B. The fate of nitrogen is linked to iron(II) availability in a freshwater lake sediment. *Geochim Cosmochim Acta* 2017;**205**:84–99.
Schwientek M, Einsiedl F, Stichler W *et al.* Evidence for denitrification regulated by pyrite oxidation in a heterogeneous porous groundwater system. *Chem Geol* 2008;**255**:60–7.
Shao MF, Zhang T, Fang HHP. Sulfur-driven autotrophic denitrification: Diversity, biochemistry, and engineering applications. *Appl Microbiol Biotechnol* 2010;**88**:1027–42.
Sowers TD, Harrington JM, Polizzotto ML *et al.* Sorption of arsenic to biogenic iron (oxyhydr)oxides produced in circumneutral environments. *Geochim Cosmochim Acta* 2017;**198**:194–207.
Tominski C, Lösekann-Behrens T, Ruecker A *et al.* Insights into carbon metabolism provided by fluorescence *in situ* hybridization-secondary ion mass spectrometry imaging of an autotrophic, nitrate-reducing, Fe(II)-oxidizing enrichment culture. *Appl Environ Microbiol* 2018;**84**:1–19.
Torrentó C, Cama J, Urmeneta J *et al.* Denitrification of groundwater with pyrite and *Thiobacillus denitrificans*. *Chem Geol* 2010;**278**:80–91.
Visser AN, Lehmann MF, Rügner H *et al.* Fate of nitrate during groundwater recharge in a fractured karst aquifer in Southwest Germany. *Hydrogeol J* 2020;**29**:1153–71.
Wang J, Ma Y, Di L *et al.* Straw incorporation with nitrogen amendment shapes bacterial community structure in an iron-rich paddy soil by altering nitrogen reserves. *Microorganisms* 2021;**9**, DOI: 10.3390/microorganisms9050988.
Wuebbles DJ. Nitrous oxide: No laughing matter. *Science (80-)* 2009;**326**:56–7.
Zhou N, Keffer J, Polson S *et al.* Unravelling *Sideroxydans lithotrophicus* ES-1 Fe(II)-oxidizing pathway using transcriptomics and RT-qPCR. *Goldschmidt Conf* 2021.

Statement of personal contribiution

This work was supported by the Collaborative Research Center 1253 CAMPOS (Project 5: Fractured Aquifer), funded by the German Research Foundation (Deutsche Forschungsgemeinschaft, grant agreement SFB 1253/1). The conceptual background to this project was designed by Prof. Andreas Kappler, Jun.-Prof. Dr. Sara Kleindienst and Prof. Dr. Peter Grathwohl. Prof. Dr. Kappler was the main supervisor throughout the project and Jun.-Prof. Dr. Sara Kleindienst was the second supervisor. Unless stated otherwise, experiments were either conceptualized by myself or together with Prof. Dr. Kappler and/or Jun.-Prof. Dr. Sara Kleindienst and were carried out by me. The discussion and analysis of the obtained results, as well as writing all manuscripts were completed in cooperation with Prof. Dr. Kappler and for chapters 2, 3, 4, 5,6 and 7 also in cooperation with Jun.-Prof. Dr. Sara Kleindienst for chapters 2, 3, 6 and 7.

In detail the contributions of people other than Prof. Dr. Kappler and Jun.-Prof. Dr. Sara Kleindienst or myself were:

Deployment and collection of microbial trapping devices, groundwater sampling campaigns were supported by Dr. Nia Blackwell and Dr. Karsten Osenbrück. Visits in the quarries and collection of rock samples were organized and/or assisted by Dr. Karsten Osenbrück, Dr. Eva Blendinger, Dr. Hermann Rügner, and Dr. Fernando M. D'Affonseca.

Chapters 2 and 3: Ellen Röhm performed nitrate and nitrite analyses, Dr. André Pellerin did AVS measurements. Dr. Anna-Neva Visser developed and tested microbial trapping devices (MTDs). Franziska Schädler advised on DNA extractions. Dr. Nia Blackwell helped to conceptualize bacterial enrichment strategy and helped with sequencing data interpretation and analysis. Dr. Karsten Osenbrück, provided geochemical analysis of groundwater, Daniel Straub processed sequencing data, Dr. James M. Byrne performed Mössbauer spectroscopy and scanning electron microscopy on prepared samples. Zhe Wang and Prof. Dr. Tillmann Lueders sequenced provided long-read 16S rRNA gene sequences. David Glöckler and Prof. Dr. Martin Elsner provided isotopic analysis of gaseous nitrogen species. Prof. Dr. Peter Grathwohl and all other co-authors contributed to manuscript revisions and/or wrote parts of the manuscript. Dr. Daniel Straub was funded by the Institutional Strategy of the University of Tübingen (DFG, ZUK63). Jun-Prof. Dr. Sara Kleindienst was funded by an Emmy Noether grant (project ID 326028733) from the DFG. The authors of the manuscript acknowledge support by the state of Baden-Württemberg through bwHPC and the German Research Foundation (DFG) through grant no INST 37/935-1 FUGG (bwForCluster BinAC).

Chapters 4 and 5: NanoSIMS analysis were done at the Institute of Analytical Sciences and Physico-Chemistry for Environment and Materials (IPREM UMR 5254, CNRS/UPPA, Pau, France) with Cameca courtesy. Dr. Celine Defouilloy collected NanoSIMS data, Prof. Dr. Dirk Schaumlöffel and Dr. Maria Angels Subirana gave access to faculties at IPREM. Prof. Dr. Stefan Peiffer, Jutta Eckert

and Karel As shared protocols and practical advice for elemental sulfur measurements. Zhe Zhou measured Mössbauer samples and helped with interpretation. SEM was conducted at the Center for Light-Matter Interaction, Sensors & Analytics (LISA+) with a help of Timm Bayer. Ellen Röhm advised on IC and HPLC measurements and Franziska Schädler performed nitrate and nitrite analysis. Dr. Adrian Mellage wrote numerical reaction models and helped with interpretation. Dr. Carmen Höschen and Prof. Dr. Carsten W. Mueller helped with experimental design and NanoSIMS data collection and interpretation. Dr. Markus Maisch and Dr. James M. Byrne interpreted Mössbauer spectra. Additionally, Dr. James M. Byrne improved the experimental design and advised on mineral synthesis. Prof. Dr. Peter Grathwohl contributed to the discussion of the results. All co-authors revised the manuscript.

Chapters 6 and 7: Franziska Schädler performed nitrate and nitrite analysis. Stefanie Becker, Caroline Schlaiss, and Jonah Schooss helped with the maintenance of cultures and DNA extractions. Dr. Nia Blackwell contributed to the design of the study and interpret the data. Dr. Daniel Straub processed DNA sequences and analysed the data. All authors commented and revised the manuscript. Infrastructural support was provided by the DFG under Germany's Excellence Strategy, cluster of Excellence EXC2124 (project ID 390838134).

Chapters 8 to 11 are manuscripts describing work in associated projects to which I contributed by providing and/or analysing the data and revising the text.

I state hereby that I have not plagiarized or copied any of the text. Chapter 2 together with supplementary data included in chapter 3 have been published in Applied and Environmental Microbiology Journal. Chapter 4 together with supplementary data included in chapter 5 have been published in Environmental Science and Technology Journal. Chapters 6-11 were submitted to different scientific journals, they may be published in a slightly modified version elsewhere in the future.

List of publications and conference contributions

Accepted publications

Jakus N, Blackwell N, Osenbrück K, Straub D, Byrne JM, Wang Z, Glöckler D, Elsner M, Lueders T, Grathwohl P, Kleindienst S, Kappler A. 2021. Nitrate removal by a novel lithoautotrophic nitrate-reducing iron(II)-oxidizing culture enriched from a pyrite-rich limestone aquifer. *Appl Environ Microbiol.* https://doi.org/10.1128/AEM.00460-21.

Jakus N, Mellage A, Hoeschen C, Maisch M, Byrne JM, Mueller CW, Grathwohl P, Kappler A. 2021. Anaerobic neutrophilic pyrite oxidation by a chemolithoautotrophic nitrate-reducing iron(II)-oxidizing culture enriched from a fractured aquifer. *Environ Sci Technol.* https://doi.org/10.1021/acs.est.1c02049.

Submitted manuscripts

Jakus N, Blackwell N, Straub D, Kappler A, Kleindienst S. Presence of Fe(II) and nitrate shapes aquifer-originating denitrifying communities leading to an enrichment of autotrophic Fe(II)-oxidizing *Gallionellaceae* sp. under organic carbon limitation.

Huang Y-M, Jakus N, Straub D, Konstantinidisd KT, Blackwell N, Kappler A, Kleindienst S. '*Candidatus* Ferrigenium straubiae' sp. nov., '*Candidatus* Ferrigenium bremense' sp. nov., '*Candidatus* Ferrigenium altingense' sp. nov., are autotrophic Fe(II)-oxidizing bacteria of the family *Gallionellaceae*.

Osenbrück K, Blendinger E, Leven C, Rügner H, Finkel M, Jakus N, Schulz H, Grathwohl P. 2021. Nitrate reduction potential of a fractured Middle Triassic carbonate aquifer in southwest Germany.

Schad M, Halama M, Jakus N, Robbins LJ, Warchola TJ, Tejada J, Kirchhof R, Lalonde S V., Swanner ED, Planavsky NJ, Thorwarth H, Mansor M, Konhauser KO, Kappler A. 2021. Phosphate remobilization from banded iron formations during metamorphic mineral transformations.

Conference contribiutions

2018 **ISME 17**. Poster presentation. Jakus N, Blackwell N, Visser A-N, Grathwohl P, Kappler A, Kleindienst S. Microbial community analysis and determination of rate-limiting factors of microbial nitrate turnover in a pyrite-rich limestone aquifer.

2018 **1st CAMPOS Science Meeting & 2nd CAMPOS General Assembly.** Poster presentation. Jakus N, Blackwell N, Kurtunov J, Visser A-N, Martin J, Osenbrück K, Grathwohl P, Kleindienst S, Kappler A. Microbial key players involved in nitrate degradation in a fractured aquifer.

2019 **Goldschmidt.** Oral presentation. Jakus N, Blackwell N, Osenbrück K, Grathwohl P, Kleindienst S, Kappler A. Iron(II)- and Sulfur-Driven Autotrophic Denitrification in a Pyrite-Rich Limestone Aquifer.

2020 **2nd CAMPOS Science Meeting & 3rd CAMPOS General Assembly.** Oral Presetnation. Jakus N, Blackwell N, Straub D, Osenbrück K, Grathwohl P, Kleindienst S, Kappler. Iron(II) and sulfur driven autotrophic denitrification in a pyrite-rich limestone aquifer

2020 **CAMPOS International Conference.** Virtual poster presentation. Jakus N, Höschen C, Zhou Z, Bayer T, Byrne JM, Blackwell N, Straub D, Mueller C W, Grathwohl P, Kleindienst S, Kappler A. Insights into mechanisms of nitrate-dependent pyrite oxidation by an autotrophic enrichment culture isolated from a pyrite-rich limestone aquifer.

2020 **ISSM2020.** Accepted for oral presentation. Jakus N, Blackwell N, Straub D, Osenbrück K, Grathwohl P, Kleindienst S, Kappler A. Isolation of a novel autotrophic nitrate-reducing iron(II)-oxidizing culture from a nitrate-containing pyrite-rich aquifer.

2020 **EGU.** Poster presentation. Rügner H., Blendinger E., Osenbrück K., Jakus N., Grathwohl P. Denitrification potential and occurrence of reactive minerals in the fractured carbonate aquifer of the Upper Muschelkalk, SW-Germany.

2020 **Goldschmidt.** Virtual oral presentation. Kappler A, Jakus N, Becker S, Kleindienst S, Huang Y-M, Bayer T, Maisch M, Nikeleit V, Byrne JM, Bryce C Fe(III) Mineral Formation by Fe(II)-oxidizing Bacteria – Consequences for Removal of Nitrate.

2021 **Science: Polish Perspectives Conference.** Virtual poster presentation. Jakus N, Grathwohl P, Kleindienst S, Kappler A. The hunt for groundwater-cleaning microbes that remove harmful nitrate.

2021 **Goldschmidt.** Virtual oral presentation. Jakus N, Blackwell N, Mellage A, Straub D, Hoeschen C, Maisch M, Byrne JM, Mueller CW, Grathwohl P, Kleindienst S, Kappler A. Autotrophic nitrate reduction coupled to oxidation of Fe(II) phases by a *Gallionellaceae* sp.-dominated microbial community enriched from a pyrite-rich aquifer